Politecnico di Milano
Department of Physics
Doctoral Programme In Physics

Thin Films of Lead-Free Oxides for Piezoelectric and Ferroelectric Applications

Doctoral Dissertation of:
Chiara Groppi

Supervisor:
Dr. Marco Asa

Tutor:
Prof. Riccardo Bertacco

The Chair of the Doctoral Program:
Prof. Marco Finazzi

2021/2022 – XXXIV

Summary

Electronic technologies are becoming increasingly sophisticated and pervasive in modern everyday lives. Notably, the market for sensors and actuators is exponentially growing year after year, with a wide span of potential applications ranging from the automotive industry to biomedicine, robotics, information technology etc. As a consequence, the development of efficient functional materials for the fabrication and large-scale production of devices is receiving increasing attention and experiencing a growth in popularity. Besides, the urge towards miniaturization of components and the requirement of silicon-compatibility represent some of the key challenges for the integration of novel materials in existing technologies. For example, the need for miniaturization of memory devices requires the development of scalable materials guaranteeing CMOS compatibility and robust information storage.
Some of the most popular and promising materials for the development of actuator, sensor and memory device technologies are piezoelectric and ferroelectric materials. The advantage of such materials relies on the possibility of exploiting the correlation between mechanical deformation and permanent stored charges to electrically tune or transduce mechanical properties.
In this framework, Lead Zirconate Titanate ($PbZr_xTi_{1-x}O_3$, or PZT) now dominates the global piezo- and ferroelectric materials industry related to actuators, sensors and memory devices, estimated to be worth more than 30 billion USD. After holding this position for more than 50 years, the recent legislative activity by the European Union and many other countries in the world intending to ban harmful toxic metals in electrical and electronic components by 2025 is undermining the supremacy of PZT because of its important content of toxic lead (Pb). Indeed, the research in the field of lead-free piezo- and ferroelectrics has seen a notably increased interest in lead-free alternatives to PZT.

This work presents a thorough investigation of two of the most promising lead-free materials as potential candidates for the replacement of PZT in industrial device processes of thin films. The properties of Potassium Sodium Niobate ($K_xNa_{1-x}NbO_3$, or KNN) thin films are investigated in view of developing a viable competitor to PZT for piezoelectric actuator and sensor applications thanks to its sizable piezoelectric responses. The results of the optimization of the material have been carried out in terms of its composition, crystal structure and interfaces (substrate and electrodes). Besides, a protocol was established for the macroscopic characterization of fabricated piezoelectric cantilevers.
Moreover, a study of Zirconium-doped Hafnium Oxide ($Hf_{0.5}Zr_{0.5}O_2$, or HZO) thin films is presented, with a focus on the enhancement of its ferroelectric properties to replace PZT in ferroelectric memory devices.

Preface

This Thesis covers some of the research activity carried out by the author, Chiara Groppi, since the beginning of the Ph.D. fellowship on May 1st, 2019. Ph.D. Marco Asa (PoliFAB) and Prof. Riccardo Bertacco (Politecnico di Milano) have covered the roles of Supervisor and Tutor of this work, respectively. The experimental activity was hosted by two research facilities:

- PoliFAB, the micro- and nanotechnology center of Politecnico di Milano, Milano (Italy) and the associated Nanomagnetism laboratory of the Department of Physics.
- The Zernike Institute for Advanced Materials (ZIAM) of the University of Groningen, Groningen (Netherlands) for a period of three months (March 2022 - May 2022).

This Ph.D. work has resulted in the following publications:

1. Franchini, G., Spinelli, A. S., Nicosia, G., Fumagalli, I., Asa, M., Groppi, C., ... & Compagnoni, C. M. (2020). Characterization and modeling of current transport in metal/ferroelectric/semiconductor tunnel junctions. IEEE Transactions on Electron Devices, 67(9), 3729-3735.
2. Groppi, C., Mondonico, L., Maspero, F., Rinaldi, C., Asa, M., & Bertacco, R. (2021). Effect of substrate preparation on the growth of lead-free piezoelectric (K0. 5Na0. 5) NbO3 on Pt (111). Journal of Applied Physics, 129(19), 194102.
3. Borga, P., Milesi, F., Peserico, N., Groppi, C., Damin, F., Sola, L., ... & Bertacco, R. (2022). Active Opto-Magnetic Biosensing with Silicon Microring Resonators. Sensors, 22(9), 3292.
4. Groppi C., Spadoni S., Vangelista S., Ravizza E., Maspero F., Asa M., Castoldi L. & Bertacco R. (2022). Li diffusion and surface segregation in K0.5Na0.5NbO3 films grown by Pulsed Laser Deposition (in publication by Thin Solid Films)
5. Groppi C., Maspero F., Asa M. & Bertacco R. "Evidence for a square lattice of spontaneous ferroelectric domains in epitaxial K0.5Na0.5NbO3 thin films" (in preparation)
6. Groppi C., Spadoni S., Vangelista S., Maspero F., Asa M., Castoldi L. & Bertacco R. "Influence of Top and Bottom Metal Contacts on Electrical Properties of KNN Thin Films grown on Pt(111) by Pulsed Laser Deposition" (in preparation)

Contents

1 Introduction 1
1.1 Piezoelectric materials and devices . . . 1
1.2 Ferroelectric materials and devices . . . 3
1.3 Lead Zirconate Titanite Pb(Zr,Ti)O_3 . . . 4
1.4 Toxicity of Lead (Pb) . . . 5
1.5 Lead Guidelines and Regulations . . . 7
1.6 Lead-free piezoelectrics . . . 7
1.6.1 Potassium Sodium Niobate (K,Na)NbO_3 . . . 9
1.6.2 Hafnium Oxide . . . 10
1.7 Challenges of thin film materials . . . 12
1.8 Thesis Outlook and motivation . . . 14

2 Theoretical background 17
2.1 Crystal Structure . . . 17
2.2 Dielectric behaviour . . . 18
2.3 Piezoelectricity . . . 19
2.4 Ferroelectricity . . . 21
2.5 Perovskite structure . . . 25
2.6 Phase Boundaries . . . 26
2.7 Origin of ferroelectricity in Zr-doped HfO_2 . . . 29

3 Experimental Methods 31
3.1 Growth Techniques . . . 31
3.1.1 Pulsed Laser Deposition . . . 31
3.2 Material characterization . . . 34
3.2.1 X-ray Diffraction . . . 34
3.2.2 Reflection High Energy Electron Diffraction . . . 35
3.2.3 Scanning Electron Microscopy . . . 37
3.2.4 Energy Dispersive X-ray Spectroscopy . . . 38
3.2.5 Piezoresponse Force Microscopy . . . 39
3.3 Device Fabrication and Characterization . . . 42
3.3.1 Capacitor microfabrication . . . 42
3.3.2 Two-Points Probing . . . 42

3.3.3 Ferroelectric characterization 44

4 Growth optimization: Effect of substrate preparation on KNN/Pt(111) 47
4.1 Introduction 47
4.2 Experimental Methods 48
4.3 Comparison of KNN thin film properties depending on Pt treatment 49
4.3.1 Morphological and structural comparison 49
4.3.2 Modifications of Pt template 51
4.3.3 Dielectric and piezoelectric characterization 51
4.4 Discussion 55
4.5 Conclusions 57

5 Li-doped KNN: Li diffusion and surface segregation 59
5.1 Introduction 59
5.2 Experimental Methods 60
5.3 Analysis of Li^+ incorporation in KNN lattice 61
5.4 Effect of Li-doping on functional properties of KNN 65
5.5 Conclusions 68

6 Epitaxial growth of KNN on Nb:$SrTiO_3$ 69
6.1 Introduction 69
6.2 Experimental Methods 70
6.3 Temperature-dependent growth mode and stoichoimetry-dependent leakage . . . 71
6.4 Square pattern of spontaneous ferroelectric domains 75
6.5 Conclusions 81

7 Interfaces: Impact of top and bottom metal contacts on KNN thin films 83
7.1 Introduction 83
7.2 Experimental Methods 84
7.3 Schottky diode behaviour and differential capacitance at the bottom interface . . 85
7.4 Schottky emission-controlled charge injection at top interface 91
7.5 Conclusions 94

8 Strategies for stabilizing the polar phase in $Hf_{0.5}Zr_{0.5}O_2$ thin films 97
8.1 Introduction 97
8.2 Experimental Methods 98
8.3 Growth and Characterization of HZO/LSMO/STO thin films 98
8.4 Effect of oxygen vacancies on HZO/LSMO/STO by post-growth vacuum annealing 101
8.5 Engineering epitaxial stress: HZO/LSMO/DSO 103
8.6 Conclusions 106

9 Overall conclusions 109

Bibliography 119

CHAPTER 1

Introduction

The demand for electronic devices is on the rise, and the complex requirements of such devices are driving material development ahead. In this picture, the properties exhibited by the classes of functional materials known as piezoelectrics and ferroelectrics has received significant attention for the wide span of potential applications.
The purpose of the research will be explained in this first Chapter, starting with a wide overview on piezoelectric and ferroelectric applications and related research issues. The significance of Lead Zirconate Titanate (PZT) i.e. one of the primary, most known and utilized ferro- and piezoelectric materials is presented, and its features and limitations are highlighted in detail. Furthermore, new materials are suggested and described to overcome some of the limitations presented by PZT, especially the environmental issue related to its toxic lead (Pb) content. Lead-free Potassium Sodium Niobate ($K_{1-x}Na_xNbO_3$) is described as a potential alternative to PZT in piezoelectric actuator applications, while the excellent ferroelectric properties of lead-free Zr-doped Hafnium Oxide ($Hf_{1-x}Zr_xO_3$) at low thicknesses pave the way towards a substitution of PZT in ferroelectric memory applications.

1.1 Piezoelectric materials and devices

The physical phenomenon of piezoelectricity is defined as the appearence of an electric potential across the sides of a (piezoelectric) material when a mechanical stress is applied to it (known as the direct piezoelectric effect). The opposite effect also occurs, i.e. upon applying an electrical potential to a material, a mechanical deformation is generated (converse or reverse piezoelectric effect). The physics of piezoelectricity is described in more detail in Chapter 2.

The interconversion between mechanical energy and electrical signals holds potential for a variety of applications which have been explored since the discovery of piezoelectricity in the late XIX century. In the present day, several items, including motors, sensors, actuators, and transducers, employ piezoelectric materials [1]. Indeed, this class of materials features a wide range of industrial application fields, and new ones are constantly being sought for. Key sectors

include automotive, biomedicine, information technology, robotics, fine machineries, energy harvesting, transducers, acoustic devices, sonars for both military and civilian applications, and aerospace. One of the largest market applications for piezoelectric devices is the automobile industry sector. The number of sensors in cars, including seatbelt locks, knock sensors, airbag sensors and others, is quickly increasing and is mostly used for safety applications [2]. Piezoelectrics are also crucial in the automotive industry for applications like diesel fuel injectors because only microscopic piezoelectric actuators can accurately regulate a high pressure fluid. Another key industry for piezoelectric materials remains aerospace and defense. Their uses range from sensors to the creation of ultrasonic sonars to more cutting-edge applications like micro-robotics and bullets that can change direction [3]. Recently, interest in energy harvesting applications has increased, and by the end of the decade, it is anticipated that the business will be worth several US billions. In fact, vibration-based energy at kHz frequencies may reach an energy density of up to mW/cm^3 and can be converted into electrical energy using piezoelectric nanogenerators. Thus, this method of energy harvesting offers enormous promise for wireless sensing, battery charging, and powering electronic devices [4, 5]. Additionally, piezoelectrics contribute as an enabling technology in a variety of other fields, including microelectronics through precise element control in photolithography, medical diagnostics through ultrasonic imaging, machine control, and many more [6]. One of the most intriguing and promising uses for piezoelectrics is in microelectromechanical systems (MEMS), which are microscopic devices with moving components like gyroscopes, energy harvesters, and accelerometers. Piezoelectric materials may be used to create extremely effective sensors and actuators for MEMS, with an effectiveness independent of the size of the device, which enables further shrinking of the components [7].

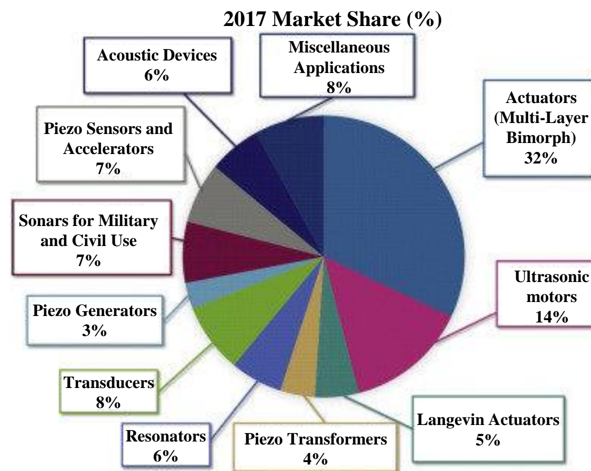

Figure 1.1: *Market share of various piezoelectric applications, from [8].*

In a general sense, all piezoelectric materials act as "energy transducers" since they convert energy from one form to another. From an application perspective, piezoelectric devices may be separated into actuators, sensors, transducers and generators. These categories are further separated in Figure 1.1, where a projected market share for piezoelectric materials for each application is shown. Besides, the market for piezoelectric materials is enormous and expanding constantly. According to projections, it will increase from USD 28.9 billion in 2019 to USD 34.7 billion in 2025, as shown in Figure 1.2 [1]. Thus, it seems logical for many companies to be interested in this kind of functional materials. As a result of technological advancements that call for precise motion actuation and transduction, as in the case of MEMS devices, the need for these materials is rising, but ongoing study is required to keep up with the market demands

for ever-higher performances.

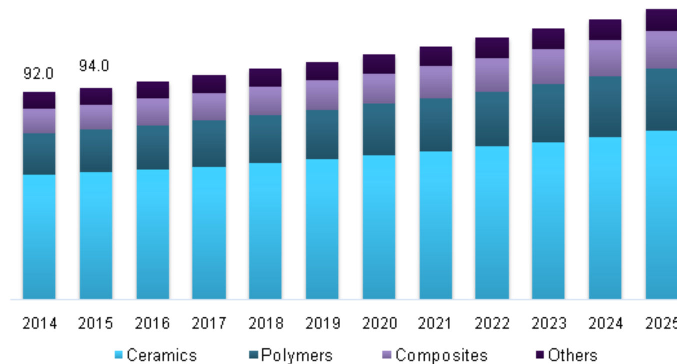

Figure 1.2: *Market revenue piezoelectric materials, 2014−2025 (USD Million), from [1].*

1.2 Ferroelectric materials and devices

As will be described later in Chapter 2, ferroelectrics are a family of materials that display spontaneous polarization below a specific temperature known as Curie temperature, and the orientation of the polarization of the material can be modified by an applied electric field. Ferroelectrics are included in the larger group of pyroelectric materials, which in turn are part of the class of piezoelectric materials. All ferroelectric materials exhibit pyro- and piezoelectric behaviour, but not the other way around.

Ferroelectrics exhibit exceptional properties because of their non-centro-symmetric crystal structure arising from a slight distortion in their structure. These materials hold a considerable potential for a variety of uses, including surface acoustic wave (SAW) devices, microactuators, sensors, capacitors, and IR detectors exploiting their pyroelectric and piezoelectric properties [9]. Besides, they have been discovered to be extremely stable to high-energy radiation, which is a quality that is crucial for space applications [10]. In addition, these materials have recently attracted more attention for applications in non-volatile random-access memory (NVRAM) devices, as they often exhibit a high dielectric constant and hysteretic behaviour of the polarization versus the electric field. The two spontaneous polarization states ("up" and "down") can serve as effective logic states for memory devices that do not need a power source to preserve the stored data [11]. In order to create NVRAMs with long endurance and high-speed access, ferroelectricity of oxide thin films can be utilized in semiconductor devices. This can help to overcome the challenges faced by existing semiconductor memory technologies. Low density integrated ferroelectric memories are already being evaluated for use in commercial products like smart cards and mobile phones [9]. Voltage-dependent and thermally sensitive resistors, as well as humidity and gas sensors, can all benefit from the use of ferroelectricity.

Ferroelectric memory devices can be produced using one of two methods. The first is ferroelectric random access memory (FeRAM), which is designed for a similar use to that of dynamic random access memory (DRAM). According to this method, each memory cell is made up of a transistor and a ferroelectric capacitor (Figure 1.3a). Although several studies have been published in this field and FeRAMs were considered a viable contender for the next generation of non-volatile memories [9], they have not yet found widespread commercial application. One drawback is that the read operation is a destructive process, requiring rewriting after each reading pulse [13]. Thus, it is highly preferable to use nondestructive read designs that measure resistance states in response to polarization changes rather than sensing capacitance changes

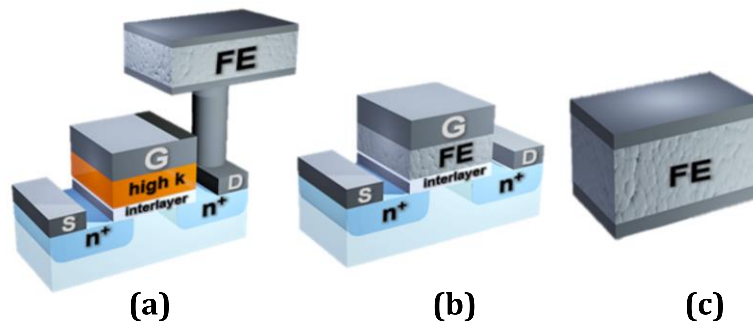

Figure 1.3: *Sketch of the structure of (a) FeRAM, (b) FeFET and (c) FTJ devices, from [12]*

[14].
As a consequence, a second method that was soon developed uses a single transistor known as a ferroelectric field-effect transistor (FeFET), which is simply a standard FET in which a thin ferroelectric film is used in place of the dielectric gate and substitutes the ferroelectric capacitor (Figure 1.3b) [12]. The ferroelectric polarization state controls the channel conductance in this device, which eliminates the need to switch polarization in order to access and read the memory cell and thus allowing for non-destructive readout.
In addition, ferroelectric tunnel junctions (FTJs) have also been developed based on the technological notions involved in FeRAMs and FeFETs [15, 16]. Ferroelectric tunnel junctions (Figure 1.3c) have sparked a great deal of interest because they offer the potential to reduce the size of ferroelectric memory devices to a few nanometers. These are two-terminal devices with a similar configuration to that of the capacitor stack in FeRAMs, but the total measured resistance changes depending on the polarization state of the ferroelectric barrier, similarly to FeFETs. Changes in the tunnel currents are caused by modifications of the electron barrier height or width, which occur as a result of surface charges at the interface with the metal electrodes. The difficulty lies in maintaining the ferroelectricity and the lack of defects in the tunnel barrier down to the $2-3$ nm thickness required for tunneling.
Ferroelectrics have been used in NVRAMs devices for over 50 years, therefore the concept is not novel [17]. However, the absence of technology for reproducible growth of high-quality ferroelectric films, which are problematic in terms of perfectly tailoring a wide spreasd of these technologies for many years. Later, in 1986, when advances driven by discovery of high-temperature superconductors, in thin film deposition techniques like sputtering and pulsed laser deposition allowed to grow complex thin films material structures as $YBa_2Cu_3O_7$, the idea of implementing ferroelectric NVRAMs attracted new interest, and novel studies on this technology are being published everyday [11].

1.3 Lead Zirconate Titanite Pb(Zr,Ti)O_3

After the groundbreaking discovery, in 1946, of the ferroelectric and piezoelectric properties of barium titanate ($BaTiO_3$ or BTO), the ferro- and piezoelectric technology really began to take off. In fact, $BaTiO_3$ is cheap to fabricate and shape, and the first $BaTiO_3$ products with phonograph pickups hit the market in 1947 [18].

Following similar methodologies made popular by research on $BaTiO_3$, other perovskite isomorphic oxides were discovered and studied, including $PbTiO_3$, $PbZrO_3$, and $SrTiO_3$ and their solid solutions. From the determination of the phase diagram of lead zirconate titanate ($Pb(Zr,Ti)O_3$ or PZT), the incredibly effective piezoelectric performances of PZT solid solutions were discovered by Jaffe in 1954 [19]. The studies on PZT also pushed forward the de-

velopment of the novel idea of Morphotropic Phase Boundary (MPB) [20], which designates a concentration range for a compound where two different phases coexist, with a consequent huge improvement in the piezoelectric response of the material (see Section 2.6 for more details). Although the MPB is still under investigation [21] and therefore cannot properly justify some of the observed phenomena, the correlation between strong ferroelectric/piezoelectric properties and MPB allowed for a more thorough understanding of these effects and represented a significant step forward in the search for new, better performing functional materials. In quest for a deeper comprehension of the phenomenon, the impact of material doping on functional properties, and new application areas, the field of ferroelectrics and piezoelectrics has grown significantly since the discovery of PZT behaviour [22, 23].

The PZT family of piezoelectrics is typically more popular than any other piezoelectric material for transducer, sensor, and actuator applications due to its high piezoelectric coefficients, simple production methods, ease in poling, and reduced costs. The only piezoelectric material that PZT hasn't outperformed is quartz in frequency control devices, due to the outstanding stability of its piezoelectric responses with time and temperature.
PZT is also one of the most promising candidates among the ferroelectric materials for ferroelectric memory devices and there have been substantial efforts to break into the FeRAM market. In fact, high-quality PZT can be grown at temperatures between 500°C and 600°C. This allows to integrate PZT with silicon technology for FeRAMs, as opposed to other materials whose growth temperatures carry the risk of affecting the stability of silicon and underlying barriers, with severe interdiffusion and oxidation of Si, and consequent poor transistor performance. Additionally, PZT shows superior ferroelectric properties, including greater dielectric constants, a low coercive field, and a high Curie temperature. PZT, however, suffers from fatigue issues that appear to be unsolvable so far, due to poor crystalline quality. Pt/PZT/Pt capacitors typically lose more than 50% of their polarization in only up to 10^{10} cycles, far below the acceptable threshold for IC technology applications (10^{14} cycles). However, it should be mentioned that cutting-edge deposition techniques like MBE are now being used to manufacture high-quality PZT in order to solve the fatigue issue [24].

Thanks to its superior characteristics, therefore, it is evident that lead-based materials of the PZT family are currently the number one choice for the fabrication of many piezoelectric and ferroelectric devices. With an annual growth rate of 6%, the global market for PZT alone is worth USD 20 billion dollars [25]. However, this class of materials holds a primary flaw that is a high lead content of over 60% by weight, which is known to be dangerous for both humans and the environment even in little amounts. Lead-free piezoelectrics is a more recent area of research driven by increasing awareness and concerns about Pb toxicity in PZT-based materials (see Section 1.4): a key publication in this field is a 2004 work by Saito et al. [26], and interest in this area has been steadily increasing over the past 20 years [8, 27]. A number of materials and solid solutions have been developed in this context, including $(K,Na)NbO_3$ (or KNN), $(Ba,Ca)(Zr,Ti)O_3$ (BCZT), $Bi_{0.5}Na_{0.5}TiO_3$ (BNT), etc. An overview on lead-free materials is provided in Section 1.6.

1.4 Toxicity of Lead (Pb)

The most significant heavy metal hazardous substance in the environment is lead (Pb). Its use can be traced back to the ancient times because of its remarkable physico-chemical characteristics. One of the first metals used by humanity, lead has been employed by human civilizations for thousands of years. Because lead is a soft, malleable, ductile metal very resistent to corrosion, it is reasonably hard to give up its use. Although it offers many technological advantages,

it is also a non-biodegradable element, and its ongoing usage is causing its concentration in the environment to increase with consequent risks for human health, nature and wildlife. Public concern about lead exposure has continued to grow over the centuries as lead contamination can result not only from lead-related occupations (leaded gasoline, industrial processes like smelting, pottery, Pb-containing paints, battery recycling, the arm industry...) but also through exposure to commercial products, home dust, soil, water and even air [28]. Despite the fact that many nations throughout the world have limited its extensive use, it is still utilized in a variety of sectors, including vehicle maintenance, battery production and recycling, refining, etc.
Lead is poisonous even in small doses and affects almost every organ in the human body. It mimics calcium (Ca) in our bodies, interfering with Ca ion channels acting as a potent selective blocker of voltage-dependent calcium channels even at low concentrations [29] and causing reduction in the number of neurons, impaired neuronal growth [30]. Like Ca, Pb can be stored in bones for years without any efficient way of getting rid of it, meaning it can continue to poison the body long after the initial exposure. The organ that is most sensitive to lead is the brain: lead breaks down the myelin shieth around the axons and prevents the release of neurotransmitters. That's why common symptoms of lead poisoning are headaches, loss of memory, concentration and coordination, nausea and tingling in the hands and feet [31].
Long-term exposure to Pb has been associated with anaemia and a rise in blood pressure, severe damage to the brain, the nervous system and kidneys at all ages. It may also result in decreased fertility in males and pregnancy abortion in females [32]. The Centres for Disease Control and Prevention and the World Health Organization have set a Pb blood concentration of 10 μg/mL to be the standard elevated blood level for adults, and 5 μg/mL for children. A blood concentration above this standard is to be considered cause of concern, but in reality there is no real proven threshold value that can be considered safe. Worsened academic performance, learning disorders and behavioural problems was found to be significantly correlated with blood lead concentrations even lower than 5 μg/dL [33]. Lower IQ and behavioral issues including aggressiveness have been linked to blood lead levels below 10 μg/dL [34]. Additionally, elevated blood lead levels are linked to diminished cognitive function and other mental problems like depression and anxiety. Long-term impairment of central nervous system functions in adults was correlated to 50 to around 100 μg/dL Pb concentrations in the blood [35].
Exposure to Pb and other heavy metals also affects mechanisms at the cellular level, in that they can produce reactive radicals that damage DNA and cell membranes [36]. Lead also affects the enzymes that contribute to vitamin D production and those that protect cell membranes. Additionally, it was discovered that lead impedes DNA transcription. It may also affect the permeability of blood arteries and collagen formation, according to certain theories [37]. In case of damaged cells of the immune system, immune activity is also impaired.
Current estimates of deaths caused by lead range from 500 to 900 thousands per year. The 2020 UNICEF report warns that 1 in 3 children globally, that's over 800 million children, have blood lead levels at or above 5 μg/dL. A lot of this lead now comes from batteries and industrial processes.
As a response to the increased awareness of the health and environmental hazards risen by the use of Pb, a series of legislative standards were set by different countries around the world that regulate the amount of Pb and other hazardous substances in air, water, paint, soil, and consumer products. As knowledge of lead toxicity and exposure increased, rules and standards for certain types of lead were released.

1.5 Lead Guidelines and Regulations

According to historical records, the first lead restrictions date back to the Roman Empire, when Germanic tribes banned Roman wines due to the colic they caused in its consumers [38].
The greatest worry of lead poisoning in the 19th century was to occupational exposure from industrial operations such mining, smelting, ceramics, chemical production and battery manufacturing. Even before the start of the 20th century, there were several instances of worker poisoning and fatalities in Europe and the United States [39]. Poisoning brought on by white lead paint used to paint doors and windows was one of the main issues at the time. Starting in the 1960s, more lead bans were enacted in other countries, and lead applications are regulated by several international regulations. Overall, these rules target the oral (children's toys, food, water/infrastructure, consumer goods regulations) and inhalation (occupational and environmental monitoring regulations) exposure pathways. The United Nations Environmental Programme (UNEP) and the World Health Organization (WHO) have compiled a list of lead legislations that largely focus on oral exposure in children.
Before adopting its present hazardous substance legislation, i.e. Registration Evaluation, Authorisation and Restriction of Chemicals (REACH) in 2006 [40], the European Union (EU) approved Directive 1999/45/EC ("related to the classification, packaging, and labelling of dangerous preparations"). The rule stipulated that paints and varnishes with lead levels greater than 0.15% by weight must include a warning.
Similar regulations were applied to children's toys, food, air and water and other consumer products. In particular, in February 2003 the European Union adopted the Restriction of Hazardous Substances in Electrical and Electronic Equipment (RoHS) [41], with its first directive (Directive 2002/95/EC, RoHS 1) taking effect on 1 July 2006 [42]. In order to safeguard the environment and the general public health, this EU regulation restricts and/or bans the use of hazardous materials in electrical and electronic equipment (EEE). This is accomplished by limiting the use of some hazardous materials in EEE that may be replaced with safer alternatives. Heavy metals, flame retardants, and plasticizers are some of these prohibited compounds.

Besides, the waste electrical and electronic equipment (WEEE) that is produced annually in the EU is presently among the waste streams with the quickest growth. As a matter of fact, recycling of electrical waste (e-waste) is quite infrequent: only 20% of the world's electronic waste was effectively recycled in 2016, while the other 76% was discarded, improperly recycled, or, in the case of higher-income countries, mostly shipped to underdeveloped countries like Nigeria and Ghana [43]. It should come as no surprise that several studies revealed a significant prevalence of lead poisoning among residents of these nations, particularly those who lived close to e-waste dump sites [25]. As a consequence, next to the RoHS Directive limiting the use of specific hazardous compounds in electrical and electronic equipment, the WEEE Directive encourages the collection and recycling of this type of devices.

1.6 Lead-free piezoelectrics

Due to their superior piezoelectric ferroelectric capabilities, lead oxide-based ferroelectrics of the PZT family are the most widely utilized materials for piezoelectric actuators, sensors, and transducers and a common choice for ferroelectric memory devices [44, 45]. However, a considerable amount of concern over the recycling and disposal of PZT-containing devices has recently spread due to the toxicity of Pb. Upon the adoption of the RoHS regulation, which specifies that the related products must have a lead concentration of less than 1000 ppm (less than 0.1%) by weight, it became immediately clear that PZT, with its lead level of around 60%

by weight, does not comply to the RoHS restrictions. As a matter of fact, Pb and Pb oxide are known to vaporize during processing of a number of PZT-based devices commonly utilized in consumer goods like vehicles, numerous smart systems, and sound generators. As a consequence, these substances could easily contaminate the environment for a long time and/or accumulate in organisms causing serious harm to health.

However, it is hard to give up on the huge advantages offered by the strong piezoelectric capabilities of PZT. Using PZT in medical imaging, for instance, enables a good signal resolution that is necessary for an accurate diagnosis, thus allowing to save many lives [46]. Despite this, the recent tendency toward creating lead-free, biocompatible piezoelectric materials that can be implanted as sensors and actuators right into living tissues (human body included) could envisage a desertion from PZT in the close future. It is also important to consider the strong psychological opposition to putting lead-containing items into the human body. Consequently, a growing propensity to explore for substitute materials is reported. Due to the reported low density of some lead-free materials, they can also be beneficial in transducers for undersea and medical imaging where a low acoustical impedance is required.
To achieve optimal electromechanical characteristics, the search for new alternative materials to PZT should consider MPBs and time, pressure and temperature stability, which is closely related to the various phase transition temperatures of the material. For instance, $BaTiO_3$-based materials have Curie temperatures that are too low for the majority of applications, despite their potentially strong piezoelectric capabilities. However, starting from the ground-breaking study in 2004 by Saito et al. reporting on the promising features of textured doped sodium potassium niobate (KNN) piezoceramics with a huge piezoelectric coefficient d_{33} = 416 pC/N [26], intense research activities have been conducted on lead-free materials. There are several lead-free piezoelectric materials available, including those based on alkali niobate (e.g. $(K,Na)NbO_3$ or KNN), bismuth and barium titanates ($Bi_{0.5}Na_{0.5}TiO_3$ or BNT and $BaTiO_3$ or BTO), other titanate-like solid solutions (e.g. $(Ba,Ca)(Zr,Ti)O_3$ or BCZT), bismuth ferrite ($BiFeO_3$, BFO), etc.

Despite the availability of lead-free alternatives, it is challenging to replace established methods and procedures with new ones, particularly because the performances of lead-free materials do not often prove superior than those offered by Pb-based ones. While the research of PZT device design and fabrication has been encouraged over the previous 60 years, a lead-free transition would require re-designing of devices in many cases, and the cost of this process would need to be absorbed within a very short period of time. Toxic-element-free electronic devices are being pushed by legislation and research on lead-free materials is becoming strategically beneficial for marketers and companies since, if lead is eliminated thanks to technical advancement, lead-based materials will no longer be an option. However, company investments in lead-free research still account for less than 0.2% of piezo- and ferroelectrics sales, with university research departments performing the majority of the work. Notably, the European Commission has provided relatively scarce assistance to both companies and research institutions, unlike nations like Japan and Korea, and this has contributed to reduce the interest of the industrial sector in the lead-free transition [8, 25]. This is the reason why piezoelectric and ferroelectric materials are for the time being not included in the RoHS ("RoHS Exclusions"), since lead-free alternatives haven't yet allowed to completely replace lead-based materials in manufacturing. As soon as the Pb-free transition is considered viable, with lead-free materials being more robustly considered and investigated for meaningful massive applications, this exemption from the RoHs will end. A widespread belief is that a more robust synergy and cooperation between academic research and industries can offer the right solution to this impasse, and in this way a second phase of lead-free research more oriented to real applications could begin.

1.6.1 Potassium Sodium Niobate $(K,Na)NbO_3$

One common method for comparing the piezoelectric properties of various materials is by evaluating the longitudinal piezoelectric coefficient d_{33} (see Section 2.3). This quantity measures the polarization induced by the applied stress in the same direction of the stress itself. Additionally, also the Curie temperature (T_C) of a material constitutes a typical parameter for comparison, as it is the temperature at which the ferroelectric to paraelectric phase transition occurs, with consequent loss of ferroelectric ordering and ferro- and piezoelectric properties [47]. The diagram reported in Figure 1.4 shows the piezoelectric coefficient (displacement/deformation per unit voltage) as a function of the Curie depolarizing temperature for various classes of piezoelectric materials. As is evident, PZT has so far provided the optimum trade-off between Curie temperature and piezoelectric coefficient d_{33} that are both high. Potential alternative candidates at the present time feature either high Curie temperatures (KNN-based materials) that require proper texturing, tailoring or doping to improve performances, or promising piezoelectric properties but with allowed working temperatures that can be very limiting in terms of applications (BCZT-based materials).

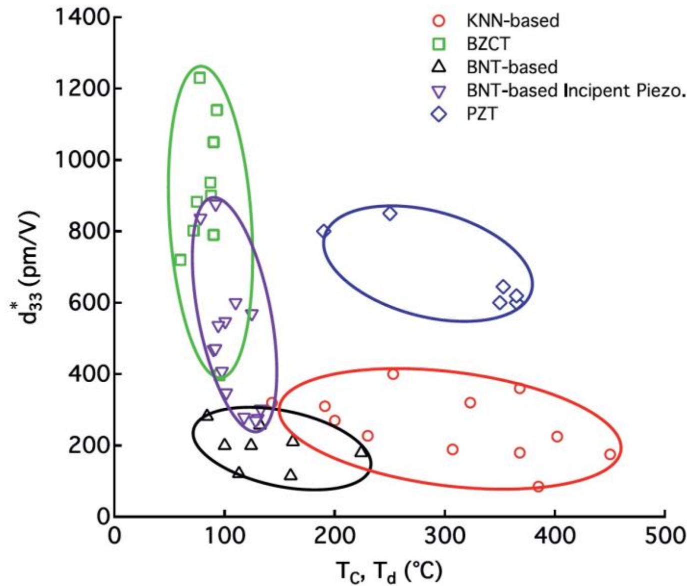

Figure 1.4: *Comparison of d_{33} piezoelectric coefficient for various classes of piezoelectric material ceramics.*

Among all available lead-free piezoelectrics, the aforementioned high-T_C $(K,Na)NbO_3$ (KNN) represents one of the most promising ones. KNN is a perovskite solid solution analogous to PZT ($Pb(Zr,Ti)O_3$). Studies on this material immediately gained momentum after the publication of a paper by Saito et al. in 2004 reporting on highly (001)-textured and doped KNN polycrystals with an extremely high piezoelectric coefficient of 416 pC/N [26]. As a result, KNN readily became one of the most researched materials in the field, and the careful engineering of its properties lead to achieved piezoelectric coefficients of KNN ceramics of up to d_{33} $\sim$570$\pm$10 pC/N in 2016 by Xu et al. [48]. Figure 1.5 shows the increased in record d_{33} value of KNN that was obtained over the years, indicating that with proper technological development the piezoelectric properties of KNN can be made comparable to those of its lead-based counterpart PZT. Besides, high Curie temperatures of up to 400°C have also been obtained in KNN, similar to those found for PZT [49].

Strong composition dependency in the KNN properties allows for precise tuning by doping (especially acceptor doping) and chemical replacements. This is relevant because, depending

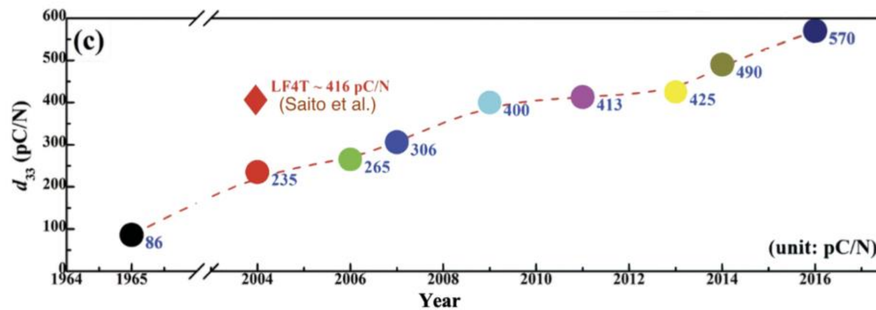

Figure 1.5: *Increase of the piezoelectric d_{33} coefficient of KNN ceramics through the years thanks to fervent research (from [48]).*

on the application, it is impractical to replace PZT with a single lead-free piezoelectric material. Instead, it is often more convenient to replace it with a variety of materials that have sightly different properties, carefully choosing everytime the most suitable one for every application.
Besides, copper, platinum, or silver are the most common electrode materials used in PZT devices [50]. The ability to use Ni-based electrodes, which are less expensive than Cu, Pt, or Ag ones, is a helpful feature of KNN [51]. Since the cost of electrodes may account for up to 80% of the overall materials cost, this would result in sizable cost savings. Although KNN electrodes can be made less costly, the raw materials required for KNN, especially niobium, are more expensive than those required for PZT, making their usage less desirable for companies and consumers.
Moreover, the lack of reproducibility of KNN properties and the high volatility of its Na and K alkali components are key challenging issues that still primarily restrict its applicability. When making KNN devices, especially based on thin films, there is a significant batch-to-batch variance that can be brought on by a number of different factors, including dishomogeneous diffusion rates that lead to local compositional non-uniformity, grain-size dependency of the properties, component volatilization, etc. [52]. For example, as already mentioned, the re-evaporation of volatile alkali metals throughout the growth and manufacturing processes really has a significant impact on the outcomes and raises reliability concerns. However, many of the reproducibility difficulties with KNN also occurred in the production of PZT, but these problems were resolved after 60 years of continuous process of optimization. Therefore, with more research, the primary KNN issues may potentially be resolved.

In conclusion, based on its characteristics, KNN is more likely to compete with PZT than other lead-free families in low and intermediate temperature regime applications, where its properties are more stable, although there are still many technical and practical obstacles to be overcome [6].

1.6.2 Hafnium Oxide

Due to the growing need for miniaturized electronics to enhance information storage, decreased size of both single components and whole devices is required.
One of the essential concerns with regard to size limitation is sample quality, which is highly dependent on growth processes and often requires precise atomic control. Dead layers, grain boundaries, and defects like oxygen vacancies all have an impact on the performances of ferroelectric thin films. Additionally, the electrostatic boundary conditions have a strong influence on the material properties with decreasing film thicknesses, especially for extremely thin films, where depolarizing effects finally become significant and eventually suppress ferroelectric be-

haviour of ultra-thin films [53]. This hinders the possibility of employing the majority of ferroelectric oxide materials for the simple production of 3D capacitor structures, which need to be only a few tens of nanometers thick [54]. Furthermore, even though current lithographic techniques enable the definition of features with precision of down to a few nanometer size, it is incredibly challenging to miniaturize ferroelectric devices because the crystal structure of complex oxides (e.g. $YBa_2Cu_3O_7$, $SrBi_2Ta_2O_9$ or SBT) does not withstand the lithographic steps at the borders of the shape features.
The Si compatibility of ferroelectric memory devices represents another challenge. CMOS (complementary metal-oxide-semiconductor) is a type of chip-based technology, typically based on silicon, that is used to build the majority of the electronic devices in our everyday lives. The most performing ferroelectric thin films, i.e. PZT, BTO, or SBT, often feature perovskite structures, which have poor CMOS compatibility, limiting their broad use in the industry. Even though certain perovskite films have been engineered to grow epitaxially onto a silicon substrate [55], the interaction of the ferroelectric film with the substrate is frequently far from ideal [56]. The quality of the perovskite films will typically be affected by the formation of an interfacial SiO_2 dead layer, which can very easily result in sizable issues with the stability of the two memory polarization states or logic circuits. Furthermore, the typical thermal budget for perovskite growth is not compatible with the constraints of CMOS process.
All these commonly known difficulties in manifacturing ferroelectric devices featured by PZT add up to the already mentioned environmental issues related to its lead content described in the previous Sections.

As a consequence, future development of ferroelectric memory and associated devices must prioritize finding solutions to the problems outlined above. Since 2011, when the first report of ferroelectricity in Si-doped HfO_2 thin films was published, significant advancements in this field have been made [57]. It was soon discovered that additional dopants, including Zr, Gd, Al, Y, La, Sr and others [58, 59], may similarly cause ferroelectric behaviour in HfO_2 thin films. Some of them produce remanent polarization that can reach up to 45 μC/cm^2, which is similar to the best perovskite ferroelectrics. Notably, hafnia-based ferroelectrics only exhibit ferroelectricity at the nanoscale, while other ferroelectrics lose it. Besides, HfO_2 is a simple oxide with a broad bandgap (larger than 5 eV) which makes it less vulnerable to leakage phenomena. It is also Si-compatible and has been widely employed as the gate insulator in the manufacture of FETs in its amorphous form. The limitations to the use of ferroelectrics in memory, including FeFET and 3D capacitors, are thought to be removed by all of these benefits over the typical perovskite ferroelectrics. Therefore, the recent finding of ferroelectricity in very thin layers of hafnia-based materials is a significant advancement in this area of research [60].

Ferroelectric HfO_2-based thin films might be a significant advancement for a number of device architectures, including:

- *Ferroelectric memory.* HfO_2-based ferroelectrics are very appealing materials for memory applications [61] exploiting their bi-stable polarization and the numerous benefits mentioned above, including nanoscale ferroelectricity and CMOS compatibility. A few studies have been conducted on this idea, using HfO_2-based ferroelectrics for random-access memories (FeRAMs) or field-effect transistors (FeFETs) [62]. For instance, in a FeFET with a ferroelectric gate oxide, the read operation can be non-destructive since the polarization orientation of the gate alters the amount of the current in the source-drain channel [63].
  Hafnia-based materials are also well suited to be incorporated into FTJ devices due to their large bandgap and advantageous features over traditional perovskite ferroelectrics at the nanoscale [64]. Additionally, the development of multiferroic tunnel junctions (MFTJs),

which permit the use of multifunctional devices, is possible if the electrodes are magnetic.

- *Synaptic devices.* Artificial intelligence has significantly improved our daily lives in recent years. However, this still relies on intricate algorithms, handles a lot of data, and uses supercomputers, which are extremely energy-costly. Exploring various computer architectures and computing techniques that can more effectively handle huge data is one method to address this issue. The human brain serves as a model for this purpose, since it processes vast quantities of sensory input and can categorize, rank, and recognize intricate patterns with a small fraction of the processing power required for a supercomputer to accomplish the same work. For this scope, it is necessary to emulate the plasticity of neurons and synapses. Thus, it is vital to create novel materials inspired by the brain, usually referred to as memristors [65]. Memristor behavior exhibits adjustable conductance and is as such particularly attractive for synaptic devices. Since the resistance of ferroelectric materials in a capacitor configuration changes with the fraction of material with switched polarization under the electrode, artificial synapses may be made by manipulating the polarization domain dynamics with various voltage pulses [66].

- *Energy harvesting.* Hafnia-based materials are also piezoelectric and pyroelectric, as are all ferroelectrics, making them appropriate for converting mechanical or thermal energy into electric power. When integrated into an external circuit, ferroelectrics can produce relatively large potential differences (which scale with their thickness), but because of their excellent insulating properties, they provide very low currents (which scale with their surface area), producing low power outputs from tens of microwatts up to miliwatts for highly optimized materials. For this reason, ferroelectrics have been ruled out as viable energy collecting options due to their low values when compared to other methods, such as photovoltaics. However, this perspective is currently evolving because of the peculiar requirements of autonomously powering sensors (the majority of which consume milliwatts or less) for the internet of things, self-driving vehicles, smart cities, etc. Low power generation today has a big potential. It is also predicted that in the not too distant future, the power needed for consumer electronics would reach the milliwatt level as microelectronic devices get smaller and consume less power (e.g., some peculiar microprocessors may be found that utilize a few microwatts). Therefore, it is important to promote research into ferroelectrics for energy harvesting. Current lead-containing materials that have been optimized are insufficient for such a future; instead, research on highly sustainable ferroelectrics consisting of common elements and simple oxides is required. Therefore, a particularly promising contender is the recently discovered ferroelectric doped HfO_2 material [67, 68].

1.7 Challenges of thin film materials

New piezoelectric and ferroelectric crystals, polymers, and lead-free materials have experienced a rapid growth over the past two decades, which has led to significant advancements in electromechanical coefficients, material characteristics, and application areas [6, 8]. The technological advancement in bulk materials was quickly transfered and integrated in thin films processes thanks to improved deposition techniques. Due to the additional functionality offered by miniaturized devices, thin films allow the development of nanoscale and microscale electronics.
The deposition of oxide thin films is carried out by two alternative approaches:

- Physical deposition processes like electron-beam evaporation, RF and RF magnetron sput-

tering, DC sputtering, ion beam sputtering and Pulsed Laser Deposition.

- Chemical deposition processes like the sol-gel method (dipping, spin coating, etc.), chemical vapour deposition (CVD), MOCVD liquid phase epitaxy, melting epitaxy, etc.

For industrial processes sol-gel is widely used, but sputtering would represent the technique of choice for ferroelectric thin films like $LiNbO_3$, PLZT, and $PbTiO_3$. Epitaxially formed films can be also achieved provided the right substrate and deposition conditions are used.

However, the growth and optimization of thin films must account for some challenging aspects intrinsically related to the reduced thickness of the samples:

- *Thickness constraints*: There could be a critical film thickness below which the ferroelectricity would vanish, similarly to a powder sample [69].
- *Stress from the substrate*: Due to the thermal expansion mismatch and difference in lattice parameters between the film and the substrate, tensile or compressive stress is produced, which might occasionally result in a larger coercive field for domain reorientation. Additionally, the Curie temperature is changed at a rate of 50°C every 1 GPa for many piezoelectric materials. Theoretically, it could be possible to engineer the Curie temperature and make it higher or lower by controlling the produced stress [22].
- *Crystal phase*: It is important to take into account the dependence on crystal orientation, as with single crystals. For example, rhombohedral PZT is believed to work at its best when the direction of the spontaneous polarization is tilted by 57° with respect to the (001) crystallographic direction normal to the thin film surface [70].
- *Thermal budget*: Low sintering temperature for the PZT coating is necessary to ensure compatibility with the Si substrate. The greatest temperature typically used to prepare PZT is 800°C for a brief amount of time in sol-gel and linquid phase sintering; this may restrict the film's ability to crystallize, with a possible negative impact on its functional properties. The crystallinity of the PZT layer is additionally constrained by a metal electrode, such as Pt, on a Si wafer, due to the substrate template and to the possible occurrence of interdiffusion phenomena at high processing temperatures.

Despite these challenges, after thorough studies and efforts, it is now feasible to include thin films into real application devices. As a matter of fact, these are becoming more and more significant in cutting-edge applications with an emphasis on miniaturization and high performance.
The state of the art of piezoelectric performances of different thin film piezoelectric materials are reported in Table 1.1. The same kind of observations mentioned for ceramics are valid also for thin films, i.e. currently there is no lead-free alternative competing with the optimal trade-off of PZT in terms of high Curie temperatures and high piezoelectric coefficients. Therefore, for the time being, piezoelectric devices are predicted to be dominated by PZT-based thin films, although cutting-edge future devices could also include other lead-free piezo films, provided that some of their properties are pushed towards those of PZT [71].

Material	ϵ/ϵ_0	$\tan\delta$	d_{33} (pC/N)	T_C ($°C$)
$K_{0.5}Na_{0.5}NbO_3$	400	0.04	95	400
$Bi_{0.5}Na_{0.5}TiO_3$	300	0.01	98	315
$BaTiO_3$	1700	0.005	190	115
$Ba_{0.5}Ca_{0.5}ZrTiO_3$	400	5	280	110
PZT-4	1300	0.004	289	328

Table 1.1: *Dielectric and piezoelectric properties of the main lead-free thin films and PZT thin films [49].*

1.8 Thesis Outlook and motivation

In the future, it is expected that most lead-based ferroelectrics and piezoelectrics will be replaced, hence research into lead-free materials holds a remarkable importance in encouraging and speeding-up the transition. The current technology is still far from creating lead-free materials with qualities similar to those of PZT and that can be produced on a big scale. However, it took 60 years to study and develop the most performing PZT, therefore every contribution to the thorough study of the properties of lead-free functional materials is beneficial for the advancement and evolution of the technologies.

Most of this study was conducted in the PoliFAB lab at Politecnico di Milano under the direction of professor Riccardo Bertacco and with financial assistance from the Joint Research Center JRC MEMS-STEAM project between Politecnico di Milano and STMicroelectronics.
In the first part of this Thesis, the study of critical aspects of Physical Vapour Deposition (PVD) of thin films of KNN is reported to investigate the feasability of a wafer-scale process for the integration of lead-free piezoelectric films in MEMS devices.
In particular, a systematic methodological characterization of the properties of KNN lead-free piezoelectric thin films grown by Pulsed Laser Deposition on small samples is provided, in view of a future transition towards an industrial sputtering machine and a scale-up of the process to 8" wafers. More specifically, the pursued objectives are related to highlighting the critical aspects of sample device development and characterization from start to end, including the critical issues and parameters impacting device functional properties related to: substrate preparation and oxide growth (with the case study of KNN(001)/Pt(111)); oxide composition, doping approach and incorporation effects (with the case study of Li doping); oxide crystalline structure (with a study on epitaxial compared to polycrystalline KNN); device interfaces (with a case study of the impact of Ti, Ni and Pt interfaces with KNN).

In the second part, the research work on Zr-doped HfO_2, carried out at the Zernike Institute for Advanced Materials of the University of Groningen and supervised by professor Beatriz Noheda, is reported. As a matter of fact, this material represents an excellent lead-free ferroelectric at low thin film thicknesses and can potentially compete with PZT in the integration of miniaturized, Si-compatible ferroelectric random access memories and ferroelectric field-effect transistors. The aim of the work is to explore and define viable strategies to increase the ferroelectric responses of HZO thin films by stabilizing the polar phase by engineering of structure and substrate-dependent lattice stress.
The Thesis is organized as follows.

Chapter 1 introduces the main concepts of piezoelectric and ferroelectric materials and their present role in industry and commercial sectors, illustrating all possible applications of bulk materials and thin films in practical devices and products.

Chapter 2 provides an overview of the general theoretical concepts behind the physical phenomena of piezoelectricity and ferroelectricity, and the main models currently employed to describe them.

Chapter 3 describes all the experimental methods and procedures employed for the purpose of this research work. The methods for thin film growth by Pulsed Laser Deposition are described, followed by techniques for structural, chemical, morphological and piezoelectric characterization of the material, and finally the fabrication of parallel capacitor devices for the macroscopic electrical and ferroelectric characterization.

Chapter 4 presents a result on the optimization of the growth of stoichiometric $K_{0.5}Na_{0.5}NbO_3$/Pt by PLD. The critical importance of pre-growth substrate template engineering is discussed, showing evidence of sizable improvement of KNN piezoelectric response upon optimization

of a suitable substrate cleaning procedure including an *ex-situ* plasma cleaning and an *in-situ* annealing in vacuum.

Chapter 5 describes the results obtained upon slight Li-doping of the KNN system. The impact of high Li mobility, leading to non-uniform concentration over the film thickness and surface segregation, is discussed in connection to the overall degradation of the functional properties upon doping, at variance with previous reports in literature. The importance of the thermal budget used in a PVD technique in order to prevent diffusion of dopants is discussed.

Chapter 6 shows the results of the characterization of epitaxial KNN thin films, representing an ideal case for investigating intrinsic properties of KNN films. The essential importance of the growth temperature in determining the 2D epitaxial or 3D island growth mode is correlated with the trade-off with respect to the volatilization of alkali components and consequent deviation from the nominal stoichiometry. Evidence of strain relaxation mechanisms by the formation of a squared periodic pattern in the spontaneous ferroelectric domains is found.

Chapter 7 reports a detailed investigation of the impact of different top electrodes (TE), namely Pt, Ni and Ti, on the functional properties of the TE/KNN/Pt capacitors.

Chapter 8 describes the work on $Hf_{0.5}Zr_{0.5}O_2$ thin films and the adopted strategies to increase the ferroelectric remanent polarization. This is done mainly by increasing the cell volume by engineering of structure and lattice stress, with the aim of enhancing ferro- and piezoelectric performances and making hafnia-based thin films a suitable competitor to PZT in ferroelectric memory and transistor devices.

CHAPTER 2

Theoretical background

The fundamental physical phenomena occurring in piezo- and ferroelectric crystals are reviewed. In particular, the origin and classification of crystal classes and symmetries are discussed ni Section 2.1, together with an overview of the theoretical models to describe piezoelectricity and ferroelectricity (Sections 2.3 and 2.4). Moreover, the origin of ferroelectricity in KNN and HZO system is discussed in Sections 2.5 and 2.7 considering their perovskite and fluorite lattice structures, respectively.

2.1 Crystal Structure

There is a quite number of ways in which functional materials can be classified. Categorization depends on the specific material properties and physical behaviour of interest. When considering the electrical and conducting properties, materials can be divided into conductors, semiconductors and insulators.
Insulators are often also called *dielectrics*, because in most cases an applied electric field results in a redistribution of the bounded electrons with a resulting polarization being a linear function of the electric field (see Section 2.2).

Another classification of interest for this work is based on the atomic structure and ordering. A material is defined as a *crystal* when it is composed of units, be it atoms, ions or molecules, packed in an ordered regular pattern of unit cells. Single crystals are defined as crystals in which the entire lattice is continuous, lacking any grain boundary or dislocation. Otherwise, the material is a polycrystal made up of small crystalline domains called crystallites. At the opposite extreme, when a material exhibits no symmetry or regular ordering in its structure, it is *amorphous*.

As shown in Figure 2.1, crystals can be classified into 32 point groups depending on the crystallographic symmetry and in two classes: centrosymmetric and non-centrosymmetric crystals. The former cannot be polar because there is no net dipole moment in the unit cell. The latter can be polar because they can develop a net dipole moment, and thus a local polarization, either

spontaneously or in response to an external stimulus. In this regard, non-centrosymmetric crystals can be divided into materials with a unique polarization axis which develop a spontaneous polarization and materials with no unique polarization axis which do not show a spontaneous polarization. Within the first group, switchable and non-switchable materials can in turn be distinguished.

Dielectric crystals, i.e. insulating materials with ordered lattices of unit cells with a polarization response to an electric field, can exhibit a series of specific electrical phenomena depending on their crystalline structure and symmetric properties. In particular, *piezoelectric* materials are able to generate an electric field when an external stress deformation is applied (and viceversa); *pyroelectric* materials produce an electric potential when heated or cooled; *ferroelectric* materials are polar crystals with a defined spontaneous polarization that can be reversed by applying an electric field. All piezoelectric materials are dielectrics, i.e. electrical insulators, and belong to the non-centrosymmetric crystal class, because a mechanical stimulus can generate a net dipole moment. In some piezoelectrics, pyroelectrics, dipoles can be induced by structural modifications occurring upon heating or cooling the non-centrosymmetric material. Similarly, being polar non-centrosymmetric materials with a spontaneous polarization, all ferroelectrics are also pyroelectric.
These physical phenomena mentioned above are described in more detail in the following Sections.

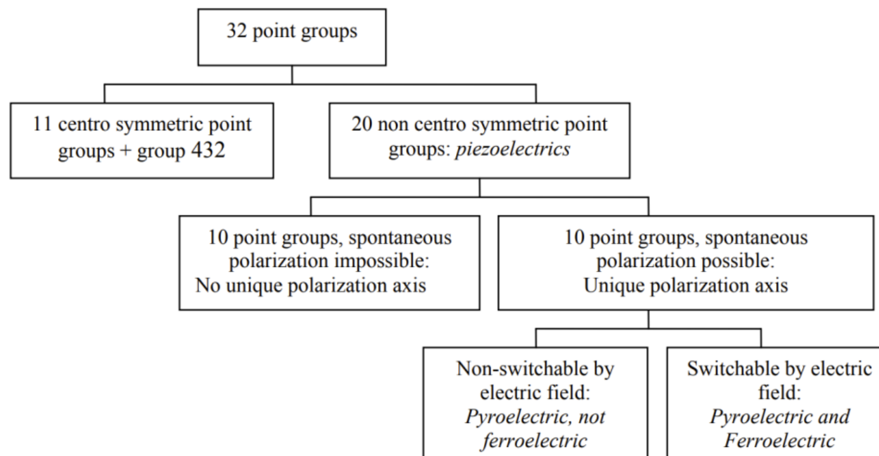

Figure 2.1: *Diagram of 32 crystal point groups. The symmetry of the crystal determines its functional properties, i.e. whether a material shows dielectric, piezoelectric, pyroelectric, ferroelectric behaviour.*

2.2 Dielectric behaviour

Dielectrics are insulating materials with electrons strongly bound to their atoms or molecules, but in which the overall charge surrounding the single atoms can be polarized by applying an external electric field. Possible mechanisms of polarization in dielectric materials are shown in Figure 2.2. Polarization can either occur by shifting the electron cloud with respect to the nucleus (electronic polarization), by displacing the ions from their crystal lattice position (ionic polarization), by aligning permanent dipoles (orientation polarization) or also by spatial inhomogeneities of charge carrier density (space-charge polarization).
Upon polarization, electric dipole moments are created within the material consisting of two opposite charges $+q$ and $-q$ separated by a distance d and can be expressed as:

$$\boldsymbol{p} = q\boldsymbol{d} \tag{2.1}$$

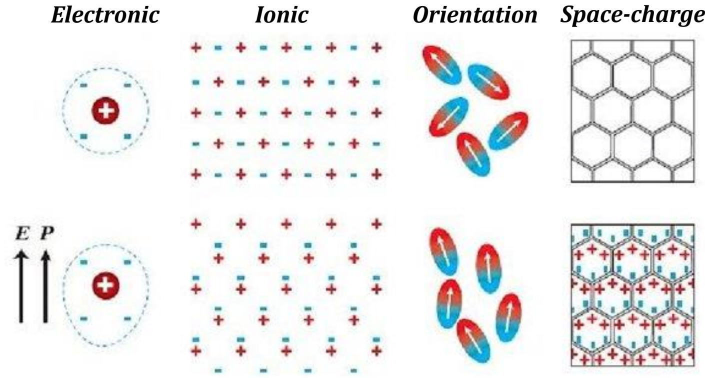

Figure 2.2: *Schematic of the different polarization mechanisms that can occur in dielectric materials depending on their nature. Reprinted from [72].*

The dipole moment per unit volume is defined as the polarization $\boldsymbol{P}$:

$$\boldsymbol{P} = N\boldsymbol{p} \tag{2.2}$$

with N the dipole density. The behaviour of dielectrics under an applied electric field can be described in terms of a linear relationship:

$$\boldsymbol{P} = \epsilon_0 \chi \boldsymbol{E} \tag{2.3}$$

ϵ_0 being the electric permittivity of free space and χ the electric susceptibility, which is a tensor in the most general case and a scalar for isotropic media.
The susceptibility is related to the relative permittivity ϵ_r of the medium using the definition of the electrical displacement $\boldsymbol{D}$:

$$\boldsymbol{D} = \epsilon_0 \boldsymbol{E} + \boldsymbol{P} = \epsilon_0 \boldsymbol{E} + \epsilon_0 \chi \boldsymbol{E} = \epsilon_r \epsilon_0 \boldsymbol{E} \tag{2.4}$$

so that $\epsilon_r = 1 + \chi$ for isotropic media.

2.3 Piezoelectricity

The piezoelectric effect is defined as the generation of a charge in response to an applied mechanical stress. Discovered by the brothers Jacques and Pierre Curie in 1880, it was named taking inspiration from the Greek word $\pi\iota\acute{\epsilon}\zeta\epsilon\iota\nu$, which means to press, to squeeze. The opposite effect, called the converse or inverse piezoelectric effect, can also take place if a mechanical deformation is generated by applying an external electric field. Piezoelectricity results from the linear electromechanical coupling between electrical and mechanical states in non-centrosymmetric crystalline materials.

Matrix formulation

The direct piezoelectric effect is described by the following general relationship:

$$P_j = d_{jkl} X_{kl} \tag{2.5}$$

In this expression, P_j is the component of the polarization vector along the $j-$direction, i.e. the polar axis (commonly expressed in μC/cm^2); d_{jkl} is the piezoelectric coefficient in the form

of a rank-3 tensor (in units of pC/N); and X_{kl} (in Pa) represents the rank-2 tensor of the stress components, with k being the direction of the force and l the normal to the surface it acts upon.
Similarly, the inverse piezoelectric effect is expressed as:

$$x_{ij} = d_{ijk}E_k \tag{2.6}$$

where x_{ij} is the rank-2 tensor of the (dimensionless) strain components, d_{ijk} (pm/V) is the rank-3 tensor of the inverse piezoelectric coefficients and E_k (kV/cm) is the applied electric field vector component along the $k-$direction.

The piezoelectric tensor is made of 27 distinct coefficients, only 18 of which are independent terms according to symmetry constraints. It is conventionally represented in a 6×3 matrix form. Stress tensor is a symmetric tensor, i.e. the relationship $X_{ij} = X_{ji}$ holds for all terms, therefore it can be reduced to a 6×1 vector using: $11 \rightarrow 1$, $22 \rightarrow 2$, $33 \rightarrow 3$, and for the shear deformation planes: 23 or $32 \rightarrow 4$, 13 or $31 \rightarrow 5$, 12 or $21 \rightarrow 6$.

$$\begin{pmatrix} P_1 \\ P_2 \\ P_3 \end{pmatrix} = \begin{pmatrix} d_{11} & d_{12} & d_{13} & d_{14} & d_{15} & d_{16} \\ d_{21} & d_{22} & d_{23} & d_{24} & d_{25} & d_{26} \\ d_{31} & d_{32} & d_{33} & d_{34} & d_{35} & d_{36} \end{pmatrix} \begin{pmatrix} X_1 \\ X_2 \\ X_3 \\ X_4 \\ X_5 \\ X_6 \end{pmatrix} \tag{2.7}$$

A similar approach applies for writing the converse piezoelectric effect in matrix form, where strain is also a symmetric tensor, so the final form is:

$$\begin{pmatrix} x_1 \\ x_2 \\ x_3 \\ x_4 \\ x_5 \\ x_6 \end{pmatrix} = \begin{pmatrix} d_{11} & d_{12} & d_{13} & d_{14} & d_{15} & d_{16} \\ d_{21} & d_{22} & d_{23} & d_{24} & d_{25} & d_{26} \\ d_{31} & d_{32} & d_{33} & d_{34} & d_{35} & d_{36} \end{pmatrix} \begin{pmatrix} E_1 \\ E_2 \\ E_3 \end{pmatrix} \tag{2.8}$$

Using the matrix form of the piezoelectric coefficient allows to easily represent the effect of symmetry constraints on the piezoelectric response of a crystal. Some of the most common crystal symmetries shared by many piezoelectric materials are the cubic, tetragonal, orthorombic and rhombohedral structures (Figure 2.3). Only the crystal point group of non-centrosymmetric

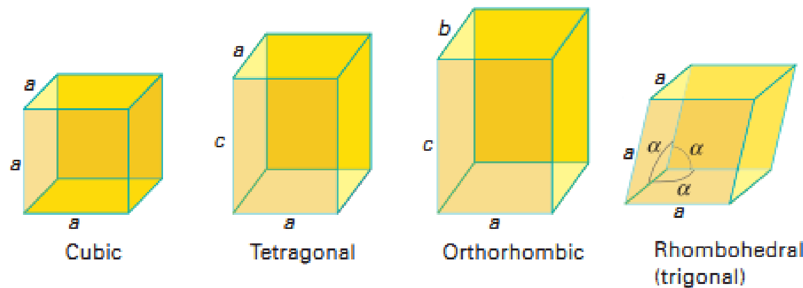

Figure 2.3: *Most typical crystal structure symmetries for piezoelectric materials.*

structures retains one or more non-zero d_{ij} in the matrix. Even in this group some of the piezoelectric coefficients can be zero because depending on the specific crystal structure there can be invariance with respect to some specific symmetry transformations. The d_{33} coefficient is related to the force and polarization being both perpendicular to the sample surface; d_{31} represents the case of force and polarization being perpendicular to each other; and d_{51} is the shear piezoelectric coefficient corresponding to the application of a shear force.

Thermodynamic description

In the thermodynamic model description of matter, piezoelectric properties can be derived from inspection and proper differentiation of the Gibbs free energy. In particular, the elastic Gibbs free energy in isothermal conditions is the quantity of interest for this purpose:

$$G\left(T, X, D\right) = U - TS - X_{ij}x_{ij} \tag{2.9}$$

$$dG = -SdT - x_{ij}dX_{ij} + E_i dD_i \tag{2.10}$$

with the independent variables T, X and D being the temperature, the elastic stress and the electric displacement respectively, and the variables U, S, E, x being the internal energy, the entropy, the electric field and the elastic strain.
From partial derivatives of G with respect to the independent variables, relationships between dependent and independent values can be obtained, and a set of (D, X, T) for a stable phase is identified.

$$S = \left(\frac{\partial G}{\partial T}\right)_{X=0,E=0}, x = \left(\frac{\partial G}{\partial X}\right)_{T=0,E=0}, D = \left(\frac{\partial G}{\partial E}\right)_{X=0,T=0} \tag{2.11}$$

The second-order partial derivatives of the expressions above describe different physical phenomena including the dielectric coefficient (Equation 2.12) and two piezoelectric coefficients (Equation 2.13 and 2.14):

$$\epsilon = \left(\frac{\partial^2 G}{\partial E \partial E}\right)_{X=0,T=0} = \left(\frac{\partial D}{\partial E}\right)_{X=0,T=0} \tag{2.12}$$

$$d = \left(\frac{\partial^2 G}{\partial X \partial E}\right)_{T=0} = \left(\frac{\partial D}{\partial X}\right)_{T=0,E=0} \tag{2.13}$$

$$d' = \left(\frac{\partial^2 G}{\partial E \partial X}\right)_{T=0} = \left(\frac{\partial x}{\partial E}\right)_{X=0,T=0} \tag{2.14}$$

The first coefficient d is the direct piezoelectric coefficient and defines the electric displacement in response to a stress. Instead, d' represents a strain dependent on electric field and is the converse piezoelectric coefficient. The thermodynamic effects resulting from the two piezoelectric coefficients result identical. As a matter of fact, the order of differentiation is in principle irrelevant, but depending on the chosen one, two different expressions corresponding to the double manifestation of the piezoelectric effect are highlighted.

2.4 Ferroelectricity

As stated above, if the spontaneous dipole of a pyroelectric material can be reversed by an external electric field, the material is also a ferroelectric (see Section 2.1). The name comes

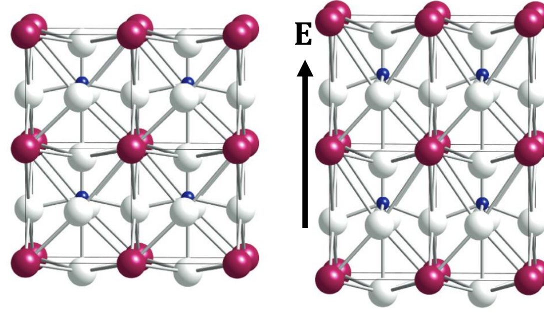

Figure 2.4: *Atomic lattice made of centrosymmetric unit cells (left), and of non-centrosymmetric distorted unit cells (right).*

from the analogy with *ferro*magnetic materials characterized by a non-zero magnetic moment. Ferroelectric materials retain a non-vanishing dipole moment even in absence of an electric field or, equivalently, after an external electric field is removed. If the polarization generated in the material by an external polarizing field vanishes upon removal of the electric stimulus, the material is said to be *paraelectric*. This behaviour is due to the randomization of the alignment of electric dipoles by thermal energy.

In the analytical description of ferroelectric materials, an extra term represented by the spontaneous polarization $\boldsymbol{P_s}$ is added in the expression of the electrical displacement:

$$\boldsymbol{D} = \epsilon_0 \boldsymbol{E} + \epsilon_0 \chi \boldsymbol{E} + \boldsymbol{P_s} \tag{2.15}$$

As already mentioned, the spontaneous polarization can only be developed in the case of non-centrosymmetric unit cells. This occurs in most ferroelectrics due to the Jahn-Teller distortion, which produces an ionic displacement within the unit cell of a non-polar centrosymmetric prototype phase, generating an electric dipole [73]. An example is shown in Figure 2.4 in the case of a perovskite ABO_3 structure, where either the B (or A) cation is shifted to reach a lower potential energy state. More on the structure of perovskites is presented in Section 2.5.

Landau theory of ferroelectricity

In order for a non-zero macroscopic polarization to be generated, the local distortion of the unit cell must be associated to long range ordering. A very famous description of ferroelectric ordering is offered by the general Landau theory [74]. This approach uses a thermodynamic formulation and symmetry considerations to represent a system equilibrium state in the proximity of a phase transition. The approach is based on expanding the free energy F as a power series of an order parameter and keeping only the compatible terms with the symmetry of the system. In this context, the order parameter is the polarization P, and all odd-power terms can be removed for symmetry reasons:

$$F(P) = \frac{1}{2}aP^2 + \frac{1}{4}bP^4 + \frac{1}{6}acP^6 - EP \tag{2.16}$$

The coefficients a, b and c are temperature- and pressure-dependent and can be obtained experimentally or analytically [75].
To find the equilibrium state, the free energy must be minimized:

$$\frac{\partial F(P)}{\partial P} = 0 \tag{2.17}$$

The minimum is found at $P = 0$ for paraelectric materials and at a non-zero position for ferroelectric materials.
Near the phase transition, with T approaching T_0, $a = a_0 (T - T_0)$, and both a_0 and c coefficients are positive for all ferroelectrics. The sign of b determines the nature of the phase transition from a paraelectric ($T > T_0$) to a ferroelectric state ($T < T_0$). In particular, if $b > 0$ a second-order phase transition will occur and the free energy will progressively evolve from a parabolic, single-minimum profile into a new one with two opposite minima of equal energy (Figure 2.5a). In this case, $T_C = T_0$, and below this temperature the polarization grows continuously, as shown in the inset of Figure 2.5a.
On the other hand, the case of $b < 0$ is sketched in Figure 2.5b. The transition occurs through the appearance, above T_0, of auxiliary local minima with non-zero polarization and progressively decreasing energy. When T_C is reached, all minima have the same energy, and further cooling the system will cause the polarization to jump to a non-zero value (inset of Figure 2.5b).

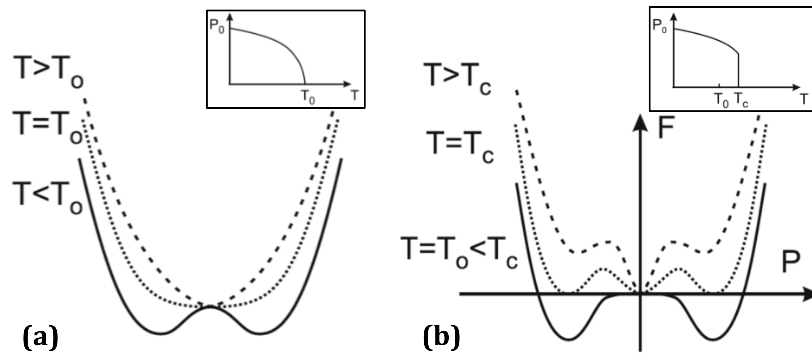

Figure 2.5: *Evolution of the free energy in the case of a (a) second-order (b) first-order phase transition. Insets show the spontaneous polarization as a function of temperature, assuming zero polarization above T_0 (from [76]).*

Above the Curie temperature T_0 the behaviour of the dielectric constant in the ferroelectric material is described by the Curie-Weiss law:

$$K \cong \frac{C}{T - T_0} \tag{2.18}$$

with K the dielectric constant, C the Curie constant and T_0 the Curie temperature. At the phase transition temperature, the dielectric constant diverges and a series of structural modifications induce a new polar phase. These changes come with the observation of strong anomalies in the values of the dielectric, elastic, thermal and piezoelectric properties [77].
As explained later in Section 2.6, most ferroelectrics can usually undergo multiple phase transitions, some above the Curie temperature and some below. Depending on the composition and structural changes, these transitions are always accompanied by the anomalous behaviour of many physical properties and can be also exploited to improve the piezoelectric response.

Polarization Hysteresis

In a ferroelectric material the permanent dipole can be switched by an external electric field, and cycling through positive and negative fields leads to the observation of a hysteretic behaviour. In Figure 2.6 the characteristic P−E curve in the shape of a hysteresis loop is shown. The polarization starts initially from zero (or a pristine, unknown value) and increases up to a *saturation*

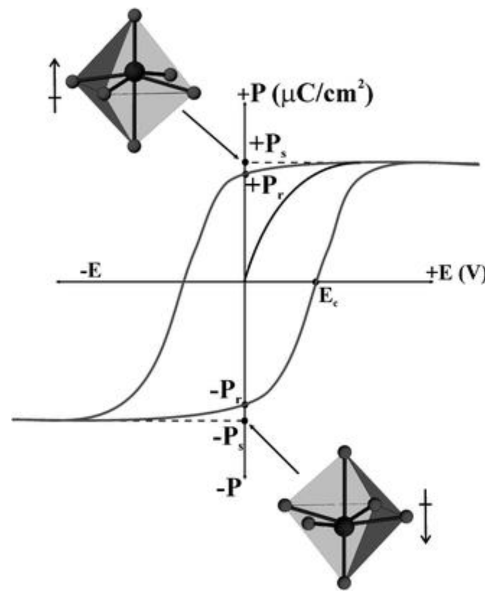

Figure 2.6: *Polarization hysteresis loop of a ferroelectric material upon application of an exteral electric field (from [78]).*

value P_{sat} with all dipoles within the materials pointing upwards. As the field is decreased, the polarization decreases down to a *remanent polarization* P_r at zero field. The electric field required to bring the polarization back to zero is the *coercive field*, $-E_c$ for this side of the cycle. The same applied for negative applied electric fields, with the polarization reaching the limit of $-P_{sat}$, evolving towards $-P_r$ at zero field and going to zero at $+E_c$. The switching event in correspondence of E_c results in sudden peaks in the I−E loop (switching current), due to the reorientation of internal charges.

Ferroelectric Domains

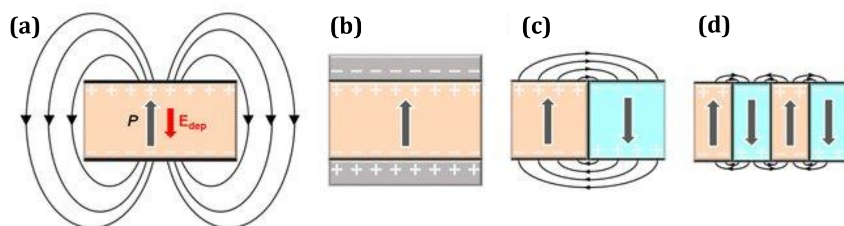

Figure 2.7: *Domain formation in ferroelectrics. (a) Single-domain state leads to the formation of an electrical stray field (black lines). (b) The formation of surface charges provides a complete screening of the ferroelectric polarization. (c) 180-domain wall reduces the electric stray field and the depolarizing field contributing to the electrostatic energy. (d) Formation of multiple domains reduces the electric stray field (from [79]).*

From a morphological point of view, ferroelectric crystals are usually made of separated and well-distinguished grains. Within each grain, multiple polarization domains are formed, i.e. finite regions with a defined polarization, because adjacent dipoles tend to assume the same orientation. The appearence of spontaneous polarization results in surface charges that generate a *depolarizing field* E_d (Figure 2.7a−b). The formation of domains is energetically favourable because it reduces the electrostatic energy of the depolarizing field and the elastic energy of the mechanical strain within the material (Figure 2.7c−d) [79]. Ferroelectric domains are separated by domain walls, mainly classified into 180°-walls and 90°-walls depending on

the relative orientation of P in adjacent domains.

2.5 Perovskite structure

Piezo- and ferroelectric oxides can display a variety of different structures, composition and atomic ordering. The most known types of structures are perovskites, pyrochlores, wurtzites and Aurivillius structures.

Among these, the structure with the most compositional adaptability is that of the perovskite.

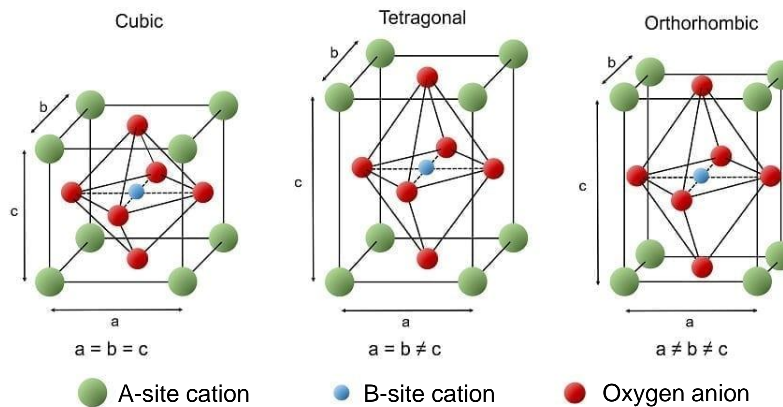

Figure 2.8: *Schematic of the perovskite structure. Left: centrosymmetric simple cubic unit cell. Tetragonal (center) and orthorombic (right) unit cells allow for the ionic displacement leading to the formation of a ferroelectric polarization.*

Perovskites generally have the chemical formula ABO_3, where A and B stand for cation elements, cation mixtures, or vacancies. The distinctive structure features a cubic lattice with a simple base of 5 atoms. The cubic cell is made up of A atoms, and at the center of each of the four edges is an oxygen atom. The B cation is found at the center of the oxygen octahedron, which is made up of 6 oxygen atoms [80]. Figure 2.8 displays a schematic of the perovskite structure unit cell. Since practically every element of the periodic table may be included in a perovskite structure, it can accommodate a variety of cation sizes and charges, within the values of tolerance factor $t \sim 1$ which prevent unacceptable distortions. This explains the enormous interest this crystal class has generated [77]. The potential for A, B, or both atoms to be partly replaced by a third element, creating a solid solution with stoichiometry $A_{1-x}C_xBO_3$ or $AC_{1-x}B_xO_3$, is a crucial aspect of perovskite structure. Even though the replacing ions usually have comparable electrical structures relative to the replaced ones, the substitution results in a far more intricate lattice structure. $PbZr_{1-x}Ti_xO_3$ and $K_{1-x}Na_xNbO_3$ are representative examples of these solid solutions.

The perovskite oxide family, which contains several noteworthy ferroelectrics (such as (K, Na)NbO_3, $BaTiO_3$, Pb(Zr, Ti)O_3, and others), is the largest and most researched family of ferroelectrics [80, 76]. The perovskite mineral ($CaTiO_3$), which is made of calcium titanate, gives rise to the name of the group of perovskites. Depending on composition, these materials can be both conductive and insulating, and they display a variety of structural and magnetic ordering.

By changing the composition of the solid, particularly in binary systems, it is possible to produce polar states, transitions between them, and distortions of the unit cell. However, functional properties often do not exhibit a considerable dependence on composition [76]. The cubic reference state of a perovskite is naturally centrosymmetric (Figure 2.8, left), and corresponds to the high-temperature paraelectric phase. The ferroelectric polarization charge in the structure is a

result of the displacement of one type of ion within the crystal lattice. In the most general case, the core cation will be somewhat displaced by a composition- or temperature-dependent phase transition, and a non-zero polarization will be produced in the new tetragonal/orthorombic unit cell (Figure 2.8, center and right, respectively), which allows to host atomic displacements more easily. For instance, the dipole moment of PZT is generated by the displacement of Ti^{4+} or Zr^{4+} cations with respect to the center of the oxygen octahedron. Based only on the movement of the central atom, the structure of the unit cell will not change. Instead, the dimensions of the cell can be altered in a variety of ways depending on the polarization direction, which may lie along various axes, such as parallel to a cube edge, a face diagonal, or a cube diagonal [81], as shown in Figure 2.9. Charge generation through the displacement of the central atom of the unit cell is the most frequent case, but additional structural transitions could be present depending on the solid, giving rise to different polarization mechanisms and resultinng in a more complicated phase diagram.

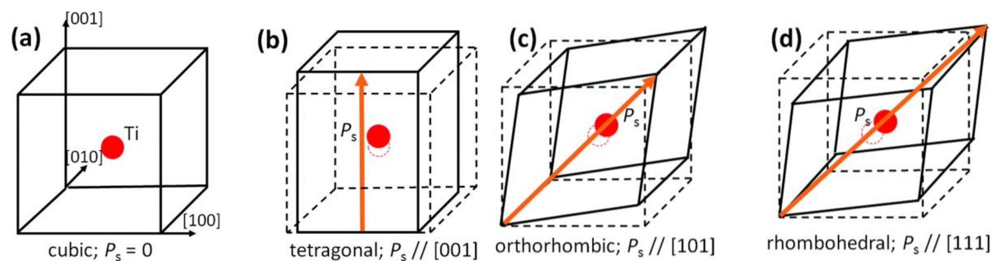

Figure 2.9: *Sketch of some possible polarization configurations depending on the crystal structure.*

2.6 Phase Boundaries

The ease with which their properties can be tuned is a characteristic quality of perovskite ferro- and piezoelectrics that makes their research particularly attractive. In fact, many elements can be substituted in the different sites of perovskites, allowing for beneficial compositional alterations. Phase transitions of perovskite materials are particularly related to parameter tunability and, more specifically, to the improvement of dielectric and piezoelectric properties in correspondence of some phase boundaries [82]. For instance, perovskites often exhibit excellent properties when approaching the temperature-driven ferroelectric to paraelectric transition, also known as Polymorphic Phase Transitions (PPT) and located at a Polymorphic Phase Boundary (PPB) in the phase diagram [83, 84]. The potential uses are, however, constrained by the inherent temperature dependency of this variation in functional responses since such temperature dependency might be detrimental to optimal material performances.

Another interesting category of phase transitions is that of the so-called Morphotropic Phase Transitions (MPT), i.e. composition-driven transitions in which substantial alterations in a solid structure are triggered by a change in its composition. This type of transition occurs in correspondence of the Morphotropic Phase Boundary (MPB), which is a boundary line in the phase diagram where multiple phases coexist in an equal percentage [86, 87]. Both types of phase transitions can be found in the phase diagram of PZT, and the most important are shown in red arrows in Figure 2.10: PPTs (vertical arrow) are vertical transitions at a constant composition (e.g. between a ferroelectric and a paraelectric phase), while MPTs (horizontal arrow) are horizontal transitions with a varying composition (e.g. between 45% and 52% Zr) at a constant temperature. The experimental dielectric and piezoelectric responses can be enhanced by up to even an order of magnitude in the vicinity of such phase transitions [88, 89]. The existence of

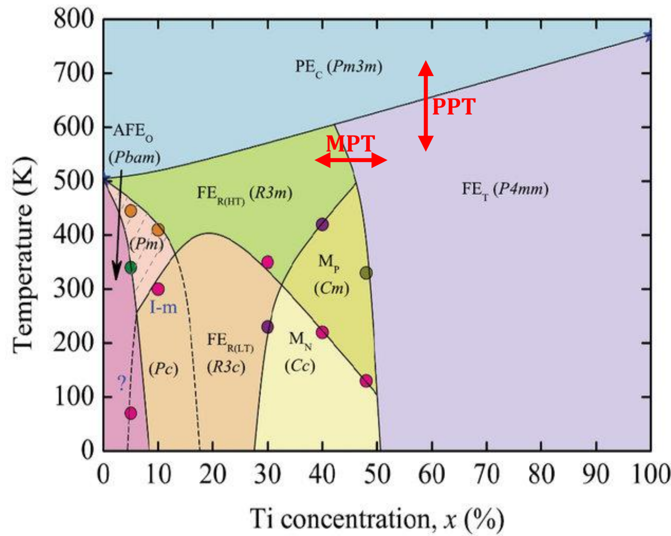

Figure 2.10: *Phase diagram of lead zirconate titanate (PZT) perovskite (from [85]). A typical MPT between the ferroelectric tetragonal (FE_T) phase and ferroelectric rhombohedral (FE_R) phase, is indicated by a horizontal red arrow, while a vertical red arrow indicates a typical PPT between the ferroelectric tetragonal (FE_T) phase and paraelectric cubic (PE_C) phase.*

two roughly thermodynamically equivalent states is the basic principle behind this phenomenon. This makes it easier to align polarization dipoles or domains because of the presence of a flattened free energy profile which strongly favours polarization rotation and reorientation. In this sense, Pb(Zr, Ti)O_3 system provides a very representative example of how functional properties can be improved near or at the MPB. The piezoelectric properties of PZT, which were first described by Jaffe in 1955 [87], are at their apex when equal amounts of lead titanate ($PbTiO_3$) and lead zirconate ($PbZrO_3$) are present in the binary solid solution. For this composition, the material exhibits a Morphotropic Phase Boundary where the ferroelectric rhombohedral phase and the ferroelectric tetragonal phase coexist.

The study of novel, lead-free piezoelectric materials having similar piezoelectric characteristics to those of lead zirconate titanate is of special interest in the rapidly expanding field of piezoelectric materials research. When seeking for novel materials, it makes sense to focus on those that have MPB properties comparable to those of PZT. Examples are $BiFeO_3$-$PbTiO_3$, $BiScO_3$-$PbTiO_3$, and $Pb(Zn_{1/3}Nb_{2/3})O_3$-$PbTiO_3$. Even now, scientists are looking for a material that can simultaneously provide MPB and PPB. Ceramics based on potassium sodium niobate ($K_{1-x}Na_xNbO_3$), which have high T_C and a relatively high piezoelectric coefficient d_{33}, seem to be the most promising lead-free piezoelectrics. In analogy to PZT, also in KNN phase transitions can be found that boost piezoelectric performances [90, 91]. Despite the promising features of the material, Figure 1.4 shows that it still performs much worse than market-dominant PZT. Although transitions occur at higher temperatures, the temperature dependence of its piezoelectric characteristics are similar to those of the BTO. As was already mentioned in Chapter 1, KNN has drawn a lot of interest since since Saito et al. in 2004 observed a significant d_{33} of 416 pC/N [26]. This is because for the first time huge piezoelectric responses were observed in highly textured lead-free KNN ceramics with a composition near the MPB, with piezoelectric coefficients even larger than those of PZT. After this publication, in-depth research on this subject was started, also prompted by the complexity of the phase diagram of KNN (shown in Figure 2.11).

KNN features three primary phase transitions: from rhombohedral to orthorhombic transition at T_{R-O}, from orthorhombic to tetragonal at T_{O-T}, from rhombohedral to tetragonal at T_{R-T}. The first two transitions (shown as blue arrows in Figure 2.11) are present in pure KNN, the third one, instead, can occur in KNN-based materials upon the specific composition changes. These phase transitions behave in a way that is more consistent with PPT than MPT. The O-T phase transition area in particular is where optimal properties are found, yet they are very temperature dependent given their PPT nature [6]. Thus, more recent research studies attempt to introduce an R-T phase boundary or an MPB into the material in an effort to potentially improve its properties [82, 93]. It appears possible to create an R-T phase boundary by doping and compositionally tailoring the temperatures T_{R-O} and T_{R-T} to be equal. Wu et al. succeeded in doing this, obtaining high piezoelectric coefficients (d_{33} = 450−490 pC/N) [93]. The feasibility of this method of piezoelectric coefficient enhancement was demonstrated by the formation of KNN-based materials with both a high piezoelectric coefficient and a high Curie temperature T_C > 340°C, despite the fact that their initial results showed relatively low T_C of less than 200°C. A morphotropic phase boundary is present even in pure KNN, as was very just revealed (2017) [94]. In fact, for practically any Na percentage, KNN is in an orthorhombic phase at ambient temperature (green area in Figure 2.11). However, a tetragonal phase is observed when the Na concentration is x_{Na} = 0.55, seen as an intermediate phase driving the MPT between two orthorhombic structures (red arrow in Figure 2.11). At this composition, a spike in the d_{33} coefficient can be observed. The polarization rotation is simpler in the orthorhombic phase than in the tetragonal phase, which results in an improved piezoelectric response and a maximum piezoelectric coefficient of d_{33} = 203 pC/N.

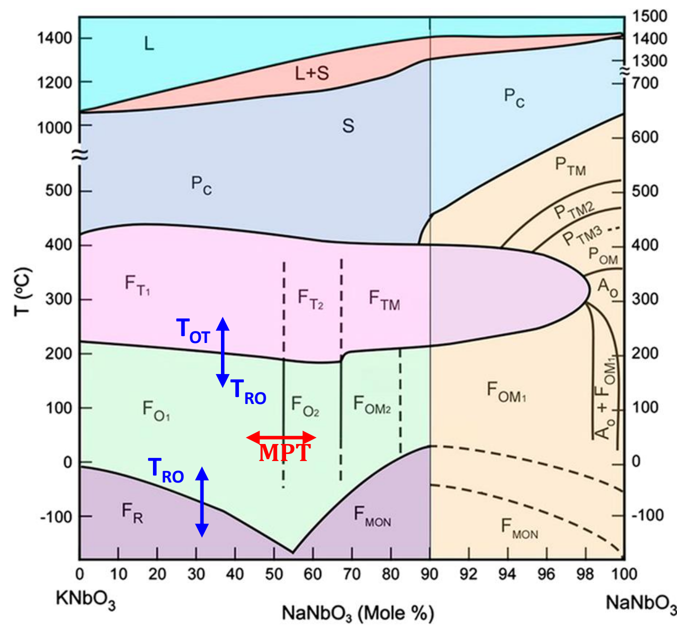

Figure 2.11: *Phase diagram of pure potassium sodium niobate (KNN) perovskite (from [92]). Blue arrows indicate transitions: between ferroelectric orthorhombic, F_O and ferroelectric tetragonal, F_O (T_{OT}); between ferroelectric rhombohedral, F_R and ferroelectric orthorhombic, F_O (T_{RO}); since the figure represents pure KNN, the transition between ferroelectric rhombohedral, F_R and ferroelectric tetragonal, F_T (T_{RT}) is not shown. MPT between two orthorhombic phases through the intermediate tetragonal phase at x_{Na} = 0.555 is indicated in red.*

2.7 Origin of ferroelectricity in Zr-doped HfO_2

In terms of physical properties, HfO_2 has a lot in common with ZrO_2, as very comparable crystal structure and phase diagrams result from the same valence and ionic radius. Besides, ZrO_2 substitutions are greatly desired due to the greater availability of Zr with respect to Hf. The unusual behavior of the solid solution between HfO_2 and ZrO_2 is caused, interestingly, by differences in the surface energy of these materials as well as in their phase stability under size reduction [95]. At room temperature, the monoclinic phase (*P21/c*, m-phase) constitutes the bulk stable structure of HfO_2- and ZrO_2-based compounds [96, 96]. On the other hand, the tetragonal (*P42/nmc*, t-phase) and cubic (*Fm3m*, c-phase) structures, corresponding to high-temperature and high-pressure phases, may be stabilized at ambient temperature by performing doping [97] or by nanostructuring [95]. Additionally, by appropriate doping and by carefully adding engineered mechanical strains, rhombohedral phases (r-phase) have also been produced [98]. The tetragonal and rhombohedral phases have a substantially smaller volume than the monoclinic phase and are distortions of the cubic phase.
According to reports, none of the aforementioned phases are polar. The potential phases that might result in ferroelectric behaviour in this novel class of materials have recently been modeled in a number of theoretical papers [99], and include a polar orthorhombic phase (space group *Pca21*, o-phase), which was initially discovered for Mg-doped ZrO_2 ceramics upon cooling them down to cryogenic temperatures [100]. Calculations show that this phase is the most likely polar distortion of the tetragonal fluorite phase (relatively close in energy), and, as a consequence, this polar phase is believed to represent the structural basis for the newly observed ferroelectricity in thin films based on HfO_2. The origin of the polarization in this structure is believed to lie in the displacement of oxygen atoms in the lattice cell (Figure 2.12).
The stabilization of HfO_2-based ferroelectric films has been reported in literature with a variety

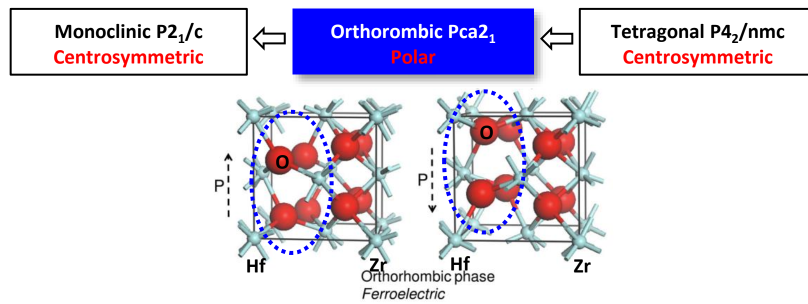

Figure 2.12: *Fluorite structure of hafnium oxide. Oxygen distortions lead to a spontaneous polarization in the orthorhombic phase, which is an intermediate transition phase between tetragonal and monoclinic structures.*

of methods employed, featuring a wide span of growth techniques (such as atomic layer deposition (ALD) [57], chemical solution deposition [101], pulsed laser deposition (PLD) [102], and chemical vapour deposition [103]) on various substrates (e.g. Si [104], $SrTiO_2$ and Y-ZrO_2 [105]), the wide choice of dopants and of electrode material (such as Pt [106], TiN [107], Si [108]). The ferroelectric phase was proposed to be stabilized by a number of different methods, including stress [109], doping [110], confinement by the top electrode [107], or surface energy [111]. The polar o-phase has been suggested to be the intermediate phase in the transition between the t- and m-phases, as seen in Figure 2.12 [110]. For thicknesses below 10−15 nm, the ground state at room temperature of undoped hafnia is its monoclinic phase, whereas ZrO_2 is transitioned to the low volume tetragonal phase, because ZrO_2 has a higher surface energy than HfO_2. In light of this observation, a phase transition between the monoclinic and tetragonal

phases of the $Hf_{1-x}Zr_xO_2$ solid solution should occur at intermediate concentrations. The polar orthorhombic phase serves as the intermediate connecting phase for this transition, having a cell volume between that of the tetragonal and the monoclinic phases. More specifically, the ferroelectric phase appears at a $Hf_{0.5}Zr_{0.5}O_2$ composition in specific conditions for thicknesses below $10-15$ nm [112]. Basically, the molar volume of the intermediate ferroelectric phase is increased relative to that of the fluorite phase by all of the above-mentioned mechanisms (doping, confinement, and nanostructuring), concurring at the stabilization of the polar orthorombic phase.

The size of the ferroelectric domains is always in the range of 10 nm, regardless of the employed method for achieving ferroelectricity (doping or confinement). Initially, only ultrathin films (typically 10 nm thick) were found to have the greatest ferroelectric properties [57]. With increasing thickness, the non-polar monoclinic phase appeared, and the polarization dramatically decreased as a direct consequence [113]. In thicker films (50 to 390 nm) [101] that have been discovered to contain ferroelectricity more recently, the typical grain size is still $10-20$ nm. Because tiny crystallites are the common denominator throughout all reported ferroelectric hafnia-based films, this emphasizes the critical role that size effects play in maintaining the ferroelectric phase [112]. In fact, it is known that surface energy (σ) in nanoparticles with radius r can lead to high internal pressures ($p = 2\sigma/r$) of up to a few GPa [114]. Small crystals will thus favour the stability of the lower volume cubic or tetragonal phases over the monoclinic phase at room temperature to decrease the contribution of surface energy σ [115]. The bulk m-phase is always present in thicker films above 10 nm (where the crystals have the possibility of growing further) [60].

The majority of studies discuss polycrystalline films grown by ALD technique with various phases (monoclinic, tetragonal, and orthorombic). A thorough structural characterization is further complicated by the similarity of these structures and the relatively small size of crystallites. To explore the parameters influencing ferroelectricity, well-oriented or epitaxial samples, ideally in a single phase, are preferred. On yttria-stabilized ZrO_2 substrates, single-crystal, epitaxial Y-doped HfO_2 films have been produced using the PLD process, achieving a polarization of 16 μC/cm^2 [105].

CHAPTER 3

Experimental Methods

The primary experimental techniques and equipments employed in this research work are described in this Chapter. Most of the processes and characterizations described in the following were carried out in a cleanroom of class ISO 08 or superior. Thin films of KNN on Pt and HZO/LSMO on STO single crystals were grown by Pulsed laser deposition (PLD). The main principles and fundamental parameters to optimize the growth of an oxide thin film by means of this technique are reported in Section 3.1.1. The techniques for material characterization are introduced in Section 3.2, including morphological characterization by Scanning Electron Microscopy, chemical characterization by Energy Dispersive X-ray Spectroscopy, structural characterization by X-ray and electron Diffraction and piezoelectric characterization by Piezoresponse Force Microscopy. Section 3.3 presents the procedures for device fabrication with the deposition of top electrodes, and device characterization in terms of macroscopic electrical and ferroelectric properties.

3.1 Growth Techniques

3.1.1 Pulsed Laser Deposition

Pulsed Laser Deposition (PLD) is a Physical Vapour Deposition (PVD) process employing a short intense laser pulses to produce the ablation of a target material into a hot plasma of particles and subsequently depositing it as a thin film. In case of a heated substrate, crystalline and epitaxial thin films can be obtained. The origin of this technique dates back to 1965, and since then it has experienced a great increase in popularity for research applications thanks to its numerous advantages as flexibility, good reproducibility, precise transferring of stoichiometric ratios even for complex materials [116]. The possibility to grow in an oxygen environment makes PLD one of the most suitable techniques for the growth of oxides, oxide heterostructures and superlattices. An important drawback of PLD is that it is limited to small-area deposition processes (up to $1-2$ cm^2), which is usually only suitable for research application purposes. With regard to this issue, however, some efforts towards a mass production adaptation of PLD

are being made by some companies such as Solmates (Eschede, The Netherlands), although the technology is still in the early phases [117]. Another typical problem is related to the formation and deposition of droplets, which is a phenomenon also known as "splashing". Droplets are big portions of ablated material with diameters usually in the range of one or a few micrometers, that do not vaporize and are deposited directly on the sample surface, thus increasing the roughness and degrading its uniformy. Droplets are likely caused by hydrodynamical instabilities of the molten target surface, and the formation is strongly dependent on the quality of the fabricated target.

Basic Principles

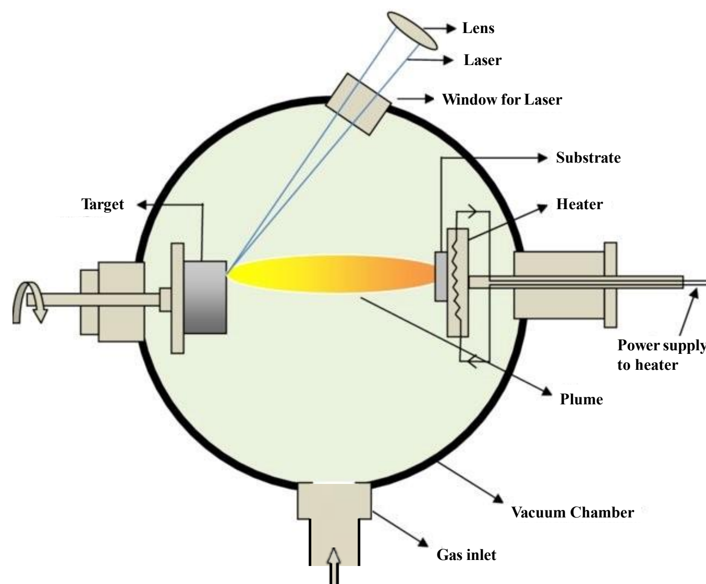

Figure 3.1: *Schematic of the Pulsed Laser Deposition equipment components.*

A schematic of a generic PLD system is shown in Figure 3.1. A UV-wavelength laser in Q-switching pulsed mode is fired and channeled into the PLD chamber through an *ad hoc* optical path made of slits, mirrors and focusing lenses, which also help shaping the laser spot size in the chamber and controlling the laser fluence.

Within the main chamber, the target and the substrate are located facing each other. The former is a ceramic material with the chosen composition and can be fixed onto a target carousel which is able to host multiple targets at once for the growth of multilayers and heterostructures. The latter is attached to a heating lamp or heating system with controlled temperature to keep the surface hot to promote crystallization of the ablated material coming from the target.

The laser is focused onto the target with a spot size of area of mm^2 and occasionally below 1 mm^2. Upon hitting the target with a pulse, provided that the ablation threshold is overcome, a plasma of ablated material is formed, which is composed of individual atoms, ions, molecules or atomic clusters. In order to prevent burning holes in one single target spot and to average out on all local compositional inhomogeneities, the target is rastered during the deposition keeping the laser spot fixed. The target can be put in rotation and moved continuously in such a way that the laser spot scans the whole surface area, leading to a more uniform material ablation. Some setups are based on the opposite mechanism, i.e. moving the laser spot while keeping the target fixed.

Despite the PLD setup being rather simple, the physical process of material ablation from

the target and thin film nucleation and growth onto the substrate is quite complex, as the combination of several thermal, mechanical and chemical phenomena is involved.
When the target is hit by a high-energy pulsed laser beam, a layer of dense plasma of ionized material is formed near the target surface, whose pressure and temperature increase with the absorption of the whole energy of the laser pulse. The plasma composition depends on the laser energy and wavelength, as these control the penetration depth of the laser pulse. The plasma, having on average the same stoichiometry of the target, expands from the target surface due to its high pressure, forming the characteristic plume shape. Thanks to this expansion, the thermal energy and ionization energy of the plasma are converted into kinetic energy, favouring particle propagation in the ambient gas atmosphere of the chamber. Here, multiple collisions occur between the plasma particles and the background gas, adsorbing part of the kinetic energy. Eventually, during this expansion the plasma material is able to reach towards the heated substrate maintaining the desired target stoichiometry.
Upon reaching the substrate, the plasma has enough energy to overcome most of the thermodynamic barriers, and adatoms undergo a process of diffusion, collision and nucleation while rearranging on the surface of the heated substrate.

Growth Parameters

In a complex process like that of PLD, many growth parameters are involved which can have a strong impact on the combination of physical phenomena taking place during ablation, plasma plume expansion, particle deposition and crystallization. As such, they also determine the quality of the final thin film, the composition, the structure and the growth rate.
The laser parameters such as the laser wavelength, spot size, pulse width and energy can notably influence the ablation of the material and the formation and composition of the plasma plume, determining the penetration depth of the pulse energy within the target, the ablated particle size and energy.
Another control parameter related to the laser the laser fluence, i.e. energy per unit area on the target, usually expressed in J/cm^2. In order to assure the reproducibility between samples it is essential to employ a controlled and well-defined fluence by adjusting the laser energy and appropriately focusing the laser beam onto the target. The laser fluence impacts on the growth rate because it determines the amount of material ablated per unit time, which in turn can have an influence on atomic ordering during deposition on the substrate surface.
The distance between the substrate and the target performs a similar role, as it determines the amount of collisions and thus the final kinetic energy of the material upon deposition. Besides, in case of ablation of very light and/or strongly volatile elements, the distance they are able to travel before losing the plume trajectory and getting lost in the chamber atmosphere can be crucial in determining the final stoichiometry of the film.
The ambient gas parameters, i.e. type of atoms, mass and pressure, determine the interaction with the plasma plume in terms of collisions and reactions, with an impact on the kinetic energy and momentum of the particle material and on the shape of the plume as well. The gas pressure is typically tuned from the base vacuum pressures of around $10^{-8}-10^{-7}$ mbar up to 0.5 mbar, producing a strong effect on film growth. The ambient gas employed for the growth of oxide materials is oxygen, which provides reactive atoms to prevent oxygen loss from the growing material and reduces the plasma kinetic energy.
The substrate temperature influences the substrate template condition upon arrival of the first ablated adatoms, provides the thermal energy for overcoming the necessary activation barriers for crystallization and assures the annealing of the first thin film monolayers while new ones are still being deposited. For these reasons, this parameter is essential in determining the

thermodynamic phenomena, atomic mobility and local arrangement and structural modifications governing the crystallization process. To allow for crystallization to occur, enough energy needs to be provided, which is why PLD of functional oxides is typically a high-temperature growth process, with substrate temperatures usually chosen above 500°C and ranging up to 900°C. Besides, because the sample is kept at such high temperatures during the whole growth process, the long annealing of the layers of the thin film while new ones are being deposited can also strongly impact the composition of the material. As a matter of fact, it can promote re-evaporation of volatile elements or wrong incorporation into the lattice of very light and mobile atoms, affecting the overall final crystalline quality.

The necessity to achieve control on all these growth parameters is what allows for the high flexibility of the PLD process, but also implies that the aim of growing thin films of new materials requires a good deal of efforts in the optimization of the growth process. The procedure involves varying and co-varying the values of the growth parameters to study the modifications in material properties, composition and structure and/or to obtain thin films with the desired performances. The optimization stage can take several iterations because of the complex interplay between different deposition parameters in influencing the physical phenomena occurring during PLD growth, but the high amount of potential combinations of growth parameters available is what also constitutes one of PLD's greatest strengths.

3.2 Material characterization

Optimization of thin films requires understanding the interplay between chemical composition, structural order and morphology. The relevant techniques employed in this works are presented in the next sections. Electron and X-Ray diffraction are introduced in Section 3.2.1 and 3.2.2. Electron Microscopy and microanalysis of chemical composition are described in Section 3.2.3 and 3.2.4. The principles of Piezoresponse Force Microscopy technique for the evaluation of the local piezoelectric behaviour are reported in Section 3.2.5. Finally, Section 3.3 describes the fabrication process and characterization of oxide microcapacitor devices.

3.2.1 X-ray Diffraction

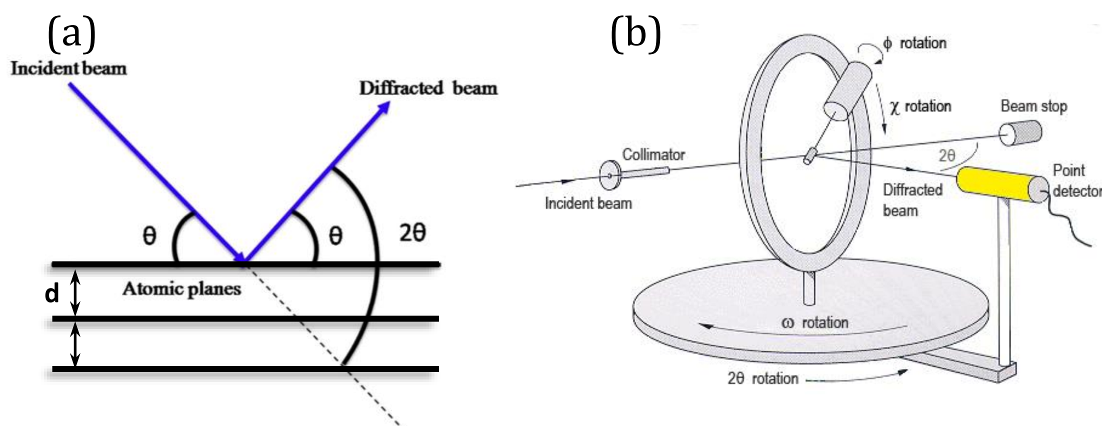

Figure 3.2: *(a) Schematic of the X-ray interaction with a specimen, (b) sketch of an X-Ray diffractometer (from [118]).*

X-ray Diffraction (XRD) is a very popular, non-destructive technique to perform structural analyses of samples such as resolving structural parameters, determining lattice phases and

orientations and sometimes even determining the composition. Its application is particularly relevant in the characterization of epitaxial thin films where additional informations on defects, lattice relationships, domains and stresses can be obtained.
In order to produce an interaction between the sample and the probing beam, whether it is an ordered crystal or an amorphous sample, X-ray beams are the most suited because X-ray wavelength lie in a similar range to the spacing between atoms in materials, i.e. a few Å (1.5406 Å for the Cu Kα wavelength typically employed in thin films diffraction). The X-ray interaction with a specimen is depicted in Figure 3.2a. In the case of a crystal species composed of an ordered lattice of atoms arranged in a periodic structure, diffraction of the X-ray beam from multiple atomic planes occurs, generating constructive or distructive interference of the diffracted beam depending on the incident angle θ according to Bragg's law:

$$2d \sin\theta = n\lambda \tag{3.1}$$

where λ represents the wavelength of the X-ray beam, θ is the incident diffraction angle, n an integer number and d the spacing between atomic planes. Therefore, when the term on the left is equal to an integer number of the incident beam wavelength, constructive interference occurs. By scanning the θ angle all the possibile reflections from the sample under investigation can be collected. This gives a diffractogram from which it is possible to obtain information about the lattice arrangement, lattice parameters, crystal cell dimensions and overall structure of the sample.
The sketch of a typical diffractometer is reported in Figure 3.2b. The incident beam aligned with optical components impinges onto the sample, positioned on a goniometer, and is subsequently collected by a detector (through an appropriate antiscattering slit). Aligning and scanning the θ angle to collect multiple out-of-plane reflections is made possible by the movement of the detector (2θ rotation) and rotation of the sample on the goniometer (ω rotation). Moreover, azimuthal (ϕ rotation) and tilt (χ rotation) angles can also be varied. This approach is commonly adopted to obtain pole figures, which are useful for assessing the orientation texture of a thin film. The diffraction angle 2θ is fixed at a specific value corresponding to the sample reflection of interest, and the diffracted beam is collected while scanning ϕ and χ angles. Besides, by combining into a single measurement scan out-of-plane XRD with in-plane XRD (diffracted intensities from lattice planes normal to the sample surface, Reciprocal Space Maps (RSM) can be built, showing diffracted intensities as a function of in-plane and out-of-plane reciprocal space constants (Q_x and Q_z, respectively). This technique is very useful to acquire information on the overall ordering of the thin film, in-plane and out-of-plane lattice parameters, stress and strain, etc.

In this thesis, XRD analysis on KNN thin films was carried out with a Bruker D8 advance X-Ray diffractometer, whereas analysis on HZO thin films with a Panalytical X'pert Pro MRD (both opearting with Cu Kα radiation at 1.5406 Å).

3.2.2 Reflection High Energy Electron Diffraction

Reflection High-Energy Electron Diffraction (RHEED) is a well known and very useful technique for low pressure qualitative investigations of solid surfaces [119]. A beam of high energy electrons accelerated by a 10−50 kV high voltage is directed against the sample at grazing incidence ($\leq 5°$). After interaction with the surface, the beam is back-diffracted and the electrons travel towards a phosphorus screen that reveals the diffraction pattern. Since the incidence angle is very small and the interaction of the beam with the sample is strong, the electrons cannot penetrate into the material more than a few unit cells, which makes RHEED a surface sensitive technique [119]. RHEED is mostly used to determine the crystallographic orientation, the unit

cell size and surface ordering of the sample by analyzing the periodic properties of the diffraction pattern. Besides, from the shape of the diffraction stripes or spots also considerations on the morphology and the growth mode can be made (Figure 3.3a). A flat 2-dimensional layer-by-layer growth leads to straight sharp diffraction elongated spots, which are characteristic of surface grazing incidence (Figure 3.3b). The presence of islands and 3-dimensional features in general, instead, generates a pattern of diffraction spots due to the transmission of the electron beam through the islands themselves (Figure 3.3g), while other RHEED patterns can be attributed to all kinds of surface morphologies (Figure 3.3c−f). Finally, by analyzing the temporal evolution of the brightness of the spot, information on the growth mode (e.g. layer-by-layer, or via formation and coalescence of islands) can also be acquired.

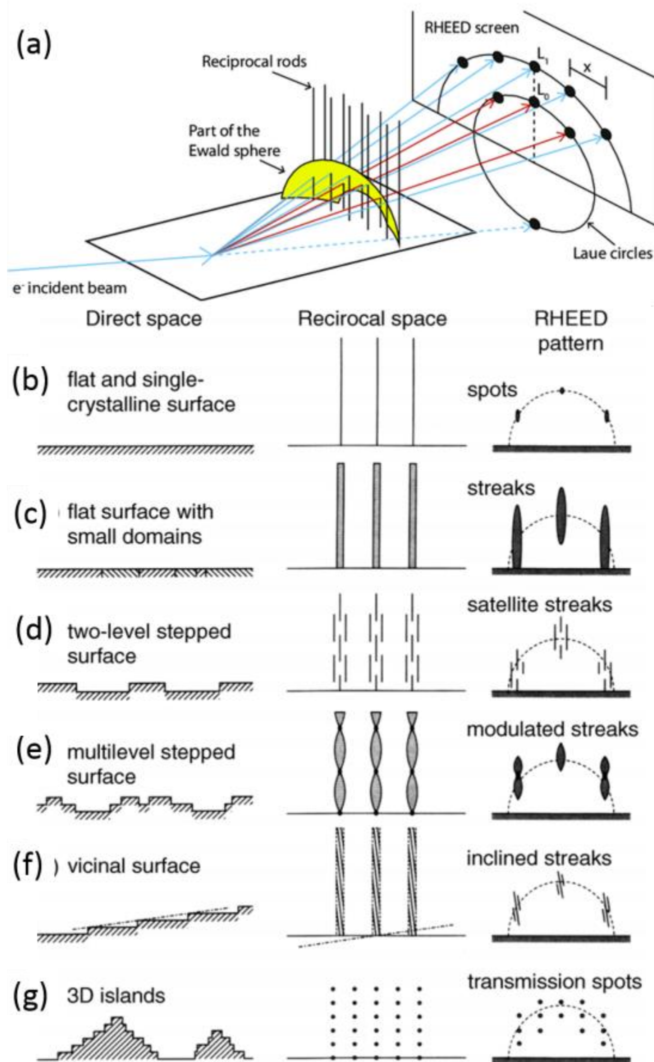

Figure 3.3: *(a) RHEED diffraction geometry and (b)−(g) diffraction patterns attributed to different thin film surface morphologies. Reprinted from [120].*

The RHEED apparatus employed in this study is a STAIB RH 50TM equipped within the PLD main chamber. As a consequence, contrary to X-Ray Diffraction, RHEED offers the advantage of typically being an *in-situ* characterization technique. For the purpose of structural analysis, to acquire patterns with sufficient intensity the energy of the electron beam was varied between 30 kV and 50 kV and the grazing incidence angle can be adjusted between $\pm 7°$ so

as to ensure enough surface sensitivity with the High Pressure RHEED installed in the PLD machine. The penetration depth calculated with the inelastic mean free path ($0.54E_k^{0.5}$) is on the order of 10 nm at 50 keV. The system maintains a focus spot smaller than 100 μm and a beam divergence smaller than 2 mrad. The sample can be rotated around its axis to allow acquisition and investigation of the RHEED diffraction pattern along different crystallographic directions. The pattern formed on the fluorescent screen is recorded by a CCD camera for software analysis and manipulation. The electron gun is equipped with a differential pumping system that, together with the high mean free path of the high energy electrons, allows to work in both UHV and low vacuum conditions, so that real-time RHEED signal can also be acquired during thin film growth.

3.2.3 Scanning Electron Microscopy

Scanning Electron Microscopy is a technique used to gain information on surface morphology, crystal structure and composition of a specimen. Topographic features can be very small, down to nanometers or tens of nanometers in size, therefore a smaller wavelength of the imaging beam than that of visible light is required in such conditions to achieve a better resolution. Since smaller features than the wavelength of the probe cannot be observed at the diffraction limit, employing electrons as a probe instead of photons allows for a smaller diffraction limit and for acquiring images with higher resolution [121].

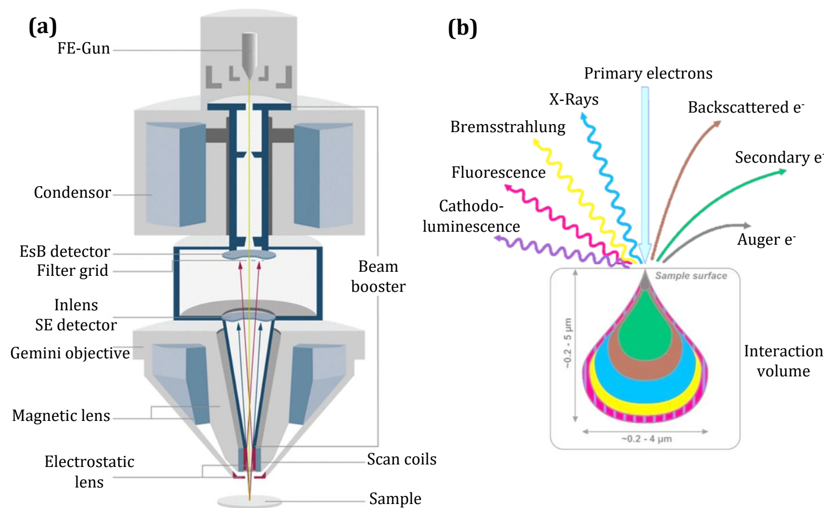

Figure 3.4: *(a) Schematic of a Scanning Electron Microscope, with all the internal components (gun, electromagnetic lenses etc.) for the focusing of the electron beam onto the sample (reprinted from [122]). (b) Electron penetration volume into a material, from [123]. All different emission phenomena generated by the interaction of the electrons with matter are displayed, and different emission signals can be detected by specific techniques.*

In a Scanning Electron Microscope (or SEM) (Figure 3.4a), a beam of incident electrons is emitted from an electron gun with energies typically in the range of $2-40$ keV. A system of electromagnetic lenses shapes the electron beam into a fine probe to be scanned across the chosen area of the sample. The penetration volume (Figure 3.4b) of the electrons into the sample, which has the characteristic "pear" shape, depends on the beam energy, on the mass of the atomic species, the beam incident angle. Within such volume, a variety of interactions between the beam and the material occur, causing the emission of backscattered, secondary and Auger electrons, X-rays and light. These different signals can be separately collected by appropriate detectors placed in the microscope chamber to acquire different kinds of information on the specimen.

In this thesis, a Raith LEO 1525 high-resolution field-emission scanning electron microscope (FE-SEM) is employed. It is equipped with a GEMINI column in which the beam is generated by emission from a Schottky-type field emission gun, i.e. a finely sharpened tungsten tip (coated in ZrO_2 to reduce the work function) heated at about 1800°C held at $4-5$ kV negative potential relative to the extractor element nearby. In this way the potential gradient at the tip surface allows the field electron emission even though the temperature is not sufficient for a sizable thermionic emission. The beam can be accelerated from 0.5 kV up to 20 kV reaching a spatial resolution of 1.5 nm at 20 kV and 3.5 nm at 1 kV on the sample. The microscope operates at base pressures of 10^{-5} mbar in the vacuum chamber, and it is equipped with an In-Lens detector to collect the electrons of the beam re-emitted by the sample, and an Everhardt-Thornley detector for secondary electrons generated within the sample by several scattering events and emitted from the surface with energies of a few eV.

3.2.4 Energy Dispersive X-ray Spectroscopy

One of the advantageous features of the SEM is the possibility to couple the morphological analysis to the chemical composition of the sample. This can be done employing the Energy Dispersive X-ray Spectroscopy technique (EDS or EDX), which can be performed within the SEM system itself provided a suitable X-Ray retector is installed. EDX is one of the most standard and widely used methods for chemical quantification in the field of electron microscopy [123].

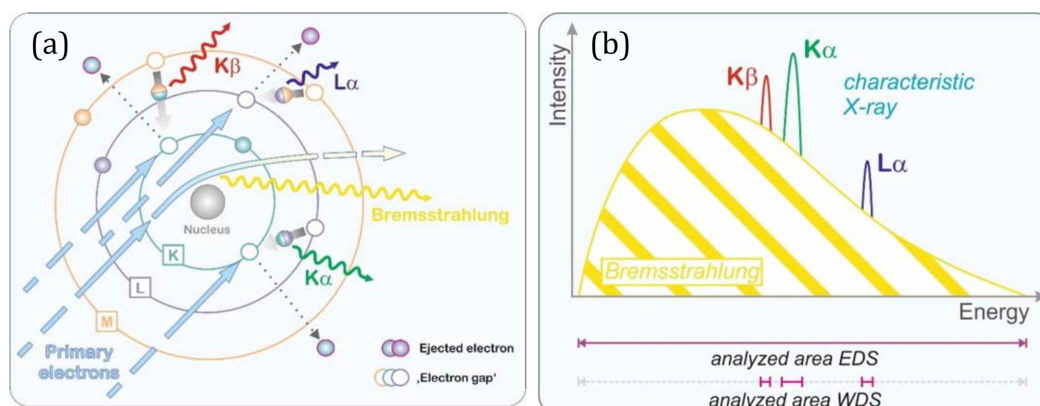

Figure 3.5: *(a) Characteristic X-Ray emission process from an atom upon interaction with the electron beam. (b) Typical EDX emission spectrum, featuring the X-Ray peaks characteristic of the atomic species and the bremsstrahlung background emission. Reprinted from [123].*

The technique relies on the emission of X-rays by inner-shell excitation with the incident electron beam from the SEM. When an electron from one of the inner shells of an atomic species is excited to a higher energy level, it leaves a hole behind which is in turn filled by another electron from a high energy shell. The phenomenon comes with the emission of characteristic X-ray with energy matching the difference between the two energy shells. As indicated in Figure 3.5a, the characteristic X-rays are labeled $K\alpha_1$, $K\alpha_2$, $K\beta_1$, $K\beta_2$, $L\alpha_1$, $L\alpha_2$, etc., where the combination of the capital letter, the greek letter and the number subscript specify the transition between two particular electron shells. The energy of the emitted X-rays is characteristic for every atomic species, therefore the element can be identified from the energy position of the emitted X-ray intensity peak. Besides, by integrating the peak it is also possible to gain quantitative information about the amount of element present in the analyzed area of the sample.
Generally speaking, the probability of X-ray emission increases with the atomic number, there-

fore EDX is more suited for the detection of heavy elements, especially when small concentrations are being analyzed, although in general almost all the elements of the periodic table emit detectable X-rays (only H and He do not emit X-rays, while the lightest elements such as Be or Li require dedicated analysis conditions [124]).
Beside the characteristic X-ray peaks, another contribution to the spectrum is that of the bremsstrahlung, or braking radiation, which is emitted by electrons being slowed down by the multiple inelastic scattering events with the sample. The contribution to the spectrum acts as a noise background which can sometimes limit the overall resolution [125].

EDX can be considered a "bulk" chemical characterization technique, as the interaction volume of high energy probing electrons for typical electron accelerating voltages lies in the micrometer range. The size of the interaction volume is mostly determined by the energy of the electron beam emitted from the electron gun and the atomic size of the elements within the species as well as its overall density. Employing this technique for the chemical analysis of thin films allows to have an complete insight of the sample chemical composition in the depth direction all the way down to the substrate, because the usual thickness of the layer of interest is generally below 1 μm.

In this work, the chemical microanalysis module Bruker Quantax EDS is used in the utilized SEM system. Appropriate fitting models are available for quantification upon detection of spectra, with the possibility of targeting specific elements [125].

3.2.5 Piezoresponse Force Microscopy

Piezoresponse Force Microscopy (PFM) is an extension of Atomic Force Microscopy (AFM) technique in contact mode based on the electromechanical coupling mechanism. Using a conductive AFM tip, an electric bias is applied to the sample surface and the mechanical response of the material is acquired. In this situation a piezoelectric material will by definition expand or contract as a response to the applied electric field thanks to the converse piezoelectric effect. As described in Section 2.3, in this case the strain of a piezoelectric material is related to the applied electric field through a rank-3 tensor. The coefficient of major interest is the longitudinal piezoelectric coefficient d_{33}, because it is directly coupled to the vertical motion of the AFM cantilever. The electric field generated by the bias applied to the tip is assumed to be oriented along the z direction, i.e. the vertical direction normal to the sample surface, and can be regarded as homogeneous in the volume directly under the tip. Under these assumptions, the displacement Δz generated in this direction by the change in size of the material can be written as:

$$\Delta z = d_{33} V \tag{3.2}$$

and by dividing both terms by the sample thickness, the z strain component as a function of the vertical electric field is obtained:

$$x_z = d_{33} E_z \tag{3.3}$$

Due to the small magnitude of the piezoelectric effect, the response signal to an applied field is typically smaller than a nanometer, approaching the resolution limit of the AFM itself. Moreover, topographic features can often be few nanometers in size, therefore also surface roughness is likely to hinder the piezoelectric response. For this reason, an AC voltage is tipically superimposed to the DC signal as $V(t) = V_{DC} + V_{AC} \cos(\omega t)$ and a lock-in amplifier is used for detection. As pictured in Figure 3.6 in response to the modulation stimulus, the material vibrates with a phase Φ depending on the local polarization orientation. If P is parallel to the applied electric field, the sample vibrates in phase with it and $\Phi = 0$, while it vibrates out of phase for

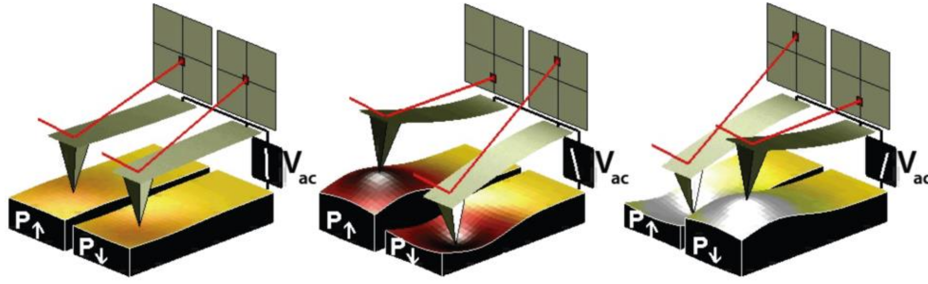

Figure 3.6: *PFM measurements on a material with ferroelectric domains (from [126]). The sign of the sample strain depends on the orientation of the domain polarization vector.*

antiparallel orientation and $\Phi = \pi$. Therefore, the relationship in Equation 3.2 becomes:

$$\Delta z\left(t\right) = \Delta z_{DC} + A\left(\omega, V_{AC}, V_{DC}\right)\cos\left(\omega t + \Phi\right) \tag{3.4}$$

which, when the AC voltage frequency is far from the resonance frequency of the cantilever, gives:

$$\Delta z\left(t\right) = d_{33}V_{DC} + d_{33}V_{AC}\cos\left(\omega t + \Phi\right) \tag{3.5}$$

The piezoelectric response signal is extracted by means of a lock-in amplifier, and can be written in the form:

$$A_{PFM} = d_{33}V_{AC}\cos\left(\Phi\right) \tag{3.6}$$

where $d_{33}V_{AC}$ constitutes the signal amplitude and Φ its phase, providing information about the magnitude and the orientation of the polarization vector, respectively.

The lateral piezoresponse can also be detected in a similar way by lateral PFM, correlating the in-plane surface displacement vibration with the transverse component of the piezoelectric tensor and in-plane polarization. Combining vertical and lateral PFM allows to provide a complete picture of the piezoelectric behaviour and polarization orientation of the material.

PFM Imaging

The PFM signal unveils the properties of the local polarization under the tip in terms of both the magnitude and the orientation. To acquire information about the local polarization state of the material on large areas, the PFM tip can be scanned along the desired surface to visualize ferroelectric domains. Data from the topographic signal, from the PFM amplitude and the PFM phase is collected separately in different channels, allowing for point-to-point comparison of the different signals. With this method, both vertical and lateral PFM imaging can be performed to acquire information about out-of-plane and in-plane domains respectively.

In order to perform this so-called "reading" procedure, the AC voltage applied across the sample should be high enough to allow a sufficient signal-to-noise ratio, but it shouldn't be greater than the coercive field, otherwise polarization switching will occur in the material upon the scanning of the tip. Besides, spurious effects arising from cantilever resonant behaviour should be avoided by setting the modulation frequency well below that of the resonance of the AFM cantilever. Low scanning speeds can reduce the cross-talk between the piezoelectric respose and the topography signal.

PFM Lithography

PFM technique can also be used to apply modifications to the ferroelectric polarization of the material to implement proper engineering of domains for specific applications. This is achieved

by applying a larger bias than the coercive field to a specific area for a suitable amount of time ("poling") to "write" the polarization in the desired patterns without changing the topography. The applied voltage amplitude and poling time should be high enough to enable polarization switching, but not too high to avoid recrystallization by Joule heating within the material. After the biased tip with the chosen parameters is rastered along the surface for the writing procedure, a reading procedure can be performed for assessment of the obtained results. An example of a PFM writing followed by a reading operation is reported in Figure 3.7.

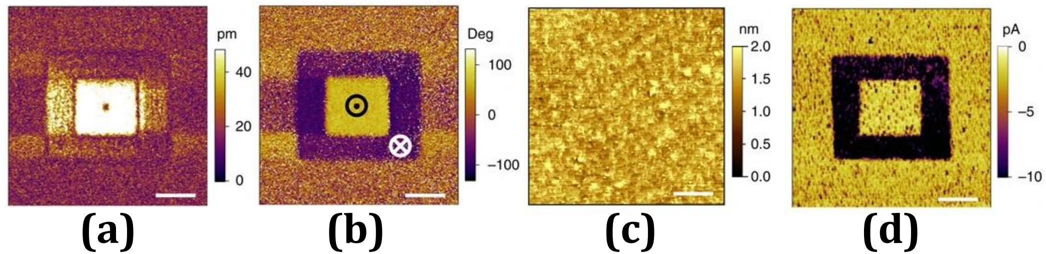

Figure 3.7: *(a)–(b) PFM signal amplitude and phase upon writing concentric squared domains with a specific bias voltage. (c) AFM topography of the sample, which remains unchanged in this process. (d) Low-bias current reading after the "poling" still reveals the written squared pattern (from [127]).*

PFM Spectroscopy

In Spectroscopy mode, it is possible to generate local ferroelectric hysteresis loops of the sample to acquire information on the ferroelectric behaviour. The standard procedure is to apply a DC bias in incremental pulses and superimposing an AC voltage to measure the deflection at every DC voltage, as sketched in Figure 3.8. The maximum and minimum values of the DC bias can be adjusted and the final voltage profile is that of a bipolar triangular wave of pulses to probe the complete cycle. In the end the static-like displacement behaviour is captured.

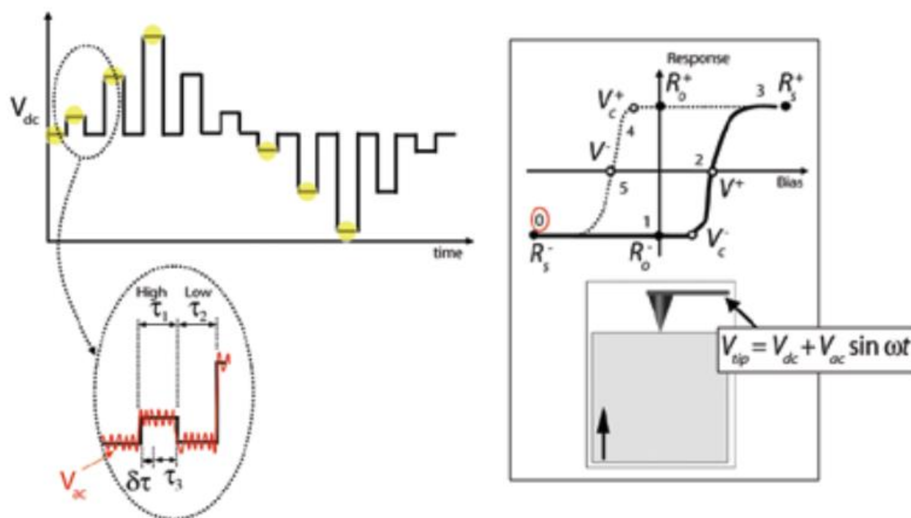

Figure 3.8: *Diagram of the PFM switching spectroscopy, from [126]. Applied signal profile on the left, and corresponding probed hysteresis loop on the right.*

3.3 Device Fabrication and Characterization

To perform the electrical characterization of a dielectric, a proper device of known geometry must be fabricated. The most suitable and commonly employed device structure for leakage current, capacitance and macroscopic ferroelectric measurements is the metal-insulator-metal (MIM) heterostructure which defines a capacitor with the dielectric sandwiched between two conducting electrodes. The method employed for fabrication of MIM capacitor is described in Section 3.3.1, while the electrical and ferroelectric characterizations are reported in Section 3.3.2 and 3.3.3, respectively.

3.3.1 Capacitor microfabrication

While the bottom electrode is already defined as the substrate onto which the functional thin film material is deposited, the first step in the fabrication of planar capacitors is the depostion of the second electrode layer. Top electrode metals were deposited *ex-situ* with Evatec BAK640 electron-beam evaporator (Ti, Ni electrodes) and AJA ATC Orion 8 magnetron sputtering system (Pt electrodes).
The first technique is based on the thermoionic emission of an electron beam which is then accelerated by a high voltage of $7-10$ kV towards a crucible of the desired material. The impinging beam is shaped and focused onto the crucible with the aid of a magnetic field, and the heated material melts down and evaporates (or directly sublimates, depending on the type of material). The whole process is carried out at low pressure ($\sim 10^{-6}$ mbar), so that the evaporated material is able to travel towards the sample and deposit onto it in the form of a thin film. In the magnetron sputtering deposition method, instead, an inert gas (commonly Ar) is introduced within the chamber in high vacuum conditions and subsequently ionized by applying a discharge bias voltage so that a plasma is ignited. Ar^+ ions generated by this cascade process are accelerated towards the target material, which is eroded and ejects particles that will travel towards the substrate and coat it with a thin film of the sputtered material. The use of a system of magnets placed behind the target allows to confine free electrons near the target and increase the probability of ionizing Ar atoms.

Ti electrodes ~ 100 nm thick were directly evaporated on KNN through a copper shadow mask made of a grid of ~ 300 squared openings 40×40 μm^2 in size as sketched in Figure 3.9 (top part). In this way, an array of parallel plate capacitor devices is defined.
Since Ni evaporation and Pt sputtering were found not directional enough to produce well defined capacitors through a shadow mask, for the fabrication of Ni and Pt electrodes, instead, (Figure 3.9 (bottom part)) a continuous layer of material ($\sim$20$-$50 nm) was first deposited, and subsequently the array of Ti pillars was deposited with the shadow mask to define the electrode shapes. Afterwards, the heterostructure was separated into isolated pillars by Ion Beam Etching, taking advantage of the low etch rate of Ti ($\sim$1 nm/min) with respect to that of Ni and Pt ($\sim$3 nm/min and $\sim$4 nm/min, respectively).

Similarly to Ti, Au electrodes (50 nm) for the HZO/LSMO/STO heterostructures were fabricated by e-beam evaporation, but with the aid of a photolithographic mask composed of circular shapes with diameter 50 μm. After the deposition, a lift-off process in sonicated acetone defined the final shape of the contacts.

3.3.2 Two-Points Probing

Although the most popular piezoelectric materials for thin films are oxides and as such should in principle behave as insulating materials with dielectric and capacitive electrical properties, some spurious contributions to conduction will always be present in a real material in the form

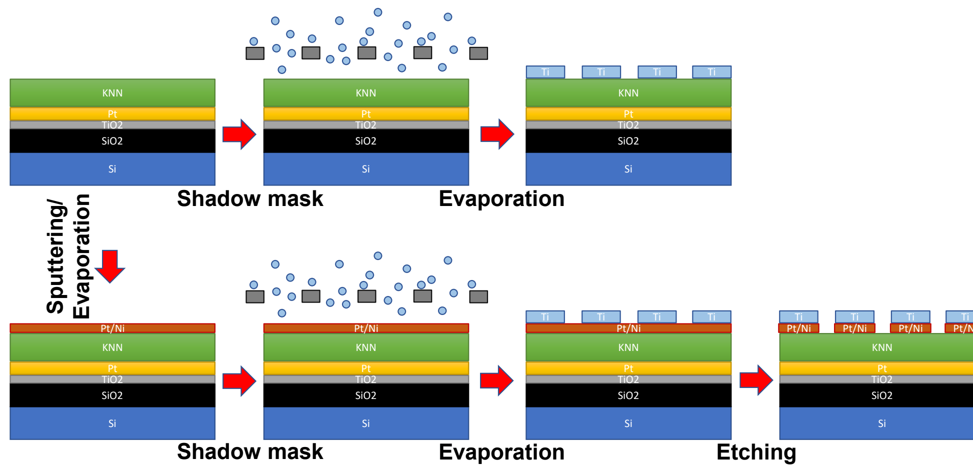

Figure 3.9: *Sketch of the fabrication process. Starting from KNN/substrate structure, Ti contacts are deposited with the shadow mask (top part). Pt and Ni, instead, are deposited as a continuous layer, the pads are defined with the shadow mask by Ti deposition, and finally the pillars are separated by a dry etching process.*

of a leakage current. Leakage current is the undesired current flowing through the oxide thin film under an applied electric field, which is detrimental for device performances and applications. Therefore, measurements, characterizations and studies of such contributions are required to gain information about behaviour of a piezoelectric material in response to an electrical stimulus to correlate it to its potential performances in a real device.
For this purpose, a SUSS MicroTec PM5 probe station equipped with 4 tungsten tips was employed, and a Keithley 2612 System SourceMeter was used to perform voltage sweeps. The typical voltage profile employed for the measurements is that of a triangular profile. The voltage is swept from zero up to the desired maximum voltage with a positive ramp at a rate of around 1 V/s, then lowered down to the negative opposite value with a negative ramp at the same rate, and finally brought back to zero with another positive ramp. Maximum voltages employed range from 3 V to 15 V depending on the thickness of the sample, the robustness of contacts and the measurement configuration.
Two measurement configurations were generally investigated:

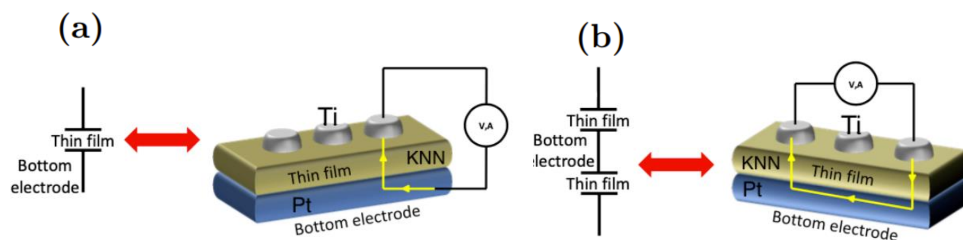

Figure 3.10: *Sketch of the (a) top-bottom and (b) top-top measurement configurations. Adapted from [128].*

- In the *top-bottom* configuration (Figure 3.10a) the voltage is applied between the electrode deposited on top of the thin film and the one at the bottom, hence probing a single capacitor defined by the oxide thin film itself.
- In the *top-top* configuration (Figure 3.10b) the voltage is applied between two identical electrodes on the top of the thin film surface. In this case, the current will flow from the first top electrode to the bottom electrode and then all the way back up towards the

second top electrode. The series of two capacitors will be probed in this way, defined by the top electrodes with the common bottom electrode. This helps to create symmetry in the measured system, which is sometimes useful to acquire better understanding of some conduction mechanisms.

3.3.3 Ferroelectric characterization

The characterization of ferroelectric properties, such as the remanent and saturation polarization, the switching current and the coercive field, can be performed by examining the curves acquired from polarization-voltage and/or current-voltage measurements on planar ferroelectric capacitors. A very common approach that is also adopted in this work is to infer all ferroelectric properties directly from I−V measurements alone. As a triangular voltage sweep of amplitude V_{max} and frequency ν_0 is applied across the ferroelectric capacitor, the measured current response presents abrupt peaks in correspondence of the positive and negative coercive fields. These peaks are due to the displacement of ions within the ferroelectric polar cell, i.e. the ferroelectric switching phenomenon. The switching charge can be calculated by integrating the current through time, and the polarization P is defined as the ratio between the charge and the area A:

$$P = \frac{\int I(t)\, dt}{A} - C_1 = \frac{1}{4AV_{max}\nu_0} \int |I(V)|\, dV - C_2 \tag{3.7}$$

where C_1 and C_2 are integration constants determined by imposing the boundary condition $P(V_{max}) = -P(-V_{max})$.

When approaching the issue of ferroelectric characterization of oxide thin films, it is necessary to take into account the fact that in such systems multiple effects and contributions as a response to an applied electric field coexist and combine into the final output response of the sample. The separate effects from different contributions to the hysteresis cycle in thin films are sketched in Figure 3.11. A ferroelectric oxide is also a dielectric material and as such, beside the pure ferroelectric effect (Figure 3.11a), dielectric charging current must be considered, whose contribution is inversely proportional to the film thickness (Figure 3.11b). Moreover, the intrinsic presence of defects in thin films can generate conductive pinholes which can cross the film and favour leakage currents (Figure 3.11c−d). This contribution can have a severe impact on the evaluation of ferroelectric quantities such as the coercive field and remanent polarization and even lead to incorrect analysis of the switching phenomenon [129]. Different coexisting phenomena will generate a combination of measured charges and thus current and polarization profiles lying in between the "pure" ones (Figure 3.11e−i).

In this work, a TF Analyzer2000 (AixACCT System GmbH) is used to characterize the ferroelectric properties, which allows applied voltages up to 25 V and frequencies between 10 mHz and 5 kHz. The instrument provides different modules for different kinds of measurements that can be chosen depending on the properties to be studied. In this work, the characterization of ferroelectric properties is performed exploiting the Dynamic Hysteresis Measurement mode and the Positive-Up-Negative-Down Measurement.

Dynamic Hysteresis Measurement (DHM)

The Dynamic Hysteresis Measurement (DHM) method consists in applying a voltage signal of four bipolar triangular pulses of frequency ν_0 separated by a delay time τ, as shown in Figure 3.12. Current signal responses are collected for all four pulses, but the final I−V loop is constructed from the negative current of the second pulse (negative voltage) and the positive current of the fourth pulse (positive voltage). The first and third pulses are necessary to bring the system in the same measurement conditions for acquiring the second and the fourth pulse.

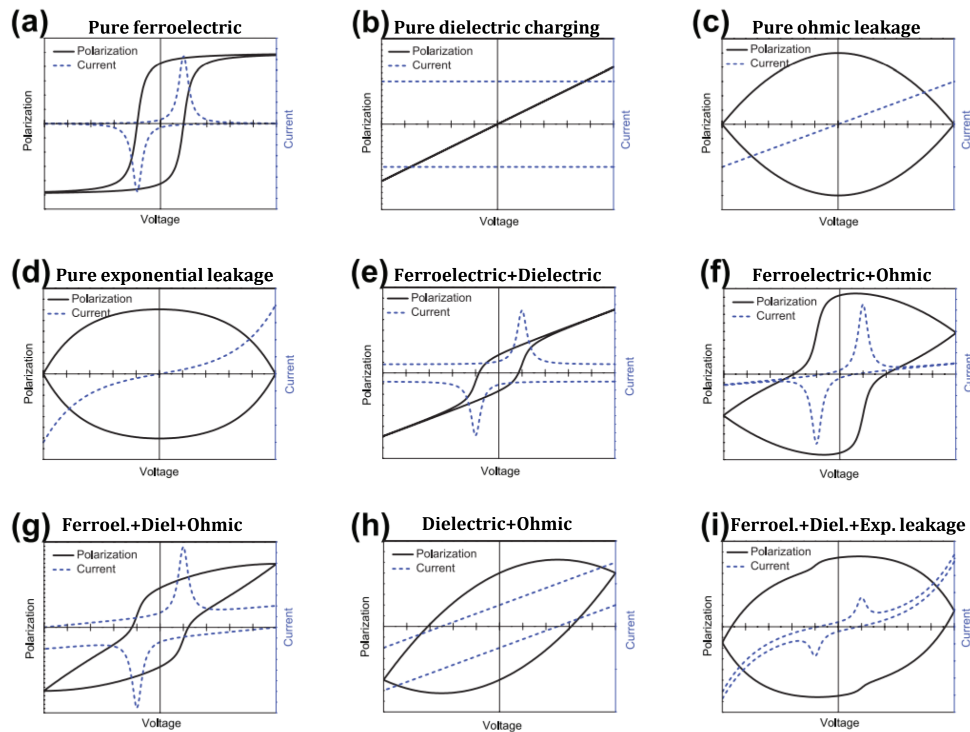

Figure 3.11: *Typical current-voltage (dashed blue) and polarization-voltage (solid black) profiles generated from different phenomena or combination of them. Reprinted from [130].*

Moreover, Dielectric Leakage Current Compensation (DLCC) method can be used to correct and compensate for leakage effects contained in the DHM measured loop. This approach is based on the assumptions that the leakage current does not depend on frequency and that the dielectric and switching currents depend linearly on the frequency. The DHM measurement signal is collected at the frequencies ν_0 and $\nu_0/2$ and the leakage current contribution can thus be substracted, and just the displacement current contribution is left.

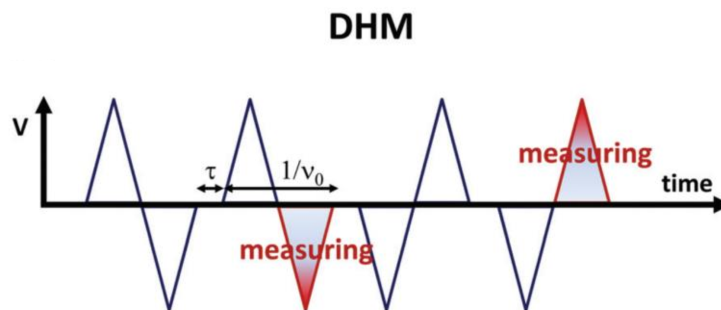

Figure 3.12: *Voltage pulse profile applied in the Dynamic Hysteresis Measurement (Sketch from [128]). Current is measured in correspondance of the coloured pulses.*

Positive-Up-Negative-Down Measurement

When measuring in DHM mode, the current signal contains both ferroelectric switching contribution (displacement current) and spurious non-switching contrubution (leakage and dielectric currents). In order to achieve reliable estimates of the remanent polarization and/or in case the DLCC method is not effective in removing the leakage contribution, the Positive-Up-Negative-

Down (PUND) measurement can be performed, consisting of a train of 5 pulses with specific polarity applied to the sample (Figure 3.13). First, a negative "writing" pulse (or pinning pulse) is applied to bring the sample from an initial unknown pristine polarization state to a known defined negative polarization state. The next pulse (P pulse, or "positive" pulse) polarizes the sample, and the generated measured current is the sum of the ferroelectric switching and non-ferroelectric non-swithing contributions. The third pulse is again positive (U pulse, or "up" pulse) and because the material is already switched in a positive polarization state, the corresponding current collected from this pulse only contains non-switching contributions. Therefore, by substracting the current of the U pulse I_U from the current of the P pulse I_P only the current contribution to the ferroelectric switching phenomenon can be obtained (Figure 3.14a). The same approach is applied to the last two pulses, N ("negative") and D ("down") being just like P and U pulses but with opposite polarity. In this way, the current loop $I_{PUND} - V$ is obtained from $I_P - I_U$ and $I_N - I_D$ positive and negative currents respectively. Finally, integrating of the switching current in time leads to the polarization hysteresis cycle, which only contains purely ferroelectric switching contributions (Figure 3.14b).

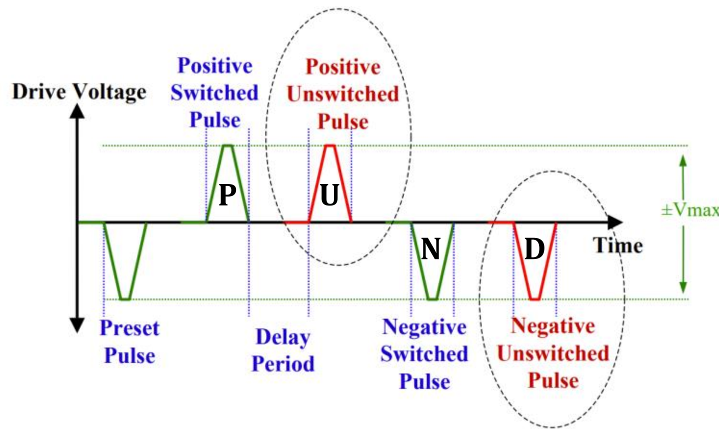

Figure 3.13: *Applied voltage PUND train of pulses. A preset writing pulse precedes the measuring pulses, then the signals from U and D pulses are subtracted from those of P and N pulses.*

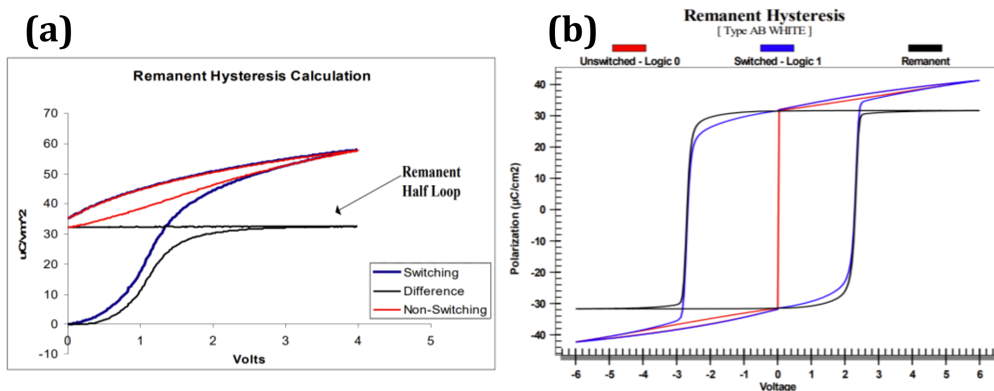

Figure 3.14: *(a) PUND Switching (blue) and Non-switching (red) half loops to be subtracted, taken from $Pb(Nb_xZr_yTi_z)O_3$ capacitors with Pt electrodes (reprinted from [131]). (b) Complete hysteresis loop. The black line represents the result of the subtraction, i.e. the pure remanence contribution.*

CHAPTER 4

Growth optimization: Effect of substrate preparation on KNN/Pt(111)

4.1 Introduction

As already described in Chapter 1, in the attempt of developing a reliable candidate to replace the wide use of PZT in most piezoelectric device applications, a good deal of attention was focused on perovskite (K,Na)NbO_3 solid solution. The discovery of its high Curie temperature and of the enhancement of piezoelectric properties in correspondence of the Morphotropic Phase Boundary have paved the way for a period of intensive study of the properties and behaviour of such material. Since Saito's publication in 2004 [26], many studies were focused on KNN due to its potential to provide record piezoelectric performances exemplified by a d_{33} of up to 800 pm/V. However, such high values are limited to bulk ceramics. As a matter of fact, when tackling the challenge of thin film growth a variety of new different phenomena arise that need to be accounted for (see Section 1.7), some of which also tend to impair piezo- and ferroelectric behaviour. Examples include domain clamping [132, 133] and the unavoidable challenge of growing a compact flat film with the correct desired stoichiometry. Investigations into the structure and characteristics of KNN thin films have initially been conducted mainly on oxide substrates, such as $SrRuO_3$/$SrTiO_3$ [134], Nb-doped $SrTiO_3$ [135], $LaNiO_3$/Si [136]. Recently, the requirement to make the synthesis of lead-free piezoelectrics compatible with already existing industrial device processes has concentrated many scientific efforts on a transition towards metallic substrates. This would allow for a facilitated integration on silicon and silicon-based established fabrication processes. Among the many possibilities, the use of Pt has risen particular interest [137, 138], due to the possibility of integration on a very common industrial stack for piezoelectric devices (Pt/Ti/SiO_2/Si), which is already well-established for PZT [139, 140]. In these studies, a significant effort is made to design appropriate growth processes to make up for the loss of highly volatile alkali components of KNN, which are a key factor in the deterioration of the electrical properties of the samples. However, not much focus has been dedicated to how the substrate affects the functional properties of KNN thin films.

This Chapter examines the growth of (001)-oriented KNN thin films on Pt(111)/TiO_2/SiO_2/Si substrates by Pulsed Laser Deposition (PLD). The critical importance of the template substrate in shaping the structure, orientation and functional properties of the KNN thin films is emphasized. The morphologic and topological quality of the film as well as the electric, ferroelectric, and piezoelectric performances all depend heavily on the development of an appropriate treatment for the Pt substrate. Based on local piezoelectric characterization by PFM, a piezoelectric coefficient d_{33} of around 80 pm/V is estimated, which is in agreement with the state of the art of undoped KNN thin films. Finally, the results of the electrical and ferroelectric characterization of microfabricated parallel-plate capacitors indicate a macroscopic ferroelectric behaviour partially hindered by a sizable leakage current.

4.2 Experimental Methods

- **Thin film deposition:** KNN thin films with thicknesses of around 300 nm were grown by Pulsed Laser Deposition technique on an industrial substrate stack of Pt(111)(100 nm)/TiO_2(20nm)/SiO_2(700 nm)/Si grown *ex-situ* by magnetron sputtering. A Nd:YAG laser with a fourth-harmonic wavelength of 266 nm was used to ablate a stoichiometric $K_{0.5}Na_{0.5}NbO_3$ ceramic target (purchased from QS Advanced Materials). An optimization process of the deposition was carried out by varying and co-varying the growth parameters to study their influence on thin film quality. Best conditions were found with a fluence of 1.3 J/cm^2 and a repetition rate of 10 Hz employed for the deposition. The growth was performed in 220 mTorr oxygen atmosphere keeping the substrate at a temperature of 615°C and at a distance of 42.5 mm from the target.
  Prior to thin film deposition, different processes for the substrate template preparation were used and its effect on KNN properties was explored. An additional annealing process was performed on as-deposited KNN thin films at 500°C for 30 minutes in oxygen to promote crystallization and reduce possible oxygen vacancies. Final cooling to room temperature was carried out with a rate of -8°C/min.

- **Morphological and structural characterization:** The morphology of the samples was analyzed using a Scanning Electron Microscope (Raith LEO 1525 FE-SEM) to assess the thin film quality of both surface and cross sections with an In-Lens detector and an acceleration voltage kept at 10 kV. The structure and crystal orientation of the thin films was characterized by room-temperature X-ray Diffraction with $\theta - 2\theta$ scans on a Bruker D8 advance X-ray diffractometer (in collaboration with M. Cabrioli and F. Di Fonzo, IIT Center of Nano Science and Technology).

- **Substrate template characterization:** Topographic scans of the surface of the Pt template were performed by Atomic Force Microscopy (Keysight 5600LS) in Tapping Mode. X-ray Photoemission Spectroscopy was employed for the *in-situ* chemical characterization of the Pt surface with Al-Kα radiation at 1.486 keV.

- **Electrical measurements:** Ti top electrodes with a thickness of 100 nm were deposited by e-beam evaporation through a shadow mask, defining a matrix of 40×40 μm^2 pads. Measurements were performed on such fabricated Ti/KNN/Pt parallel-plate capacitors in the top-top configuration, i.e. applying an electric voltage between two top electrodes.
  Leakage current measurements were performed by sweeping the voltage through a bipolar triangular pulse defined by subsequent ramps ($0 \rightarrow +15V \rightarrow 0 \rightarrow -15V \rightarrow 0$ at a rate of 2.1 V/s. Ferroelectric properties were characterized using an aix-ACCT TF-2000 Analyzer

with the switching currents PUND method (Positive-Up-Negative-Down). Bipolar triangular pulses with an amplitude of 6 V, a delay of 10 ms and a variable frequency between 100 Hz and 2 kHz were employed.

- **Piezoelectric characterization:** Piezoelectric measurements were performed by Piezoresponse Force Microscopy technique on a Keysight 5600LS Atomic Force Microscope. An AC voltage of 1 V was applied to the conductive tip at a frequency of 31 kHz (far from the tip mechanical resonance) to acquire spatial maps of the ferroelectric domains and estimate the piezoelectric coefficient d_{33}. With a low modulation frequency artifacts caused by local fluctuations in the contact resonance frequency as well as spatial changes in the resonance quality factor can be avoided [141, 142].

4.3 Comparison of KNN thin film properties depending on Pt treatment

A substrate cleaning procedure was developed to investigate the effect of the Pt(111) surface condition on the properties of deposited KNN thin film. Different substrate treatment processes were explored and compared on samples S1 to S5 (Table 4.1), progressively increasing the incidence of the procedure. These samples are considered representative of more samples, as the reproducibility of results was checked with multiple samples. KNN in sample S1 was grown onto a pristine Pt(111) surface without performing any cleaning steps. In sample S2, *ex-situ* plasma cleaning in 1 mbar Argon for 10 minutes at 300 W was performed before the growth. In samples S3 to S5 an *in-situ* vacuum annealing step at the growth temperature of 615°C was introduced, varying the time span from 10 minutes for S3 to 20 minutes for S4 and S5. Additionally, the difference between *ex-situ* Argon and Oxygen plasma before *in-situ* vacuum annealing is compared in S4 and S5.

Sample	Ar plasma	O_2 plasma	Vac. annealing time	Vac. annealing T
S1	-	-	-	-
S2	X	-	-	-
S3	X	-	10 min	615°C
S4	X	-	20 min	615°C
S5	-	X	20 min	615°C

Table 4.1: *List of substrate preparation procedures associated to each KNN sample.*

4.3.1 Morphological and structural comparison

A comparison of the surface morphologies of KNN samples grown in the same conditions with different substrate cleaning procedures is shown in Figure 4.1. KNN grown on untreated Pt (S1) presents a number of outgrows and misoriented crystallites on the order of $100-200$ nm in size studded over a predominant flat surface (Figure 4.1a). The amount of such defects slightly decreases (by around 30%) by introducing *ex-situ* plasma cleaning before the growth (S2, Figure 4.1b). Performing the *in-situ* vacuum annealing leads to a remarkable improvement of the surface quality, with a reduction in the amount the defects by 75% in S3 with respect to S1 (Figure 4.1c). Increasing the annealing time to 20 minutes further flattens the KNN surface, limiting the concentration of misoriented grains to around 6% and 4% in S4 and S5 respectively (Figure 4.1d and 4.1e) with respect to its initial amount in S1. Vacuum annealing times longer than 20 minutes did not introduce considerable improvements in the KNN surface morphology. Figure 4.1f and 4.1g show a comparison of the SEM cross section morphologies of S1 and

S5 respectively, from which a remarkable improvement in the thin film compactness emerges. From this SEM inspection, it is clearly evident that the vacuum annealing step is critical to provide a morphologically convenient starting template for the nucleation of KNN thin films. The same kind of pre-growth annealing performed on other samples in 220 mTorr oxygen pressure resulted in KNN morphologies (not shown) similar to those of untreated Pt (S1), therefore the high vacuum condition is required for optimal results.
Interestingly, in all samples a bright and dark texture is visible on the flat surface, which corresponds to the pattern of spontaneous ferroelectric domains, as confirmed by PFM measurements. Such contrast has been observed in other similar works [143] and can be attributed to local pyro- and piezoelectric effects due to the heating and surface charge accumulation interacting with the domain polarization. The (001) orientation of the thin films, as confirmed by diffraction measurements discussed in the next paragraph, enhances this effect, because the total polarization vector is oriented perpendicular to the film surface with an increased interaction with the perpendicular electron beam impinging onto the thin film.

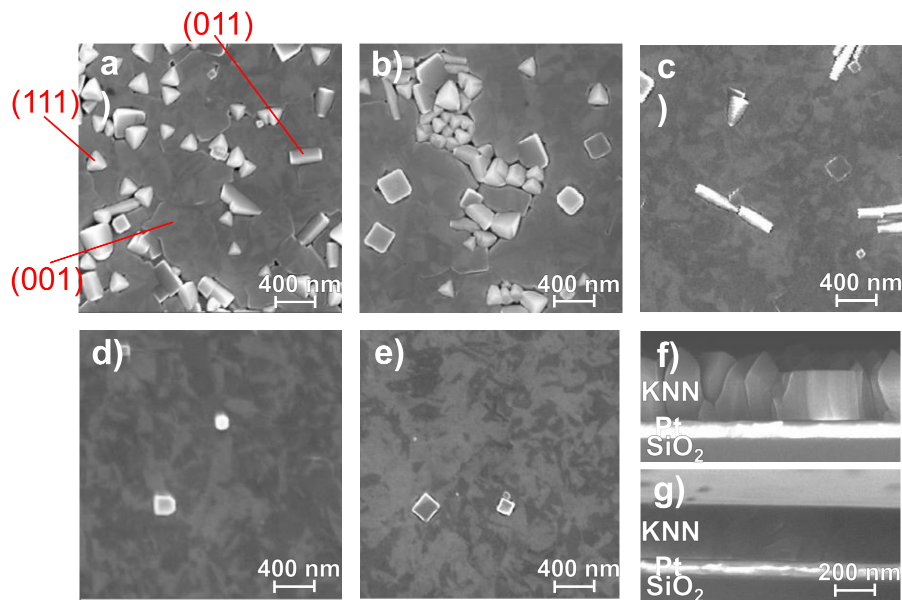

Figure 4.1: *SEM morphologies of the top surfaces of KNN samples grown with different substrate treatments. (a) and (f) S1: untreated substrate; (b) S2: 10-min Ar plasma (c) S3: 10-min Ar plasma and 10-min vacuum annealing; (d) S4: 10-min Ar plasma and 20-min vacuum annealing. (e) and (g) S5: 10-min O_2 plasma and 20-min vacuum annealing. With improved substrate cleaning and surface preparation, the amount of misoriented grains is considerably decreased.*

The structure of thin films in S1 and S5 was compared by XRD $\theta - 2\theta$ measurements. The comparison of diffraction patterns from KNN grown on untreated and vacuum-annealed substrates (S1 and S5) is displayed in Figure 4.2. The predominant peaks at 22.5° and 45° emerging from both spectra can be ascribed to KNN (001)/(100) and (002)/(200) planes. This indicates a predominant (001) orientation of the films, corresponding to the planar surface observed by SEM. The presence of residual misoriented crystallites gives rise to a minor peak at around 33° of (011)-KNN, appearing as tent-shaped outgrows in Figure 4.2a and 4.2b. The KNN(111) peak related to pyramid-like outgrows in the same samples is masked by the peak of Pt(111) [144, 138]. The (011) peak is absent in vacuum-annealed sample S5 (red), highlighting the effect of vacuum annealing in improving the morphology observed by SEM.

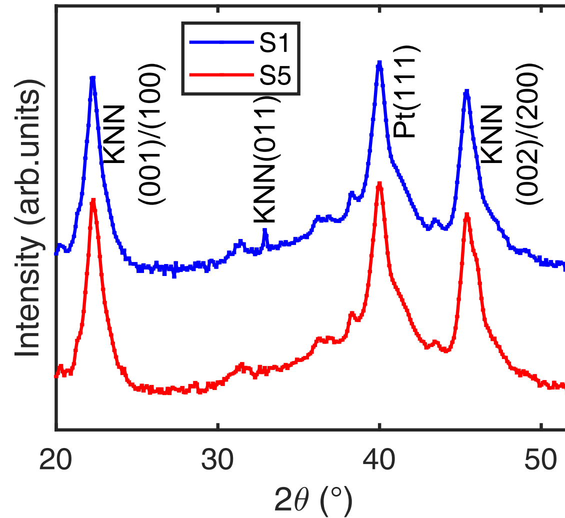

Figure 4.2: *Comparison of XRD spectra of KNN films grown on untreated Pt substrate (blue) and with plasma cleaning + vacuum annealing (red). A predominant (001) texture is revealed by the intense peak at 22.5°. A small (011) peak originated by misoriented crystallites is suppressed with a suitable substrate treatment procedure.*

4.3.2 Modifications of Pt template

Figure 4.3 shows the surface topography of Pt substrate before (4.3a) and after (4.3b) the vacuum annealing step acquired by Atomic Force Microscopy. The annealing procedure favours the coalescence resulting in an average increase of the grain size. This improves the quality of the Pt template surface because it introduces a remarkable flattening with respect to the untreated case, and the rsm roughness passes from 1.5 nm to 0.7 nm.

The annealing has also an effect reducing surface contamination. In Figure 4.4 C1s and O1s peaks obtained by X-ray Photoemission Spectroscopy are shown for both untreated (black) and vacuum-annealed (red) Pt substrates. The annealing in vacuum process produces a considerable suppression of the C1s peak and the complete disappearence of the O1s peak. This indicates that a considerable concentration of contaminants (mainly adventitious carbon and carbonates) is present on the surface of untreated Pt prior to KNN deposition due to the exposure to atmosphere. The vacuum annealing step is highly effective in removing such organic residuals because adatoms are easily detached from the surface by evaporation in a vacuum condition. This, combined with the topographic flattening, reduces the number of nucleation centers for misoriented KNN crystallites and improves the overall quality, compactness and orientation of the KNN thin films.

4.3.3 Dielectric and piezoelectric characterization

Leakage current measurements were performed in the top-top configuration of parallel-plate capacitors with Ti top electrodes and the common Pt at the bottom. Ti was chosen for practical convenience and cost for low frequency and DC electrical measurements, even though other metals (e.g. Pt) are more commonly employed in literature for such characterization. A more thorough investigation of the role of the top electrode material is discussed in Chapter 7. Leakage current density J as a function of the DC applied electric field is represented in Figure 4.5a. Leakage profiles coming from the different substrate cleaning procedures presented above are compared. In Figure 4.5b, showing a characteristic PUND ferroelectric hysteresis loop of

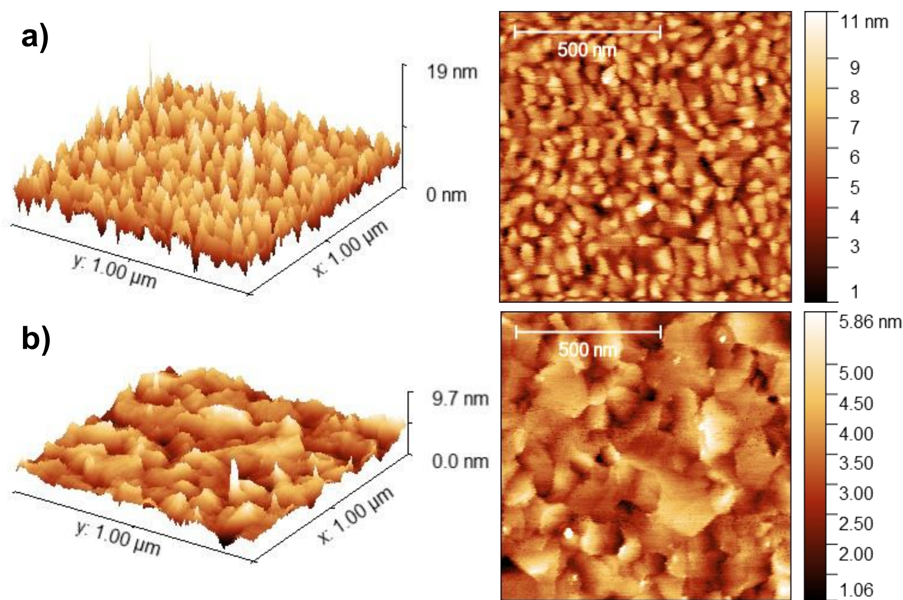

Figure 4.3: *AFM surface topography of the (a) untreated Pt(111) substrate and (b) vacuum-annealed substrate. A flattening of the surface, with increased grain size and reduced roughness, promotes an optimal template for nucleation and growth dynamics.*

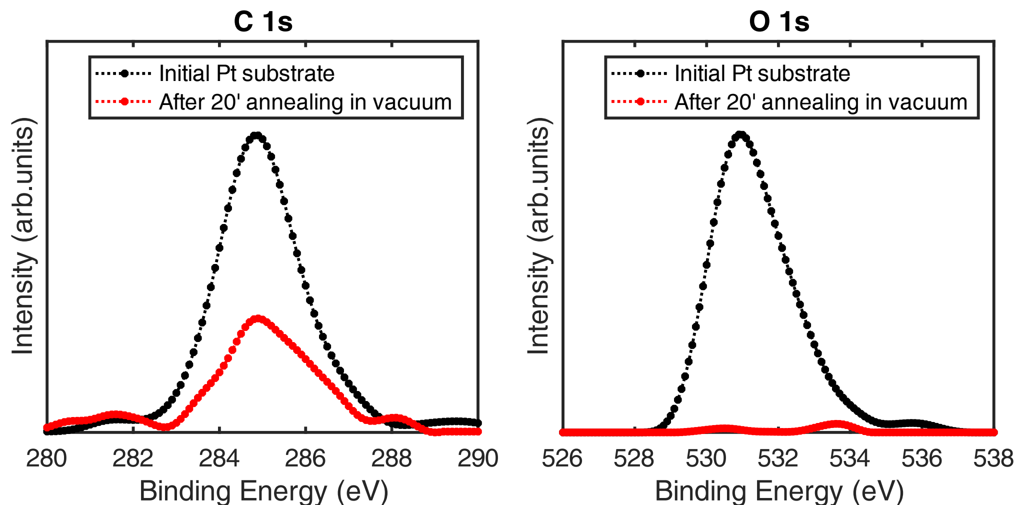

Figure 4.4: *XPS intensities of C1s and O1s peaks acquired from the Pt substrate before (black) and after (red) vacuum annealing treatment. A significant decrease in the intensity of the C 1s peak is observed after vacuum annealing, while the O1s peak is completely suppressed.*

KNN measured on sample S5, the value leakage current density at an applied external electric field E^* of 75 kV/cm is plotted as a function of the substrate cleaning. This field was selected because it slightly exceeds the coercive electric field observed on optimal films (S5), providing a sort of upper limit to the operation of KNN as a piezoelectric material. While using the same deposition conditions, vacuum annealing enables an approximately one order of magnitude reduction in leakage at E^*. This is explained by a significant suppression of the leakage caused by conduction at grain boundaries, caused by the decrease in the number of misoriented grains detected by SEM and XRD in S5. Well defined ferroelectric hysteresis behaviour was only observed from KNN films deposited on vacuum-annealed substrates. The inset of Figure

4.5b displays a sample with coercive fields of $E_c^+ = +65$ kV/cm and $E_c^- = -50$ kV/cm, as stated above. The square shape of the plot is typical of a PUND measurement, in which the loop is produced by subtracting the contributions (up and down) that are unrelated to ferroelectric switching from the switching currents (positive and negative, respectively). Comparing the remanent polarization $P_r = 2.5$ μC/cm^2 to other results from the literature (on the order of 20 μC/cm^2 [145, 146]), these films display a small remanence. This could be because our films have high leakage currents, which mask the ferroelectric switching phenomenon and prevent a reliable measurement of the corresponding current peaks. The possible presence of oxygen vacancies and Na and K deficiency is thought to be the cause of these residual electrical losses in light of what was said about the high quality of film morphology and orientation [147, 148]. This is because such local off-stoichiometries are sources of electronic states that favour charge migration through the dielectric.

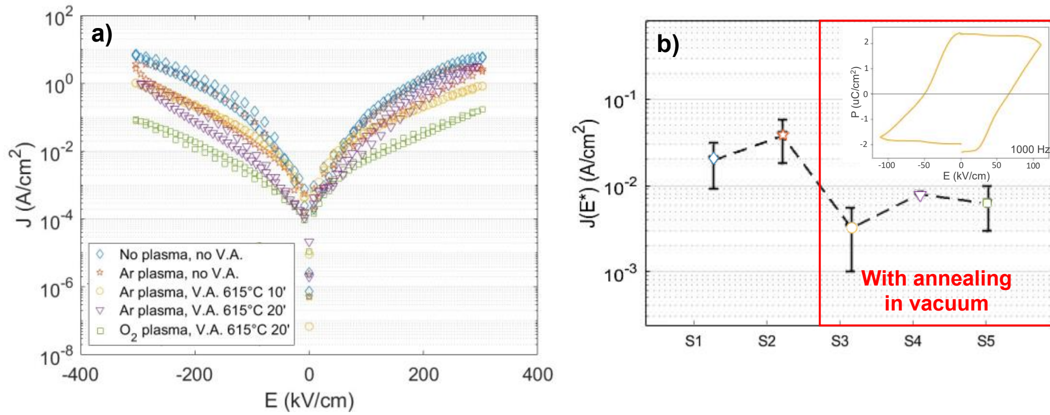

Figure 4.5: *(a) Leakage current density of KNN grown with different substrate treatments. (b) Evaluation of leakage current densities at field E* = 75 kV/cm for the different samples. Leakage currents through the thin film are reduced by performing substrate vacuum annealing before the growth. In the inset, the KNN ferroelectric polarization loop of KNN on vacuum-annealed Pt is reported.*

Studies using Piezoresponse Force Microscopy technique (PFM) were conducted with regards to the characterization of piezoelectric properties. By applying an AC voltage of 1 V to a conductive AFM tip, the piezoelectric material deforms locally in response to the applied electric field. The phase of the AC tip deflection provides an insight into the remanent polarization of the thin film, while from the signal amplitude, being proportional to the surface displacement, an estimate of the local piezoelectric coefficient d_{33} can be extracted. By moving the conductive tip along the film surface at the modulation frequency (31 kHz) while scanning specific areas of each sample, maps of the topographical, amplitude and phase signals were acquired. The spontaneous ferroelectric domain distribution of the KNN thin films can be imaged using this method. The strong local ferroelectric coercivity and depolarization strongly hinder the writing of ferroelectric domains. Sweeping the tip at a voltage drop of 10 V across the thin film (the highest voltage possible in the instrument) was not enough to produce and sustain domain switching, possibly because of the presence of some high local ferroelectric coercivity and depolarization effects that poling with an atomic-sized PFM probe tip was ineffective to counteract. Because of this phenomenon, the estimate of piezoelectric coefficient was determined by analyzing the spontaneous piezoelectric domains, exploiting the fact that the film (001) orientation is characterized by an out-of-plane spontaneous polarization.
Figure 4.6 shows the AFM topographic signal, PFM phase, and PFM amplitude (first, second and third column respectively) for KNN films deposited on Pt after various substrate treat-

ments. Sharp 180° phase contrast between neighbouring areas with spontaneous polarization oppositely oriented is seen from the phase signal. With the exception of the first sample in Figure 4.6a−c, where some link between ferroelectric polarization and local morphology was observed, no notable correlation between ferroelectric domains and sample topography emerges.

The piezoelectric coefficient d_{33} can be calculated from the PFM amplitude V_{PFM} using the

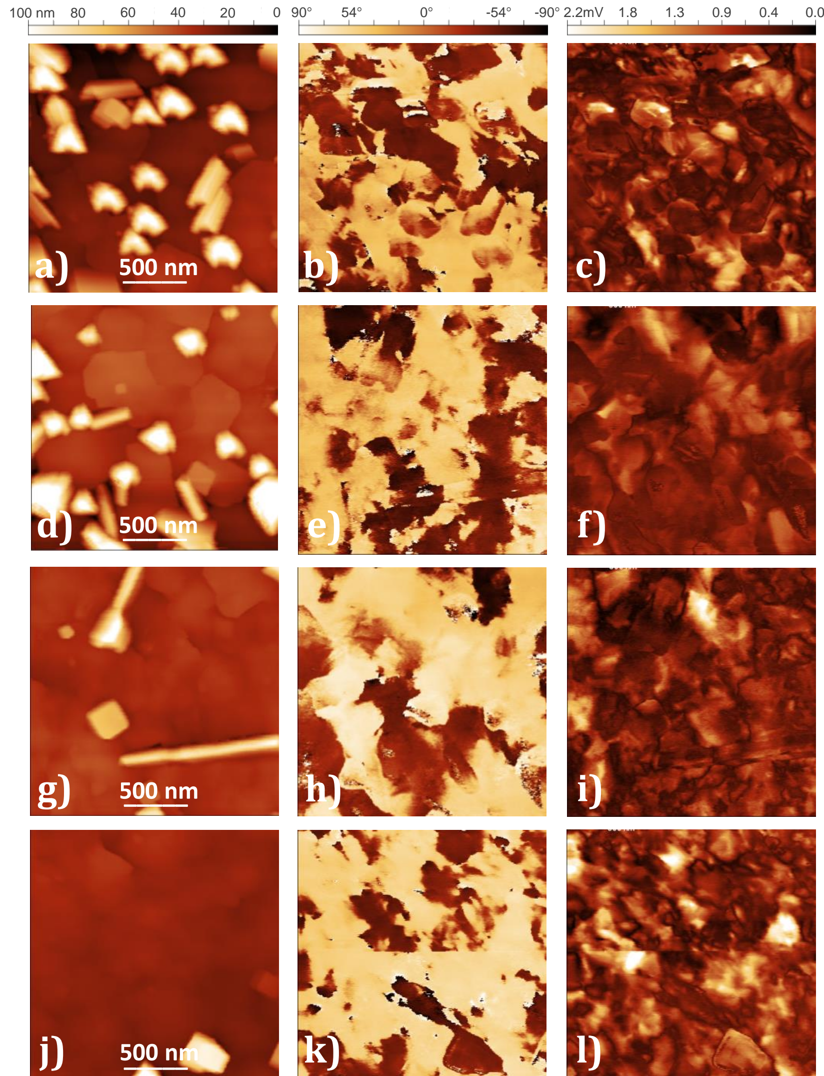

Figure 4.6: *PFM topography (left), phase (center) and amplitude (right) scans for KNN thin films with different substrate cleaning procedures. (a)−(c): S1, untreated substrate; (d)−(f): S2, 10-min Ar plasma; (g)−(i): S3, 10-min Ar plasma, 10-min vacuum annealing; (j)−(l): S5, 10-min O−2 plasma, 20-min vacuum annealing. The bright and dark pattern in the phase signal reveals the out-of-plane polarization state of spontaneous domains. The PFM amplitude is proportional to the d_{33} coefficient.*

following formula [149], which is accurate outside of the contact resonance: $d_{33} = V_{PFM} \cdot S/V_{ac}$, with the tip sensitivity S [nm/V] and the applied AC voltage V_{ac}. Force-distance curves were used to calculate the value of the tip sensitivity, which was 209 nm/V. An estimate of the d_{33} coefficient, which also accounts for any mechanical inhomogeneities, is obtained by analyzing the statistical distribution of the PFM amplitude on top of single grains of the whole region for each sample. It should be noted that the good agreement with the literature of the piezoelectric coefficients estimated with this methodology was confirmed with additional measurements

on reference samples of $LiNbO_3$ and $Pb(Zr,Ti)O_3$ [150].
The d_{33} coefficients were computed from the amplitude distribution obtained over two 2×2

Sample	R_{tot} (nm)	R_{plain} (nm)	d_{33} (pm/V)
S1	25.0	8.5	61±40
S2	23.2	7.0	40±10
S3	7.9	2.8	64±16
S5	5.6	1.8	80±20

Table 4.2: *Piezoelectric coefficient and roughness parameters for the different KNN thin film samples grown with different substrate cleaning processes.*

μm^2 maps for each sample. The values listed in Table 4.2 correspond to the average values ± standard deviation of the d_{33} estimated on 2×2 μm^2 scanned areas of each sample, including plain and non-plain regions, since no specific correlation is found between the morphological defects and the phase signal. Given the high similarity of the results obtained from S4 and S5, only the representative sample S5 is listed in the Table. The estimated surface roughness from the topographic PFM signal of each sample is also displayed. R_{plain} is the rms roughness of the film flat regions where no outgrows are present, whereas R_{tot} denotes the average of the surface rms roughness over the whole region of the scan. The piezoelectric coefficient rises in samples with less roughness, suggesting that there may be a link between the d_{33} and the roughness for treated substrates. This may occur from an enhanced grain ordering in the final film, which affects how well the lattice cells cooperate to produce the local microscopic piezoelectric response. A pretty high piezoelectric coefficient is already present in the sample without substrate treatments (S1), while it is still lower than that of S5. This could be because the film is so severely fragmented that it suffers less from the clamping effect of the substrate and is able to produce a strong local out-of-plane response [151].

4.4 Discussion

It is important to note that the fundamental properties connected to piezoelectric coefficient enhancement include aspects like film density, orientation and compositional uniformity. Such features can give rise to relevant underlying mechanisms in the observed trend in the piezoelectric properties of the samples [7]. The impact in the formation ferroelectric domains and domain growth dynamics of defects is crucial. As a matter of fact, defects are able to regulate the thermodynamic stability of local polarization states, serve as nucleation centers during the growth of films and provide pinning sites for the formation of domain walls. Point defects like oxygen vacancies, cation vacancies, and surface states are typical defects that may be seen in a variety of ferroelectric materials. These can interfere with ferroelectric ordering and reduce local polarization because they change the local configuration of the material. A similar effect can be generated by extended morphological defects such dislocations, grain boundaries, and defect dipoles. According to certain investigations on bulk PZT ceramics, the impact of extrinsic contributions to material properties can be modulated by changes in the defect concentrations [19, 152].
In addition, the surface roughness has a significant impact on the d_{33} value and, thus, on the sensing performances of the thin films. Inadequate or non-optimal grain growth causes surface roughness, which results in film diffuse porosity. This is a result of the nucleation process which strongly depends on the substrate. Surface defects can cause irregular grain growth from a few localized critical nuclei, which in turn leads to improper structural development, defects, and

fractures that impair the quality of the films. As a result, regions of the film with columnar grains separated by voids will respond differently from those with dense grain and little to no pores [153].
Generally speaking, thin film dielectric properties and piezoelectric behaviour are known to deteriorate in case small, isolated areas of porosity are present [154]. The existence of unclamped islands in the film where the mechanical clamping is reduced along with the amount of the stress of the film deformation from the substrate, can produce a sizable experimental increase of the effective piezoelectric coefficient [155]. Because of this, in light of the current study, the relatively high value of d_{33} displayed by sample S1 can be accounted for by the presence of a sizable number of unclamped islands with low levels of internal stress and interaction with the surrounding film. This phenomenon can explain the increased value of the piezoelectric coefficient that was determined by statistical analysis of the PFM signal in this study. The cause of the apparent anomalous piezoelectric behavior of sample S1 compared to the other samples is believed to lie in the trade-off between the mechanical clamping factor, which is locally lowered by the extended presence of misoriented grains, and the porosity of the film arising from the considerable surface roughness. Moreover, as was mentioned above, local film misorientations can be the cause of microscopic distortions affeting the local configuration of the material. These structural flaws may also result from off-stoichiometries and local compositional inhomogeneities that affect the stable configuration of the electric dipoles within the lattice.
On the other hand, characterization shows that in samples from S2 to S5 a gradual improvement trend in the piezoelectric coefficient is observed along with flattening of the surface morphology, decrase in amount of defects and improvement of crystalline quality. However, as defects are reduced, the films are subjected to a greater local mechanical clamping, coming from both the substrate and the highly compact surrounding film. In a more realistic estimate, the piezoelectric behaviour of thin films can be significantly influenced by the mechanical clamping phenomenon caused by the surrounding medium and the substrate stiffness. Since thin films are part of a composite structure that includes the substrate and the possible underlying stack, the other layers may have an impact on the overall elastic properties, and the stress-strain interaction between layers is often also quite anisotropic [156]. Due to deviations in lattice features and thermal expansion behavior with respect to the substrate, thin films can experience very high stresses and strains. These in-plane stress components can also affect the domain structure and shape as well as domain walls. According to some research works, piezoelectric thin films deposited onto metallic substrates can be thought of as being almost completely laterally clamped to the substrate, and this feature may considerably affect the measurement of the d_{33}. In reality, for typical film and substrate dimensions, the effective piezoelectric coefficient is decreased to 50% of its bulk value or to 80% in case it is just affected by the clamping from the surrounding film [157].
As a matter of fact, the estimated piezoelectric coefficient for the KNN films grown onto Pt substrates after plasma cleaning step followed by the annealing in vacuum turn out to be comparable to the state of the art of undoped KNN films [135, 136, 137] and larger in comparison to other lead-free piezoelectric thin films [158, 159, 160]. In order to bring the piezoelectric performances of KNN closer to those of highly textured PZT thin films ($d_{33} \sim 160 - 200$ pm/V [161, 24, 162]), it is critical to combine a suitable surface template engineering with an accurate and systematic optimization of the growth process.

4.5 Conclusions

In conclusion, the effects of the Pt(111) substrate surface preparation on the characteristics of PLD-grown KNN thin films of 300 nm were throroughly investigated. Both the influence of *ex-situ* plasma cleaning and *in-situ* vacuum annealing of Pt before KNN deposition were considered. The optimal substrate cleaning procedure was identified as a 10-minutes oxygen plasma cleaning step followed by a vacuum annealing of 20 minutes at $\sim$ 600°C inside the PLD chamber. Vacuum annealing after plasma results in a significant flattening and cleaning of the Pt surface, with increased grain size and suppressed concentration of adventitious carbon and other organic residuals. This leads to a significant increase in the crystalline quality of the thin films compared to those grown onto uncleaned substrates, with a decreased amount of defects and a high compactness. Leakage currents are decreased by one order of magnitude, as conduction at grain boundaries is strongly suppressed. Macroscopic ferroelectric hysteresis behaviour is observed, with a the remanent polarization P_r of 2.5 μC/cm^2. Such value is still lower than what is reported by previous research, likely due to the residual leakage impairing the observation and reliable measurement of ferroelectric switching phenomenon.
However, on films with optimized substrate preparation and deposition process, the local piezoelectric coefficient has an average value of 80 pm/V, which is comparable to the state of the art. This study clarified the need of substrate treatment to enhance the functional characteristics of the films toward the benchmark provided by PZT, even though optimized KNN films still exhibit a sizeable leakage, most likely caused by the non-compensated loss of volatile alkali elements.

CHAPTER 5

Li-doped KNN: Li diffusion and surface segregation

5.1 Introduction

The synthesis of KNN in the form of both bulk ceramics and thin films has so far lead to encouraging results towards the attempt to replace PZT in common piezoelectric devices (see Chapter 1). It was found that stoichiometric KNN ($K_{0.5}Na_{0.5}NbO_3$) corresponding to a Polymorphic Phase Boundary displays significantly improved ferro- and piezoelectric properties [90]. Numerous applications are made possible by these traits, and significant efforts are being devoted to enhancing the properties of KNN by texturing, tailoring, and doping to achieve an optimal competitor of PZT.

Lately, the inspection of the potential offered by doping procedures in thin films has received more focus. The piezoelectric response of KNN has been found to be significantly improved by doping [163, 164]. In this context, some computational analyses have shown that introducing Li^+ ions in the KNN perovskite matrix is able to favour the formation of boundaries at room temperature in the phase diagram that can promote exceptional piezoelectric responses [165, 166, 167]. This is due to the fact that the coexistence of multiple phases makes the material more responsive to external electric stimuli. However, a complete characterization of chemical composition and structural incorporation of Li as a dopant in KNN thin films still requires a good deal of systematic experimental studies. This may be due to the fact that several of the most widely used chemical quantification methods, such as X-ray Photoelectron Spectroscopy or Energy Dispersive X-ray Diffraction, exhibit significant issues in identifying and measuring the presence of very small and light Li^+ ions inside the oxide matrix. It is known that Li has an atomic factor and a cross section which are so small that its signal is typically impossible to detect using standard methods, especially if it is used as a dopant in extremely small concentrations. As a result, multiple approaches and detection techniques must be used and combined to examine the phenomenon of Li incorporation inside the crystal lattice of KNN.

This Chapter presents a thorough analysis of Li doping of PLD-grown KNN thin films on $Pt(111)/TiO_2/SiO_2/Si$ template. Li doping is achieved by co-ablation of a stoichiometric KNN target and a circular sector of $LiNbO_3$ single crystal. Li surface segregation and strong diffusion

phenomena are observed in Li-doped KNN leading to a significant chemical non-uniformity across the film thickness. Additionally, it is shown how Li doping mostly occurs through Na substitution, indicating that doping also affects the relative concentration of Na and K. This is particularly relevant considering the fact that the Polymorphic Phase Boundary appears at the unitary ratio of Na and K, which is the composition to aim for to achieve optimal piezoelectric responses. As a result, a general degradation of the macroscopic properties is observed in Li-doped films, with an increased leakage current and larger amount of morphological defects. This inhibits macroscopic ferroelectric switching behaviour. Nonetheless, the piezoelectric coefficient d_{33}, locally extracted from Piezoresponse Force Microscopy performed on top of single grains, is equivalent to the one measured on undoped KNN. This possibly indicates that Li mostly behaves as a mobile ion localized at interstitials and grain boundaries, mainly impacting on the macroscopic electrical properties and not on microscopic localized piezoelectric behaviour. These effects may be explained by thermally activated Li diffusion occurring during high-temperature, low-growth rate PLD deposition.

5.2 Experimental Methods

- **Thin film growth and doping:** The synthesis of 300nm-thick KNN thin film was carried out using the Pulsed Laser Deposition method on a stack of Pt(111)(100 nm)/TiO_2(20 nm)/SiO_2(700 nm)/Si using the UV fourth harmonic wavelength of 266 nm from a Nd:YAG laser. A ceramic target with stoichiometry $K_{0.5}Na_{0.5}NbO_3$ was employed for the undoped KNN sample. To achieve the desired doping of Li, a thin (~ 0.1 mm) circular sector of 7° the same radius (2.5 cm) as the KNN target was cut from a single crystal of $LiNbO_3$ and fixed on top of the ceramic target as indicated in the schematic of Figure 5.1. A circular rastering of the KNN target and $LiNbO_3$ slice assures the ablation of both components. From the target geometry, the expected composition is $Li_x(Na_{0.5}K_{0.5})_{1-x}NbO_3$ with $x = 0.02$, meeting the ideal Li concentration for enhancing KNN properties [168, 169].
  The substrate underwent a pre-treatment process prior to deposition consisting of an *ex-*

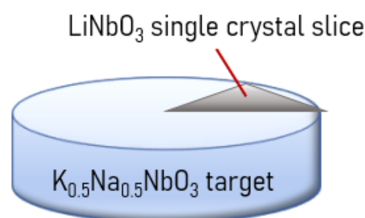

Figure 5.1: *Schematic of the doping method. A circular sector of $LiNbO_3$ single crystal is fixed onto of the KNN stoichiometric target so that with a circular rastering of the target for the laser ablation, both materials can be ablated.*

situ oxygen plasma cleaning for 10 minutes followed by an *in-situ* vacuum annealing in the PLD chamber at a temperature of 615°C and a base pressure of ($4 \cdot 10^{-7}$ mbar) for 30 minutes. In this way, optimal surface reconstruction il favoured and any organic residual adatoms or molecules are eliminated, granting best deposition dynamics and layer quality [170]. The employed laser settings were 10 Hz frequency, 1.3 J/cm^2 fluence. The PLD growth parameters for both doped and undoped KNN samples were: 220 mTorr oxygen pressure, 615°C substrate temperature, and a 42.5 mm substrate-target separation.
The thin film samples were *in-situ* annealed at 500°C for 30 minutes in 500 mbar oxy-

gen atmosphere after the growth to favour crystallization dynamics and compensate for possible oxygen vacancies.

- **Morphological and structural characterization:** Thin film surface morphology was investigated using a scanning electron microscope (Zeiss Leo 1525 FE-SEM), and crystallographic phases and orientations were identified using X-ray diffraction at room temperature ($\theta - 2\theta$ scans, Bruker D8 Advance X-ray Diffractometer, in collaboration with M. Cabrioli and F. Di Fonzo, IIT Center of Nano Science and Technology).
- **Chemical composition characterization:** X-Ray Photoelectron Spectroscopy (XPS) measurements (PHI ESCA5000 Versaprobe III equipped with a scanning micro-focused Al monochromatic source at 1486.6 eV) were used to determine the surface composition of the thin films. The distribution of the elements across the layers was examined by Time of Flight Secondary Ion Mass Spectrometry (ToF-SIMS) (IONTOF IV) employing an analyzing beam of Ga^+ ions at 25 keV and a 1 keV beam of either Cs^+ or O^- ions as sputtering beam. Negative ions are collected in the first mode, together with information on the sharpness of the interfaces, while in the second mode positive ions are acquired for the inspection of the Li profile along the thickness of the film (in collaboration with S. Vangelista, S. Spadoni and E. Ravizza, STMicroelectronics).
- **Electrical measurements:** In order to conduct electrical tests, Ti top contacts (100 nm) were deposited on top of the KNN samples with the same procedure described in Section 4.2. With a source meter (Keithley 2612), leakage current measurements were made by supplying the sequence of ramps from 0 to +15 V to 0 to -15 V to 0 with a slope of 2.1 V/s.
- **Piezoelectric characterization:** For the measurements of piezoelectricity, a Keysight 5600LS atomic force microscope was utilized in the Piezoresponse Force Microscopy mode. As described in Section 4.2 a voltage signal of amplitude 1 V was applied across the sample at 31 kHz, allowing for imaging of spontaneous ferroelectric domains and to extract a semi-quantitative value of the piezoelectric coefficient d_{33}.

5.3 Analysis of Li$^+$ incorporation in KNN lattice

Figure 5.2 reports the morphology of (a) undoped and (b) Li-doped KNN thin films grown in the same conditions inspected by SEM. The undoped film surface is nearly completely flat, with just a few misoriented crystallite grains scattered across the region that range in size from 100 to 200 nm. In contrast, the Li-doped sample exhibits a greater number of square and tent-shaped misoriented grains.

To evaluate the orientation and structure of the film, X-ray Diffraction scans were conducted. Figure 5.3 displays a comparison of the diffraction spectra from undoped (blue) and Li-doped (green) KNN. The undoped film diffraction peaks at 22.3° and 45.4° are assigned to the (001)/(100) and (002)/(200) planes, showing that the mostly planar fraction of the surface is related to (001) texture in a pseudocubic description. The peak at $\sim$40° is caused by the Pt substrate whereas other spurious grooves are caused by the XRD sample holder. The diffraction pattern for the Li-doped KNN sample is relatively similar, except for low-intensity peak at 33.5 degrees indicating that there is residual (011) orientation within the film, which is most likely generated by the tent-like oriented crystallites shown in Figure 5.2. Besides, Li-doped samples show a shift towards the left of the (001) and (002) peaks by around 0.1° and 0.2° respectively. This can be generated by the incorporation of a minor concentration of Li, which causes an out-of-plane lattice expansion. Vegard's law for a solid solution of two constituents can be applied

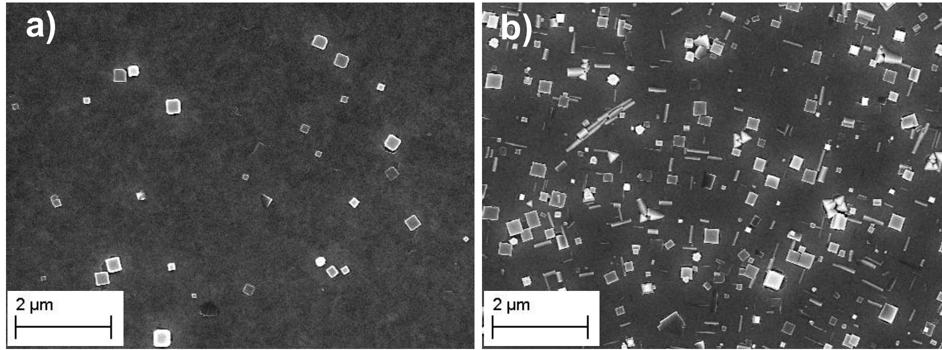

Figure 5.2: *SEM surfaces of the (a) undoped and (b) Li-doped KNN thin films. Upon doping, an increase in the amount of defects and misoriented crystallites arises.*

to calculate the experimental quantity of Li introduced in the KNN compound [171]:

$$a_{Li-KNN} = (1 - x)\, a_{KNN} + x a_{LiNbO_3} \tag{5.1}$$

where x is the amount of Li-doping experimentally introduced. The obtained doping estimated using the experimental lattice parameters for undoped (3.98 Å), Li-doped (4.01 Å) KNN and the lattice parameter of $LiNbO_3$ (5.12 Å) is $x = 0.03$. This concentration is very close to the first estimate of $x = 0.02$ based on geometrical model of the circular sector of $LiNbO_3$ single crystal placed on top of the KNN target.

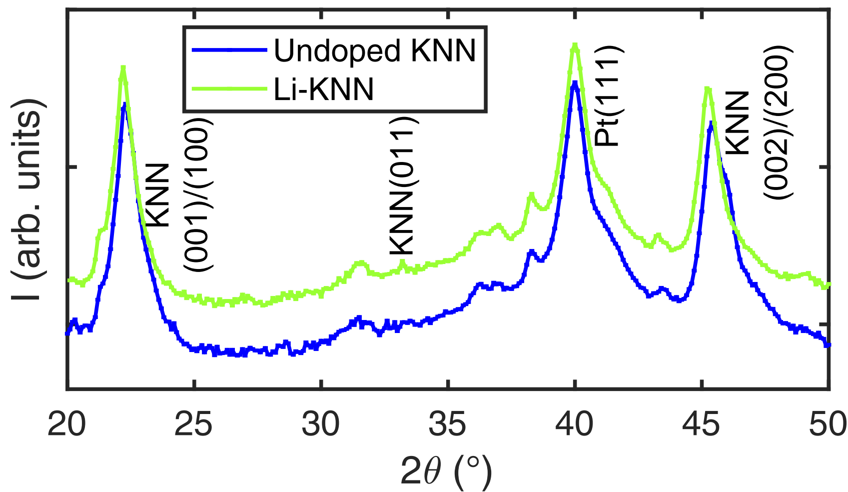

Figure 5.3: *Comparison of XRD diffraction spectra from undoped (blue) and Li-doped (green) samples. In both cases, the peaks at 22.5° and 45.4° are attributed to a (001) orientation of the films. A small amount of (001) phase is revealed by the small peak at 33.5° in doped KNN. The shift in the KNN peaks towards smaller angles in Li-doped KNN suggests the occurrence of an out-of-plane lattice expansion.*

Surface XPS measurements on undoped and Li-doped samples were carried out in order to offer another estimate of the exact experimental doping. Beause of the low cross section held by Li 1s photoelectrons and very low Li concentration, the doping amount is below the XPS detection limit, which is around 5−10%. Furthermore, the Li 1s peak, which is predicted to have a binding energy of about 55−56 eV, lies within the range of the Na 2s and Nb 4s peaks. Because Li is meant to replace the alkali elements, the investigation was thus concentrated on

the variation of Na and K in the doped sample with respect to the undoped one. According to the structure of the target, $Li_{0.02}K_{0.49}Na_{0.49}NbO_3$ would be the predicted stoichiometry of the doped KNN thin films in case of equivalent substitution of K and Na.
The samples were subjected to XPS analysis of the initial pristine surface, of the surface after C_{60}^+ cleaning to remove organic residuals, and finally of the thin film "bulk" exposed after extended C_{60}^+ sputtering. The outcomes from the quantification study are summarized in Table 5.1. While K is virtually unaltered in Li-doped samples compared to undoped KNN, the concentration of Na is consistently lower. This indicates that Na is preferentially replaced by Li in this system with respect to K, resulting in a stoichiometry of $Li_xK_{0.5}Na_{0.5-x}NbO_3$, unlike what was observed in other studies reporting a preferential substitution of K [172]. The XPS data indicate that the difference in Na bulk signal between undoped and Li-doped samples is by approximately a fraction 1/15 (Table 5.3), therefore the experimental doping of Li may be calculated as $x = 1/15 \cdot 0.5 = 0.03$, where 0.5 refers to the stoichiometric concentration of Na in KNN. The obtained value for the dopant matches the one derived using Vegard's law and XRD lattice parameters exactly.
An additional result emerging from the XPS data is related to the difference in Na concentration between undoped and Li-doped KNN thin films at various depths. There is a systematic deficit of Na in Li-doped KNN with respect to the undoped sample. Such difference by 39% on the pristine surface (Table 5.1) sizably decreases to 19% after surface C_{60}^+ cleaning (Table 5.2) and down to 6% in the bulk after C_{60}^+ sputtering (Table 5.3). This can also be seen from the XPS Na/Nb atomic ratios shown in Figure 5.4 acquired in the three different conditions for undoped and doped samples. If the variation of Na is assumed to be caused by Li substitution, as stated above, this result may be attributed to a surface segregation phenomenon of the Li dopant.

Surface	Na (at%)	K (at%)	Nb (at%)	O (at%)
Undoped KNN	10.7±0.3	9.1±0.2	16.0±0.2	64.2±0.3
Li-KNN	6.5±0.3	8.9±0.2	16.8±0.2	67.8±0.3

Table 5.1: *XPS quantitative data for undoped and Li-doped KNN: pristine surface.*

Surf. + C_{60} cleaning	Na (at%)	K (at%)	Nb (at%)	O (at%)
Undoped KNN	15.1±0.3	10.7±0.2	18.4±0.2	55.8±0.3
Li-KNN	12.2±0.3	11.0±0.2	19.0±0.2	57.9±0.3

Table 5.2: *XPS quantitative data for undoped and Li-doped KNN: surface after soft C_{60}^+ cleaning.*

Bulk	Na (at%)	K (at%)	Nb (at%)	O (at%)
Undoped KNN	15.5±0.3	9.9±0.2	20.3±0.2	54.3±0.3
Li-KNN	14.6±0.3	9.9±0.2	20.6±0.2	54.9±0.3

Table 5.3: *XPS quantitative data for undoped and Li-doped KNN: bulk after consistent C_{60}^+ sputtering.*

On both doped and undoped KNN samples, ToF-SIMS studies were carried out to acquire a further insight into the incorporation of Li into the KNN matrix, and the results are shown in Figure 5.5. Initially, Cs^+ ions at an energy of 1 keV were employed as sputtering beam and Ga^+ ions at 25 keV as analyzing beam. In this mode, the beam of Ga^+ ions is used to stimulate the emission of secondary ions with negative charges in the material (Figure 5.5a and 5.5b). This allows to examine the primary components of the KNN matrix and the sharpness of interfaces between different layers. Li^- ion cannot be detected in this measurement mode because it is

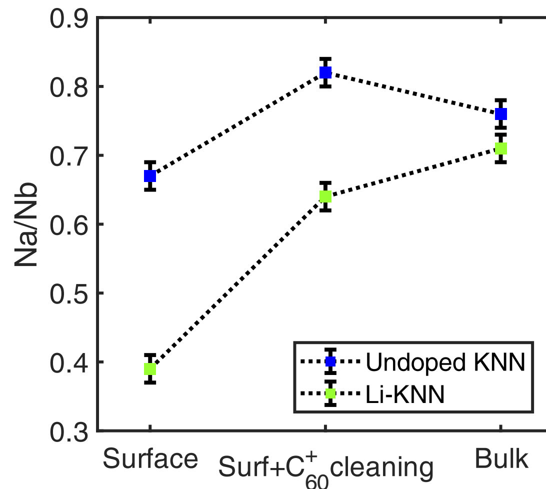

Figure 5.4: *XPS atomic ratio of Na/Nb for undoped (blue) and doped (green) KNN samples. The ratio is consistently more intense in all cases of undoped KNN, and with a greater difference in Na concentration between the samples in surface sensitive measurements. This suggests the occurrence of Li surface segregation phenomena if Li is assumed to mainly substitute Na.*

formed with a very low probability. Since the preferred ionization state of Li is the positively charged Li^{+}, 1 keV O^{-} ions were employed as sputtering beam to promote the creation of positive ions and thus capture the Li profile (Figure 5.5c and 5.5d). Less defined interfaces are created with this oxygen beam because of charging effects occurring within the oxide matrix.

By examining the acquired signals of undoped and doped films (Figure 5.5a−b and 5.5c−d respectively), the profiles of all the atomic species belonging to KNN (Na, K, Nb, and O) are flat in both cases. This suggests that the composition across the depth of the film is mostly uniform. On the other hand, the panels corresponding to doped KNN reveal a sizable gradient of Li along the thin film thickness and a very high peak in the concentration at the surface (Figure 5.5b), which is consistent with the surface segregation of Li suggested by XPS. It should be noted that at the interface with the Pt substrate the Li signal slightly rises locally due to the effect of matrix modification, thus the peak of the Li profile observed at the KNN/Pt interface is probably an artifact. Finally note that, because of the extremely small quantity of Li introduced and the high intensity of the Na and K signals, it is not possible to discern whether Li is substituting Na or K. In addition, the KNN/Pt interface is found to be sharper than the Li-KNN/Pt interface. This might be explained by taking into account the greater number of misoriented crystallites at the surface of Li-doped KNN. These defects, which are 30−50 nm high, are additional material to be sputtered. The LKNN components will thus provide an additional, delayed signal since the sputtering in the portion of surface covered by these defects will reach the interface with the bottom Pt with a minor delay relative to the rest of the sample. Furthermore, there may even be a difference in the sputtering rate of the crystallites with respect to the main layer due to their different orientation, which would contribute to the broadening of the interface.

A gradient in the concentration of a dopant species is often seen in thermally-activated doped systems, in which the dopant is deposited on the surface and an annealing step is performed to activate the diffusion of the element into the thin film. In this case, however, the Li dopant is located within the target itself, thus a homogeneous distribution should be expected, similar to that exhibited by K and Na SIMS profiles. The observed behaviour of Li seems to indicate a phenomenon of severe migration and subsequent segregation at the surface due to its extreme atomic mobility.

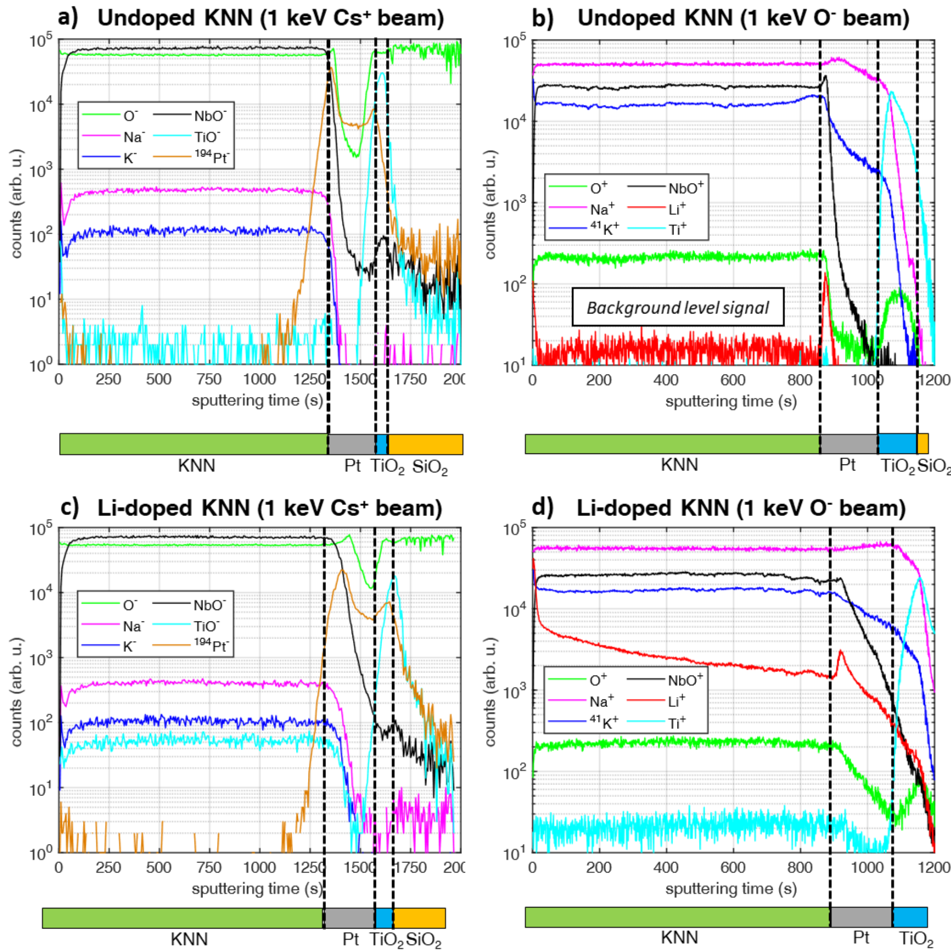

Figure 5.5: *ToF-SIMS depth profiles for undoped (top) and and Li-doped (bottom) KNN samples. Depth profiles acquired with Cs^+ sputtering beam to identify interfaces with higher precision are shown in panels a) and c). Depth profiles acquired with oxygen sputtering beam allowing to detect Li^+ ions are reported in panels b) and d).*

5.4 Effect of Li-doping on functional properties of KNN

For both undoped and Li-doped KNN films, the DC leakage current density J is measured across microcapacitors defined by Ti electrodes on top of the KNN/Pt structure. The results are shown in Figure 5.6 as a function of the external electric field E applied in the top-top configuration, i.e. between adjacent Ti top electrodes. As seen in 5.4, Li-KNN sample showed an order-of-magnitude increase in leakage current with respect to undoped KNN. The decrease in film morphological compactness and the enhanced ionic mobility brought on by Li doping are believed to be the causes of this rise in electrical losses. In fact, Li^+ ions may occupy defects and interstitial sites due to their decreased dimensions, especially at grain boundaries where they are not strongly attached to their location and promote free charge transport through the thin film [173, 174, 175].

These leakage currents completely mask the macroscopic ferroelectric switching currents and inhibit the piezoelectric response. Thus, Piezoresponse Force Microscopy was used to carry out the piezoelectric characterization. By sending a low-amplitude AC voltage signal of 1 V to the conductive AFM tip, the material deformation in response to the stimulus is recorded by measuring the deflection of the tip. As discussed in Chapter 4, writing and stabilizing do-

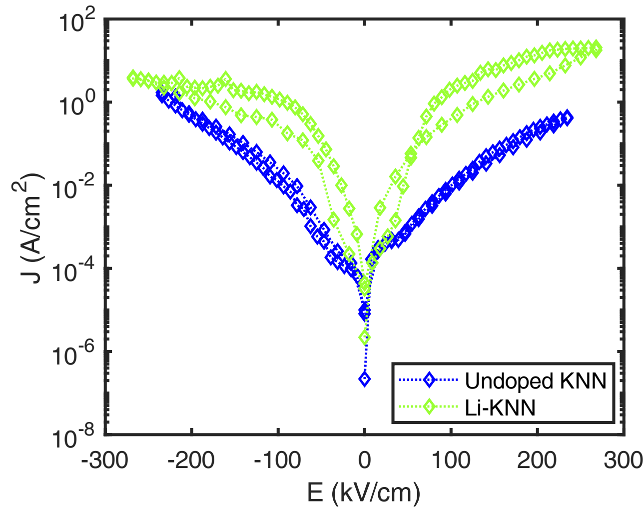

Figure 5.6: *Leakage current density profiles of undoped (blue) and Li-doped (green) KNN thin films. Li doping introduces a degradation of electrical properties with a leakage increase by one order of magnitude.*

E (kV/cm)	J (A/cm^2	J (A/cm^2
25 kV/cm	$7.0 \cdot 10^{-4}(\pm 6.0 \cdot 10^{-4})$	$1.5 \cdot 10^{-3}(\pm 2.5 \cdot 10^{-3})$
50 kV/cm	$3.3 \cdot 10^{-3}(\pm 2.3 \cdot 10^{-3})$	$5.1 \cdot 10^{-2}(\pm 5.8 \cdot 10^{-2})$

Table 5.4: *Comparison of leakage currents evaluated at 25 kV/cm and 50 kV/cm for undoped and Li-doped KNN.*

mains was made challenging by the high local ferroelectric coercivity, clamping of the thin film to the substrate, and depolarization effects. Therefore, the piezoelectric coefficient was calculated from the imaging of the spontaneous ferroelectric domains (Figure 5.7). Using the same methods as for undoped KNN films, the estimation of the d_{33} coefficient was derived from the evaluation of the average piezoelectric signal amplitude on top of single grains for both oppositely polarized domains. The introduction of Li into the material did not produce an increase of the piezoelectric signal, as the d_{33} value of 80 pm/V$\pm$20 pm/V is the same as that extracted from undoped KNN. The incorrect integration of Li into the lattice might be used to explain this finding. On one hand, XPS suggests a preferential substitution of Na, which alters the ideal $0.5-0.5$ stoichiometry for Na and K leading to MPB. On the other hand, the same tendency to macroscopic Li surface segregation seen both by XPS and SIMS could reflect in Li diffusion and accumulation at grain boundaries, thus preventing the targeted uniform doping of KNN. In this scenario, Li is unable to produce a substantial alteration in the crystal properties that would have increased its piezoelectric response.

In order to discuss how these observations differ from those of earlier research works based on Li-doping it is essential to consider the differences of the doping procedures and the specific implications they are responsible for. In general, sol-gel processes for thin films [175, 176] or sintering techniques for ceramics [177] are frequently used to incorporate Li into KNN as a dopant with small concentrations. Such approaches generally employ high growth rates at low temperatures (500°C or below) oftentimes accompanied by rapid annealing steps at high temperatures. Instead, a Physical Vapour Deposition technique for the synthesis of thin films, like PLD, is featured with low growth rates ($\sim$ a few nm/min) while the sample is kept at high temperatures ($600-800$°C) for extended amounts of time ($\sim$ hours). These alternative approaches can result in different atomic dynamics during growth, which have a big impact on the structure and composition of the obtained thin film. Diffusion processes in a crystal lattice

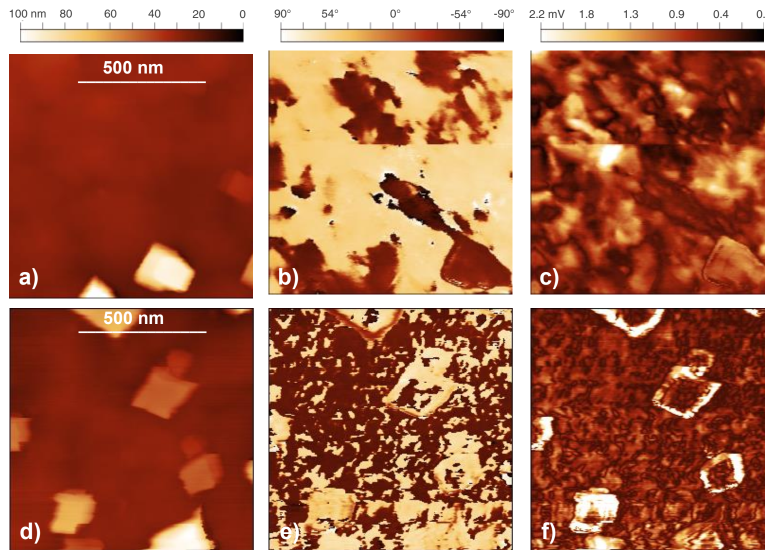

Figure 5.7: *Topography (a,d), phase (b,e) and amplitude (c,f) PFM scans for undoped (a)−(c) and Li-doped (d)−(f) KNN samples. The phase signal reveals the orientation of the out-of-plane polarization, whereas the amplitude is proportional to the piezoelectric coefficient.*

can activate migration through interstitials, through a cascade of successive replacements with other atomic species in the crystal lattice, or through point vacancies. The random walk model provides the description of the travel distance of an atom as $r = \sqrt{kt}$ for a single atom in a three-dimensional lattice, where k indicates the jump frequency and t the time span [178]. Assuming the general scenario when a mix of interstitial, substitutional, and point-vacancy lattice diffusion takes place, the jump frequency k relies on the number of point vacancies, the number of leaps it is capable of performing, and the activation energy. Besides, the diffusion rate must rise with temperature since k is given by an Arrhenius-like equation. Furthermore, in polycrystalline thin films a number of grain boundaries, defects, cracks and dislocations can serve as diffusion sites with low activation energies. Since Li dopant has a high atomic mobility due to its small size, diffusion processes are expected to be easily activated by the high thermal budget provided in a PVD growth method like PLD. In these procedures, the substrate and growing thin film are held at high temperatures for a few hours usually required for the growth of the desired thickness (hundreds of nm) at relatively low growth rates before being further annealed for 30 to 60 minutes. Besides, a modest positive temperature gradient towards the surface is predicted since the heating lamp is positioned beneath the substrate. This may assist in understanding the concentration gradient observed in the ToF-SIMS measurements, which is probably the result of an important Li^+ ion migration phenomenon. The longer Li^+ ions remain in the heated crystal template at high temperatures, the further they can travel to the colder as-grown and still-growing superficial layers, which is why the gradient in Li concentration is found to be directed towards the thin film surface.
Last but not least, it should be noted that the same phenomenon of Li segregation seen at the surface occurs also at grain boundaries, where dopants are only weakly bonded to their sites and this may promote leakage current losses through ionic conduction. As a result, Li-dopants have little impact on microscopic PFM measurements made on top of single grains, where the leakage current is small (as seen in some conductive AFM experiments like those reported in Chapter 6) and also the local doping is expected to be small due to diffusion towards grain boundaries. This is probably the reason why the measured piezoelectric coefficient in Li-doped KNN thin films is unchanged compared to undoped samples.

5.5 Conclusions

A thorough characterization of Li-doped KNN thin films grown by Pulsed Laser Deposition was reported. An effective approach to achieve Li doping of KNN was presented as an alternative to commonly employed procedures: a small slice of $LiNbO_3$ crystal of the desired dimension is placed on the stoichiometric $K_{0.5}Na_{0.5}NbO_3$ target for co-ablation. According to XPS analyses, the introduction of Li^+ ions into the KNN lattice primarily reflects in the substitution of Na. The experimental doping estimate was determined to be 0.03, pretty close to the one (0.02) expected from the geometrical structure of the employed composite target. Li doping was found to cause a degradation of macroscopic morphological and electrical properties. As a consequence, macroscopic ferroelectric measurements in the doped samples are hindered by the sizable rise in DC leakage currents compared to undoped samples. Interestingly, the concentration of the dopant rises by an order of magnitude across the thin film thickness from the interface with the substrate to the surface. In agreement with the macroscopic tendency to surface segregation of Li revealed by XPS and ToF-SIMS, the deterioration of macroscopic functional characteristics is suggested to be due to the diffusion of the dopant from the bulk to grain boundaries, producing local conductive channels for ionic charge migration responsible for the increase of leakage currents. This phenomenon does not impact on the local PFM measurements giving access to the evaluation of the d_{33}, which turns out to be the same both in undoped and Li-doped films. On the other hand, the same local piezoelectric behaviour of doped and undoped films indicates that the incorporation of Li in the films was not effective to produce the expected improvement of functional properties.

According to these results, identifying the appropriate growth technique is crucial to getting a slight doping of light elements such as Li for KNN thin films, because the atomic mobility can be easily triggered in high-temperature PVD techniques with slow growth rates. It is crucial to optimize a uniform incorporation of Li dopant into the crystal lattice as a substitutional atom for both K and Na in order to provide the necessary enhancement in thin film functional properties. High-rate and low-temperature deposition processes in combination with quick thermal annealing treatments may be used for this purpose.

CHAPTER 6

Epitaxial growth of KNN on Nb:$SrTiO_3$

6.1 Introduction

Considerable research was devoted to the characterization of the KNN bulk ceramic material [48, 49], but KNN thin films are the focus of new scientific and technological investigations for their potential integration in micromechanical applications [179]. However, KNN thin films frequently experience volatilization of alkali elements and the resulting deviation from the optimal stoichiometric atomic ratios, as well as large leakage currents [52], due to their finite thickness and high growth temperatures intrinsically required (500-700°C). Nonetheless, the attempts to optimize KNN films are beginning to yield successful results. In support of technological and commercial applications of silicon-based industrial processes, such as in miniaturized devices for micro-electromechanical systems (MEMS devices), some studies have shown the feasibility of achieving highly oriented KNN thin films on Pt/Ti/SiO_2/Si by both sol-gel and Physical Vapour Deposition processes like sputtering or Pulsed Laser Deposition [137, 138, 170].
Epitaxial KNN films deposited on different perovskite substrates, however, still hold a good deal of scientific interest, as a result of their suitability for structural analyses and characterizations that might offer information on the underlying phenomena responsible for leakage currents. Indeed, working with epitaxial thin films prevents the interference of extrinsic factors common to polycrystalline films on metal-terminated templates, such as morphological defects and grain boundaries. In this way, the investigation of intrinsic physical processes in single crystalline heterostructures can be singled out. Some previous papers specifically addressing this issue have attributed the intrinsic origin of leakage currents to A-vacancies in the perovskite structure caused by significant Na and K losses during film deposition [180, 181].
Besides, while bulk ceramics and polycrystalline thin films are often featured with grain boundaries and the random orientation of the grains that contribute to complicate the study of microscopic properties, the structure of epitaxial thin films closely resembles that of single crystals with a preferential orientation, making them ideal case studies for examining the mechanism of high piezoelectricity at the Phase Boundaries. Such research studies are especially relevant

and beneficial considering that KNN material has a more complicated phase diagram than its well-known lead-containing analog PZT [92].
This Chapter presents the study of the structural, chemical, electrical and piezoelectric properties of epitaxial KNN thin films grown on Nb:$SrTiO_3$(001) single crystals. At substrate temperatures above 600°C a two-dimensional (2D) growth is obtained, along with a significant rise in leakage current, while lower leakage currents at the expenses of a 3D growth and plenty of morphological defects is observed for lower growth temperatures. The significant Na and K losses experienced during film deposition are strongly activated by high growth temperatures and are responsible for the leakage current increase in KNN thin films. The measurement of the d_{33} coefficient from both spontaneous ferro- and piezoelectric domains as well as from piezoelectric local butterfly loops is provided by PFM. Sizable piezoelectric behaviour is observed in 2D flat films, although with a lower d_{33} compared to polycrystalline thin films [170].
Additionally, the emergence in 2D thin films of a periodic ($\sim 0.8 - 1$ μm) square configuration of the spontaneous domain pattern can be observed by looking at the PFM phase, conductive AFM, and SEM backscattered electrons signals. This phenomenon is ascribed to a mechanism of relief of internal lattice stresses by forming domain walls along crystallographic axes, which occurs in addition to typical misfit dislocations [182, 183]. These findings suggest that strain engineering strategies in thin films hold the potential to stabilize specific configurations of piezo- and ferroelectric domains.

6.2 Experimental Methods

- **Thin film growth:** By using Pulsed Laser Deposition (PLD) and a Nd:YAG laser operating at its fourth harmonic wavelength of 266 nm, KNN thin films were deposited on single crystal Nb:$SrTiO_3$ substrates with (001) orientation and a 0.5%wt Nb doping. The substrates were cleaned prior to deposition with a treatment process that included *ex-situ* oxygen plasma cleaning (10 minutes) and *in-situ* annealing at 700°C in oxygen atmosphere (220 mTorr). The optimized growth conditions comprise the following deposition parameters: oxygen pressure 220 mTorr, substrate-target distance 40 mm, laser fluence 1.3 J/cm^2, laser frequency 10 Hz. Different samples were grown varying the substrate temperature from 740°C progressively lowering it down to 470°C. Following the growth, *in-situ* 30-minute annealing in 500 mbar of oxygen pressure was carried out at sample temperature of 500°C. The KNN sample thin films have a thickness of around 300 nm, with the exception of the sample grown at 740°C, in which a strong temperature dependence of the growth rate yielded a thickness of 400 nm due to and increased growth rate at higher temperatures.

- **Structural and chemical characterization:** *in-situ* Reflection High Energy Electron Diffraction (RHEED) was conducted to evaluate the thin film orientation obtained in epitaxial growth conditions. The morphological properties of thin films were examined using a scanning electron microscope (Zeiss LEO 1525 FE-SEM operated at 10 kV). A dedicated module of the SEM microscope was used to perform Energy Dispersive X-ray Spectroscopy to analyze the chemical composition of the samples under a probing electron beam at 10 keV. Reciprocal Space Maps (RSM) for the evaluation of lattice parameters were acquired by *ex-situ* XRD with X-Ray Diffractometer Rigaku SmartLab X (wavelength 1.5406 Å) (performed by M. Badillo, PoliFAB).

- **Electrical measurements:** In order to conduct electrical tests, a matrix of capacitors was created by fabricating Ti electrode pads on top of the films by e-beam evaporation through a physical mask as described in Section 4.2. Leakage current was measured with a source meter (Keithley 2612) in the top-top configuration by supplying a triangle signal of $0 \rightarrow$

$+10V \rightarrow 0 \rightarrow -10V \rightarrow 0$ with a slope of 2.1 V/s. Ferroelectric switching measurements were performed on a aix-ACCT TF-2000 Analyzer with triangular pulses in the PUND mode (positive-up-negative-down) at a frequency of 1 kHz and with a delay of 10 ms.

- **Piezoelectric characterization:** Piezoelectric measurements and the extraction of the d_{33} piezoelectric coefficient were carried out using the Piezoresponse Force Microscopy (PFM) method. A Keysight 5600LS Atomic Force Microscope was utilized. By applying a small AC voltage of 2 V to the tip at a frequency of 281 kHz (out of resonance, with $f_{res} \sim 300$ kHz), it was possible to image spontaneous ferroelectric domains and acquire an estimate for the piezoelectric coefficient with the same method described in Chapter 4 and 5. The evaluated tip sensitivity utilized for this purpose was 209 nm/V. Piezo- and ferroelectric switching response loops were recorded by progressively applying a DC voltage across the thin film in steps of 1 V up to 7 V for 5 s per step, and measuring the tip displacement at each step with an AC signal of amplitude 2 V with a 1 s read time. The measurements were done using an effective Q-factor of 7.5 to take into account the amplification due to the fact that the working point ($f_{meas} \sim 281$ kHz) was not completely "out of resonance" but on the tail of the resonance peak ($f_{res} \sim 296.4kHz$). The piezoelectric coefficient in this mode can be evaluated as [184]: $d_{33} = S \cdot A_{PFM}/(Q_{eff} \cdot G \cdot V_{ac})$, where S indicates the tip sensitivity, A_{PFM} the maximum amplitude span in the stress butterfly loop, G the gain, V_{ac} the applied reading voltage. Q_{eff} is the effective Q-factor at the base of the resonance peak estimated by multiplying the resonance Q-factor $Q = f_{res}/\Delta f \sim 30$ by the ratio of the tip signal intensities $I(f_{meas})/I(f_{res}) \sim 0.25$, giving $Q_{eff} \sim 7.5$.
In order to identify a possible relationship of morphological features with the configuration of ferro- and piezoelectric spontaneous domains and current conduction, Current Sensing Atomic Force Microscopy (CS-AFM) scans were performed. Sample areas of $1-5$ μm^2 were scanned at variable bias voltages in the range $1-6$ V.

6.3 Temperature-dependent growth mode and stoichoimetry-dependent leakage

KNN samples were synthesized under varying growth temperatures with the goal of finding the best conditions for epitaxial growth to produce perfect oriented flat surfaces without defects or grain boundaries. As a matter of fact, substrate temperature is known to be the parameter that mostly affects the variation of sample composition, crystal structure, and electrical properties. Therefore, six KNN thin film samples were deposited with different substrate temperatures in the range 740°C $-$470°C. In Figure 6.1, the top view of the surface of all epitaxial KNN thin films is shown for comparison. The employed growth temperatures are 740°C, 660°C, 610°C, 560°C, 520°C, and 470°C. A growth temperature of 740°C (Figure 6.1a) leads to a film with a flat oriented texture littered with some rod- and square-shaped crystallites and some cracks. These defects, ranging in lateral size from 100 to 300 nm and several hundreds of nanometers (400 to 600 nm) high, are aligned with the [100] or [010] crystallographic directions of the STO substrate and are possibly originated by the Stransky-Krastanov growth mode activated by large lattice mismatch. Sample grown at 660°C (Figure 6.1b) only displays square-shaped oriented crystallites a few tens of nanometers ($20-40$ nm) high, still aligned along [100] and [010] directions of STO. For lower growth temperatures, the amount of defects tends to slightly increase (Figure 6.1c). This trend continues until the thermal budget is insufficient to permit full crystallization, in which case the thin film formation becomes non-uniform and the surface roughness rises (temperatures 570°C and below, Figure 6.1d$-$f).

After the growth, *in-situ* RHEED diffraction patterns were acquired from each sample. Fig-

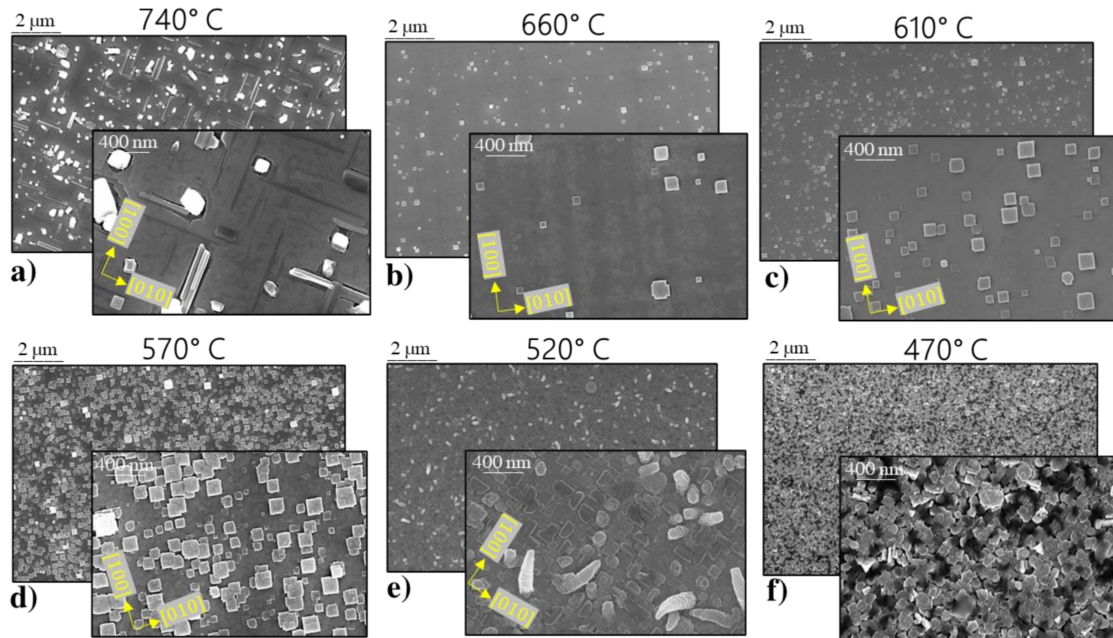

Figure 6.1: *SEM top view of the surfaces of KNN thin films deposited at different growth temperatures. The epitaxial crystalline ordering below 600° C is disrupted by an inadequate thermal budget during growth, leading to increased roughness and worse compactness.*

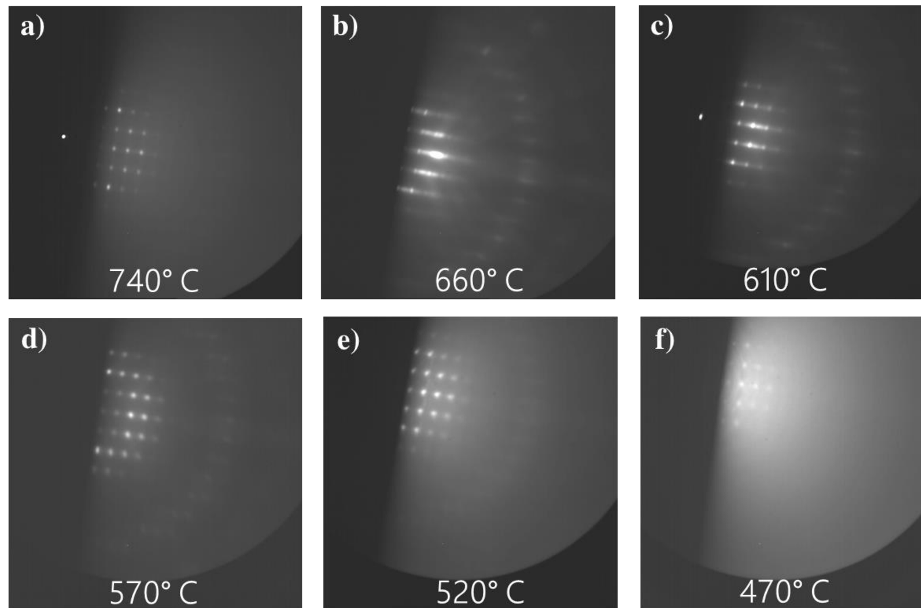

Figure 6.2: *RHEED diffraction pattern of KNN thin films collected along [100] in plane direction of the STO substrate. Grazing incidence diffraction stripes are only displayed by 660° C- and 610° C-samples, confirming 2D ordered epitaxial growth. In all other samples, transmission diffraction spots appear from roughness features generated by a 3D island growth mode.*

ure 6.2 compares the reflections that were recorded for all samples along the [100] in-plane direction. From diffraction patterns of the STO substrate (not shown) almost the same stripe spacing is observed, indicating a cube-on-cube growth of KNN on STO, as expected from the relatively low lattice mismatch between the two: a_{STO} = 3.905 Å [185], a_{KNN} = 3.947 Å [186].

The RHEED signal of the sample grown at 740°C shown in Figure 6.2a features some bright spots in the pattern. The appearance of spots is consistent with the sizable 3D features observed in the morphology of Figure 6.1a: the probing electron beam passes through these defects, therefore a bulk-like transmission signal contribution is generated in the final diffraction pattern. The distinctive "2D-like" RHEED striped pattern is only exhibited by samples deposited at 660°C and 610°C, confirming two dimensional growth dynamics (Figure 6.2b−c) and epitaxial growth matching the Nb:STO substrate (001) orientation. The bright spot structures related to rough 3D deposition modes reappear at lower growth temperatures, below 570°C (Figure 6.2d−e). The diffraction pattern is less distinct in the final sample at 470°C, which suggests the formation of a less organized crystal structure originated from a non-epitaxial growth condition (Figure 6.2f).

The electrical properties of all samples were examined and compared by acquiring leakage current curves between adjacent top electrodes (i.e. in the top-top configuration) as a function of the applied electric field. For samples grown at different substrate temperatures, leakage current density profiles are displayed in Figure 6.3. A clear relationship between the leakage profiles and the growth temperature is seen: by evaluating the leakage current at 50 kV/cm, in the vicinity of the coercive field E_c estimated in Chapter 4, a drop in deposition temperature of 270°C, from 740°C (black) to 470°C (green), results in a drop in the leakage current by almost eight orders of magnitude. This trend may appear at odds with the general belief that the existence of defects, pinholes, and grain boundaries in the porous, rough, fractured and non uniform surfaces provides a major contribution to increasing leakage currents. This thus suggests that there are intrinsic conduction mechanisms strictly associated with substrate deposition temperature that generate additional leakage current contributions unrelated to morphological features.

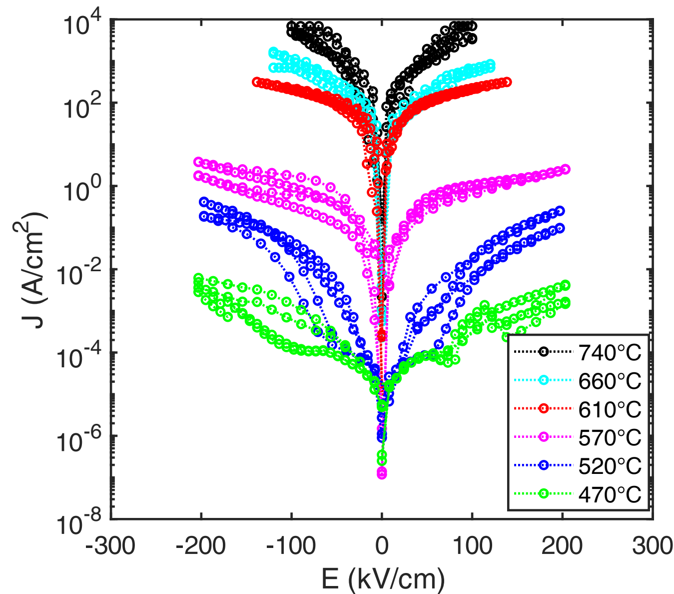

Figure 6.3: *Comparison of leakage current density curves for all KNN samples grown from 740°C to 470°C. Lowering the growth temperature by almost 300°C is able to reduce leakage currents by almost 8 orders of magnitude.*

An indication of the origin of these mechanisms is provided by the chemical analysis using EDS technique (Figure 6.4). For samples with lower leakage currents grown at low tem-

peratures, greater Na/Nb and K/Nb percentage ratios are found than for flat epitaxial films. 2D epitaxial samples are notably under-stoichiometric, whereas those deposited at temperatures below 600°C exhibit a chemical composition similar to the desired stoichiometric one, i.e. $K/Nb = 0.5$ and $Na/Nb = 0.5$. The explanation of the observed trend can be attributed to the volatility of Na and K present in KNN. As a matter of fact, alkali elements are significantly volatile and can easily re-evaporate from the thin film upon deposition, therefore the way they are incorporated into the lattice is considerably influenced by the growth temperature. Due to the lack of alkali atoms at the A-sites for the volatilization phenomenon of Na and K, many intrinsic charged lattice vacancies are created in the ABO_3 perovskite matrix. These vacancies can readily serve as hopping sites for charge transport, causing enhanced charge mobility through the thin film and deteriorating electrical performances [147, 148].

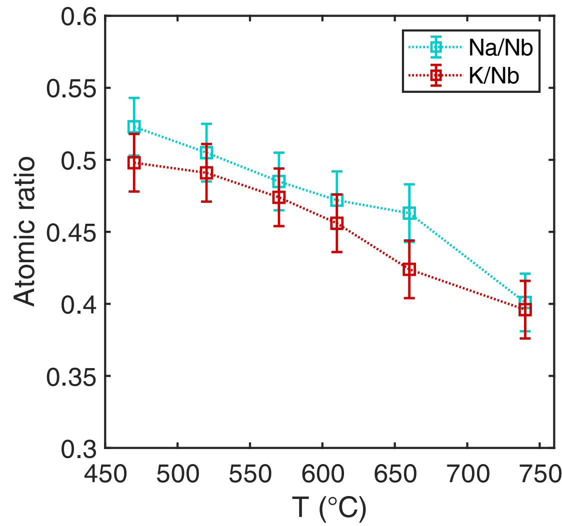

Figure 6.4: *Trend of the atomic ratios acquired by EDS as a function of the substrate growth temperature. High growth temperatures trigger the volatilization of the alkali elements, and the resulting samples are thus understoichiometric, whereas the atomic ratios of 3D non-epitaxial samples deposited at lower temperatures are close to the stoichiometric values.*

A comparison of ferroelectric switching polarization and current curves is displayed in Figure 6.5. Only for thin films grown at 520°C the polarization at remanence is above 1 μC/cm^2, with $P_r = 2\mu$C/cm^2 at coercive voltages of $V_c^- = -1.61$ V and $V_c^+ = +1.54$ V, corresponding to electric fields of $E_c^- = -26.8kV/cm$ and $E_c^+ = +25.6kV/cm$ over a single capacitor device. The obtained coercive fields are within the range observed in literature for epitaxial KNN (from below 10 kV/cm [187] up to some tens of kV/cm [188]) and lower than those obtained on Pt substrates, which are around 50−60 kV/cm in our films and can go up to 100 kV/cm in literature [189]. This can be due to the intrinsic high quality of epitaxial samples displaying essentially no grain boundaries which can act as pinning sites for ferroelectric domain walls. Finally, ferroelectric behaviour of 2D epitaxial thin films grown at 660°C is barely detectable, with a remanence of 0.35 μC/cm^2, $V_c^- = -2.31$ V and $V_c^+ = +3.27$ V, i.e. $E_c^- = -38.5$ kV/cm and $E_c^+ = +54.5$ kV/cm. Note, however, that even the remanent polarization measured for low-temperature thin films is quite low: this is likely because sizable ferroelectric switching is still strongly impaired by leakage currents, which easily mask the low-intensity switching peaks, hindering the switching of dipoles into a measurable remanent polarization.

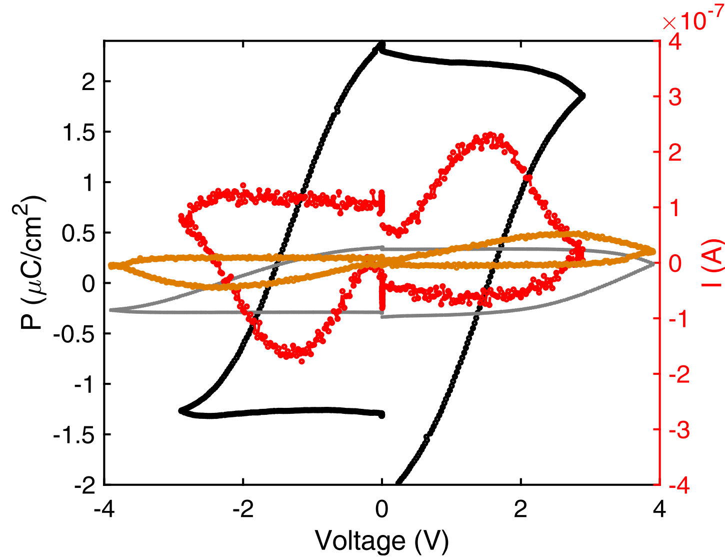

Figure 6.5: *Comparison between switching behaviour observed in 660°C film (grey and orange) and in 520°C film (black and red). The magnitude of both the switching current peaks and the remanent polarization increase by almost one order of magnitude.*

6.4 Square pattern of spontaneous ferroelectric domains

The piezoelectric properties were investigated for the flat epitaxial KNN with optimal surfaces using the PFM method. Since RHEED and SEM reveal that a flatter surface is produced at 660°C growth temperature, with the fewest number of defects and crystallites, in Figure 6.6 results are shown for the sample deposited in this condition, which allows for a more accurate analysis of the intrinsic properties of the epitaxial thin film. On the other hand, scanning on low-temperature 3D surfaces was severely hampered by artifacts on the PFM tip arising from a significant correlation with high-roughness defects.

Figure 6.6 displays the topography (Figure 6.6a) of a 660°C sample together with maps of the PFM phase (Figure 6.6b) and amplitude (Figure 6.6c) obtained by scanning the conductive tip on the sample surface. Spontaneous ferroelectric domains can be detected with inwards and outwards polarization, as from RHEED patterns the films are known to be (001)-oriented. With the exception of a few crystallite-related anomalies, the pattern is composed of narrow yellow domains with irregular rugged edges, emerging from brown domains and defining a sort of square lattice with a cell size of around 0.8 μm. The phase map shows a sizable contrast of the signal changing from +5 V for yellow domains to -5 V for brown domains, which corresponds to a phase difference of 180°. The magnitude of the signal in the amplitude map (Figure 6.6c) of the two types of domains is, as expected, approximately the same, given the fact that the amplitude is not sensitive to the orientation of the ferroelectric polarization, demonstrating the consistency between the phase and amplitude images. The borders of the yellow domains, instead, appear black in the amplitude map, and this is consistent with the existence of a ferroelectric domain wall, where the PFM amplitude is decreasing to zero, separating the brown from the yellow domains, which are ascribed to c-domains with inward and outward polarization (parallel to the c-axis). Notably, some exeptions to this straightforward interpretation of the PFM signals subsist in some areas of the image (for example, the elongated black area on the left of the dashed square in Figure 5c), which is much larger in size than the black

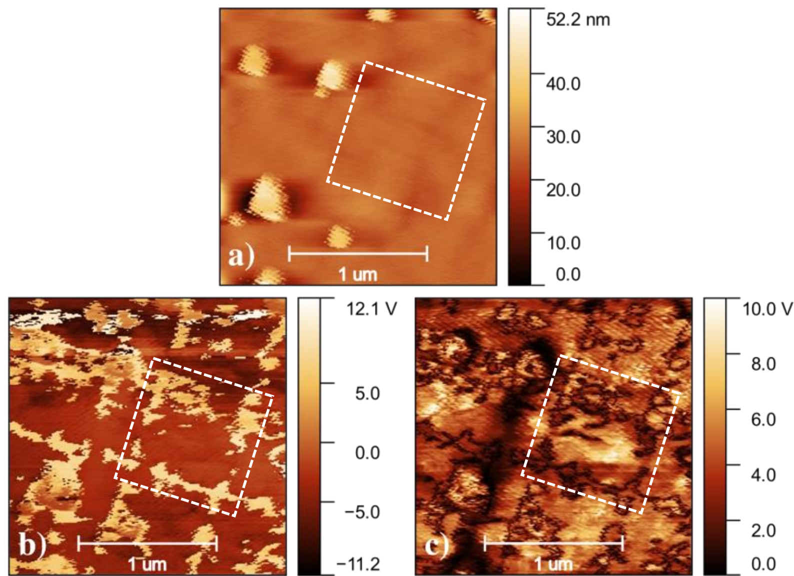

Figure 6.6: *Topography (a), phase (b) and amplitude (c) scans acquired by PFM on 2D epitaxial sample grown at 660° C. Ferroelectric spontaneous domains exhibit sharp domain contrast by 10 V in the phase signal coming from 180° domain walls. The domain configuration appears as periodic square shapes due to strain/stress relaxation mechanisms.*

edges of yellow domains corresponding to ferroelectric domain walls. These black areas might instead be assigned to a- or b-domains with some tilting, which produce basically no amplitude signal but still some detectable phase in the phase map. The alignment of the domain pattern to the [001] and [010] directions of the substrate suggests a possible connection to the particular phenomenon of ferroelectric domain generation detailed below, which results from lattice strain relaxation. This theory is further supported by the possible presence of a- or b-domains since c/a/c domain configurations have been theoretically suggested as an effective method for strain relaxation [182].

From the PFM amplitude signal, an evaluation of the d_{33} coefficient over the PFM amplitude map (Figure 6.6c) of spontaneous domains can be obtained, employing the same statistical method described in Chapter 4 and 5. With this approach, a semi-quantitative estimate of 43.5±17 pm/V was obstained, possibly affected by the estimate of the effective Q-factor discussed above.

Investigating the PFM switching hysteresis involves applying DC voltage pulses with increasing amplitude and superimposing an AC signal to detect the deflection at each DC bias. In this way, the displacement response at each bias is recorded and a complete loop can be plotted. The 2D epitaxial sample that was grown at 660°C was subjected to DC bias in increments of 1 V up to a maximum of 7 V in order to generate the piezoelectric switching hysteresis loops seen in Figure 6.7. Due to the weak signal but with the aim to operate in an area where a trustworthy estimate of the d_{33} may be made, the measurement was carried out near the base of the tip resonance peak (i.e. at 281 kHz with $f_{res} = 296.4$ kHz). From the signal amplitude A(V) (Figure 6.7 left), the semi-quantitative estimate for the piezoelectric coefficient is determined to be 37.5 ± 10 pm/V, similarly to that obtained from spontaneous domains, confirming the soundness of the two different methods. However, this value of the d_{33} is around half that obtained from polycrystalline KNN films on Pt [170], even though the absolute value of the d_{33} on epitaxial films could be affected by a large uncertainty on the Q_{eff} value employed. This could be partially attributed to some residual effects of substrate clamping [132, 133] while the

major reason for such reduction is probably related to the losses of Na and K which alter the film stoichiometry.

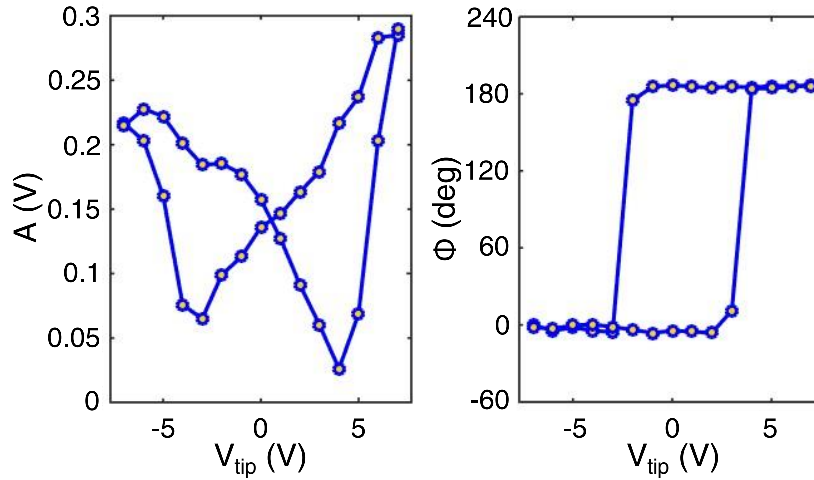

Figure 6.7: *PFM local hysteresis cycles of the amplitude (left, proportional to the stress) and phase (right) acquired from the 660° C film.*

Interestingly, by performing CS-AFM scans of the vertical current across the thin film, evidence is found of the same squared lattice shape imaged by the collected current. This can be seen in both the 5×5 μm^2 area scanned at +5 V (applying the bias to the back side of the sample and keeping the tip grounded) and a zoomed-in 2×2 μm^2 area at +2 V (Figure 6.8b and 6.8d, respectively), while the corresponding topography is provided in Figure 6.8a and 6.8c. The current signal reproduces quite precisely the spontaneous domain pattern with opposite out-of-plane polarizations of Figure 6.6b, with a compatible periodicity of ~ 1 μm and no significant correlation with the topography. A sizable current signal is collected from one of the two possible domain orientations and a nearly zero signal from the other. Besides, almost no pattern is observed for a scan with negative bias voltage (not shown). This means that the collected current signal can be related to the local switching behaviour, only acting on re-orienting one of the two possible polarization configurations for a fixed bias tip during the scan. In general, the current signal acquired from consecutive scans was found to be quite reproducible, indicating the depolarizing ferroelectric relaxation occurs over a time scale ranging from fractions of a second up to possibly a few minutes required to complete a single scan before starting a new one. The weaker contrast observed for maps taken at negative bias voltage can be explained looking in more detail at the local I(V) curves.

In order to coherently interpret these experimental results, local I(V) current loops were acquired. A typical I(V) curve is shown in Figure 6.8e, taken at the place marked by white crosses in the topographic picture of Figure 6.8c and 6.8d. Looking at the obtained typical I(V) curve presented in Figure 6.8e, it clearly exhibits the distinctive profile predicted for a ferroelectric material. Positive and negative current peaks are shown at about ±3 V, corresponding to the ferroelectric coercive voltage observed in PFM loops in Figure 6.7. Note that, however, the effective polarization obtained by normalizing the charge corresponding to a current peak to an estimated tip circular area of diameter of around 10 nm is higher with respect to the expected one for a realistic value of the ferroelectric polarization by up to 6 orders of magnitude. This means that the observed current peaks in conductive AFM are not simply related to ferroelectric switching. The increased local conductivity can be possibly accounted for by considering the presence of domain wall conductance, associated to electronic reconstructions or charge-

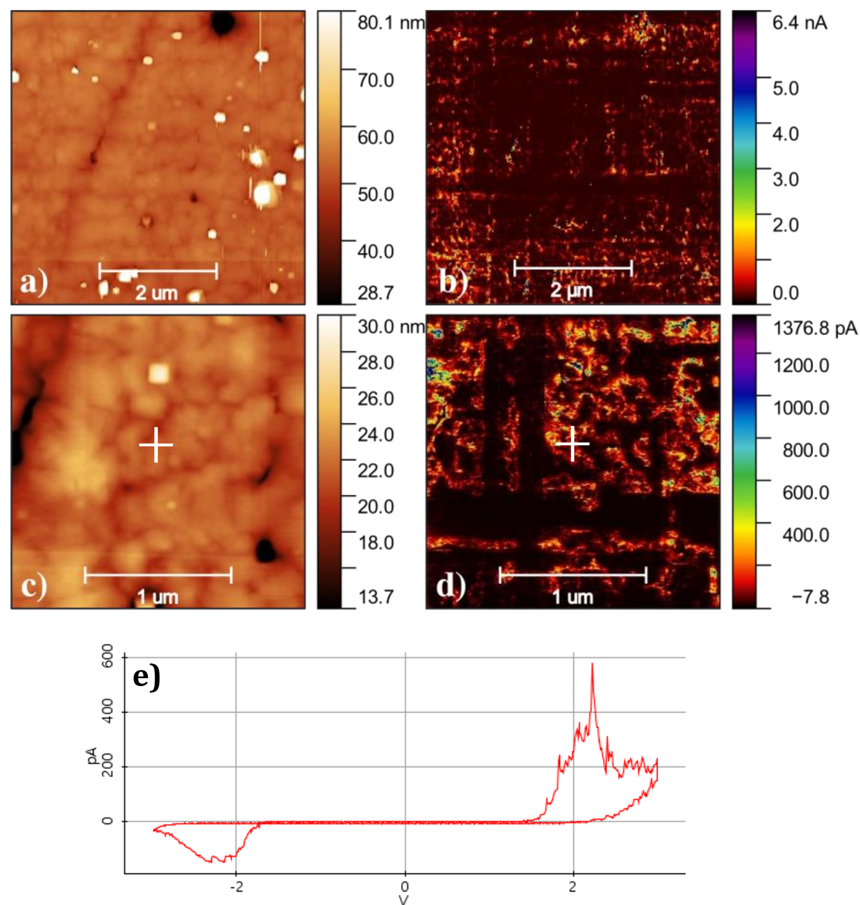

Figure 6.8: *CSAFM scans on the 660°C-sample. On the top, (a) topography and (b) current signal collected with a bias of 5 V on an area of 5×5μm^2. A the bottom, (c) topography and (d) current signal collected with a bias of 2 V on an area of 2×2μm^2. The squared configuration of the domains can clearly be imaged by domain switching current signal. (e) I(V) loop measured at the cross position in the topography.*

trapping defects. As a matter of fact, domain walls can reconstruct in an applied field and form partially charged and more conducting configurations [190]. Moreover, the negative current amplitude and associated peak are much lower, possibly pointing to the presence of an asymmetric conduction mechanism in the tip/KNN/Nb:STO heterostructure system in analogy to what is discussed in Chapter 7, and this explains why the domain-related pattern does not appear for negative tip biases. Therefore, it appears reasonable that by scanning the tip with a sufficiently high applied voltage bias (i.e. at or above 2 V, marking the onset of the ferroelectric switching peaks), the spontaneous domain pattern with opposite out-of-plane polarizations of Figure 6.6b can be quite accurately reproduced. Indeed, a sizeable current signal is collected from one of the two possible domain orientations (that which can be switched for the specific applied bias polarity) and a nearly zero signal from the other.
Interestingly, beside PFM and CS-AFM, the same pattern is observed also in the morphological imaging by SEM with the in-lens detector for backscattered electrons, clearly visible in Figure 6.1b for the sample grown at 660°. As a matter of fact, backscattered electrons are suggested to be sensitive to ferroelectric polarization due to charge accumulation effects and/or pyroelectric phenomena [143]. A similar pattern can be seen in the sample deposited at 740°C (Figure 6.1a) but not in the sample grown at 610°C (Figure 6.1c) despite having fewer crystallites. This suggests, as explained below, that the formation of the aforementioned square pattern is con-

nected to a significant loss of Na and K alkali metals, as experimentally observed for thin film samples grown at 660°C and 740°C.

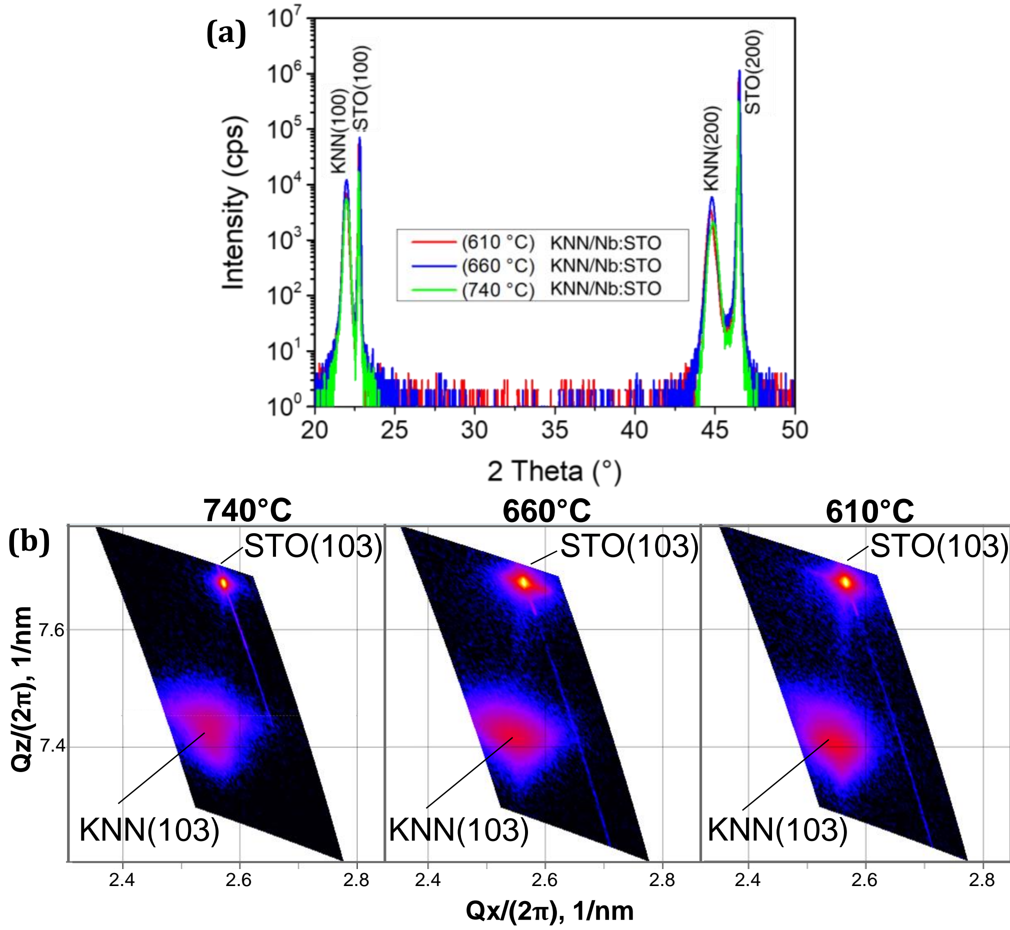

Figure 6.9: *Comparison of lattice reflections of 2D epitaxial KNN grown at 740°C, 660°C and 610°C. (a) $\theta - 2\theta$ pattern, (b) Reciprocal Space Maps around (103) lattice reflection.*

In order to correlate the observed periodic domain pattern to lattice structure and strain deformations, XRD data are collected from the set of three 2D epitaxial samples (740°C, 660°C and 610°C). Figure 6.9a shows $\theta - 2\theta$ line scans of the three samples, demonstrating the epitaxial orientation of KNN, growing with 001-orientation on STO. In Figure 6.9b, a comparison of Reciprocal Space Maps of 740°C, 660°C and 610°C samples collected around the (103) lattice reflection of STO and KNN is reported. All films have a tetragonal structure with a similar in-plane lattice periodicity, whereas a slight deformation in the out-of-plane direction is observed, with a smaller c lattice parameter with increasing growth temperature. The extracted lattice parameters are summarized in Table 6.1, compared with the values displayed by a pseudo-tetragonal relaxed KNN ceramic (referred to as "bulk KNN" in Table 6.1) [186]. The uncertainty on the obtained average lattice parameters is calculated to be ± 0.002 Å for the c parameter and ± 0.004 Å for the a parameter, evaluated by refining several reflections and acquiring the corresponding interplanar spacings."

The explanation for the formation of a square-like periodic domain configuration observed in 2D epitaxial samples on Nb:STO can lie in stress relaxation phenomena generated by the interplay of the elastic properties of the thin film and the substrate. There are two primary categories of stress relaxation mechanisms [182]: the emergence of ferroelectric domain structures

Lattice parameter	bulk KNN	740°C-KNN	660°C-KNN	610°C-KNN
a (Å)	3.947	3.930	3.930	3.935
c (Å)	4.016	4.036	4.043	4.050

Table 6.1: *In-plane (a) and out-of-plane (c) lattice parameters of 2D epitaxial KNN thin films retrieved from Reciprocal Space Maps around (103) reflection.*

and the creation of misfit dislocations. Concerning the first type, some studies have shown that the areas near domain boundaries in epitaxial ferroelectric thin films operate to elastically accommodate strains brought on by lattice mismatch between the film and the substrate [191]. In this picture, if the release of the elastic energy of one monodomain is possible by introducing a second domain orientation, multiple domain formation is stimulated. On the other hand, the formation of misfit dislocations along the interface between the film and the substrate is able to screen the lattice mismatch, and thus promote a stress release mechanism. This especially occurs above a critical thin film thickness at which the release of elastic energy provided by the edge portion of a dislocation equals the energy gain brought on by the line energy of the dislocation itself. In the relaxation of the epitaxial strains for c-domains, this gives rise to an orthogonal dislocation array made of a single dislocation density [192].
In light of what was discussed above, the simple cubic structure of the STO substrate ($a = 3.905$ Å) is expected to exert a bi-axial compressive strain onto the KNN thin film (in the tetragonal bulk $a_b = 3.947$ Å), as the lattice mismatch $f = 100 \cdot \frac{a_{STO} - a_{KNN,b}}{a_{KNN,b}} = -1.06\%$. As a matter of fact, the mismatch-induced deformation of KNN is reflected by a smaller a parameter and a larger c parameter in all samples with respect to the tetragonal bulk reference. As regards the effect of the growth temperature, a volume decrease occurs with increasing growth temperature, as both the c and a parameters decrease, which can be associated to higher alkali evaporation. This points to a larger compressive strain and in-plane stress of the lattice cell, which can favour strain relaxation mechanisms connected to the formation of peculiar periodic domain patterns.
A similar morphology and associated domain pattern has been observed in similar works on the growth of perovskite oxides on SrTiO$_3$. The surface morphology that has been seen is similar to what Saito et al. [180] had previously reported in NaNbO$_3$ films on SrTiO$_3$ substrates. This phenomenon has been associated to surface undulations and is ascribed to surface relieve patterns and ferroelastic domains [193, 181]. They represent a secondary stress relief process which only occurs in thick films in addition to stress release through the creation of misfit dislocations [193]. The generation of this kind of surface morphology is suggested to be due to the interaction between greater surface energy and the release of strain energy by mass transport mechanisms activated during film slow deposition at high temperatures and/or during the post-growth final cooling step [180, 181].
It should be noted that 2D films grown at lower growth temperatures (610°C) the formation of domains becomes less pronounced, possibly because the appearance of an increasing density of crystallites interferes and concurs at the overall film relaxation process.

In general, whenever misfit dislocations are formed, polarization instabilities and the deterioration of the piezoelectric properties can occur [194, 195], which explains the difference between the piezoelectric coefficient measured on these samples with respect to results on KNN thin films grown on other substrates in literature [137, 138]. As a matter of fact, the ferroelectric polarization close to the dislocation regions can be suppressed by the strain field developed around the dislocation sites, which also creates a strongly confined polarization gradient [195]. On the other hand, the pinning of the ferroelastic domain walls due to the strain coupling of ferroelastic domains and misfit dislocations may limit the mobility of the ferroelastic domain

walls in an applied electric field and thereby decrease the extrinsic contribution to piezoelectric effects [195]. Notably, the structural properties of perovskite oxide thin films can be deliberately altered by suitably engineering the strain coupling of ferroelastic domains and misfit dislocations.

6.5 Conclusions

To summarize, a structural analysis of PLD-grown epitaxial KNN thin films on Nb:STO(001) was provided as a function of substrate deposition temperature. By correlating *in-situ* RHEED diffraction patterns with sample surface morphology with SEM, a low-roughness, 2D epitaxial growth window was identified for growth temperatures approximately between of 600 and 700°C.
According to the electrical measurement, a striking correlation between leakage current and growth temperature is found, with a difference in leakage current between the 740°C-sample and the 470°C-sample by up to 8 orders of magnitude. Consequently , the leakage cannot be directly connected with morphological defects, because the largest leakage currents are observed in the high-temperature 2D epitaxial samples, despite their low roughness and uniformity. The intrinsic leakage current found for epitaxial 2D samples is ascribed to charge motion caused by Na and K vacancies, due to the high volatility of the alkali elements. In fact, from the assessment of the chemical composition by EDS only for growth temperatures lower than 600°C do both Na/Nb and K/Nb approach the stoichiometric ratio of 0.5. This emphasizes the high impact on structural and electrical properties of the volatility of alkali elements during the lengthy growth times required by high-temperature, low-growth-rate techniques like PLD. As a consequence, sizable macroscopic ferroelectric switching behaviour is only observed for low-temperature samples, with a weak remanent polarization of 2 μC/cm^2.
Good coherence was found between the semi-quantitative estimate of the d_{33} coefficient from the statistical evaluation of the piezoelectric signal from spontaneous out-of-plane domains (43.5±17 pm/V) and the one derived from the local switching hysteresis butterfly loop (37.5±10 pm/V). The value is still smaller with respect to the one obtained for polycrystalline KNN grown on Pt, possibly because the clamping effects from the substrate on epitaxial thin films hampers the deformation capabilities.
A peculiar square-shaped pattern aligned with STO [100] and [010] directions is observed in the spontaneous domain distribution, which is also imaged by SEM backscattered electrons and conductive AFM maps. This phenomenon is ascribed to a stress release phenomenon through the accomodation of strain at domain walls and misfit dislocation sites. Such accumulation of stress in the epitaxial lattice is suggested to be correlated with the high degree of evaporation of alkali elements at high growth temperatures, which induces deformations in the lattice cell, as shown by XRD. These results highlight the possibility of exploiting thin film strain engineering to stabilize peculiar ferroelectric domain patterns.

CHAPTER 7

Interfaces: Impact of top and bottom metal contacts on KNN thin films

7.1 Introduction

In view of designing and fabricating compact sensors, actuators, lab-on-a-chip electronics and memory devices, the development of a solid knowledge and understanding of KNN in thin films is still required, as KNN films still need improvement on a number of fronts (control of stoichiometry, doping, texturing, suppression og leakage currents). In addition, KNN may be widely used if deposition and device manufacturing procedures were made inexpensive and cost-effective for the industrial sector. In this sense, the additional components required for KNN-based electronics to function reliably are just as crucial to full device manufacturing as the piezoelectric material itself. Specifically, electrodes are essential for the development of KNN films for both effective operation and better control electrical losses. Platinum (Pt) is frequently used as a metal electrode because of its excellent chemical resistance to oxidation and high work function [137, 196]. As a substrate, Pt also affects the growth of KNN and results in the preferential orientation of grains [170]. However, platinum is a fairly expensive metal, and the cost aspect has a significant impact on the final price of KNN devices. As a result, the choice of Pt for commercial devices should to be avoided or at the very least restricted. Less expensive alternatives can be identified to replace Pt, but other metal electrodes often rise reliability issues which may make KNN devices less effectively performing [196]. Therefore, it is important to properly evaluate and characterize these other metal electrodes.
This Chapter describes the fabrication and characterization metal-insulator-metal (MIM) capacitors with M = Pt, Ni, Ti as top metal contacts of the M/KNN/Pt/TiO_2/SiO_2/Si heterostructure. I(V) leakage curves acquired in the top-bottom mode show an asymmetric behavior with respect to positive and negative applied voltages for all samples. Even with symmetric Pt electrodes at the top and bottom, a similar asymmetric behaviour in the current is seen. This can be related to the different process for the creation of the top and bottom interfaces, as detailed below. This finding supports the idea that there is a substantial difference in charge injection at the bottom

interface with respect to the top one. From the top-top measurements, on the other hand, symmetric leakage currents are observed in all cases, with a low conductance both for positive and negative voltages. With regard to these phenomena, a model is suggested to explain the asymmetric behaviour that involves the creation of a rectifying Schottky-like barrier at the bottom interface and the presence of an almost ohmic contact at the top interface, due to the smaller work function of top electrodes and a high concentration of oxygen vacancies acting as KNN dopants.
In addition, due to the high affinity for oxidation at the expenses of oxygen extraction from KNN, Ti top contacts show low reproducibility and unreliable performances. Therefore, Ti does not appear to be suitable metal for KNN electric contacts, compared to Pt or Ni. A good option among the examined metal electrodes is Ni, since it costs less than Pt but leads to a comparable behaviour in the heterostructures.

7.2 Experimental Methods

- **Thin film deposition:** The KNN thin films were grown on Pt(111) substrate which is part of the industrial stack Pt(111)/TiO_2/SiO_2/Si with the same procedure as that described in Chapter 4: PLD growth was performed after a pre-treatment of the substrate template comprising 10 minutes of O_2 plasma cleaning *ex-situ* and 30 minutes of annealing in vacuum *in-situ* at 615°C at a base pressure of $4 \cdot 10^{-7}$ mbar directly inside the PLD chamber. The employed laser is a Nd:YAG IR laser with a fourth harmonic wavelength of 266 nm, which was set at a pulse frequency of 10 Hz. A stoichiometric target was used for ablation, and the growth parameters were: laser fluence 1.3 J/cm^2, distance between target and substrate 42.5 mm, oxygen partial pressure 220 mTorr, substrate temperature 615°C. The substrate was fixed with metallic clamps that also protected a small region from the thin film deposition, so that an access to the bottom Pt contact is provided for electrical measurements.
  The deposition was followed by an annealing process at 500°C for 30 minutes in 0.5 bar oxygen atmosphere.
  With this procedure, three identical KNN/Pt samples were prepared with a KNN thickness of approximately 300 nm, so that each one could be devoted to the characterization of a different metal as top electrode.

- **Fabrication of top electrodes:** For top contacts deposition, the metals chosen for comparative characterizations were Pt, Ni and Ti. Ti contacts were fabricated *ex-situ* with the method illustrated in Section 4.2, i.e. by e-beam evaporating (with Evatec BAK 640 evaporator) 100 nm Ti onto the KNN thin film through a shadow mask comprising a matrix of $40\times40\mu$m^2 contact pads. For the deposition of Pt and Ni, instead, it was not possible to directly take advantage of the shadow mask, because the deposition (by e-beam evaporation for Ni and magnetron sputtering for Pt) was less directional than that of Ti and the pads showed a tendency to coalesce. Therefore, the whole KNN surface was first coated *ex-situ* with 20 nm layer of Pt and Ni metals by RF magnetron sputtering (AJA ATC Orion 8) and e-beam evaporation respectively, then 100 nm Ti pads were deposited on top with the shadow mask. Afterwards, the samples were etched by Ion Beam Etching (Kenosistec VS80) exploiting the considerable difference in etching rates of Pt and Ni ($\sim$4 and $\sim$3 nm/min) with respect to Ti ($\sim$1 nm/min) to separate the pillars of Ti/Pt/KNN/Pt and Ti/Ni/KNN/Pt and expose the rest of KNN again. A schematic of the fabrication process is reported in Figure 3.9 in Section 3.3.1.

- **Electrical measurements:** Two measurement configurations were investigated in order to analyze leakage current profiles as a function of the external applied voltage (V_b in Figure

7.1): in the top-bottom configuration (Figure 7.1a), the voltage is applied across the thin film between one of the contacts at the top and the Pt metal at the bottom, while in the top-top configuration (Figure 7.1b), the bias is applied between two top electrodes. The applied ramp-like bias voltage profile is sketched in Figure 7.1c. The voltage is raised from zero to a positive value, then lowered to the equivalent negative voltage, and then raised back to zero. The employed instrument is a source meter Keithley 2612, the maximum applied biases are 3 V in the top-bottom configuration and 6 V in the top-top configuration.
Small signal capacitance measurements were performed with a Precision LCR Meter Agilent E4980A (in collaboration with G. Malavena, M. Dossena, A. Spinelli and C. M. Compagnoni, DEIB, Politecnico di Milano).
Current Sensing Atomic Force Microscopy (CS-AFM) scans were performed for higly localized I−V measurements in top-bottom configuration with bias voltage ranges of 2−6 V to compare local microscopic behaviour with macroscopic conduction to check the soundness of the model.

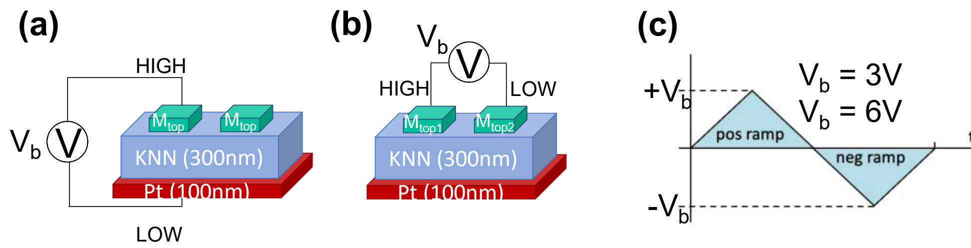

Figure 7.1: *Schematic of (a) top-bottom and (b) top-top measurement configurations. (c) bipolar triangular voltage profile applied for the characterization.*

7.3 Schottky diode behaviour and differential capacitance at the bottom interface

The leakage current density curves as a function of the applied bias across KNN thin films of different samples are reported in Figure 7.2a for the top-bottom (TB) and in Figure 7.2b for the top-top (TT) configuration. The profiles of three different samples are compared: KNN thin films are sandwiched between the common Pt electrode at the bottom and Pt (Pt-KNN, green), Ni (Ni-KNN, orange) and Ti (Ti-KNN, blue) electrodes at the top.

As can be seen, in both top-bottom and top-top curves Pt-KNN and Ni-KNN show a very similar behaviour and a high reproducibility, with Pt performing slightly better than Ni in terms of hampering leakage current conduction. For Ti-KNN instead, more than one curve is represented to highlight the sizable dispersion and low reproducibility of the measurements. Moreover Ti-KNN curves show in all cases higher leakage currents with respect to Pt-KNN and Ni-KNN, on average. Besides, top-bottom configuration curves in Figure 7.2 display an evident "diode-like" rectifying behaviour, with asymmetric current conduction with respect to the applied bias (V_{TB}). On the other hand, the leakage trend in the top-top configuration is clearly symmetric for V_{TT}.

In order to identify conduction mechanisms, ohmic behaviour was first considered, which is a bulk-limited mechanism caused by the movement of the small number of mobile electrons in the oxide conduction band. The magnitude of this current is very small, therefore it may be observed if there is no significant contribution from other mechanisms of current transport, thus

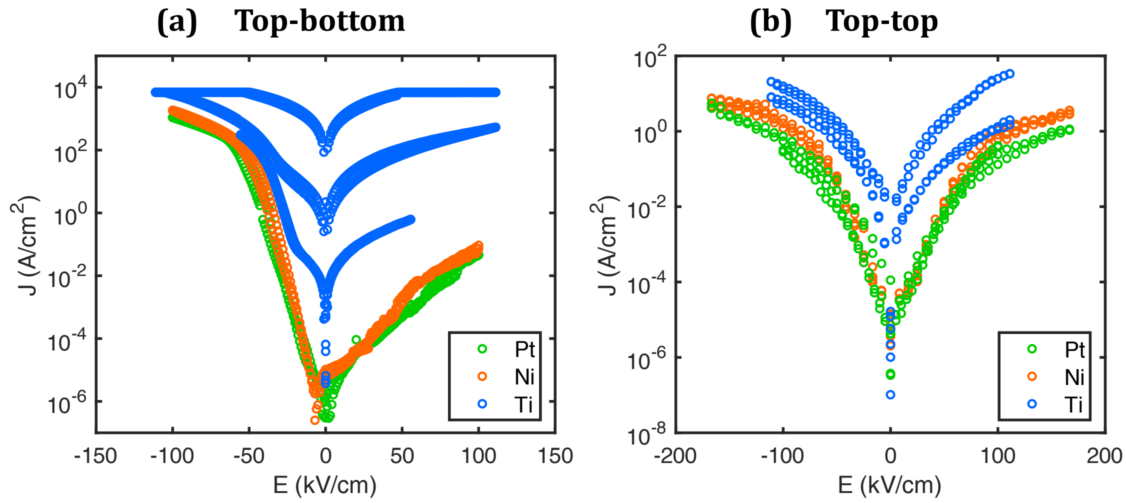

Figure 7.2: *Leakage current density J acquired in the (a) top-bottom and (b) top-top configuration for: Pt/KNN/Pt (green), Ni/KNN/Pt (orange), Ti/KNN/Pt (blue).*

at very low applied fields. The characteristic equation for ohmic conduction is:

$$J = \sigma E = nq\mu E \tag{7.1}$$

$$n = N_C \exp\left\{\frac{-(E_C - E_F)}{k_B T}\right\} \tag{7.2}$$

where σ is che conductivity of the material, μ the electron mobility, n the carrier density and N_C the effective density of states in the conduction band depending on the position of the conduction band minimum (E_C) with respect to the Fermi energy (E_F).

Given the linear relationship between the current density J and the field E, a linear fit was

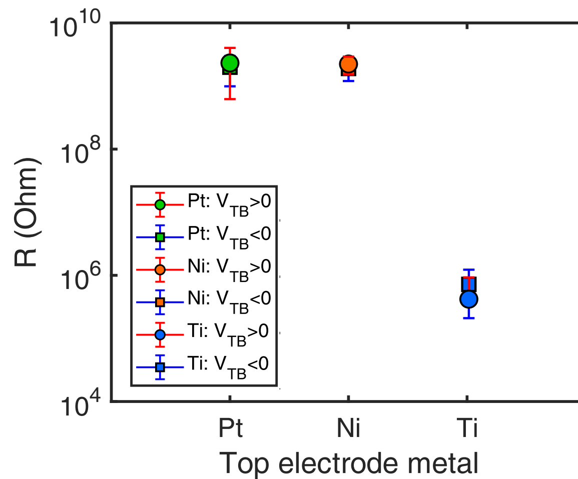

Figure 7.3: *Calculated low-field top-bottom resistance values for Pt-, Ni- and Ti-KNN. The values for $V_{TB} > 0$ (red) and $V_{TB} < 0$ (blue) overlap, in agreement with the fact that the resistance is an intrinsic property of the material and is bias-independent.*

performed on the low bias portion of the curves for positive and negative applied bias separately. The linear fit was consistent for $E < 5$ kV/cm for Pt-KNN and Ni-KNN, and $E < 10$ kV/cm for Ti-KNN, and the corresponding resistance was calculated for positive and negative biases in

this range. The calculated resistance from top-bottom curves R_{TB} is reported in Figure 7.3. As can be seen, R_{TB} is symmetric for opposite biases, coherently with the fact that the resistance depends on the scattering events within the oxide and not on the direction of the current. As such, it should also be independent from the electrode material, which is confirmed for Pt-KNN and Ni-KNN with $R_{TB} \sim 2$ GΩ. Ti-KNN, instead, displays a much lower value of the resistance $R_{TB} \sim 0.7$ MΩ: the reason might lie in the fact that Ti is a very reactive material with gettering action for oxygen, thus stealing oxygen atoms from the oxide and creating a number of intragap impurity states very close to the oxide conduction band [197].

The "diode-like" asymmetry developed at higher applied fields in the top-bottom configuration suggests the presence of a barrier at one of the interfaces, which is likely generated by the different "history" of formation of the KNN/Pt interface at the bottom and Metal/KNN at the top. This already points towards Schottky-like emission phenomenon, because depending on which way the mobile charges are moved, there are two different interface barrier they have to overcome.

In order to describe the behaviour of the barrier, the bottom interface (KNN/Pt) is first considered, which is the same for all three samples. The "diode-like" barrier behaviour is assumed to be at the bottom interface, which is thus modelled as a Schottky metal/n-type semiconductor diode. N-type doping is assumed considering the presence of oxygen vacancies, acting as donor-like native point defects. In Figure 7.4 a schematic of the metal-semiconductor band diagram at the KNN/Pt bottom interface is reported.

In this configuration, a barrier Φ_B of Pt at the interface with the semiconductor ($E_g^{KNN} \sim 3.5$

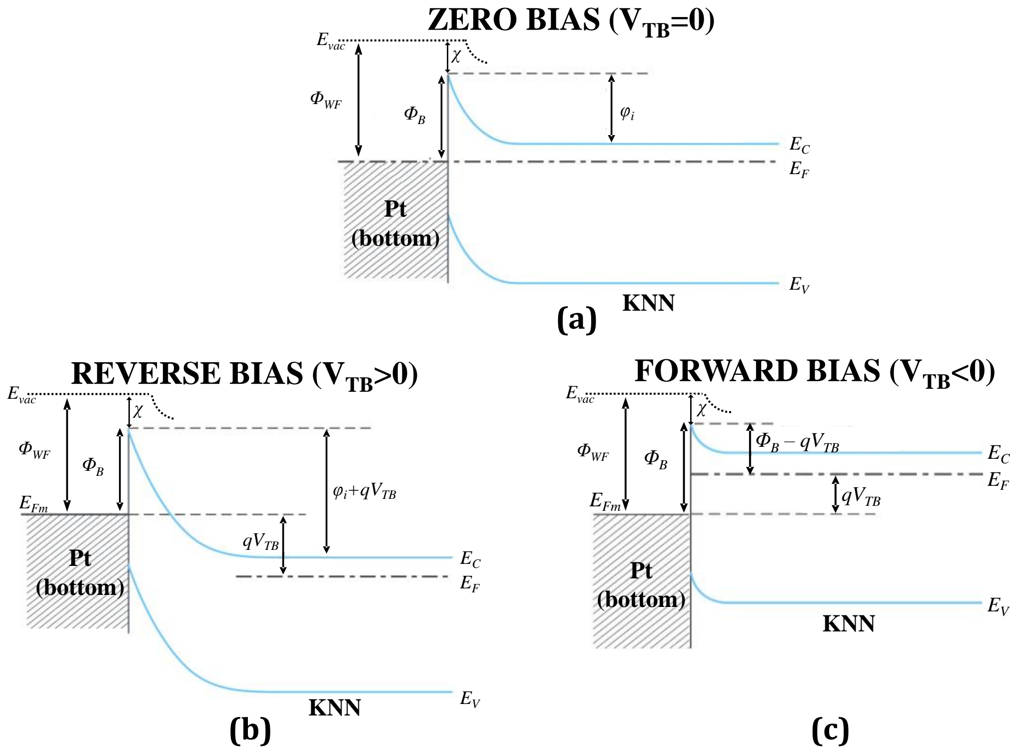

Figure 7.4: *Schematic of the band diagram at the KNN/Pt interface: (a) zero bias condition ($V_{TB} = 0$), (b) reverse bias condition ($V_{TB} > 0$), (c) forward bias condition ($V_{TB} < 0$).*

eV [198]) is formed, which depends on the large work function of Pt ($\Phi_{WF} \sim 5.65$ eV), since in a simple model $\Phi_B = \Phi_{WF} - \chi$, where χ is the electron affinity of the semiconductor. For the present case, under the assumption of $\Phi_{WF}^{Pt} \sim 5.65$ eV and $\chi_{KNN} \sim 1.1$ eV similarly to

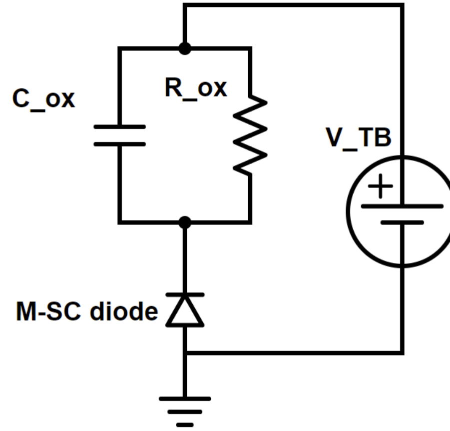

Figure 7.5: *Electrical circuit diagram of the overall top-bottom configuration. The model accounts for the leaky behaviour of the oxide with a capacitor (C_{ox}) and a resistor (R_{ox}) in parallel, while the metal-semiconductor diode ($M - SC$ diode) is positioned at the bottom interface.*

other niobates [199], $\Phi_B \sim 4.55$ eV. A value greater than the bandgap would be unphysical, however it is well known that interface states strongly affect the barrier height Φ_B [200, 201], so that a smaller value is expected in practice. Whatever the exact value of Φ_B, the large work function of Pt determines the fact that, upon creation of the interface, some charges migrate across until the Fermi energy levels are aligned (Figure 7.4a) and a depletion layer (bending of semiconductor bands) is formed at the interface together with a built-in voltage ϕ_i. When a positive bias is applied between the KNN-semiconductor and the bottom Pt (i.e. $V_{TB} > 0$), the size of $\phi_i = E_F + \Phi_B - E_C$ increases, and the field-favoured injection of free electronic charges from Pt to KNN is impaired by the energy barrier Φ_B at the interface, and the reverse bias condition of the diode occurs (Figure 7.4b). Nevertheless, some current will always be present, for example because the barrier can always be overcome by thermal activation in addition to the presence of surface states [202]. On the other hand, for negative applied biases (i.e. $V_{TB} < 0$) ϕ_i decreases and flattening of the bands is favoured, promoting charge injection through the interface and the forward bias condition of the diode occurs (Figure 7.4c). In principle, a "diode-like" behaviour would be expected for similar reasons also at the top interface, but with forward and reverse bias conditions for $V_{TB} > 0$ and $V_{TB} < 0$, respectively. However, this behaviour is not observed, either because it does not occur or because it is overshadowed by the effect of the bottom interface. This means that the bottom barrier has a dominant effect on the overall structure at high fields and the top interface can be thought of as an ohmic contact. The corresponding circuit diagram of the whole heterostructure in which all electrical components are arranged is sketched in Figure 7.5. The leaky KNN oxide is modelled as a capacitor with a resistor in parallel, while the Schottky diode lies at the bottom interface.

By applying a bias, the forward or reverse modes are determined by the modulation of the depletion layer formed in the semiconductor near the interface, which can in turn be modelled as a differential capacitance C_{diff}.

$$C_{diff} = \sqrt{\frac{q\epsilon_s N_d}{2\left(\phi_i - qV_a\right)}} \tag{7.3}$$

where $V_a = V_{metal} - V_{semicond} = V_{Pt} - V_{KNN}$, while ϵ_s and N_d are the dielectric constant and number of charge donors of the semiconductor, respectively. In the present case, $V_{TB} = -V_a$,

therefore, assuming that an ohmic contact is present at the top interface:

$$C_{diff} = \sqrt{\frac{q\epsilon_s N_d}{2\left(\phi_i + qV_{TB}\right)}} \tag{7.4}$$

$$\phi_i + qV_{TB} = \frac{q\epsilon_s N_d}{2} \cdot \frac{1}{C_{diff}^2} \tag{7.5}$$

From Equation 7.4 it can be seen that the capacitance is bias-dependent, which reflects the presence of a space charge at the metal-semiconductor junction. The capacitance C_{diff} increases for $V_a > 0$ ($V_{TB} < 0$) towards the flat-band condition, and decreases for $V_{TB} < 0$.
In order to experimentally verify this capacitive behaviour, an analysis of small signal capacitance acquired by measuring the frequency-dependent impedance of the equivalent RC circuit was carried out, and a representative result on Ti-KNN is shown in Figure 7.6a. The capacitance slightly decreases with frequency, as expected, and is strongly decreases upon application of $V_{TB} > 0$ (reverse bias). A similar trend was observed also for Ni-KNN and Pt-KNN, as can be seen in Figure 7.6b, comparing the small signal capacitances of the three samples for the representative voltages of 0 V and 1 V. Besides, the Figure also shows that Pt-KNN has a smaller capacitance with respect to Ti- and Ni-KNN.
By extracting the capacitance values at low frequency, a linear trend was found in $1/C^2$ as

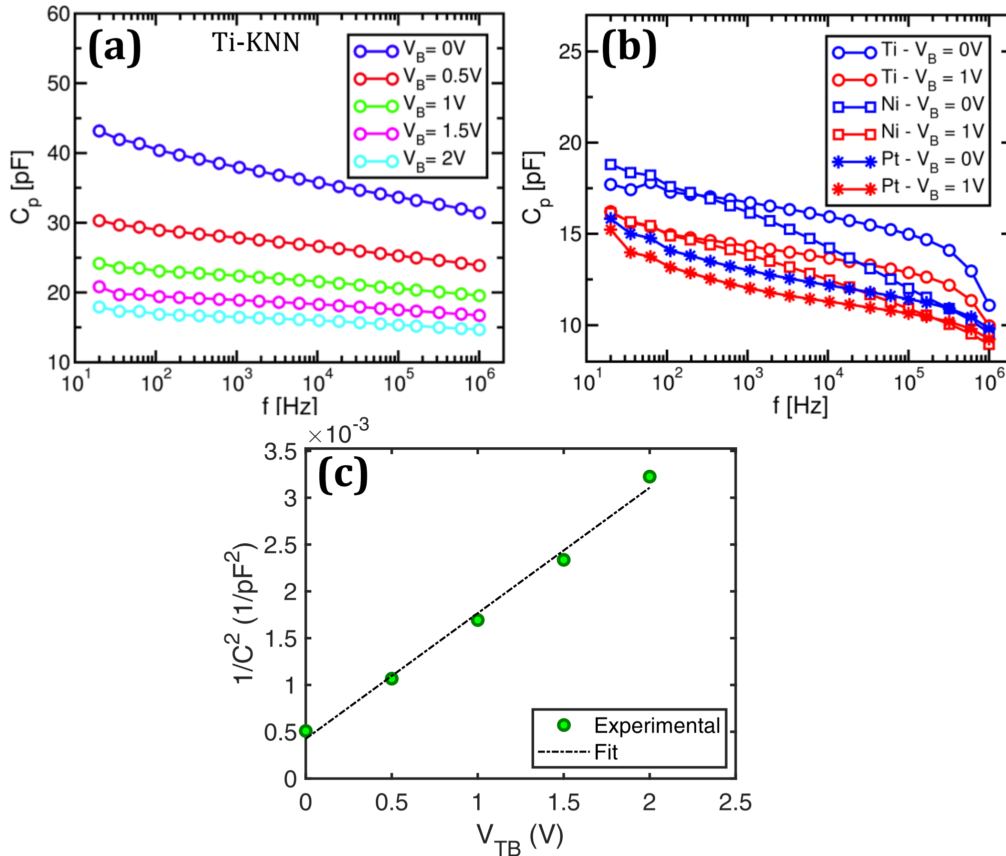

Figure 7.6: *(a) Small signal differential capacitance for Ti-KNN in top-bottom measurement at various applied biases. (b) Average comparison of small signal capacitances for Pt-, Ni- and Ti-KNN. (c) The evaluated $1/C^2$ trend at zero frequency is linear with the applied bias, coherently with the model.*

a function of the applied bias V_{TB}, as expected for a Schottky diode differential capacitance

C_{diff} in Equation 7.5 (Figure 7.6c). This means that for $V_{TB} > 0$, in the reverse bias condition, most of the applied voltage difference experimentally drops onto the depletion layer capacitance C_{diff}. As a consequence, the measured capacitance of the circuit in Figure 7.6a is not the one related to the oxide, but the one related to the depletion layer at the Schottky barrier, which is responsible for the dependence on the applied bias. Moreover, a ϕ_i on the order of 0.5 eV is found from the fit, which is not very high as would be expected from the model, but in a real metal-semiconductor contact the presence of surface states at the interface can pin the Fermi level and reduce the effective barrier [200, 201].
These findings support the assumption that the "diode-like" barrier is positioned at the bottom interface: if it were at the interface with the top metal contact, the model would work the other way around, with a reverse bias condition under negative applied V_{TB}, and forward bias condition for positive V_{TB}.

A possible explanation to why no barrier at the top is clearly visible can lie in the fact that the top and bottom interfaces were created in different conditions: at the bottom, Pt was annealed in vacuum for 30 minutes before the growth of KNN, and the growth of the oxide itself was performed in partial oxygen atmosphere (220 mTorr); instead, the top interface was created by the *ex-situ* deposition of the top electrode materials, and no specific annealing of the samples was performed before the measurements, in order to avoid the activation of metal interdiffusion phenomena and/or alkali volatilization. Therefore, in correspondence of the untreated top interface it seems reasonable to assume the possible presence of a heavy doping by charged defects, e.g. oxygen vacancies, that are sources of intra-gap surface states that significantly reduce the effective barrier, up to the extreme case of the creation of an ohmic contact [200, 203, 204]. In particular, because of its high reactivity, Ti is expected to induce a higher density of oxygen vacancies (and thus of donor defects), which are sources of free electrons promoting the n-type behaviour of the semiconductor. This amount of oxygen vacancies is also expected to be responsible for the increased capacitance measured in Ti-KNN with respect to Ni- and Pt-KNN, as C_{diff} also depends on the concentration of donors/acceptors (Equation 7.3). In fact, as mentioned in the previous paragraph, Pt-KNN shows a lower capacitance with respect to Ti- and Ni-KNN (Figure 7.6b), likely due to its limited chemical reactivity with oxygen (enthalpies of formation of oxides of Pt, Ni and Ti are -80, -240, -945 kJ/mol in standard conditions).

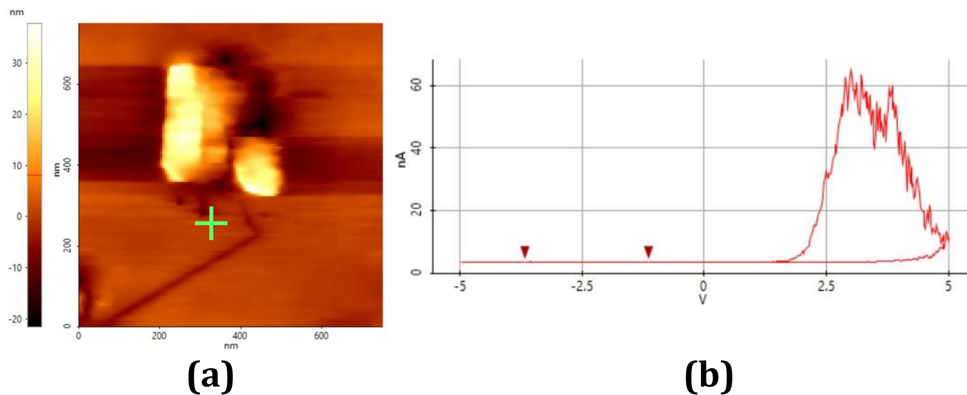

Figure 7.7: *(a) Topography scan with green cross indicating the position at which the local I(V) was acquired (i.e. on a flat defectless surface position). (b) CS-AFM I(V) current curve acquired with a bias $V_{sample} = 5$ V. Conduction is impaired on the left side and promoted on the right side, coherently with the model. The opening of conduction allows for the switching mechanism to occur.*

Evidence of the strong asymmetry in current profiles is also revealed by CS-AFM measurements shown in Figure 7.7. Local I$-$V curves were acquired by applying a voltage bias

to the sample V_{sample} with a grounded AFM conductive tip, so that in the present picture $V_{sample} = -V_{TB}$. As can be seen, the same kind of asymmetric behaviour is observed in Figure 7.7b collected in correspondence of the green cross in Figure 7.7a (with the conductive branch being for positive sample biases, coherently with $V_{sample} = -V_{TB}$). Because in this case the top electrode interface is defined by the AFM tip, which is only a few atoms large, very small areas can be probed. Such a highly localized measurement allows to collect a signals filtering through many large-area leakage current contributions, so that ferroelectric switching is not masked by other current transport phenomena and can be measured. Only for $V_{sample} > 0$ switching behaviour is observed, while for opposite biases the measured current is close to zero. This is in agreement with the suggested model, since the diode at the bottom Pt interface is in reverse mode for $V_{sample} < 0$ and stores the whole voltage drop.

As regards the top-top configuration, the equivalent circuit which derives from the proposed model is sketched in Figure 7.8. When a bias is applied between two top electrodes, the relatively small thickness of the thin film allows for the current from one top electrode to reach the Pt at the bottom through the oxide and one "diode-like" barrier, and subsequently reach the second top electrode through the corresponding second part of the circuit. Symmetric trends are observed in all three samples (see Figure 7.2b) with similar leakage values to the right branch of the top-bottom measurements (reverse bias condition). This is explained by the fact that independently of the bias polarity, in the top-top configuration there is always one of the two diodes at the bottom interface which is in reverse mode. Thus, most of the applied voltage drops across this diode, hampering the charging of the KNN oxide capacitance and the passage of most of the leakage current.

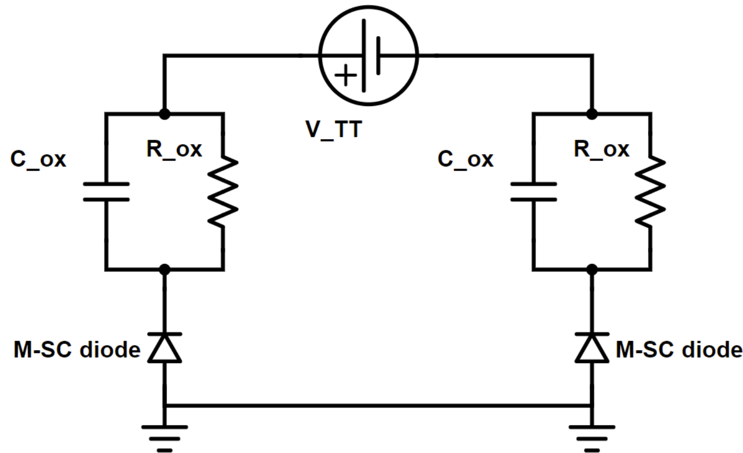

Figure 7.8: *Electrical circuit diagram of the top-top configuration. Whatever the sign of the applied V_{TT}, there is always a reverse bias diode that absorbs the majority of the voltage drop.*

7.4 Schottky emission-controlled charge injection at top interface

When considering the high-field regime for $V_{TB} < 0$, all curves for different samples appear to assume a similar behaviour below -50 kV/cm (see Figure 7.2a), which seems to indicate the presence of a common conduction mechanism. In this configuration, the diode at the bottom interface is in the forward bias condition, thus the electronic charges are able to migrate across the barrier according the polarity of the field, i.e. towards the bottom Pt. Therefore, it seems reasonable to assume that for $V_{TB} < 0$ the high-field predominant phenomenon is regulated

by an emission process of either electrons at the top interface or of negative charges within the oxide itself. The primary high-field conduction mechanisms in oxide thin films corresponding to said processes are Schottky and Poole-Frenkel emission phenomena [205]. In the Schottky emission process, the electrons in the metal overcome the energy barrier at the metal-oxide interface by thermal activation. In the present case, according to the polarity of the field the possible presence of a Schottky emission would be related to the top interface, in which, as discussed in the previous paragraph, no "diode-like" barrier is observed. This interface was previously assumed as an ohmic contact since it does not influence the conduction asymmetry determined by the bottom interface. However, this assumption can be relaxed in this case to account for a Schottky emission at large negative bias: indeed, the presence of an effective barrier between the top electrode and the KNN oxide can be suggested to describe the phenomenon, thus considering for the top interface a model like the one sketched in Figure 7.9a. Note that this is not in contrast with the assumption of an almost ohmic top contact, as this can arise from a thin barrier due to a large carrier concentration, in the present case due to oxygen vacancies created by the scavenging action of top electrodes. Charge injection through this barrier can become a limiting factor at high bias.
On the other hand, in the Poole-Frenkel process electrons (or mobile negatively charged defects) are emitted from traps in the dielectric thanks to a field-induced reduction of their potential barrier. In this case, oxygen vacancies can be considered as one of the possible negatively charged defects whose mobility can be activated by an external electric field. The corresponding model is sketched in Figure 7.9b.
In order to identify a possible current transport phenomenon able to describe the experimentally

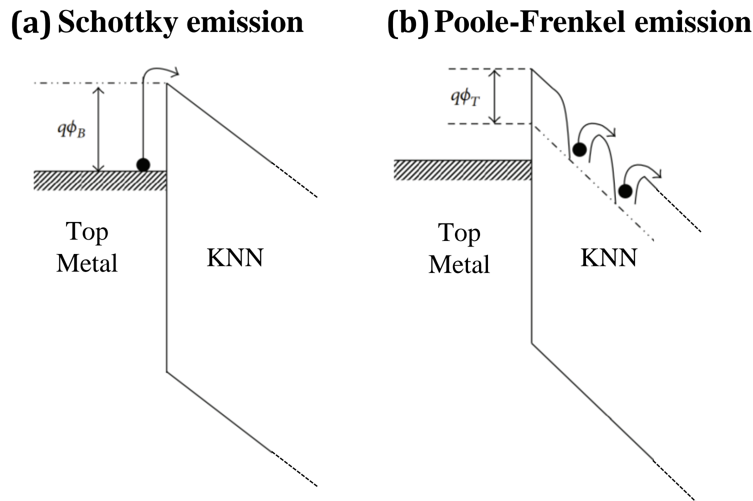

Figure 7.9: *Sketch of the suggested model to account for (a) Schottky and (b) Poole-Frenkel emission phenomena, assuming the presence of an effective barrier at the top interface. Adapted from [205]*

observed trend, the theoretical expression of both mechanisms was considered. The expression for the Schottky emission process is:

$$J = A \cdot E \exp\left\{ \frac{-q\left(\Phi_B - \sqrt{qE/4\pi\epsilon_r\epsilon_0}\right)}{k_B T} \right\} \tag{7.6}$$

where A is a theoretical coefficient (depending on the electron mobility in the oxide, the temperature, the theoretical and effective electron masses), Φ_B the Schottky barrier and ϵ_r the optical dielectric constant. The model holds under the assumption that the electron mean free path l

is smaller than the thicknes t_o of the oxide, i.e. $l < t_{ox}$, which seems reasonable for ∼300 nm KNN thicknesses. The expression for the Poole-Frenkel emission process in which the electrons will be emitted from traps in the dielectric thanks to a field-induced reduction of their potential barrier is:

$$J = B \cdot E \exp\left\{ \frac{-q\left(\Phi_T - \sqrt{qE/\pi\epsilon_r\epsilon_0}\right)}{k_B T} \right\} \tag{7.7}$$

where B is a theoretical coefficient (depending on the electron charge and mobility in the oxide, and on the density of states in the conduction band) and Φ_T is the trap barrier. The frequency-independent optical dielectric constant is used in both cases under the hypothesis that the electron transit time during the emission event is shorter than the dielectric oxide relaxation time, thus the oxide does not have enough time to be polarized.

Since both expressions contain the term ϵ_r, which is a measurable physical quantity, a fit was performed with the experimental data to extract a value for ϵ_r. It was found that only when considering the expression of the Schottky emission the extracted value for $\epsilon_r = 5.04$ inside the exponential and of the refractive index $n = \sqrt{\epsilon_r} = 2.24$ are in agreement with values retrieved from literature [206, 207]. This was done by considering the slope M of the plot $\ln(J/E)$ as a function of $\sqrt{E}$ in the regime of interest (i.e. $E < -50$ kV/cm):

$$M = \frac{d \ln\left(J/E\right)}{d\sqrt{E}} = \frac{q}{k_B T}\sqrt{\frac{q}{4\pi\epsilon_r\epsilon_0}} \tag{7.8}$$

The same experimental value of $M = (6.51 \pm 0.2) \cdot 10^{-4}$ was computed for all three Metal-KNN samples as shown in Figure 7.10, and in this way both ϵ_r and n were extracted from M. Besides, the intercept Q of the $\ln(J/E) - \sqrt{E}$ plot contains the effective barrier height Φ_B:

$$Q = \ln\left(A\right) + \left(-\frac{q}{k_B T}\Phi_B\right) \tag{7.9}$$

As previously stated, in a simple model not considering interface states Φ_B depends on the metal work function Φ_{WF} ($\Phi_B = \Phi_{WF} - \chi_{KNN}$), and as a consequence a trend in the intercept of the "Schottky-saturated" leakage current with the metal work function in observed in Figure 7.10, considering that $\Phi_{WF}^{Pt} \sim 5.01$ eV, $\Phi_{WF}^{Ni} \sim 5.01$ eV, $\Phi_{WF}^{Ti} \sim 4.33$ eV. The intercept increases in absolute value with increasing metal work function, which is an additional confirmation of electrode-dependent Schottky mechanism.

Therefore, at the top interface a work function-dependent Schottky barrier is observed that controls charge injection into the oxide below -50 kV/cm. At the same time, no formation of "diode-like" depletion layer and consequent differential capacitance is observed, likely because of the diffuse presence of a high number of acceptor/donor surface impurity states at the untreated top interface, many of which are possibly originated by oxygen vacancies. As a result, the voltage drop across the KNN thin film is only regulated by the diode at the bottom interface, allowing for conduction only in forward mode, i.e. for negative biases.

These observations highlight the importance of interface engineering, in addition to KNN material engineering, in achieving the desired functional properties. As a matter of fact, the presence of a Schottky diode found at the bottom interface is detrimental for device performances because it hinders the voltage drop across the KNN capacitor, and thus polarization switching is not favoured for reverse bias. At the same time, the reactivity of the electrode material is an important factor to consider in device design, as a high reactivity with oxygen can determine an increase in leakage currents, likely due to the creation of oxygen vacancies. As a matter of fact, these vacancies constitute additional mobile charges that can significantly

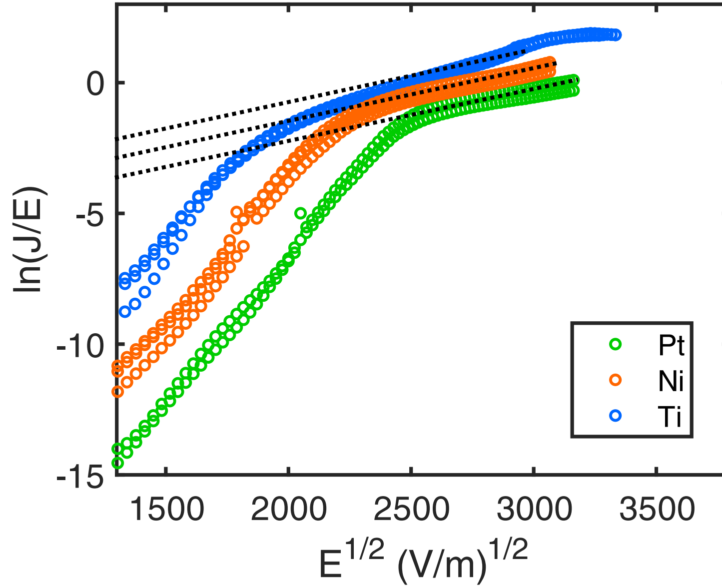

Figure 7.10: *Plot of* $\ln(J/E)$ *as a function of* $\sqrt{E}$ *for negative* V_{TB}. *A linear behaviour with the same slope is observed for all Metal-KNN samples, with a trend of the intercept with the metal work function, indicating a Schottky-controlled charge injection phenomenon.*

contribute to n-doping the material and determining its semiconductor rather than pure dielectric behaviour. In light of these observations, to avoid the asymmetric behaviour of the current ohmic contacts should be desired at both interfaces of the oxide thin film, so that no additional barrier is formed and the majority of the applied voltage bias drops on the KNN film. Moreover, electrodes with low reactivity should be used, either noble metals or also conductive oxides, to prevent the formation of oxygen vacancies near the interfaces.

7.5 Conclusions

A characterization of I$-$V leakage current curves was carried out on KNN/Pt thin film samples with different top electrode metals: Ti, Ni, Pt. A model was proposed to account for the asymmetric behaviour with respect to the applied bias in top-bottom mode, considering the KNN as a semiconductor and the presence of a Schottky diode at the bottom interface. In reverse mode i.e. for positive applied V_{TB}, all of the applied voltage drops onto the diode, impairing conduction (and ferroelectric switching) through the KNN thin films. The observed voltage dependence of the small-signal capacitance confirms the existence of a differential capacitance at the bottom interface generated by the depletion layer in the semiconductor.
In forward mode ($V_{TB} < 0$), conduction across the oxide occurs, and a predominant Schottky emission process attributed to the top interface was identified below -50 kV/cm by fitting the theoretical expression with the experimental optical dielectric constant. Since Schottky emission depends on the Schottky barrier height, which in turn depends on the metal work function, the observed trend of leakage current magnitude was correlated with the barrier of the Schottky emission process. The low leakage symmetric behaviour observed in the top-top configuration was also explained in terms of the intrinsic constant presence of a reverse bias diode at the bottom interface.
Finally, the importance of interface template engineering in optimizing a ferro- or piezoelectric heterostructure for optimal device performances was discussed. The desired suppression

of asymmetric conduction mechanisms is achievable by optimizing the interfaces with ohmic contacts, preventing the formation of an interface diode that accomodates most of the voltage drop and impairing ferroelectric switching. Besides, the formation of oxygen vacancies should be prevented by choosing low-reactivity contacts such conductive oxides, which do not have a scavenging action on oxygen nor give rise to interfacial rectifying barriers.
Generally speaking, Pt metal was found to display a proper behaviour both thanks to its high work function and because the low chemical reactivity. These properties hinder the formation of interface surface charges and oxygen vacancies within the oxide which strongly affect charge transport and are detrimental for device performances. At the same time, Ni was found to be a potential suitable cheaper candidate to replace expensive Pt, which is an encouraging result towards process cost reduction. As a matter of fact, Ni-KNN samples display a solid reproducible behaviour in leakage currents and Ni features a high work function and lower reactivity with respect to Ti.

CHAPTER 8

Strategies for stabilizing the polar phase in $Hf_{0.5}Zr_{0.5}O_2$ thin films

8.1 Introduction

Due to its unexpected ferroelectricity at nanometer scale and outstanding advantage of complementary metal-oxide-semiconductor (CMOS) compatibility, the ferroelectricity in doped HfO_2 material has attracted a lot of interest from research in recent years, as it enables the widespread application of non-volatile ferroelectric memories [208]. The majority of research on this novel class of ferroelectrics, however, focuses on polycrystalline thin film samples grown by ALD that contain different types of phases, such as the monoclinic *P21/c* phase, the tetragonal *P42/nmc* phase and the orthorhombic *Pca21* phase [209, 210, 211].
A thorough structural characterization is further complicated by the fact that the size of crystallites is considerably small and that these structures appear very similar to one another. As a consequence, in order to investigate the causes of ferroelectricity, well-oriented samples, ideally in a single phase, would be desirable. Some works reported on epitaxial Y-doped HfO_2 films on ZrO_2 substrates grown by PLD that displayed the polar orthorhombic phase and a polarization of up to 16 μ/cm^2, which constitutes an encouraging result in the field [105, 212, 213].
In this Chapter, PLD growth technique is used to grow highly oriented epitaxial $Hf_{0.5}Zr_{0.5}O_2(111)$ with a perovskite $La_{0.7}Sr_{0.3}MnO_3$ buffer layer also serving as a bottom electrode. This work was carried out in a different system with respect to the growth of KNN relative to the previous Chapters. The two systems are however comparable in their technical characteristics and components, with the exception of the laser, which is a KrF excimer laser in this case and can provide pulses of smaller wavelength (248 nm) with respect to the Nd:YAG laser without the need of non-linear crystals for the generation of harmonic wavelengths (266 nm for the fourth harmonic of Nd:YAG).
In order to understand how strain affects the ferroelectricity in hafnia-based thin films, first, the PLD growth process is established and optimized for HZO(111)/LSMO(001)/STO(001) heterostructure. Different HZO thicknesses in the range of $3-18$ nm are then characterized and

compared to identify the highest thickness with a stable polar phase. Afterwards, different strategies are adopted with the aim of increasing the HZO cell volume to further stabilize the polar phase and increase the ferroelectric remanent polarization. First, the effect of increasing the amount of oxygen vacancies in the HZO/LSMO system is investigated by introducing a vacuum annealing and cooling after the growth of the heterostructure. As a matter of fact, the distortion from oxygen vacancies is able to generate an increase in the volume of the lattice cell. Moreover, oxygen vacancies are able to migrate at interface between HZO and LSMO and create conducting monolayers of Hf and Zr to improve screening effect. As a second strategy, the engineering of lattice stress on the properties of HZO thin films is investigated by optimizing the growth of HZO/LSMO onto $DyScO_3$ (DSO) substrate, which presents a higher lattice parameter than STO.

8.2 Experimental Methods

- **Thin film deposition:** Thin film samples were grown by PLD onto (001)-oriented $SrTiO_3$ (STO) substrates. First, a buffering layer of perovskite $La_{0.7}Sr_{0.3}MnO_3$ (LSMO) conductive oxide, also serving as a bottom electrode, was deposited on the STO substrate. The growth was performed by ablating a polycrystalline LSMO target with a KrF excimer laser with 248 nm wavelength at a frequency of 2 Hz and a laser fluence of 1 J/cm^2. The substrate was kept at a temperature of 775°C in a 0.15 mbar oxygen atmosphere at a distance of 50 mm from the substrate. The targeted thickness of LSMO thin films was around 40 nm. Afterwards, $Hf_{0.5}Zr_{0.5}O_2$ thin films of thicknesses ranging from 3 to 18 nm were grown on top of the LSMO layer. A stoichiometric HZO ceramic target was employed, and the following growth parameters were used: laser frequency of 2 Hz, fluence of 1.1 J/cm^2, substrate temperature 800°C, oxygen pressure 0.1 mbar. After the growth, the samples were cooled down to room temperature with a controlled rate of -5°C/min in a 300 mbar oxygen atmosphere.

- **Structural characterization:** XRD was used to determine the orientation and structure of the thin film heterostructure employing a Panalytical X'pert Pro diffractometer (Cu Kα source with wavelength 1.54 Å) with a 1/4° anti-scatter slit and a 7.5 mm detector slit. The high-resolution line focus mode was employed to perform $\theta - 2\theta$ scans and Reciprocal Space Maps to determine lattice orientation and parameters. High-intensity point focus mode was used to build pole figures of the samples by scanning the azimuthal and tilt angles of the sample plane, while keeping the detector fixed at the particular Bragg reflection of interest, which in this case was that of the polar orthorhombic HZO located at around 30°.

- **Electrical measurements:** Top electrode circular pads of diameter 50 μm and thickness 50 nm were fabricated by defining the shapes with a photolithographic process with a silver mask and afterwards depositing a Au thin film by e-beam evaporation. A lift-off process in acetone with low-power ultrasound sonication removed the excess Au. The Au/HZO/LSMO capacitors defined in this way were characterized by means of a ferroelectric tester (AiXACCT, TF analyzer 2000) in both DHM and PUND mode to examine and compare the ferroelectric response of the thin films.

8.3 Growth and Characterization of HZO/LSMO/STO thin films

To compare the properties of different thicknesses of HZO, a PLD growth process was established for the bottom electrode LSMO (40 nm) and then HZO, and different samples were

prepared featuring HZO thin film thicknesses ranging from 3 to 18 nm. Figure 8.1 shows AFM topographic scans of a lowest thickness (3 nm) and highest thickness (18 nm) HZO sample surfaces. No outgrows nor sign of splashing from the target are observed, and the overall thin film surface appears compact and flat with increasing thickness. A slight increase in the roughness R_{rms} with thickness is evidenced in Figure 8.1c, but all samples display a value of R_{rms} of few hundreds of picometers, indicating the high quality of the epitaxially-grown thin films.

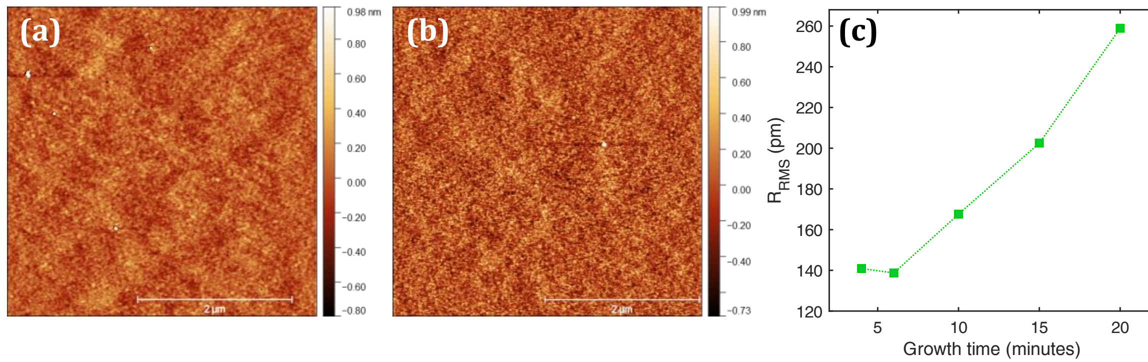

Figure 8.1: *AFM topographic scan of (a) 3-nm HZO and (b) 18-nm HZO, showing coherent 2D growth and crystal ordering at different thicknesses. (c) Evaluation of the average roughness trend with thickness.*

The crystal structure of different thicknesses was compared by XRD. Diffraction patterns collected from $\theta - 2\theta$ line scans are shown in Figure 8.2a. The peak with the highest intensity located at 22.7° belongs to the (001)-oriented STO substrate, and the peak at 23.1° by its side marks the (001) reflection of the epitaxially-grown LSMO buffer layer. The larger peak at 30° with Laue fringes is attributed to the main Bragg reflection of the orthorhombic phase of (111)-oriented HZO thin films, which is at slightly smaller 2θ values with respect to other results from literature [113]. This is an indication of an expanded out-of-plane (111)-spacing, which in this

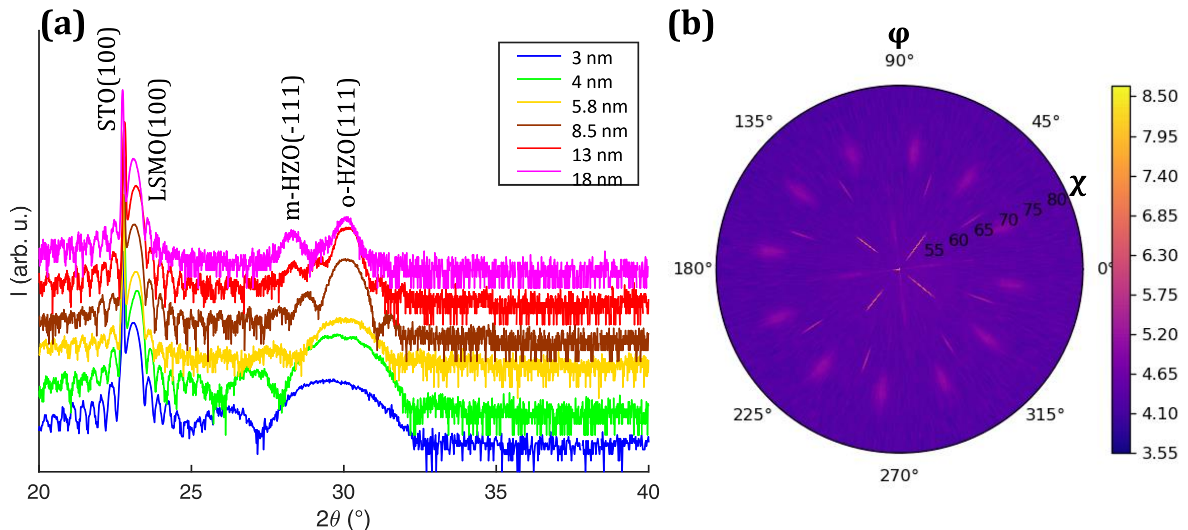

Figure 8.2: *(a) XRD $\theta - 2\theta$ patterns of HZO/LSMO/STO heterostructure with different HZO thicknesses. Epitaxial growth of LSMO and HZO is confirmed, with orthorombic o-HZO stabilized at low thicknesses (< 10 nm) and monoclinic m-HZO developing at higher thicknesses (> 10 nm). (b) Pole figure of 8.5 nm-HZO collected at the HZO(111) peak at $2\theta = 30°$. 12 peaks from (111) in-plane directions are detected, indicating the presence of 4 reciprocally perpendicular crystallographic domains.*

case is calculated to be $d_{111} = 2.98$ Å. Besides, an evident trend of the shape and position of the peak is observed as a function of the thickness of the HZO thin film: at lower thicknesses, the orthorhombic peak is significantly wider and located at smaller 2θ values than 30°, indicating highly elongated unit cells with a larger d-spacing. At higher thicknesses, above around 10 nm, the appearance of the monoclinic phase is revealed by the presence of a peak at 28.3°, confirming the stabilization of this phase at greater crystal sizes. This phase appears at higher thicknesses as a result of the relaxation and relief of the internal pressures developed by the HZO crystallites in the elongated polar orthorombic unit cell phase. In this sense, the best compromise of the available samples between the degree of orthorhombic (111) orientation and reduced in-plane compressive strain is identified as 8.5 nm, which will be employed as standard thickness for the investigations described in the next Sections.

Since the XRD scans show a (111) orientation of the films, pole figure measurements were performed at the orthorhombic (111) peak at an angle $2\theta = 30°$ on the 8.5 nm thick film. The azimuthal (ϕ) and tilt (χ) were varied continuously to acquire information on the in-plane orientation of the crystalline HZO film. The results in Figure 8.2b show that instead of the three in-plane reflections from the (-111), (1-11) and (11-1) planes which are expected from a single domain film at $\chi \sim 71°$ and at 120° distance from one another in the ϕ angle, 12 reflections are found at $\chi \sim 71$, separated by $\Delta\phi = 30°$. This suggests the presence of four crystallographic domains with defined in-plane orientation, i.e. rotated by 90° with respect to each other, coherently with the 4-fold symmetry of the (001) template. The most intense peaks located at $\chi \sim 54°$ and $\chi \sim 66°$ are due to a spurious signal caught from STO(001) reflections with 4-fold multiplicity, possibly due to the large dimension of the used slit.

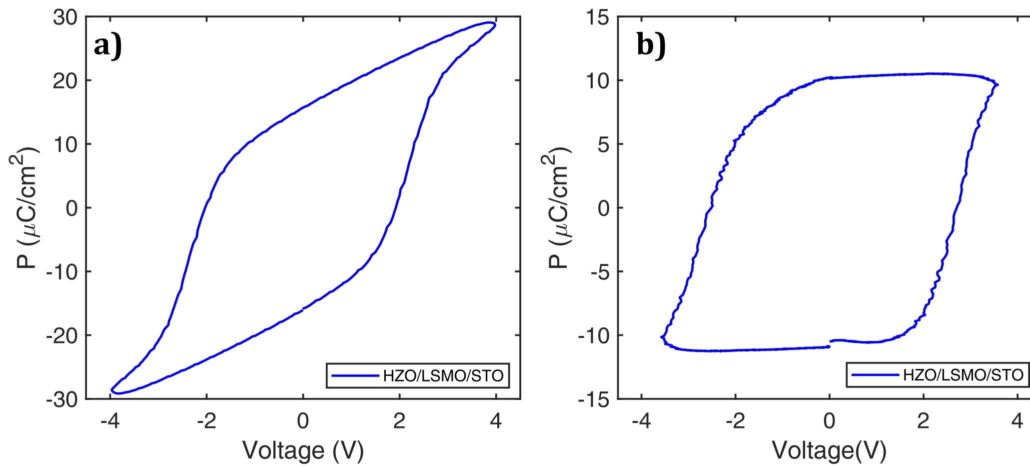

Figure 8.3: *Ferroelectric hysteresis loop from (a) DHM and (b) PUND (remanence) measurements of Au/HZO/LSMO capacitor devices.*

Ferroelectric measurements were performed to fully characterize 8.5 nm samples with Au circular electrodes of diameter 50 μm fabricated by photolithography and e-beam evaporation. Figure 8.3a shows the P−V loop obtained from a Dynamic Hysteresis Measurement at 1 kHz. Bistable symmetric switching may be seen at a coercive field of 2.5 MV/cm, which is somewhat larger than the observed one for similar ALD-grown HZO [107], possibly due to the influence of the clamping effect of the substrate on the strained film. The observed saturation polarization P_{sat} is 28.8 μC/cm^2, while $P(0) = 15.9$ μC/cm^2. The hysteresis loop at remanence collected from a PUND measurement at 1 kHz is shown in Figure 8.3b obtained after removing the non-switching component, and a remanent polarization P_r of 10.2 μC/cm^2 can be observed.

Moreover, Figure 8.4a and 8.4b of I−V loops and P−V loops, respectively, obtained by cycling at 1 kHz under a 4 V applied voltage show that the ferroelectric switching response of the thin films is able to endure up to 10'000 cycles before becoming leaky. Therefore, the overall endurance of the device should be further optimized likely by domain or interface engineering to improve its performances [214]. The coercive field remains stable over the cycles, while the remanent polarization and switching current slightly increase between 10 and 100 cycles, hence indicating a slight wake-up effect that is sometimes observed for HZO and other ferroelectric thin films such as PZT [215, 216, 217].

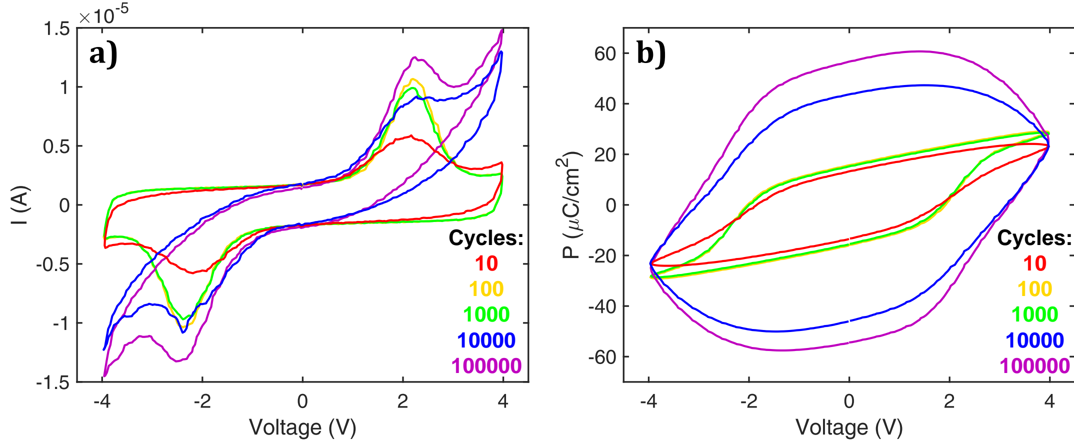

Figure 8.4: *Cycling tests of 8.5 nm-HZO with Au top electrodes. The devices show an endurance of up to 10'000 cycles. Current hysteresis is plotted in (a), and corresponding polarization loops are shown in (b).*

8.4 Effect of oxygen vacancies on HZO/LSMO/STO by post-growth vacuum annealing

Having selected 8.5 nm as a target thickness for comparative studies with different methods, the first approach adopted with the aim of stabilizing the polar orthorhombic phase of HZO is to willingly introduce a certain amount of oxygen vacancies in the HZO/LSMO system. This is achieved by performing an *in-situ* annealing in vacuum of the as-grown HZO/LSMO structure with a duration of 30 minutes at a chamber pressure of around 10^{-7} mbar, followed by a slow cooling step at a rate of -5°C/min, similarly to the standard samples.

No detectable difference in the AFM topography scans is observed in 8.5 nm vacuum-annealed and standard HZO, reported in Figure 8.5a, and the average roughness R_{rms} parameter remains almost unvaried ($R_{rms} \sim 200$ pm). Furthermore, from the comparison of XRD $\theta - 2\theta$ line scans of vacuum-annealed and standard samples (Figure 8.5b), no shift in the position of the relatively narrow LSMO peak is detected, at least not within the resolution limits of the instrument, which indicates no significant difference in the lattice strain in LSMO. This appears reasonable, given the fact that LSMO is often reported to show a certain degree of relaxation at thicknesses higher than a few tens of nanometers [218].

However, the results of the ferroelectric characterization show in the DHM hysteresis P−V loop (Figure 8.6a) a saturation polarization of 33.6 μC/cm^2 with $P(0) = 18.1$ μC/cm^2 with an increase by 17% with respect to the standard sample, while in the PUND measurement (Figure 8.6b) the remanent polarization P_r increases by 32% upto 13.5 μC/cm^2.

The observed behaviour is a further confirmation of the well-discussed fact that vacancy migration is intertwined with the ferroelectric polarization switching, as both have been reported to lead to hysteretic responses in thin film devices [219, 220]. Concerning this phenomenon,

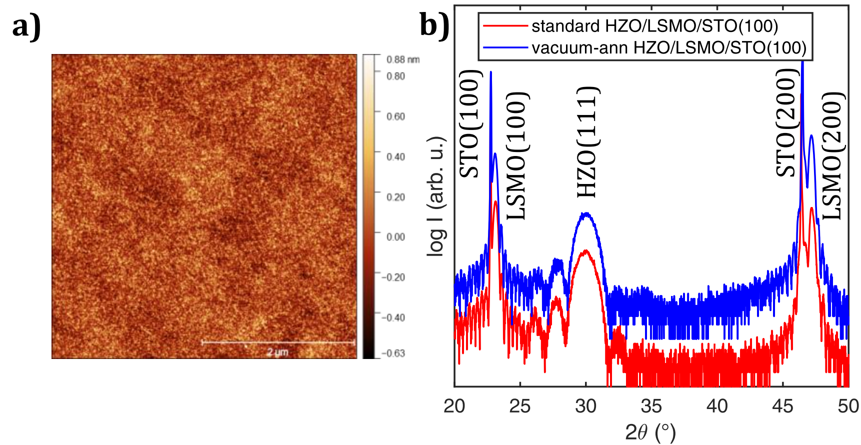

Figure 8.5: *(a) AFM topography of 8.5 nm-vacuum annealed-HZO thin film. (b) XRD scans comparing standard and vacuum-annealed heterostructures, showing no detectable phase deformations in HZO and LSMO layers.*

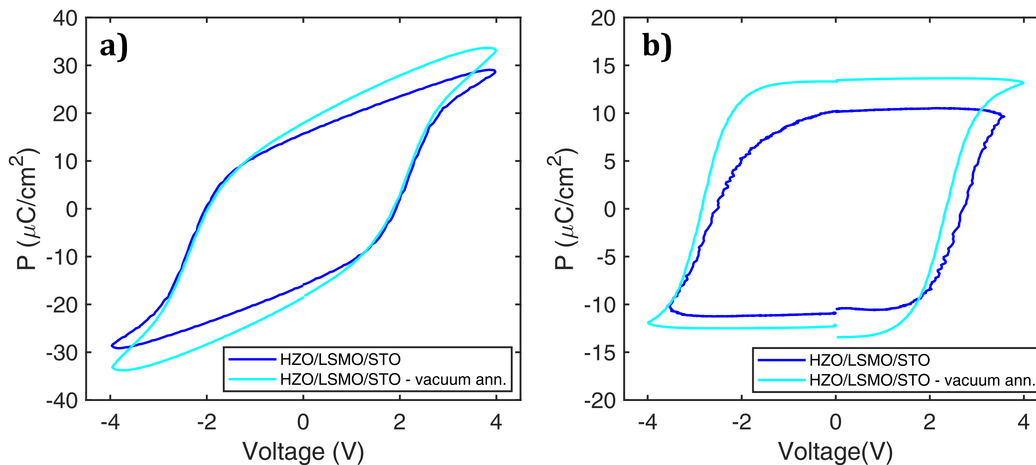

Figure 8.6: *Comparison of ferroelectric hysteresis loop from (a) DHM and (b) PUND (remanence) measurements of Au/HZO/LSMO capacitor devices with standard (blue) and vacuum-annealed (light blue) samples.*

studies on reversible migration of oxygen vacancies between the bottom LSMO electrode and the HZO thin layer have shown that both films act as source/sink of oxygen vacancies when a noble metal like Au is used as a top electrode [221]. The mutual exchange of charged oxygen vacancies through the HZO/LSMO interface and the vacancy redistribution in the bilayer upon cycling is associated to a hysteretic behaviour that concurs with actual ferroelectric switching. Besides, the structural modifications operated by oxygen vacancies can create local distortions in the cell volume (although this is not visible by XRD) up to generating phase transitions and/or stabilizing a specific phase in HZO upon voltage cycling [222]. In this sense, the results on the vacuum-annealed HZO/LSMO samples seem to suggest an oxygen vacancy-mediated stabilization of the orthorhombic phase in the HZO thin film. Some further investigations by TEM analysis could possibly unveil the origin, position and migration dynamics of oxygen vacancies between the two oxides through the interface. This could also help attribute with more precision the effect of vacancies on ferroelectric switching to either an extra "spurious" current contribution that gets integrated with the dipole switching current or to an increase in "pure" ferroelectric polarization due to an increase in charge separation of the single microscopic dipoles.

Nevertheless, this result is coherent with other results from literature suggesting that oxygen defects can affect both the crystalline phase and the performance of devices in undoped and doped HfO_2: as a matter of fact, simulations show that vacancies can decrease the energy of the polar orthorhombic and tetragonal phases with respect to that of the non-polar monoclinic phase while, on the other hand, the presence of oxygen interstitials encourages the t- to m-phase phase transition, thus affecting the ferroelectric properties [223, 224]. This tendency is also confirmed by some experiments carried out on sample growth with varying oxygen partial pressure and oxygen-rich annealing atmospheres which agree on the fact that higher oxygen environments correspond to increasing m-phase fractions in the film and lead to a decrease in the remanent polarization [225].
Moreover, some first-principle calculations have shown that the oxygen-deficient phases formed in the HZO, often tetragonal, can actually be conductive [226]. Since, exploiting their mobility, oxygen vacancies are able to travel to the HZO/LSMO interface, conducting monolayers of HfO_2 and ZrO_2 are locally created between the two film layers in this way. This phenomenon can sizably help enhance the electrostatic screening capability of LSMO providing a further stabilizing mechanism for the orthorhombic polar phase. Besides, the migration of vacancies towards the interface reduces the amount of defects within LSMO, improving the conductivity of the layer and the screening effect.

8.5 Engineering epitaxial stress: HZO/LSMO/DSO

Another approach towards the stabilization of the HZO orthorhombic phase involves strain engineering. This strategy has been used on a variety of materials to carefully tune the lattice structure of the desired film and hence gain control over the ferroelectric properties and the microstructure. [227, 228] Since the electrode serves as the epitaxial template on which HZO develops, the stabilization and final lattice parameter of LSMO is crucial for the stability of the epitaxial growth of HZO. In this framework, the choice of the substrate becomes essential as a method to finely control the properties of LSMO and in turn those of HZO, because the overall strain in the heterostructure will ultimately be determined by the specific lattice mismatch with the substrate crystal. Whenever the substrate lattice parameter is larger than that attributed to the relaxed, bulk LSMO ($a_{LSMO,b} = 3.874$ Å), tensile strain will develop, while compressive strain will form in the opposite case. At the same time, the choice of too large of a lattice mismatch with respect to LSMO will cause the system to relax and the impossibility for strain, whether it is tensile or compressive, to build up in the system. Therefore, the choice of the substrate for the heterostructure and its lattice mismatch with LSMO should be carefully evaluated, and in view of increasing the lattice cell volume of LSMO and HZO to stabilize the polar phase, tensile strained LSMO should be targeted. Among the commonly available set of popular substrates, the family of scandate oxides appears as an interestingly suitable candidate due to its relatively larger pseudocubic lattice parameter with respect to that of simple cubic STO as shown in Table 8.1.
Among the scandates, $DyScO_3$ (DSO) was chosen as a starting point, since a lattice mismatch of $100 \cdot \frac{a_{sub}-a_{LSMO,b}}{a_{LSMO,b}} = 1.85\%$ appears as a reasonable value for the preservation of LSMO in its unrelaxed, strained state.

DSO naturally comes with a double-terminated surface, with a mixture of DyO and ScO_2 terminations at the surface that can result in differences in the physics of thin film nucleation. To account for this issue, a sample of HZO/LSMO was grown on untreated double-terminated DSO and another on treated single-terminated DSO for comparison.
The treatment steps [229] take into account the miscut angle, as single crystal substrates are

Material	a (Å)	b (Å)	$a_{PC} = 0.5\sqrt{a^2 + b^2}$ (Å)
$SrTiO_3$	3.905	-	-
$DyScO_3$	5.440	5.717	3.946
$TbScO_3$	5.466	5.731	3.960
$GdScO_3$	5.480	5.746	3.970
$SmScO_3$	5.527	5.7758	3.965
$NdScO_3$	5.575	5.776	4.014

Table 8.1: *Comparison of lattice parameter of simple cubic STO and pseudocubic lattice parameters (a_{PC}) of the scandate family. The in-plane lattice constants of the orthorhombic structure are also shown (from [130]).*

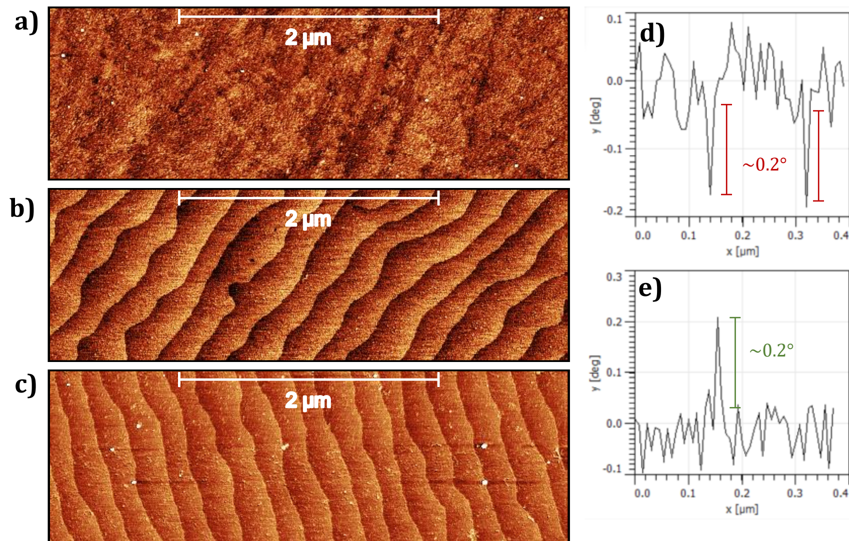

Figure 8.7: *Surface of the DSO substrate scanned by AFM for (a) untreated DSO, (b) annealed DSO, (c) annealed and etched DSO. Line scans of the (d) trace and (e) retrace phase signal of DSO after etching show opposite phase contrast at step edges but of equal magnitude, which suggests the presence of single-terminated step edges.*

cut at with a little miscut. This is either intentionally introduced to make it simpler to work with the substrates thereafter, as well as accidentally introduced because it is difficult to have a precise 0° miscut angle. The step edges resulting from the miscut angle serve as nucleation sites for substrate treatments and for the following growth of thin films. Therefore, the first step in treating the DSO substrate is to heat it in a furnace to achieve straight step edges, and this was done with an annealing process at 900°C for 5 hours in an oxygen flux of 18 L/h. As shown in the AFM topographic surface scans in Figure 8.7, the step edges are not yet visible on the untreated surface (Figure 8.7a), whereas straight step edges around 400 pm high readily appear after the annealing step in the furnace (Figure 8.7b).

Afterwards, a chemical etching step is required to selectively get rid of one of the two aforementioned terminations of DSO. This is achieved by exposing the substrate to a NaOH solution, as its reactivity is higher with DyO with respect to ScO_2. In spite of this, the overall reactivity of NaOH is generally quite low, thus the substrate was etched in a 12 M NaOH solution in ultrasound vibrations for upto 4 hours to assure single termination. To prevent particle precipitation, the 12 M solution was subsequently diluted to 1 M and etched for an extra 30 minutes. Finally, washing steps in DI water and EtOH conclude the treatment procedure. The final topography of treated DSO is shown in Figure 8.7c, with edges appearing as lines in the phase signal map. Due to the different adhesive forces experienced by the tip, the phase locally increases or decreases

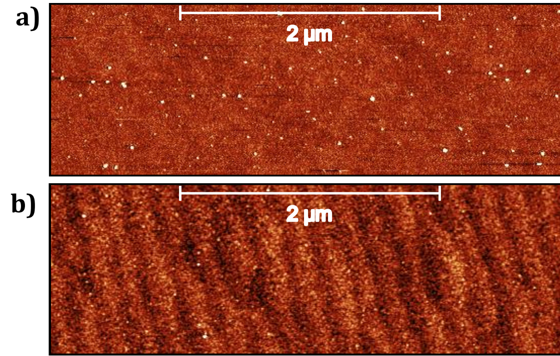

Figure 8.8: *Topography of the surface of HZO films acquired by AFM for HZO/LSMO grown on (a) untreated DSO and (b) treated DSO. Traces of particles in untreated DSO generate particulate defects in HZO, while the step-edged topography of the treated substrate is reproduced on top of HZO as well.*

in magnitude depending on the tip scanning direction, but single-terminated step edges should exhibit the same absolute value of the phase contrast (Figure 8.7d and 8.7e).

Figure 8.8 shows the resulting topography of 8.5 nm-HZO grown with LSMO on top of untreated (Figure 8.8a) and treated (Figure 8.8b) DSO. The traces of particles on the untreated DSO appear as particle defects on top of the HZO surface as well, whereas the HZO on top of the DSO appears to "follow" the step-edged topography of the substrate template.

To compare the lattice structures, XRD $\theta - 2\theta$ patterns of HZO/LSMO bi-layer on STO, untreated DSO and treated DSO is displayed in Figure 8.9a. The key factor for the growth of HZO is the lattice structure of LSMO. There is a much larger lattice mismatch of bulk LSMO with DSO (1.85%) with respect to STO (0.8%), and this results in a larger tensile strain of LSMO/DSO with respect to LSMO/STO. Indeed, the out-of-plane lattice spacing of LSMO results to be 3.84 Å for LSMO/STO and 3.80 Å for LSMO/DSO (with both untreated and treated DSO). This corresponds to a lattice out-of-plane strain of LSMO, defined as $s = 100 \cdot \frac{c_{LSMO,f} - c_{LSMO,b}}{c_{LSMO,b}}$, of -0.65% when grown on STO and -1.83% on DSO.
Reciprocal space maps of LSMO/STO and LSMO/DSO are shown in Figure 8.9b and 8.9c. The data was collected around the (103) pseudocubic lattice reflection of the substrate and LSMO. From the measurements, in-plane lattice parameters of 3.90 Å and 3.95 Å were obtained for the LSMO grown onto STO and DSO respectively, corresponding to in-plane strains of $+0.62\%$ and $+1.85\%$, coherently with the values obtained for out-of-plane spacings from $\theta - 2\theta$ scans. In contrast, the position of the HZO(111) peak near 30° in the $\theta - 2\theta$ pattern is substantially unchanged, indicating the (out-of-plane) lattice constant of LSMO has little influence on that of HZO, possibly because HZO is plastically relaxed. Further measurements would be required on the influence of LSMO structure on in-plane parameters as well to verify this hypothesis.

This tensile strain in LSMO leads to deformations in the volume of HZO cell as well, which results from ferroelectric measurements by DHM and PUND modes in Figure 8.10a and 8.10b in an increase in both the saturation polarization by upto 58% ($P_{sat} = 45.6$ μC/cm^2, $P(0) = 24.7$ μC/cm^2) and remanent polarization by 86% ($P_r = 19.6$ μC/cm^2).
This result clearly indicates the considerable impact of epitaxial stress on the general properties of a heterostructure of functional oxides. Indeed, the energy of the overall substrate + film system is significantly impacted by epitaxial stress, which can help stabilize a particular metastable phase over multiple competing possible polymorphic phases. Thus, this strategy can be exploited to achieve stabilization of unstable phases in a complex material [230, 231]. At the same time, epitaxial stress can result in elastic strain, which can alter the energy of different phases [232, 233] and have significant implications on the polarization switching responses of

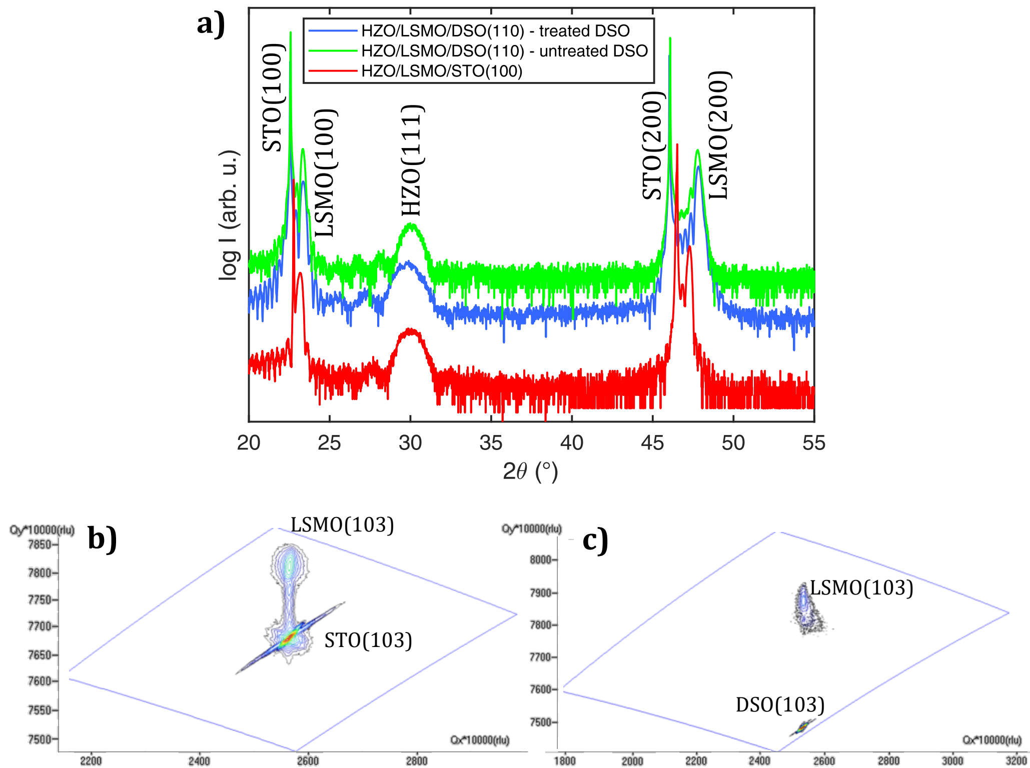

Figure 8.9: *XRD analysis of HZO/LSMO on STO and treated/untreated DSO. (a) $\theta-2\theta$ scans show an out-of-plain deformation of LSMO. RSMs of (b) LSMO/STO and (c) LSMO/DSO peaks around the (103) Bragg reflection confirm larger in-plane strain of LSMO on DSO.*

the oxide [234]. As a matter of fact, tensile strain conditions are well known to favour oxygen vacancies to form [235]. In this case, the oxygen vacancies formed in tensile-strained LSMO, similarly to the vacuum annealed samples described in the previous Section, could contribute to both polarization switching mechanisms and stabilization of the electrostatic screening effect of LSMO.

8.6 Conclusions

To conclude, it was shown that HZO thin films display low-thickness (8.5 nm) ferroelectricity with a $P_r = 10.2$ μC/cm^2, whereas the monoclinic phase stabilizes at higher thicknesses as a form of internal relief of stress, gradually substituting the orthorhombic phase. Further optimization of the growth and of the material composition could potentially increase the limit thickness for the stabilization of the polar phase.
Phase engineering can be used to achieve improved ferroelectric behaviour in thin HZO films by controlling the oxygen vacancy amount and migration mechanisms and by tuning the epitaxial (tensile) strain.
More specifically, oxygen vacancies introduced by post-growth vacuum annealing of the heterostructure can increase the HZO cell volume and improve the screening of LSMO, yielding to an improvement of the ferroelectric remanent polarization by 32%. Additional work is required for a deeper understanding of the underlying phenomenon. For example, TEM cross sectional images could help correlate with higher precision the location and amount of oxygen vacancies with the observed enhanced switching phenomenon.

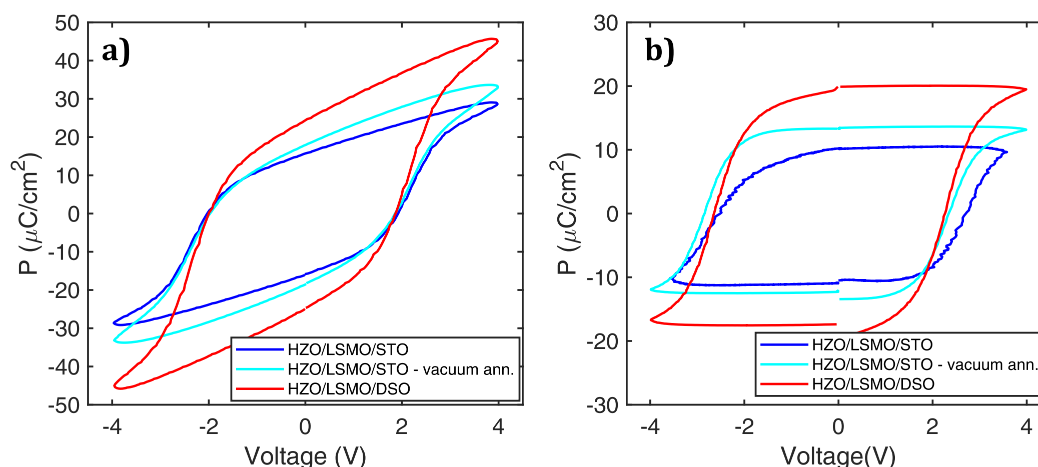

Figure 8.10: *Comparison of ferroelectric hysteresis loop from (a) DHM and (b) PUND (remanence) measurements of Au/HZO/LSMO capacitor devices: standard sample on STO (blue), vacuum-annealed sample on STO (light blue) and sample on DSO (red).*

Moreover, the strain developed in the LSMO layer is strictly influenced by the substrate template and lattice structure, and this in turn determines the properties of the HZO unit cell volume and predominant phase. With regard to these findings, further investigations on HZO/LSMO bi-layers grown on different substrate templates is strongly encouraged and can help better understand the inter-dependence between ferroelectric polarization and lattice structure.
Further work is required to explore these aspects more thoroughly both as separated refinement strategies and as a combination of vacuum annealing processes with controlled epitaxial strain engineering of the thin films. With the appropriate optimization of its ferroelectric properties, HfO_2-based devices can prove to be valid candidates for ferroelectric memory applications, in terms of both non-volatile FeRAMs and FeFETs. Notably, in FeFET devices hafnia is already well integrated as high-k gate material [57], but its ferroelectric properties can be exploited in the transistor for an efficient unification of memory and logic functions.

CHAPTER 9

Overall conclusions

The work presented in the Thesis comprised the investigation of two of the most promising lead-free materials for the replacement of PZT in ferroelectric and piezoelectric thin film processes for industrial devices.

The properties of piezoelectric (and ferroelectric) KNN thin films grown by PLD were investigated in view of developing a viable competitor to PZT for piezoelectric actuator and sensor applications. The results of the optimization of the material pointed out some of the critical aspects impacting device performances related to thin film interfaces (substrate and electrodes), composition and crystal structure.

The study of the impact of the Pt(111) substrate surface preparation on the properties KNN thin films clarified the need of substrate treatment to enhance the functional properties of the films toward the benchmark provided by PZT. In particular, *in-situ* vacuum annealing results in a significant flattening and cleaning of the Pt surface, with increased grain size and suppressed concentration of adventitious carbon and other organic residuals. This leads to a significant increase in the crystalline quality and high compactness of the thin films compared to those grown onto uncleaned substrates, with a suppression of leakage currents by one order of magnitude and the achievement of local piezoelectric coefficients of 80 pm/V comparable to the state of the art.

In the study of Li doping in KNN to investigate the effect of compositional variations, an alternative approach with respect to common techniques was presented to achieve Li doping, which involves the co-ablation of the KNN target and an appropriately sized $LiNbO_3$ slice. The observed deterioration of macroscopic functional properties upon slight (0.03at%) Li doping was suggested to be due to the diffusion of the dopant from the bulk to grain boundaries, producing local conductive channels for ionic charge migration responsible for the increase of leakage currents, in agreement with the macroscopic tendency to surface segregation of Li revealed by XPS and ToF-SIMS. According to these results, identifying the appropriate growth technique is crucial to getting a slight doping of light elements such as Li for KNN thin films, because the atomic mobility can be easily triggered in high-temperature PVD techniques with

slow growth rates. High-rate and low-temperature deposition processes in combination with quick thermal annealing treatments may be used for this purpose.

A structural analysis of epitaxial KNN thin films on Nb:STO(001) as a function of substrate deposition temperature shed light onto the correlation between electrical losses, morphological defects and chemical composition. A striking correlation between leakage current and growth temperature was found, with a strong suppression of current losses for low-temperature 3D sample growths. This trend, decoupled from morphological defects, was rather associated to charge motion caused by Na and K vacancies, due to the high volatility of the alkali elements: as a matter of fact, the alkali content was found to be close to the stoichiometric composition for lower growth temperatures. The evaporation of alkali elements at high growth temperatures was also correlated with deformations in the lattice cell and accumulation of stress in the epitaxial lattice. The observed peculiar square-shaped pattern aligned with STO [100] and [010] directions was consequently associated to a stress release phenomenon through the accomodation of strain at domain walls and misfit dislocation sites.

The importance of interface template engineering in optimizing a ferro- or piezoelectric heterostructure for optimal device performances was also discussed, by investigating I(V) leakage current curves of KNN/Pt thin film samples with different top electrode metals: Ti, Ni, Pt. A model was proposed to account for the asymmetric behaviour with respect to the applied bias in top-bottom mode, considering the KNN as a semiconductor and the presence of a Schottky diode at the bottom interface. The desired suppression of asymmetric conduction mechanisms is achievable by optimizing the interfaces with ohmic contacts, preventing the formation of an interface diode that accomodates most of the voltage drop and impaires ferroelectric switching. Besides, the formation of oxygen vacancies should be prevented by choosing low-reactivity contacts such conductive oxides, which do not have a scavenging action on oxygen. Generally speaking, Pt metal was found to display a proper behaviour both thanks to its high work function and because the low chemical reactivity. Ni was found to be a potential suitable cheaper candidate to replace expensive Pt, which is an encouraging result towards process cost reduction.

Finally, a study of HZO thin films was presented, with a focus on the enhancement of its ferroelectric properties to replace PZT in ferroelectric memory devices. Potential strategies to increase the ferroelectric polarization of HZO thin films by stabilizing the polar phase comprise the engineering of structure and substrate-dependent lattice stress. The polar orthorhombic phase is stabilized at low thickness (<8.5 nm), whereas the monoclinic phase stabilizes at higher thicknesses as a form of internal relief of stress. Phase engineering can be used to achieve improved ferroelectric behaviour by controlling the oxygen vacancy composition and by tuning the epitaxial (tensile) strain. Oxygen vacancies introduced by post-growth vacuum annealing of the heterostructure can stabilize the orthorhombic phase and improve the screening of LSMO. Additional work is required for a deeper understanding of the underlying phenomenon. At the same time, the strain developed in the LSMO layer is strictly influenced by the substrate template and lattice structure, and this in turn determines the properties of the HZO unit cell volume and predominant phase. With regard to these findings, further investigations on HZO/LSMO bi-layers grown on different substrate templates is strongly encouraged and can help better understand the inter-dependence between ferroelectric polarization and lattice structure.

This contribution to lead-free thin films synthesis, optimization and characterizations points out that, with the appropriate optimization of material properties and functional device performances, lead-free-based devices hold an interesting potential towards producing valid candidates with qualities similar to those of PZT that can be employed in reliable large-scale fabrication processes of actuator and sensor devices as well as memory and logic transistor devices.

List of Figures

1.1 Market share of various piezoelectric applications, from [8]. 2
1.2 Market revenue piezoelectric materials, 2014−2025 (USD Million), from [1]. . . 3
1.3 Sketch of the structure of (a) FeRAM, (b) FeFET and (c) FTJ devices, from [12] 4
1.4 Comparison of d_{33} piezoelectric coefficient for various classes of piezoelectric material ceramics. 9
1.5 Increase of the piezoelectric d_{33} coefficient of KNN ceramics through the years thanks to fervent research (from [48]). 10

2.1 Diagram of 32 crystal point groups. The symmetry of the crystal determines its functional properties, i.e. whether a material shows dielectric, piezoelectric, pyroelectric, ferroelectric behaviour. 18
2.2 Schematic of the different polarization mechanisms that can occur in dielectric materials depending on their nature. Reprinted from [72]. 19
2.3 Most typical crystal structure symmetries for piezoelectric materials. 20
2.4 Atomic lattice made of centrosymmetric unit cells (left), and of non-centrosymmetric distorted unit cells (right). 22
2.5 Evolution of the free energy in the case of a (a) second-order (b) first-order phase transition. Insets show the spontaneous polarization as a function of temperature, assuming zero polarization above T_0 (from [76]). 23
2.6 Polarization hysteresis loop of a ferroelectric material upon application of an exteral electric field (from [78]). 24
2.7 Domain formation in ferroelectrics. (a) Single-domain state leads to the formation of an electrical stray field (black lines). (b) The formation of surface charges provides a complete screening of the ferroelectric polarization. (c) 180-domain wall reduces the electric stray field and the depolarizing field contributing to the electrostatic energy. (d) Formation of multiple domains reduces the electric stray field (from [79]). 24
2.8 Schematic of the perovskite structure. Left: centrosymmetric simple cubic unit cell. Tetragonal (center) and orthorombic (right) unit cells allow for the ionic displacement leading to the formation of a ferroelectric polarization. 25
2.9 Sketch of some possible polarization configurations depending on the crystal structure. 26

2.10 Phase diagram of lead zirconate titanate (PZT) perovskite (from [85]). A typical MPT between the ferroelectric tetragonal (FE$_T$) phase and ferroelectric rhombohedral (FE$_R$) phase, is indicated by a horizontal red arrow, while a vertical red arrow indicates a typical PPT between the ferroelectric tetragonal (FE$_T$) phase and paraelectric cubic (PE$_C$) phase. 27
2.11 Phase diagram of pure potassium sodium niobate (KNN) perovskite (from [92]). Blue arrows indicate transitions: between ferroelectric orthorhombic, F$_O$ and ferroelectric tetragonal, F$_O$ (T$_{OT}$); between ferroelectric rhombohedral, F$_R$ and ferroelectric orthorhombic, F$_O$ (T$_{RO}$); since the figure represents pure KNN, the transition between ferroelectric rhombohedral, F$_R$ and ferroelectric tetragonal, F$_T$ (T$_{RT}$) is not shown. MPT between two orthorhombic phases through the intermediate tetragonal phase at x$_{Na}$ = 0.555 is indicated in red. 28
2.12 Fluorite structure of hafnium oxide. Oxygen distortions lead to a spontaneous polarization in the orthorhombic phase, which is an intermediate transition phase between tetragonal and monoclinic structures. 29

3.1 Schematic of the Pulsed Laser Deposition equipment components. 32
3.2 (a) Schematic of the X-ray interaction with a specimen, (b) sketch of an X-Ray diffractometer (from [118]). 34
3.3 (a) RHEED diffraction geometry and (b)−(g) diffraction patterns attributed to different thin film surface morphologies. Reprinted from [120]. 36
3.4 (a) Schematic of a Scanning Electron Microscope, with all the internal components (gun, electromagnetic lenses etc.) for the focusing of the electron beam onto the sample (reprinted from [122]). (b) Electron penetration volume into a material, from [123]. All different emission phenomena generated by the interaction of the electrons with matter are displayed, and different emission signals can be detected by specific techniques. 37
3.5 (a) Characteristic X-Ray emission process from an atom upon interaction with the electron beam. (b) Typical EDX emission spectrum, featuring the X-Ray peaks characteristic of the atomic species and the bremsstrahlung background emission. Reprinted from [123]. 38
3.6 PFM measurements on a material with ferroelectric domains (from [126]). The sign of the sample strain depends on the orientation of the domain polarization vector. 40
3.7 (a)−(b) PFM signal amplitude and phase upon writing concentric squared domains with a specific bias voltage. (c) AFM topography of the sample, which remains unchanged in this process. (d) Low-bias current reading after the "poling" still reveals the written squared pattern (from [127]). 41
3.8 Diagram of the PFM switching spectroscopy, from [126]. Applied signal profile on the left, and corresponding probed hysteresis loop on the right. 41
3.9 Sketch of the fabrication process. Starting from KNN/substrate structure, Ti contacts are deposited with the shadow mask (top part). Pt and Ni, instead, are deposited as a continuous layer, the pads are defined with the shadow mask by Ti deposition, and finally the pillars are separated by a dry etching process. . . . 43
3.10 Sketch of the (a) top-bottom and (b) top-top measurement configurations. Adapted from [128]. 43
3.11 Typical current-voltage (dashed blue) and polarization-voltage (solid black) profiles generated from different phenomena or combination of them. Reprinted from [130]. 45

3.12 Voltage pulse profile applied in the Dynamic Hysteresis Measurement (Sketch from [128]). Current is measured in correspondance of the coloured pulses. . . . 45

3.13 Applied voltage PUND train of pulses. A preset writing pulse precedes the measuring pulses, then the signals from U and D pulses are subtracted from those of P and N pulses. 46

3.14 (a) PUND Switching (blue) and Non-switching (red) half loops to be subtracted, taken from $Pb(Nb_xZr_yTi_z)O_3$ capacitors with Pt electrodes (reprinted from [131]). (b) Complete hysteresis loop. The black line represents the result of the subtraction, i.e. the pure remanence contribution. 46

4.1 SEM morphologies of the top surfaces of KNN samples grown with different substrate treatments. (a) and (f) S1: untreated substrate; (b) S2: 10-min Ar plasma (c) S3: 10-min Ar plasma and 10-min vacuum annealing; (d) S4: 10-min Ar plasma and 20-min vacuum annealing. (e) and (g) S5: 10-min O_2 plasma and 20-min vacuum annealing. With improved substrate cleaning and surface preparation, the amount of misoriented grains is considerably decreased. 50

4.2 Comparison of XRD spectra of KNN films grown on untreated Pt substrate (blue) and with plasma cleaning + vacuum annealing (red). A predominant (001) texture is revealed by the intense peak at 22.5°. A small (011) peak originated by misoriented crystallites is suppressed with a suitable substrate treatment procedure. 51

4.3 AFM surface topography of the (a) untreated Pt(111) substrate and (b) vacuum-annealed substrate. A flattening of the surface, with increased grain size and reduced roughness, promotes an optimal template for nucleation and growth dynamics. 52

4.4 XPS intensities of C1s and O1s peaks acquired from the Pt substrate before (black) and after (red) vacuum annealing treatment. A significant decrease in the intensity of the C 1s peak is observed after vacuum annealing, while the O1s peak is completely suppressed. 52

4.5 (a) Leakage current density of KNN grown with different substrate treatments. (b) Evaluation of leakage current densities at field E* = 75 kV/cm for the different samples. Leakage currents through the thin film are reduced by performing substrate vacuum annealing before the growth. In the inset, the KNN ferroelectric polarization loop of KNN on vacuum-annealed Pt is reported. 53

4.6 PFM topography (left), phase (center) and amplitude (right) scans for KNN thin films with different substrate cleaning procedures. (a)−(c): S1, untreated substrate; (d)−(f): S2, 10-min Ar plasma; (g)−(i): S3, 10-min Ar plasma, 10-min vacuum annealing; (j)−(l): S5, 10-min O−2 plasma, 20-min vacuum annealing. The bright and dark pattern in the phase signal reveals the out-of-plane polarization state of spontaneous domains. The PFM amplitude is proportional to the d_{33} coefficient. 54

5.1 Schematic of the doping method. A circular sector of $LiNbO_3$ single crystal is fixed onto of the KNN stoichiometric target so that with a circular rastering of the target for the laser ablation, both materials can be ablated. 60

5.2 SEM surfaces of the (a) undoped and (b) Li-doped KNN thin films. Upon doping, an increase in the amount of defects and misoriented crystallites arises. 62

5.3 Comparison of XRD diffraction spectra from undoped (blue) and Li-doped (green) samples. In both cases, the peaks at 22.5° and 45.4° are attributed to a (001) orientation of the films. A small amount of (001) phase is revealed by the small peak at 33.5° in doped KNN. The shift in the KNN peaks towards smaller angles in Li-doped KNN suggests the occurrence of an out-of-plane lattice expansion. . 62
5.4 XPS atomic ratio of Na/Nb for undoped (blue) and doped (green) KNN samples. The ratio is consistently more intense in all cases of undoped KNN, and with a greater difference in Na concentration between the samples in surface sensitive measurements. This suggests the occurrence of Li surface segregation phenomena if Li is assumed to mainly substitute Na. 64
5.5 ToF-SIMS depth profiles for undoped (top) and and Li-doped (bottom) KNN samples. Depth profiles acquired with Cs^+ sputtering beam to identify interfaces with higher precision are shown in panels a) and c). Depth profiles acquired with oxygen sputtering beam allowing to detect Li^+ ions are reported in panels b) and d). 65
5.6 Leakage current density profiles of undoped (blue) and Li-doped (green) KNN thin films. Li doping introduces a degradation of electrical properties with a leakage increase by one order of magnitude. 66
5.7 Topography (a,d), phase (b,e) and amplitude (c,f) PFM scans for undoped (a)−(c) and Li-doped (d)−(f) KNN samples. The phase signal reveals the orientation of the out-of-plane polarization, whereas the amplitude is proportional to the piezoelectric coefficient. 67

6.1 SEM top view of the surfaces of KNN thin films deposited at different growth temperatures. The epitaxial crystalline ordering below 600°C is disrupted by an inadequate thermal budget during growth, leading to increased roughness and worse compactness. 72
6.2 RHEED diffraction pattern of KNN thin films collected along [100] in plane direction of the STO substrate. Grazing incidence diffraction stripes are only displayed by 660°C- and 610°C-samples, confirming 2D ordered epitaxial growth. In all other samples, transmission diffraction spots appear from roughness features generated by a 3D island growth mode. 72
6.3 Comparison of leakage current density curves for all KNN samples grown from 740°C to 470°C. Lowering the growth temperature by almost 300°C is able to reduce leakage currents by almost 8 orders of magnitude. 73
6.4 Trend of the atomic ratios acquired by EDS as a function of the substrate growth temperature. High growth temperatures trigger the volatilization of the alkali elements, and the resulting samples are thus understoichiometric, whereas the atomic ratios of 3D non-epitaxial samples deposited at lower temperatures are close to the stoichiometric values. 74
6.5 Comparison between switching behaviour observed in 660°C film (grey and orange) and in 520°C film (black and red). The magnitude of both the switching current peaks and the remanent polarization increase by almost one order of magnitude. 75
6.6 Topography (a), phase (b) and amplitude (c) scans acquired by PFM on 2D epitaxial sample grown at 660°C. Ferroelectric spontaneous domains exhibit sharp domain contrast by 10 V in the phase signal coming from 180° domain walls. The domain configuration appears as periodic square shapes due to strain/stress relaxation mechanisms. 76

6.7 PFM local hysteresis cycles of the amplitude (left, proportional to the stress) and phase (right) acquired from the 660°C film. 77
6.8 CSAFM scans on the 660°C-sample. On the top, (a) topography and (b) current signal collected with a bias of 5 V on an area of $5\times5\mu m^2$. A the bottom, (c) topography and (d) current signal collected with a bias of 2 V on an area of $2\times2\mu m^2$. The squared configuration of the domains can clearly be imaged by domain switching current signal. (e) I(V) loop measured at the cross position in the topography. 78
6.9 Comparison of lattice reflections of 2D epitaxial KNN grown at 740°C, 660°C and 610°C. (a) $\theta - 2\theta$ pattern, (b) Reciprocal Space Maps around (103) lattice reflection. 79

7.1 Schematic of (a) top-bottom and (b) top-top measurement configurations. (c) bipolar triangular voltage profile applied for the characterization. 85
7.2 Leakage current density J acquired in the (a) top-bottom and (b) top-top configuration for: Pt/KNN/Pt (green), Ni/KNN/Pt (orange), Ti/KNN/Pt (blue). 86
7.3 Calculated low-field top-bottom resistance values for Pt-, Ni- and Ti-KNN. The values for $V_{TB} > 0$ (red) and $V_{TB} < 0$ (blue) overlap, in agreement with the fact that the resistance is an intrinsic property of the material and is bias-independent. 86
7.4 Schematic of the band diagram at the KNN/Pt interface: (a) zero bias condition ($V_{TB} = 0$), (b) reverse bias condition ($V_{TB} > 0$), (c) forward bias condition ($V_{TB} < 0$). 87
7.5 Electrical circuit diagram of the overall top-bottom configuration. The model accounts for the leaky behaviour of the oxide with a capacitor (C_{ox}) and a resistor (R_{ox}) in parallel, while the metal-semiconductor diode ($M - SC$ diode) is positioned at the bottom interface. 88
7.6 (a) Small signal differential capacitance for Ti-KNN in top-bottom measurement at various applied biases. (b) Average comparison of small signal capacitances for Pt-, Ni- and Ti-KNN. (c) The evaluated $1/C^2$ trend at zero frequency is linear with the applied bias, coherently with the model. 89
7.7 (a) Topography scan with green cross indicating the position at which the local I(V) was acquired (i.e. on a flat defectless surface position). (b) CS-AFM I(V) current curve acquired with a bias $V_{sample} = 5$ V. Conduction is impaired on the left side and promoted on the right side, coherently with the model. The opening of conduction allows for the switching mechanism to occur. 90
7.8 Electrical circuit diagram of the top-top configuration. Whatever the sign of the applied V_{TT}, there is always a reverse bias diode that absorbs the majority of the voltage drop. 91
7.9 Sketch of the suggested model to account for (a) Schottky and (b) Poole-Frenkel emission phenomena, assuming the presence of an effective barrier at the top interface. Adapted from [205] 92
7.10 Plot of $\ln(J/E)$ as a function of $\sqrt{E}$ for negative V_{TB}. A linear behaviour with the same slope is observed for all Metal-KNN samples, with a trend of the intercept with the metal work function, indicating a Schottky-controlled charge injection phenomenon. 94

8.1 AFM topographic scan of (a) 3-nm HZO and (b) 18-nm HZO, showing coherent 2D growth and crystal ordering at different thicknesses. (c) Evaluation of the average roughness trend with thickness. 99

8.2 (a) XRD $\theta - 2\theta$ patterns of HZO/LSMO/STO heterostructure with different HZO thicknesses. Epitaxial growth of LSMO and HZO is confirmed, with orthorombic o-HZO stabilized at low thicknesses (< 10 nm) and monoclinic m-HZO developing at higher thicknesses (> 10 nm). (b) Pole figure of 8.5 nm-HZO collected at the HZO(111) peak at $2\theta = 30°$. 12 peaks from (111) in-plane directions are detected, indicating the presence of 4 reciprocally perpendicular crystallographic domains. 99
8.3 Ferroelectric hysteresis loop from (a) DHM and (b) PUND (remanence) measurements of Au/HZO/LSMO capacitor devices. 100
8.4 Cycling tests of 8.5 nm-HZO with Au top electrodes. The devices show an endurance of up to 10'000 cycles. Current hysteresis is plotted in (a), and corresponding polarization loops are shown in (b). 101
8.5 (a) AFM topography of 8.5 nm-vacuum annealed-HZO thin film. (b) XRD scans comparing standard and vacuum-annealed heterostructures, showing no detectable phase deformations in HZO and LSMO layers. 102
8.6 Comparison of ferroelectric hysteresis loop from (a) DHM and (b) PUND (remanence) measurements of Au/HZO/LSMO capacitor devices with standard (blue) and vacuum-annealed (light blue) samples. 102
8.7 Surface of the DSO substrate scanned by AFM for (a) untreated DSO, (b) annealed DSO, (c) annealed and etched DSO. Line scans of the (d) trace and (e) retrace phase signal of DSO after etching show opposite phase contrast at step edges but of equal magnitude, which suggests the presence of single-terminated step edges. 104
8.8 Topography of the surface of HZO films acquired by AFM for HZO/LSMO grown on (a) untreated DSO and (b) treated DSO. Traces of particles in untreated DSO generate particulate defects in HZO, while the step-edged topography of the treated substrate is reproduced on top of HZO as well. 105
8.9 XRD analysis of HZO/LSMO on STO and treated/untreated DSO. (a) $\theta - 2\theta$ scans show an out-of-plain deformation of LSMO. RSMs of (b) LSMO/STO and (c) LSMO/DSO peaks around the (103) Bragg reflection confirm larger in-plane strain of LSMO on DSO. 106
8.10 Comparison of ferroelectric hysteresis loop from (a) DHM and (b) PUND (remanence) measurements of Au/HZO/LSMO capacitor devices: standard sample on STO (blue), vacuum-annealed sample on STO (light blue) and sample on DSO (red). 107

List of Tables

1.1 Dielectric and piezoelectric properties of the main lead-free thin films and PZT thin films [49]. 13

4.1 List of substrate preparation procedures associated to each KNN sample. 49
4.2 Piezoelectric coefficient and roughness parameters for the different KNN thin film samples grown with different substrate cleaning processes. 55

5.1 XPS quantitative data for undoped and Li-doped KNN: pristine surface. 63
5.2 XPS quantitative data for undoped and Li-doped KNN: surface after soft C_{60}^{+} cleaning. 63
5.3 XPS quantitative data for undoped and Li-doped KNN: bulk after consistent C_{60}^{+} sputtering. 63
5.4 Comparison of leakage currents evaluated at 25 kV/cm and 50 kV/cm for undoped and Li-doped KNN. 66

6.1 In-plane (a) and out-of-plane (c) lattice parameters of 2D epitaxial KNN thin films retrieved from Reciprocal Space Maps around (103) reflection. 80

8.1 Comparison of lattice parameter of simple cubic STO and pseudocubic lattice parameters (a_{PC}) of the scandate family. The in-plane lattice constants of the orthorhombic structure are also shown (from [130]). 104

Bibliography

[1] Markets and markets. "Piezoelectric Devices Market by Material (Piezoelectric Ceramics, Crystals, Polymers), Product (Piezoelectric Actuators, Transducers, Motors), Application (Aerospace and Defense, Industrial, Consumer), and Region - Global Forecast to 2025". In: *marketsandmarkets.com/ Market-Reports/piezoelectric-devices-market-256019882.html* ().

[2] Hrishikesh Kulkarni et al. "Application of piezoelectric technology in automotive systems". In: *Materials Today: Proceedings* 5.10 (2018), pp. 21299–21304.

[3] Hassan Elahi et al. "A review on applications of piezoelectric materials in aerospace industry". In: *Integrated Ferroelectrics* 211.1 (2020), pp. 25–44.

[4] Zhengbao Yang et al. "High-performance piezoelectric energy harvesters and their applications". In: *Joule* 2.4 (2018), pp. 642–697.

[5] Steven R Anton and Henry A Sodano. "A review of power harvesting using piezoelectric materials (2003–2006)". In: *Smart materials and Structures* 16.3 (2007), R1.

[6] Jürgen Rödel et al. "Transferring lead-free piezoelectric ceramics into application". In: *Journal of the European Ceramic Society* 35.6 (2015), pp. 1659–1681.

[7] Paul Muralt. "Recent progress in materials issues for piezoelectric MEMS". In: *Journal of the American Ceramic Society* 91.5 (2008), pp. 1385–1396.

[8] Chang-Hyo Hong et al. "Lead-free piezoceramics–Where to move on?" In: *Journal of Materiomics* 2.1 (2016), pp. 1–24.

[9] JF Scott. "Applications of modern ferroelectrics". In: *science* 315.5814 (2007), pp. 954–959.

[10] Fei Huang et al. "HfO 2-based highly stable radiation-immune ferroelectric memory". In: *IEEE Electron Device Letters* 38.3 (2017), pp. 330–333.

[11] T Mikolajick, U Schroeder, and S Slesazeck. "The past, the present, and the future of ferroelectric memories". In: *IEEE Transactions on Electron Devices* 67.4 (2020), pp. 1434–1443.

[12] Hsin-Hui Huang et al. "A comprehensive modeling framework for ferroelectric tunnel junctions". In: *2019 IEEE International Electron Devices Meeting (IEDM)*. IEEE. 2019, pp. 32–2.

[13] Pavlo Zubko and Jean-Marc Triscone. "A leak of information". In: *Nature* 460.7251 (2009), pp. 45–46.

[14] Chen Ge et al. "Recent progress in ferroelectric diodes: explorations in switchable diode effect". In: *Nano-Micro Letters* 5.2 (2013), pp. 81–87.

[15] Evgeny Y Tsymbal and Hermann Kohlstedt. "Tunneling across a ferroelectric". In: *Science* 313.5784 (2006), pp. 181–183.

[16] M Ye Zhuravlev et al. "Giant electroresistance in ferroelectric tunnel junctions". In: *Physical Review Letters* 94.24 (2005), p. 246802.

[17] Robin Khosla and Satinder K Sharma. “Integration of ferroelectric materials: An ultimate solution for next-generation computing and storage devices”. In: *ACS Applied Electronic Materials* 3.7 (2021), pp. 2862–2897.

[18] Walter Heywang, Karl Lubitz, and Wolfram Wersing. *Piezoelectricity: evolution and future of a technology*. Vol. 114. Springer Science & Business Media, 2008.

[19] Hans Jaffe. “Piezoelectric ceramics”. In: *Journal of the American Ceramic Society* 41.11 (1958), pp. 494–498.

[20] Muhtar Ahart et al. “Origin of morphotropic phase boundaries in ferroelectrics”. In: *Nature* 451.7178 (2008), pp. 545–548.

[21] Wenfeng Liu and Xiaobing Ren. “Large piezoelectric effect in Pb-free ceramics”. In: *Physical review letters* 103.25 (2009), p. 257602.

[22] Kenji Uchino. *Advanced piezoelectric materials: Science and technology*. Woodhead Publishing, 2017.

[23] Thomas R Shrout and Shujun J Zhang. “Lead-free piezoelectric ceramics: Alternatives for PZT?” In: *Journal of Electroceramics* 19.1 (2007), pp. 113–126.

[24] N Izyumskaya et al. “Processing, structure, properties, and applications of PZT thin films”. In: *Critical reviews in solid state and materials sciences* 32.3-4 (2007), pp. 111–202.

[25] Andrew J Bell and Otmar Deubzer. “Lead-free piezoelectrics-The environmental and regulatory issues”. In: *MRS Bulletin* 43.8 (2018), pp. 581–587.

[26] Yasuyoshi Saito et al. “Lead-free piezoceramics”. In: *Nature* 432.7013 (2004), pp. 84–87.

[27] M Demartin Maeder, D Damjanovic, and Njj Setter. “Lead free piezoelectric materials”. In: *Journal of Electroceramics* 13.1 (2004), pp. 385–392.

[28] Enrico Rossi. “Low level environmental lead exposure–a continuing challenge”. In: *The Clinical Biochemist Reviews* 29.2 (2008), p. 63.

[29] D Büsselberg et al. “Calcium Channels by Lead”. In: *Neurotoxicology* 14 (1993), pp. 2–3.

[30] LJ Casarett, CD Klaassen, and J Doull. “Toxic effects of metals”. In: *Casarett and Doull’s Toxicology: The Basic Science of Poisons* 1 (2007), pp. 1–4.

[31] Lyn Patrick. “Lead Toxicity, a review of the literature. Part I: Exposure, Evaluation, and treatment.” In: *Alternative medicine review* 11.1 (2006).

[32] RZ Sokol and N Berman. “The effect of age of exposure on lead-induced testicular toxicity”. In: *Toxicology* 69.3 (1991), pp. 269–278.

[33] David C Bellinger. “Very low lead exposures and children’s neurodevelopment”. In: *Current opinion in pediatrics* 20.2 (2008), pp. 172–177.

[34] Tee L Guidotti and Lisa Ragain. “Protecting children from toxic exposure: three strategies”. In: *Pediatric clinics of North America* 54.2 (2007), pp. 227–235.

[35] David E Jacobs et al. “The prevalence of lead-based paint hazards in US housing.” In: *Environmental health perspectives* 110.10 (2002), A599–A606.

[36] Lyn Patrick. “Lead toxicity part II: the role of free radical damage and the use of antioxidants in the pathology and treatment of lead toxicity.” In: *Alternative medicine review* 11.2 (2006).

[37] Herbert Needleman. “Lead poisoning”. In: *Annual review of medicine* 55.1 (2004), pp. 209–222.

[38] Hana R Pohl, Susan Z Ingber, and Henry G Abadin. “Historical view on lead: guidelines and regulations”. In: *Met. Ions Life Sci* 17 (2017), pp. 435–470.

[39] Thomas Morison Legge and Kenneth W Goadby. *Lead Poisoning & Lead Absorption, the Symptoms, Pathology & Prevention...* Vol. 5. E. Arnold, 1912.

[40] RJ Slack, JR Gronow, and N Voulvoulis. “The management of household hazardous waste in the United Kingdom”. In: *Journal of environmental management* 90.1 (2009), pp. 36–42.

[41] *DIRECTIVE 2002/95/EC OF THE EUROPEAN PARLIAMENT AND OF THE COUNCIL*. URL: Eur-lex.europa.eu. Archived from the original on 7 January 2016. Retrieved 3 July 2015. 2015.

[42] *Turnkey RoHS & RoHS II Module*. URL: assentcompliance.com. Archived from the original on 28 May 2016. Retrieved 17 May 2016. 2016.

[43] I Dalrymple et al. “An integrated approach to electronic waste (WEEE) recycling”. In: *Circuit world* (2007).

[44] B Jaffe. *WR COOK and H. JAFFE,“Piezoelectric Ceramics”*. 1971.

[45] JW Waanders. *Piezoelectric ceramics: properties and applications*. Philips Components, 1991.

[46] QQ Zhang et al. “High frequency broadband PZT thick film ultrasonic transducers for medical imaging applications”. In: *Ultrasonics* 44 (2006), e711–e715.

[47] Shujun Zhang et al. “Piezoelectric materials for high power, high temperature applications”. In: *Materials letters* 59.27 (2005), pp. 3471–3475.

[48] Kai Xu et al. “Superior piezoelectric properties in potassium–sodium niobate lead-free ceramics”. In: *Advanced materials* 28.38 (2016), pp. 8519–8523.

[49] Ahmad Safari and Maryam Abazari. “Lead-free piezoelectric ceramics and thin films”. In: *IEEE transactions on ultrasonics, ferroelectrics, and frequency control* 57.10 (2010), pp. 2165–2176.

[50] Feng Chen et al. “Reduction-induced Fermi level pinning at the interfaces between Pb (Zr, Ti) O3 and Pt, Cu and Ag metal electrodes”. In: *Journal of Physics D: Applied Physics* 44.25 (2011), p. 255301.

[51] Shinichiro Kawada et al. “(K, Na) NbO3-based multilayer piezoelectric ceramics with nickel inner electrodes”. In: *Applied physics express* 2.11 (2009), p. 111401.

[52] Hao-Cheng Thong et al. “The impact of chemical heterogeneity in lead-free (K, Na) NbO3 piezoelectric perovskite: Ferroelectric phase coexistence”. In: *Acta Materialia* 166 (2019), pp. 551–559.

[53] IP Batra, P Wurfel, and BD Silverman. “Phase transition, stability, and depolarization field in ferroelectric thin films”. In: *Physical Review B* 8.7 (1973), p. 3257.

[54] Doo Seok Jeong et al. “Emerging memories: resistive switching mechanisms and current status”. In: *Reports on progress in physics* 75.7 (2012), p. 076502.

[55] James W Reiner et al. “Crystalline oxides on silicon”. In: *Advanced Materials* 22.26-27 (2010), pp. 2919–2938.

[56] Mitsue Takahashi and Shigeki Sakai. “Self-aligned-gate metal/ferroelectric/insulator/semiconductor field-effect transistors with long memory retention”. In: *Japanese journal of applied physics* 44.6L (2005), p. L800.

[57] TS Böscke et al. “Ferroelectricity in hafnium oxide thin films”. In: *Applied Physics Letters* 99.10 (2011), p. 102903.

[58] Tingfeng Song et al. “Ferroelectric (Hf, Zr, La) O2 films”. In: *Applied Materials Today* 29 (2022), p. 101661.

[59] Tao Li et al. “Origin of ferroelectricity in epitaxial Si-doped HfO2 films”. In: *ACS applied materials & interfaces* 11.4 (2019), pp. 4139–4144.

[60] Uwe Schroeder, Cheol Seong Hwang, and Hiroshi Funakubo. *Ferroelectricity in Doped Hafnium Oxide: Materials, Properties and Devices*. Woodhead Publishing, 2019.

[61] Min Hyuk Park et al. “Review and perspective on ferroelectric HfO2-based thin films for memory applications”. In: *Mrs Communications* 8.3 (2018), pp. 795–808.

[62] Thomas Mikolajick et al. “Ferroelectric hafnium oxide for ferroelectric random-access memories and ferroelectric field-effect transistors”. In: *Mrs Bulletin* 43.5 (2018), pp. 340–346.

[63] S Mathews et al. “Ferroelectric field effect transistor based on epitaxial perovskite heterostructures”. In: *Science* 276.5310 (1997), pp. 238–240.

[64] Shosuke Fujii et al. “First demonstration and performance improvement of ferroelectric HfO 2-based resistive switch with low operation current and intrinsic diode property”. In: *2016 IEEE Symposium on VLSI Technology*. IEEE. 2016, pp. 1–2.

[65] Duygu Kuzum, Shimeng Yu, and HS Philip Wong. “Synaptic electronics: materials, devices and applications”. In: *Nanotechnology* 24.38 (2013), p. 382001.

[66] H Mulaosmanovic et al. “Novel ferroelectric FET based synapse for neuromorphic systems”. In: *2017 Symposium on VLSI Technology*. IEEE. 2017, T176–T177.

[67] Min Hyuk Park et al. “Effect of acceptor doping on phase transitions of HfO2 thin films for energy-related applications”. In: *Nano Energy* 36 (2017), pp. 381–389.

[68] S Kirbach, K Kühnel, and W Weinreich. "Piezoelectric hafnium oxide thin films for energy-harvesting applications". In: *2018 IEEE 18th International Conference on Nanotechnology (IEEE-NANO)*. IEEE. 2018, pp. 1–4.

[69] Kenji Uchino, Eiji Sadanaga, and Terukiyo Hirose. "Dependence of the crystal structure on particle size in barium titanate". In: *Journal of the American Ceramic Society* 72.8 (1989), pp. 1555–1558.

[70] Xiao-hong Du, Uma Belegundu Uma Belegundu, and Kenji Uchino Kenji Uchino. "Crystal orientation dependence of piezoelectric properties in lead zirconate titanate: theoretical expectation for thin films". In: *Japanese Journal of Applied Physics* 36.9R (1997), p. 5580.

[71] C Kunisch and H Holleck. "Design of piezoelectric thin films in the system AlN-ZnO". In: *Surface and Coatings Technology* 74 (1995), pp. 1028–1032.

[72] MUHAMMAD USMAN. "Studies of Ferroelectric and Multiferroic Behavior in [Ba (Zr, Ti) O3] 1-y:[CoFe2O4] y System". PhD thesis. Quaid-i-Azam University, Islamabad, 2015.

[73] Lan Chen et al. "Electric-field control of magnetization, jahn-teller distortion, and orbital ordering in ferroelectric ferromagnets". In: *Physical Review Letters* 122.24 (2019), p. 247701.

[74] RA Cowley. "Structural phase transitions I. Landau theory". In: *Advances in physics* 29.1 (1980), pp. 1–110.

[75] Biljana D Stojanovic. *Magnetic, ferroelectric, and multiferroic metal oxides*. Elsevier, 2018.

[76] Karin M Rabe et al. "Modern physics of ferroelectrics: Essential background". In: *Physics of Ferroelectrics*. Springer, 2007, pp. 1–30.

[77] Kenji Uchino and Shoichiro Nomura. "Critical exponents of the dielectric constants in diffused-phase-transition crystals". In: *Ferroelectrics* 44.1 (1982), pp. 55–61.

[78] Kang Min Ok, Eun Ok Chi, and P Shiv Halasyamani. "Bulk characterization methods for non-centrosymmetric materials: second-harmonic generation, piezoelectricity, pyroelectricity, and ferroelectricity". In: *Chemical Society Reviews* 35.8 (2006), pp. 710–717.

[79] Donald M Evans et al. "Domains and domain walls in multiferroics". In: *Physical Sciences Reviews* 5.9 (2020).

[80] Joginder Singh Galsin. *Solid state physics: An introduction to theory*. Academic Press, 2019.

[81] AF Devonshire. "Theory of ferroelectrics". In: *Advances in physics* 3.10 (1954), pp. 85–130.

[82] Jiagang Wu. *Advances in lead-free piezoelectric materials*. Springer, 2018.

[83] Jamshed Anwar and Dirk Zahn. "Polymorphic phase transitions: Macroscopic theory and molecular simulation". In: *Advanced Drug Delivery Reviews* 117 (2017), pp. 47–70.

[84] Jun Li and Thomas B Brill. "Kinetics of Solid Polymorphic Phase Transitions of CL-20". In: *Propellants, Explosives, Pyrotechnics: An International Journal Dealing with Scientific and Technological Aspects of Energetic Materials* 32.4 (2007), pp. 326–330.

[85] MJ Li et al. "Interband electronic transitions and phase diagram of PbZr1-xTixO3 ceramics: Ellipsometric experiment and first-principles theory". In: *Journal of Physics D: Applied Physics* 49.27 (2016), p. 275305.

[86] Dragan Damjanovic. "A morphotropic phase boundary system based on polarization rotation and polarization extension". In: *Applied Physics Letters* 97.6 (2010), p. 062906.

[87] B Jaffe, RS Roth, and S Marzullo. "Properties of piezoelectric ceramics in the solid-solution series lead titanate-lead zirconate-lead oxide: tin oxide and lead titanate-lead hafnate". In: *Journal of research of the National Bureau of Standards* 55.5 (1955), pp. 239–254.

[88] Ye Tian et al. "Phase transition behavior and electrical properties of lead-free (Ba1- xCax)(Zr0. 1Ti0. 9) O3 piezoelectric ceramics". In: *Journal of Applied Physics* 113.18 (2013), p. 184107.

[89] Ruzhong Zuo, Jian Fu, and Danya Lv. "Phase transformation and tunable piezoelectric properties of lead-free (Na0. 52K0. 48- xLix)(Nb1- x- ySbyTax) O3 system". In: *Journal of the American Ceramic Society* 92.1 (2009), pp. 283–285.

[90] Yang Zhang et al. "Effect of orthorhombic–tetragonal phase transition on structure and piezoelectric properties of KNN-based lead-free ceramics". In: *Dalton Transactions* 44.17 (2015), pp. 7797–7802.

[91] Cheol-Woo Ahn et al. "Correlation between phase transitions and piezoelectric properties in lead-free (K, Na, Li) NbO3–BaTiO3 ceramics". In: *Japanese journal of applied physics* 47.12R (2008), p. 8880.

[92] Jurij Koruza et al. "(K,Na)NbO3-based piezoelectric single crystals: Growth methods, properties, and applications". In: *Journal of Materials Research* 35.8 (2020), pp. 990–1016.

[93] Jiagang Wu, Dingquan Xiao, and Jianguo Zhu. "Potassium-sodium niobate lead-free piezoelectric materials: past, present, and future of phase boundaries". In: *Chemical reviews* 115.7 (2015), pp. 2559–2595.

[94] Dong Yang et al. "First-principles calculations of electrical properties, structure, and phase transition of K 1- x Na x NbO 3 solid solutions". In: *Physical Chemistry Chemical Physics* 19.40 (2017), pp. 27368–27373.

[95] Michael Shandalov and Paul C McIntyre. "Size-dependent polymorphism in HfO 2 nanotubes and nanoscale thin films". In: *Journal of Applied Physics* 106.8 (2009), p. 084322.

[96] Osamu Ohtaka et al. "Phase relations and volume changes of hafnia under high pressure and high temperature". In: *Journal of the American Ceramic Society* 84.6 (2001), pp. 1369–1373.

[97] Choong-Ki Lee et al. "First-principles study on doping and phase stability of HfO 2". In: *Physical Review B* 78.1 (2008), p. 012102.

[98] Hideo Hasegawa. "Rhombohedral phase produced in abraded surfaces of partially stabilized zirconia (PSZ)". In: *Journal of Materials Science Letters* 2.3 (1983), pp. 91–93.

[99] Mehmet Dogan et al. "Causes of ferroelectricity in HfO 2-based thin films: an ab initio perspective". In: *Physical Chemistry Chemical Physics* 21.23 (2019), pp. 12150–12162.

[100] Erich H Kisi, Christopher J Howard, and Roderick J Hill. "Crystal structure of orthorhombic zirconia in partially stabilized zirconia". In: *Journal of the American Ceramic Society* 72.9 (1989), pp. 1757–1760.

[101] S Starschich et al. "Ferroelectric and piezoelectric properties of Hf1-xZrxO2 and pure ZrO2 films". In: *Applied Physics Letters* 110.18 (2017), p. 182905.

[102] Fei Huang et al. "Fatigue mechanism of yttrium-doped hafnium oxide ferroelectric thin films fabricated by pulsed laser deposition". In: *Physical Chemistry Chemical Physics* 19.5 (2017), pp. 3486–3497.

[103] Takao Shimizu et al. "Study on the effect of heat treatment conditions on metalorganic-chemical-vapor-deposited ferroelectric Hf0. 5Zr0. 5O2 thin film on Ir electrode". In: *Japanese Journal of Applied Physics* 53.9S (2014), 09PA04.

[104] Min Hyuk Park et al. "Ferroelectricity and antiferroelectricity of doped thin HfO2-based films". In: *Advanced Materials* 27.11 (2015), pp. 1811–1831.

[105] Takao Shimizu et al. "The demonstration of significant ferroelectricity in epitaxial Y-doped HfO2 film". In: *Scientific reports* 6.1 (2016), pp. 1–8.

[106] Min Hyuk Park et al. "Effect of forming gas annealing on the ferroelectric properties of Hf0. 5Zr0. 5O2 thin films with and without Pt electrodes". In: *Applied Physics Letters* 102.11 (2013), p. 112914.

[107] Si Joon Kim et al. "Large ferroelectric polarization of TiN/Hf0. 5Zr0. 5O2/TiN capacitors due to stress-induced crystallization at low thermal budget". In: *Applied Physics Letters* 111.24 (2017), p. 242901.

[108] Karine Florent et al. "Understanding ferroelectric Al: HfO2 thin films with Si-based electrodes for 3D applications". In: *Journal of Applied Physics* 121.20 (2017), p. 204103.

[109] Takahisa Shiraishi et al. "Impact of mechanical stress on ferroelectricity in (Hf0. 5Zr0. 5) O2 thin films". In: *Applied Physics Letters* 108.26 (2016), p. 262904.

[110] M Hoffmann et al. "Stabilizing the ferroelectric phase in doped hafnium oxide". In: *Journal of Applied Physics* 118.7 (2015), p. 072006.

[111] Min Hyuk Park et al. "Surface and grain boundary energy as the key enabler of ferroelectricity in nanoscale hafnia-zirconia: a comparison of model and experiment". In: *Nanoscale* 9.28 (2017), pp. 9973–9986.

[112] Johannes Muller et al. "Ferroelectricity in simple binary ZrO2 and HfO2". In: *Nano letters* 12.8 (2012), pp. 4318–4323.

[113] Min Hyuk Park et al. "Evolution of phases and ferroelectric properties of thin Hf0. 5Zr0. 5O2 films according to the thickness and annealing temperature". In: *Applied Physics Letters* 102.24 (2013), p. 242905.

[114] Anna N Morozovska, Maya D Glinchuk, and Eugene A Eliseev. "Phase transitions induced by confinement of ferroic nanoparticles". In: *Physical Review B* 76.1 (2007), p. 014102.

[115] Chih-Hsin Lu et al. "Cubic phase stabilization in nanoparticles of hafnia-zirconia oxides: Particle-size and annealing environment effects". In: *Journal of Applied Physics* 103.12 (2008), p. 124303.

[116] Douglas B Chrisey, Graham K Hubler, et al. "Pulsed laser deposition of thin films". In: (1994).

[117] James A Greer. "History and current status of commercial pulsed laser deposition equipment". In: *Journal of Physics D: Applied Physics* 47.3 (2013), p. 034005.

[118] J Epp. "X-ray diffraction (XRD) techniques for materials characterization". In: *Materials characterization using nondestructive evaluation (NDE) methods*. Elsevier, 2016, pp. 81–124.

[119] PA Maksym and J L_ Beeby. "A theory of RHEED". In: *Surface Science* 110.2 (1981), pp. 423–438.

[120] Shuji Hasegawa. "Reflection high-energy electron diffraction". In: *Characterization of Materials* 97 (2012), pp. 1925–1938.

[121] KD Vernon-Parry. "Scanning electron microscopy: an introduction". In: *III-Vs Review* 13.4 (2000), pp. 40–44.

[122] URL: https://www.zeiss.com/corporate/int/home.html.

[123] URL: https://www.nhm-wien.ac.at/.

[124] Simon Burgess, Xiaobing Li, and James Holland. "High spatial resolution energy dispersive X-ray spectrometry in the SEM and the detection of light elements including lithium". In: *Microscopy and Analysis* 6 (2013), S8–S13.

[125] Daisuke Shindo and Tetsuo Oikawa. "Energy dispersive x-ray spectroscopy". In: *Analytical electron microscopy for materials science*. Springer, 2002, pp. 81–102.

[126] Nina Balke, Stephen Jesse, and Sergei Kalinin. "Roger Proksch, Asylum Research". In: ().

[127] Wei Jin Hu et al. "Optically controlled electroresistance and electrically controlled photovoltage in ferroelectric tunnel junctions". In: *Nature Communications* 7.1 (2016), pp. 1–9.

[128] Fina Ignasi et al. "Ferroelectricity and magnetoelectric coupling in magnetic ferroelectrics and artificial multiferroic heterostructures". In: (2012).

[129] Nikhil Karunakaran Ponon. "Fabrication and nano-scale characterisation of ferroelectric thin films". PhD thesis. Newcastle University, 2014.

[130] Arnoud Everhardt. "Novel phases in ferroelectric BaTiO3 thin films: Enhanced piezoelectricity and low hysteresis". In: (2017).

[131] J Joe T Evans. "The Relationship between Hysteresis and PUND Responses". In: *Radiant Technologies, Inc* (2008).

[132] Nicolas Ledermann et al. "100-Textured, piezoelectric Pb(ZrxTi1-x)O3 thin films for MEMS: integration, deposition and properties". In: *Sensors and Actuators A: Physical* 105.2 (2003), pp. 162–170.

[133] Nazanin Bassiri-Gharb et al. "Domain wall contributions to the properties of piezoelectric thin films". In: *Journal of Electroceramics* 19.1 (2007), pp. 49–67.

[134] Jiagang Wu and John Wang. *Phase transitions and electrical behavior of lead-free (K 0.50 Na 0.50) NbO 3 thin film*. 2009.

[135] Qi Yu et al. "Electrical properties of K0. 5Na0. 5NbO3 thin films grown on Nb: SrTiO3 single-crystalline substrates with different crystallographic orientations". In: *Journal of Applied Physics* 113.2 (2013), p. 024101.

[136] Tao Li et al. "Influence of LNO top electrodes on electrical properties of KNN/LNO thin films prepared by RF magnetron sputtering". In: *Journal of the American Ceramic Society* 96.3 (2013), pp. 787–790.

[137] Minh D Nguyen et al. "Lead-free (K0. 5Na0. 5) NbO3 thin films by pulsed laser deposition driving MEMS-based piezoelectric cantilevers". In: *Materials letters* 164 (2016), pp. 413–416.

[138] Lee-Seung Kang et al. "Growth Behavior and Electrical Properties of a (Na0. 5K0. 5) NbO3Thin Film Deposited on a Pt/Ti/SiO2/Si Substrate Using RFMagnetron Sputtering". In: *Journal of the American Ceramic Society* 94.7 (2011), pp. 1970–1973.

[139] Kenta Takagi et al. "Fabrication and evaluation of PZT/Pt piezoelectric composites and functionally graded actuators". In: *Journal of the European Ceramic Society* 23.10 (2003), pp. 1577–1583.

[140] Kenta Takagi et al. “Design and fabrication of functionally graded PZT/Pt piezoelectric bimorph actuator”. In: *Science and Technology of Advanced Materials* 3.2 (2002), p. 217.

[141] Roger Proksch. “In-situ piezoresponse force microscopy cantilever mode shape profiling”. In: *Journal of Applied Physics* 118.7 (2015), p. 072011.

[142] Catalin Harnagea et al. “Contact resonances in voltage-modulated force microscopy”. In: *Applied physics letters* 83.2 (2003), pp. 338–340.

[143] S Zhu and W Cao. “Imaging of 180 ferroelectric domains in LiTaO3 by means of scanning electron microscopy”. In: *physica status solidi (a)* 173.2 (1999), pp. 495–502.

[144] Hussein Nili et al. “Alkali ratio control for lead-free piezoelectric thin films utilizing elemental diffusivities in RF plasma”. In: *CrystEngComm* 15.36 (2013), pp. 7222–7229.

[145] Jin Soo Kim et al. “Frequency and temperature dependence of dielectric and electrical properties of radio-frequency sputtered lead-free K0. 48Na0. 52NbO3 thin films”. In: *Thin Solid Films* 518.22 (2010), pp. 6390–6393.

[146] Hai Joon Lee, Ill Won Kim, and Byung Moon Jin. “The effect of the substrate temperatures on (Na, K) NbO 3 ferroelectric thin films fabricated by RF magnetron sputtering”. In: *Journal of the Korean Physical Society* 56.12 (2010), pp. 417–420.

[147] Isao Tanaka et al. “Theoretical formation energy of oxygen-vacancies in oxides”. In: *Materials Transactions* 43.7 (2002), pp. 1426–1429.

[148] BS Kang, Si-Kyung Choi, and CH Park. “Diffuse dielectric anomaly in perovskite-type ferroelectric oxides in the temperature range of 400–700 C”. In: *Journal of applied physics* 94.3 (2003), pp. 1904–1911.

[149] Elisabeth Soergel. “Piezoresponse force microscopy (PFM)”. In: *Journal of Physics D: Applied Physics* 44.46 (2011), p. 464003.

[150] Roger Proksch and Sergei Kalinin. “Piezoresponse Force Microscopy”. In: *Microscopy Today* 17.6 (2009), pp. 10–15.

[151] Flavio Griggio et al. “Substrate clamping effects on irreversible domain wall dynamics in lead zirconate titanate thin films”. In: *Physical review letters* 108.15 (2012), p. 157604.

[152] VG Koukhar, NA Pertsev, and R Waser. “Thermodynamic theory of epitaxial ferroelectric thin films with dense domain structures”. In: *Physical Review B* 64.21 (2001), p. 214103.

[153] Andreas Seifert et al. “Microstructural evolution of dense and porous pyroelectric Pb1- xCaxTiO3 thin films”. In: *Journal of materials research* 14.5 (1999), pp. 2012–2022.

[154] Sudeep Joshi, MM Nayak, and K Rajanna. “Effect of post-deposition annealing on transverse piezoelectric coefficient and vibration sensing performance of ZnO thin films”. In: *Applied surface science* 296 (2014), pp. 169–176.

[155] V Nagarajan. “Scaling of the piezoelectric response in ferroelectric nanostructures: An effective clamping stress model”. In: *Applied Physics Letters* 87.24 (2005), p. 242905.

[156] Susan Trolier-McKinstry and Peter Muralt. “Thin film piezoelectrics for MEMS”. In: *Journal of Electroceramics* 12.1 (2004), pp. 7–17.

[157] R Steinhausen et al. “Clamping of piezoelectric thin films on metallic substrates: influence on the effective piezoelectric modulus d/sub 33”. In: *ISAF 1998. Proceedings of the Eleventh IEEE International Symposium on Applications of Ferroelectrics (Cat. No. 98CH36245)*. IEEE. 1998, pp. 93–96.

[158] AL Kholkin, KG Brooks, and N Setter. “Electromechanical properties of SrBi 2 Ta 2 O 9 thin films”. In: *Applied Physics Letters* 71.14 (1997), pp. 2044–2046.

[159] Ting Yu, Kin-Wing Kwok, and Helen Chan. “Sol-gel derived lead-free piezoelectric Bi 1/2 Na 1/2 TiO 3 thin film for MEMS applications”. In: *2006 15th ieee international symposium on the applications of ferroelectrics*. IEEE. 2006, pp. 186–188.

[160] Hiroshi Maiwa et al. “Electromechanical properties of Nd-doped Bi 4 Ti 3 O 12 films: A candidate for lead-free thin-film piezoelectrics”. In: *Applied physics letters* 82.11 (2003), pp. 1760–1762.

[161] Paul Muralt. “PZT thin films for microsensors and actuators: Where do we stand?” In: *IEEE transactions on ultrasonics, ferroelectrics, and frequency control* 47.4 (2000), pp. 903–915.

[162] L Lian and Nancy R Sottos. “Effects of thickness on the piezoelectric and dielectric properties of lead zirconate titanate thin films”. In: *Journal of Applied Physics* 87.8 (2000), pp. 3941–3949.

[163] M Abazari and A Safari. “Effects of doping on ferroelectric properties and leakage current behavior of KNN-LT-LS thin films on SrTiO 3 substrate”. In: *Journal of Applied Physics* 105.9 (2009), p. 094101.

[164] Barbara Malic et al. “Alkaline-earth doping in (K, Na) NbO3 based piezoceramics”. In: *Journal of the European Ceramic Society* 25.12 (2005), pp. 2707–2711.

[165] D Yang et al. “First-principles calculation of the effects of Li-doping on the structure and piezoelectricity of (K 0.5 Na 0.5) NbO 3 lead-free ceramics”. In: *Physical Chemistry Chemical Physics* 18.11 (2016), pp. 7702–7706.

[166] Jing Kong et al. “A Local Atomic Mechanism for Monoclinic-Tetragonal Phase Boundary Creation in Li-Doped Na0. 5K0. 5NbO3 Ferroelectric Solid Solution”. In: *Inorganic Chemistry* 61.10 (2022), pp. 4335–4349.

[167] Neamul H Khansur et al. “Stress-modulated optimization of polymorphic phase transition in Li-doped (K, Na) NbO3”. In: *Applied Physics Letters* 117.3 (2020), p. 032901.

[168] Jeong-Ho Cho et al. “Temperature stability and phase transition of Li0. 02 (KxNa1- x) 0.98 NbO3 ceramics”. In: *Ceramics International* 38 (2012), S315–S318.

[169] Rujie Zhao et al. “Phase structure regulation and enhanced piezoelectric properties of Li-doped KNN-based ceramics”. In: *Materials Chemistry and Physics* 245 (2020), p. 122806.

[170] C Groppi et al. “Effect of substrate preparation on the growth of lead-free piezoelectric (K0. 5Na0. 5) NbO3 on Pt (111)”. In: *Journal of Applied Physics* 129.19 (2021), p. 194102.

[171] NW Ashcroft and AR Denton. “Vegard’s law”. In: *Phys. Rev. A* 43.6 (1991), pp. 3161–3164.

[172] Phoi Chin Goh, Kui Yao, and Zhong Chen. “Lithium diffusion in (Li, K, Na) NbO3 piezoeletric thin films and the resulting approach for enhanced performance properties”. In: *Applied Physics Letters* 99.9 (2011), p. 092902.

[173] Isaac Abrahams and Peter G Bruce. “The mechanism of lithium ion mobility in solid electrolytes”. In: *Philosophical Magazine A* 64.5 (1991), pp. 1113–1118.

[174] Andreas R Stamminger et al. “Fast diffusion mechanism in Li 4 P 2 S 6 via a concerted process of interstitial Li ions”. In: *RSC advances* 10.18 (2020), pp. 10715–10722.

[175] Jie Cao et al. “Interstitial occupancy by extrinsic alkali cations in perovskites and its impact on ion migration”. In: *Advanced Materials* 30.26 (2018), p. 1707350.

[176] Jin Luo et al. “Domain evolution and piezoelectric response across thermotropic phase boundary in (K, Na) NbO3-based epitaxial thin films”. In: *ACS Applied Materials & Interfaces* 9.15 (2017), pp. 13315–13322.

[177] E Isotahdon et al. “Corrosion behaviour of sintered Nd–Fe–B magnets”. In: *Materials Chemistry and Physics* 135.2-3 (2012), pp. 762–771.

[178] Paul Heitjans and Jörg Kärger. *Diffusion in condensed matter: methods, materials, models*. Springer Science & Business Media, 2006.

[179] Asif Khan et al. “Piezoelectric thin films: an integrated review of transducers and energy harvesting”. In: *Smart Materials and Structures* 25.5 (2016), p. 053002.

[180] Takehisa Saito et al. “Pulsed-laser deposition of ferroelectric NaNbO3 thin films”. In: *Japanese journal of applied physics* 44.9S (2005), p. 6969.

[181] Maryam Abazari Torghabeh. *Development of lead-free piezoelectric thin films by pulsed laser deposition*. Rutgers The State University of New Jersey-New Brunswick, 2010.

[182] JS Speck and W Pompe. “Domain configurations due to multiple misfit relaxation mechanisms in epitaxial ferroelectric thin films. I. Theory”. In: *Journal of applied physics* 76.1 (1994), pp. 466–476.

[183] JS Speck et al. “Domain configurations due to multiple misfit relaxation mechanisms in epitaxial ferroelectric thin films. III. Interfacial defects and domain misorientations”. In: *Journal of applied physics* 78.3 (1995), pp. 1696–1706.

[184] R Proksch and S Kalinin. “Piezoresponse Force Microscopy with Asylum Research AFMs”. In: *Oxford Instruments Asylum Research, Inc.* 10 (2022), pp. 1–20.

[185] Anderson Janotti et al. "Effects of doping on the lattice parameter of SrTiO3". In: *Applied Physics Letters* 100.26 (2012), p. 262104.

[186] Takehisa Saito et al. "Pulsed laser deposition of high-quality (K, Na) NbO3 thin films on SrTiO3 substrate using high-density ceramic targets". In: *Japanese journal of applied physics* 43.9S (2004), p. 6627.

[187] M Abazari, EK Akdoğan, and A Safari. "Dielectric and ferroelectric properties of strain-relieved epitaxial lead-free KNN-LT-LS ferroelectric thin films on Sr Ti O 3 substrates". In: *Journal of Applied Physics* 103.10 (2008), p. 104106.

[188] Tao Li et al. "Electrical properties of lead-free KNN films on SRO/STO by RF magnetron sputtering". In: *Ceramics International* 40.1 (2014), pp. 1195–1198.

[189] Sergey Khartsev et al. "Comparative characteristics of Na0. 5K0. 5NbO3 films on Pt by pulsed laser deposition and magnetron sputtering". In: *Integrated Ferroelectrics* 55.1 (2003), pp. 769–779.

[190] Jill Guyonnet et al. "Conduction at domain walls in insulating Pb (Zr0. 2Ti0. 8) O3 thin films". In: *Advanced Materials* 23.45 (2011), pp. 5377–5382.

[191] W Pompe et al. "Elastic energy release due to domain formation in the strained epitaxy of ferroelectric and ferroelastic films". In: *Journal of Applied Physics* 74.10 (1993), pp. 6012–6019.

[192] HP Sun et al. "Evolution of dislocation arrays in epitaxial BaTiO 3 thin films grown on (100) SrTiO 3". In: *Applied Physics Letters* 84.17 (2004), pp. 3298–3300.

[193] WK Simon, EK Akdogan, and A Safari. "Anisotropic strain relaxation in (Ba 0.6 Sr 0.4) TiO 3 epitaxial thin films". In: *Journal of applied physics* 97.10 (2005), p. 103530.

[194] Ming-Wen Chu et al. "Impact of misfit dislocations on the polarization instability of epitaxial nanostructured ferroelectric perovskites". In: *Nature materials* 3.2 (2004), pp. 87–90.

[195] V Nagarajan et al. "Misfit dislocations in nanoscale ferroelectric heterostructures". In: *Applied Physics Letters* 86.19 (2005), p. 192910.

[196] Shweta Sharma et al. "Influence of top metal electrode on electrical properties of pulsed laser deposited lead-free ferroelectric K0. 35Na0. 65NbO3 thin films". In: *Materials Science in Semiconductor Processing* 103 (2019), p. 104618.

[197] Xiyue Zhang et al. "Oxygen defects in promoting the electrochemical performance of metal oxides for supercapacitors: recent advances and challenges". In: *Small Methods* 4.6 (2020), p. 1900823.

[198] Yizhu Sun et al. "Improved ferroelectric and photovoltaic properties of BiMnO3 modified lead-free K0. 5Na0. 5NbO3 solid-solution films". In: *Applied Physics Letters* 111.25 (2017), p. 253901.

[199] W-C Yang et al. "Polarization-dependent electron affinity of LiNbO 3 surfaces". In: *Applied Physics Letters* 85.12 (2004), pp. 2316–2318.

[200] Ching-Yuan Wu. "Interfacial layer theory of the Schottky barrier diodes". In: *Journal of Applied Physics* 51.7 (1980), pp. 3786–3789.

[201] KC Hwang and Sheng S Li. "A study of new surface passivation using P2S5/(NH4) 2S on GaAs Schottky barrier diodes". In: *Journal of applied physics* 67.4 (1990), pp. 2162–2165.

[202] C Hu. "PN and metal-semiconductor junctions". In: *UC, Berkeley, EE Class Note* (2009), pp. 89–156.

[203] MW Allen and SM Durbin. "Influence of oxygen vacancies on Schottky contacts to ZnO". In: *Applied Physics Letters* 92.12 (2008), p. 122110.

[204] W Jiang et al. "Mobility of oxygen vacancy in SrTiO3 and its implications for oxygen-migration-based resistance switching". In: *Journal of Applied Physics* 110.3 (2011), p. 034509.

[205] Fu-Chien Chiu. "A review on conduction mechanisms in dielectric films". In: *Advances in Materials Science and Engineering* 2014 (2014).

[206] Xumei Zhao et al. "Improved transmittance and ferroelectric properties realized in KNN ceramics via SAN modification". In: *Journal of the American Ceramic Society* 101.11 (2018), pp. 5127–5137.

[207] Mahesh Peddigari et al. "Microwave dielectric and nonlinear optical studies on radio-frequency sputtered Dy2O3-doped KNN thin films". In: *Journal of the American Ceramic Society* 100.7 (2017), pp. 3013–3023.

[208] J Müller et al. "Ferroelectric hafnium oxide: A CMOS-compatible and highly scalable approach to future ferroelectric memories". In: *2013 IEEE International Electron Devices Meeting*. IEEE. 2013, pp. 10–8.

[209] Yu Yun et al. "Intrinsic ferroelectricity in Y-doped HfO2 thin films". In: *Nature Materials* 21.8 (2022), pp. 903–909.

[210] Tingfeng Song et al. "Improved polarization and endurance in ferroelectric Hf 0.5 Zr 0.5 O 2 films on SrTiO 3 (110)". In: *Nanoscale* 14.6 (2022), pp. 2337–2343.

[211] Yingfen Wei et al. "A rhombohedral ferroelectric phase in epitaxially strained Hf0. 5Zr0. 5O2 thin films". In: *Nature materials* 17.12 (2018), pp. 1095–1100.

[212] Zimeng Zhang et al. "Epitaxial ferroelectric Hf0. 5Zr0. 5O2 with metallic pyrochlore oxide electrodes". In: *Advanced materials* 33.10 (2021), p. 2006089.

[213] Jike Lyu et al. "Robust ferroelectricity in epitaxial Hf1/2Zr1/2O2 thin films". In: *Applied Physics Letters* 113.8 (2018), p. 082902.

[214] Chun-Hu Cheng and Albert Chin. "Low-leakage-current DRAM-like memory using a one-transistor ferroelectric MOSFET with a Hf-based gate dielectric". In: *IEEE electron device letters* 35.1 (2013), pp. 138–140.

[215] Han Joon Kim et al. "A study on the wake-up effect of ferroelectric Hf 0.5 Zr 0.5 O 2 films by pulse-switching measurement". In: *Nanoscale* 8.3 (2016), pp. 1383–1389.

[216] Pengfei Jiang et al. "Wake-Up Effect in HfO2-Based Ferroelectric Films". In: *Advanced Electronic Materials* 7.1 (2021), p. 2000728.

[217] KHHK Carl and KH Hardtl. "Electrical after-effects in Pb (Ti, Zr) O3 ceramics". In: *Ferroelectrics* 17.1 (1977), pp. 473–486.

[218] Š Chromik et al. "LSMO thin films with high metal–insulator transition temperature on buffered SOI substrates for uncooled microbolometers". In: *Applied surface science* 312 (2014), pp. 30–33.

[219] Milena Cervo Sulzbach et al. "Unraveling ferroelectric polarization and ionic contributions to electroresistance in epitaxial Hf0. 5Zr0. 5O2 tunnel junctions". In: *Advanced Electronic Materials* 6.1 (2020), p. 1900852.

[220] Yingfen Wei et al. "Magneto-ionic control of spin polarization in multiferroic tunnel junctions". In: *npj Quantum Materials* 4.1 (2019), pp. 1–6.

[221] Pavan Nukala et al. "Reversible oxygen migration and phase transitions in hafnia-based ferroelectric devices". In: *Science* 372.6542 (2021), pp. 630–635.

[222] Tingfeng Song, Florencio Sánchez, and Ignasi Fina. "Impact of non-ferroelectric phases on switching dynamics in epitaxial ferroelectric Hf0. 5Zr0. 5O2 films". In: *APL Materials* 10.3 (2022), p. 031108.

[223] Max Falkowski and Alfred Kersch. "Ab initio interphase characteristics in HfO2 and ZrO2 and nucleation of the polar phase". In: *Applied Physics Letters* 118.3 (2021), p. 032905.

[224] Uwe Schroeder et al. "Temperature-Dependent Phase Transitions in HfxZr1-xO2 Mixed Oxides: Indications of a Proper Ferroelectric Material". In: *Advanced Electronic Materials* (2022), p. 2200265.

[225] Monica Materano et al. "Interplay between oxygen defects and dopants: effect on structure and performance of HfO 2-based ferroelectrics". In: *Inorganic Chemistry Frontiers* 8.10 (2021), pp. 2650–2672.

[226] Lun Xu et al. "Kinetic pathway of the ferroelectric phase formation in doped HfO2 films". In: *Journal of Applied Physics* 122.12 (2017), p. 124104.

[227] Saul Estandia et al. "Engineering ferroelectric Hf0. 5Zr0. 5O2 thin films by epitaxial stress". In: *ACS Applied Electronic Materials* 1.8 (2019), pp. 1449–1457.

[228] Tingfeng Song et al. "Positive Effect of Parasitic Monoclinic Phase of Hf0. 5Zr0. 5O2 on Ferroelectric Endurance". In: *Advanced Electronic Materials* 8.1 (2022), p. 2100420.

[229] Josée E Kleibeuker et al. "Atomically Defined Rare-Earth Scandate Crystal Surfaces". In: *Advanced Functional Materials* 20.20 (2010), pp. 3490–3496.

[230] O Yu Gorbenko et al. "Epitaxial stabilization of oxides in thin films". In: *Chemistry of materials* 14.10 (2002), pp. 4026–4043.

[231] Andrei R Kaul, Oleg Yu Gorbenko, and Anton A Kamenev. "The role of heteroepitaxy in the development of new thin-film oxide-based functional materials". In: *Russian chemical reviews* 73.9 (2004), pp. 861–880.

[232] Shi Liu and Brendan M Hanrahan. "Effects of growth orientations and epitaxial strains on phase stability of HfO 2 thin films". In: *Physical Review Materials* 3.5 (2019), p. 054404.

[233] Robin Materlik, Christopher Künneth, and Alfred Kersch. "The origin of ferroelectricity in Hf1- xZrxO2: A computational investigation and a surface energy model". In: *Journal of Applied Physics* 117.13 (2015), p. 134109.

[234] Darrell G Schlom et al. "Strain tuning of ferroelectric thin films". In: *Annual Review of Materials Research* 37.1 (2007), pp. 589–626.

[235] Anja Herpers et al. "Spectroscopic Proof of the Correlation between Redox-State and Charge-Carrier Transport at the Interface of Resistively Switching Ti/PCMO Devices". In: *Advanced materials* 26.17 (2014), pp. 2730–2735.